Nanofabrication of cell-instructive and bactericidal surfaces for bone implants

Nanofabrication

of cell-instructive and bactericidal surfaces for

bone implants

Nanofabrication

of cell-instructive and bactericidal surfaces for

bone implants

Proefschrift

ter verkrijging van de graad van doctor

aan de Technische Universiteit Delft,

op gezag van de Rector Magnificus, Prof.dr.ir. T.H.J.J. van der Hagen,

voorzitter van het College voor Promoties,

in het openbaar te verdedigen op maandag 10 Jan 2022 om 12:30 uur.

door

Mahya GANJIAN

Master of Science in Electrical Engineering,

Universiteit van Teheran, Iran,

geboren te Teheran, Iran.

Dit proefschrift is goedgekeurd door de promotor: Prof.dr. A.A. Zadpoor en copromotor: Dr.ir. L.E. Fratila-Apachitei.

Samenstelling promotiecommissie bestaat uit:

Rector magnificus,	Voorzitter
Prof.dr. A.A. Zadpoor,	Technische Universiteit Delft, promotor
Dr.ir. L.E. Fratila-Apachitei,	Technische Universiteit Delft, copromotor

Onafhankelijke leden:

Prof. dr. N. Gadegaard,	Universiteit van Glasgow
Prof. dr. U. Staufer,	Technische Universiteit Delft
Prof dr. J.M.C. Mol,	Technische Universiteit Delft
Prof. dr. R.G.H.H. Nelissen,	Leids Universitair Medisch Centrum en Technische Universiteit Delft

Overig lid:

Prof. dr. P. Breedveld,	Technische Universiteit Delft

An electronic version of this dissertation is available at http://repository.tudelft.nl/

Summary

Recurrent bacterial infection is one of the main reasons of implant failure, hugely impacting the patients' quality of life, and ultimately resulting in morbidity and even mortality. This type of infection starts with the attachment of the bacteria to the implant surface, leading to biofilm formation and, thus, high resistance against antibacterial agents. To date, numerous strategies have been proposed to prevent biofilm formation and implant-associated infections. It has been revealed that physical surface patterns with specific dimensions and mechanical properties may have the potential to kill implant associated bacteria through a mechanical mechanism, while regulating stem cell differentiation.

Therefore, the aim of this research was to advance the development of the nanofabrication methods for generation of patterns with controlled geometrical and mechanical characteristics, and assess their potential for achieving a dual surface biofunctionality for bone implants, namely osteogenic and bactericidal effects. The focus was on submicron to nanoscale patterns generated on 2D and 3D surfaces.

In chapters 2 and 3, we used electron beam-induced deposition (EBID) as a nanoscale additive manufacturing (=3D printing) method to fabricate nanopillars with precisely controlled dimensions with the aim to assess their bactericidal effects against Gram-positive *Staphylococcus aureus* and Gram-negative *Escherichia coli* bacteria, as the major types of bacteria associated with peri-implant infections. The method enabled fabrication of nanopillars with controlled height, diameter and spatial arrangement down to 10 nm height and the findings revealed that nanopillars arrays possessing characteristics that showed previously osteogenic activity are capable of killing both Gram-negative and Gram-positive bacteria. Furthermore, decreasing the interspace between the pillars significantly enhanced the bactericidal effect of the nanopillars. Direct penetration of the nanopillars into the bacterial cell wall was recognized as a possible killing mechanism.

The mechanical properties of such nanoscale structures can influence their bactericidal efficiency. In addition, these properties are key factors in determining the fate of stem cells.

Therefore, in chapter 4, a novel atomic force microscopy (AFM)-based technique was developed to measure relevant mechanical properties of the EBID nanopillars fabricated in chapters 2 and 3. A finite element model (FEM) was developed as well to calculate the interaction force between the cultured *S. aureus* bacteria and the nanopillars, and to assess the stress state of the nanopillars. In addition to generating unique quantitative data on the mechanical properties of single nanopillars interacting with cells, the currently developed method resulted in new potential strategies for enhancing the bactericidal efficiency of nanopatterned surfaces, which have to do with the geometry and mechanical properties of the nanopillars.

In chapter 5, we used inductively coupled plasma reactive ion etching (ICP RIE) as a high throughput technique, to fabricate titanium pillars on the titanium (Ti) surface (also known as black titanium surfaces, bTi). The effects of different processing parameters of ICP RIE on the resultant bTi surfaces were investigated. Thereafter, three distinct bTi surfaces were designed and fabricated using ICP RIE, each featuring different pillar designs. The interactions between the bTi surfaces, MC3T3-E1 preosteoblast cells, and *Staphylococcus aureus* bacteria were then investigated and the results pointed out that optimization of the ICP RIE process conditions is essential to maximize the two different desirable biofunctionalities, namely the osteogenic differentiation of preosteoblasts and the bactericidal efficiency against *Staphylococcus aureus*. This study demonstrated the strong potential of the ICP RIE process to generate clinically relevant titanium surfaces with a dual-biofunctionality for orthopedic and dental implants.

Although the ICP RIE method presented in chapter 5 enabled us to produce bio-instructive bTi nanopatterns on a large area of Ti substrate, this technique is only applicable to 2D samples. However, for implant applications, the 3D porous structure of Ti scaffolds needs to be decorated with such pillars. Therefore, in chapter 6, we proposed a novel metal crumpling technique to make nanopatterned 3D metallic scaffolds with desired size, porosity, and mechanical strength thereby addressing the limitation of the currently available nanofabrication techniques for creating nanopatterns on nonplanar/3D surfaces. The final porosity of such structures can be controlled by the rational design of the porosity of the initial sheet. Micro-computed tomography (μCT) scans and finite element analysis (FEA) simulations showed that applying low or high deformation velocity did not significantly

change the morphological and mechanical properties of the resultant scaffolds. Finally, the adaptation of MC3T3-E1 preosteoblast cells to the bTi nanopatterned scaffolds was found to be similar to previous reports on identical nanopatterns created on flat Ti sheets. This proof of concept for the newly developed method opens new avenues for development of 3D titanium structures decorated with biofunctional surface patterns for bone implants. The combination of volume porosity and bTi nanopatterns could be used to promote bone tissue engineering and minimize implant associated infections.

In chapter 7 we developed a facile method for high throughput patterning of various types of surfaces with nanoscale and submicron patterns whose geometries are precisely controlled. Assessing the adaptation of MC3T3-E1 preosteoblast cells to the fabricated patterns showed that the submicron pillars significantly influence the cytoskeletal organization, cell area, cell elongation, and formation of focal adhesions. These types of pillars significantly increased the expression of osteopontin (OPN) as compared with a control surface. The results of this study clearly showed the advantages of nanoimprint lithography as a unique high-throughput yet precise method for the patterning of large areas of a wide variety of substrate materials that are relevant for systematic cell studies, while guarantying the quality and resolution of the nanopatterns required for further biological assessments.

Samenvatting

Terugkerende bacteriële infecties zijn een van de hoofdredenen waardoor implantaten falen. Dit heeft een grote invloed op de kwaliteit van het leven van de patiënt en kan ervoor zorgen dat de patiënt invalide wordt of zelfs overlijdt. Een bacteriële infectie begint met bacteriën die zich hechten aan het oppervlak van een implantaat waardoor een biofilm wordt gevormd. Daardoor wordt een hoge resistentie tegen antibacteriële middelen gecreëerd. Tot op heden zijn er diverse strategieën voorgesteld om de vorming van biofilms en implantaat-gerelateerde infecties te voorkomen. Het is onthuld dat fysieke oppervlaktepatronen met specifieke afmetingen en mechanische eigenschappen verschillende types bacteriën kunnen doden door een mechanisch mechanisme. Tegelijkertijd kunnen deze nanopatronen de differentiatie van stamcellen reguleren.

Daarom is het doel van dit werk om de huidige productietechnieken op nanoschaal verder te ontwikkelen zodat nanopatronen met gewenste geometrische en mechanische eigenschappen gemaakt kunnen worden en de wisselwerking tussen de nanopatronen, bacteriën en pre-osteoblasten beter te begrijpen.

In hoofdstukken 2 en 3 hebben we electron beam-induced deposition (EBID) als een 3D-printtechniek gebruikt om op nanoschaal pilaren te produceren met nauwkeuring controle over hun afmetingen. Van deze pilaren hebben we de bacteriedodende werking tegen Grampositieve *Staphylococcus aureus* en Gramnegatieve *Escherichia coli* bacteriën, de twee meest voorkomende bacteriën op het oppervlak van een botvervanger, beoordeeld. Onze bevindingen bevestigen dat nanopatronen met een nauwkeurige gecontroleerde afmetingen Gramnegatieve en -positieve bacteriën kunnen doden. Het verminderen van de afstand tussen de pilaren heeft een significant effect op de bacteriedodende werking van de nanopatronen. Directe penetratie van de nanopatronen in de celwand was de het mechanisme waardoor de bacteriën gedood werden.

De mechanische eigenschappen van structuren op nanoschaal kunnen de bacteriedodende werking van nanopatronen beïnvloeden. Daarnaast zijn deze eigenschappen

belangrijke factoren in het differentiatieproces van stamcellen. Daarom is er in hoofdstuk 4 een nieuwe en snelle techniek ontworpen die gebaseerd is op atomic force microscopy (AFM) om de mechanische eigenschappen van de EBID nanopilaren uit hoofdstuk 2 en 3 te bepalen. Daarnaast was er een eindige-elementenmodel (EEM) ontwikkeld om de kracht van de interactie tussen de nanopilaren en de gekweekte *Staphylococcus aureus* bacteriën te berekenen en de spanning van de nanopilaren te bepalen. Naast het genereren van unieke kwantitatieve data van de mechanische eigenschappen van enkele nanopilaren tijdens hun interactie met de cellen heeft deze methode geleid tot nieuwe potentiële strategieën om de bacteriedodende werking van oppervlakken met nanopatronen te verbeteren.

In hoofdstuk 5 hebben we inductively coupled plasma reactive ion etching (ICP RIE) gebruikt om met een hoge verwerkingscapaciteit titanium pijlers aan te brengen op een titanium oppervlak. In deze studie werd het effect van de verschillende procesparameters van ICP RIE op de titanium oppervlakken onderzocht. Vervolgens werden titanium oppervlakken met drie verschillende nanopilaren ontworpen en geproduceerd met ICP RIE. De interacties van de nanopatronen met MC3T3-E1 pre-osteoblasten en *Staphylococcus aureus* bacteriën werden onderzocht en de mogelijke mechanismen achter de osteogene en bacteriedodende werking werden bekeken. De resultaten laten zien dat optimalisatie van de procesvoorwaarden essentieel is om deze bio-functionaliteiten te maximaliseren. Deze studie biedt een nieuw perspectief op de duale functionaliteit van titanium oppervlakken en laten zien hoe het ontwerp van nanopatronen en productieparameters gebruikt kunnen worden om een oppervlakte topografie te maken met een gebalanceerde bacteriedodende en osteogene werking.

Ondanks dat de ICP RIE techniek uit hoofdstuk 5 ertoe heeft geleid dat we bio-instructieve nanopatronen kunnen aanbrengen op een groot titanium substraat kan deze techniek alleen toegepast worden op tweedimensionale oppervlakken. Daarom is het onmogelijk om deze nanopatronen aan te brengen op driedimensionale structuren die gebruikt worden voor implantaten. Daarom wordt in hoofdstuk 6 een verfrommeltechniek voorgesteld. Met deze methode kunnen nanopatronen aangebracht worden op tweedimensionale metalen platen die vervolgens verfrommeld kunnen worden tot driedimensionale structuren met een gewenste grootte, porositeit en mechanische sterkte. Controle over de uiteindelijke porositeit kan met rationeel ontwerpen van de initiële plaat

bereikt worden. Microcomputertomografie (μCT) scans en eindige-elementensimulaties lieten zien dat de snelheid waarmee de platen vervormd worden geen significant effect hebben op de morfologische en mechanische eigenschappen van de uiteindelijke structuren. Als laatste werd er aangetoond dat het gedrag van MC3T3-E1 pre-osteoblasten op de verfrommelde driedimensionale structuren vergelijkbaar was met hun gedrag op de titanium platen met nanopatronen. De verschillende functionaliteiten van ons ontwerp, zoals de mogelijkheid om de afmetingen, porositeit, vervormingssnelheid en mechanische eigenschappen te controleren en het kunnen aanbrengen van complexe oppervlaktepatronen, zorgen ervoor dat de verfrommeltechniek een potentiële techniek is om botvervangers te maken met gewenste nanopatronen. De combinatie van een hoge porositeit en oppervlakte nanopatronen kunnen gebruikt worden om het botherstel te bevorderen.

In hoofdstuk 7 hebben we een eenvoudige methode ontwikkeld om met een hoge verwerkingscapaciteit oppervlaktepatronen aan te brengen op nano- en submicroschaal met een nauwkeurige controle over de geometrie. Beoordeling van de aanpassing van de MC3T3-E1 pre-osteoblasten op de geproduceerde patronen laat zien dat de submicro-pilaren een significant effect hebben op de organisatie van het cytoskelet, het celoppervlak, de langwerpigheid van de cel en de vorming van focale contacten. Deze type pilaren verbeterden significant de uitdrukking van osteopontin (OPN) ten opzichte van onbehandelde oppervlakken. De resultaten van deze studie lieten duidelijk de voordelen van nanoimprint litography zien als een unieke techniek met een hoge verwerkingscapaciteit en hoge nauwkeurigheid voor het aanbrengen van patronen op grote oppervlakken op verschillende substraatmaterialen die relevant zijn voor systematische celstudies met een garantie van de kwaliteit en resolutie die nodig is voor verdere biologische beoordeling.

In hoofdstuk 8 worden de belangrijkste bevindingen van dit proefschrift besproken. Daarnaast worden er aanbevelingen gedaan voor toekomstige onderzoeken en alternatieve toepassingen voorgesteld.

Contents

1

Introduction

1.1. Background

Increasing life expectancy worldwide has caused a growing demand for bone implants. Currently, more than two million implant surgeries are performed every year around the world [1]. Bacterial infection is one of the major reasons for the failure of orthopedic implants [2]. Implant-associated infections adversely influence the patient's quality of life, necessitate (multiple) revision surgeries, increase healthcare costs, and could eventually result in morbidity and even mortality [3].

To date, several approaches have been proposed to prevent implant-associated infections. For instance, chemical and/or physical modification of the implant surface to prevent bacterial adhesion is one of the strategies. However, this approach suffers from the problem that the attachment and proliferation of the cells of the human body, which are essential for tissue regeneration and for supporting osseointegration, may be also hampered [2]. Another strategy is killing the bacteria adhered to the surface using either physical or chemical techniques (bactericidal surfaces). Surface biofunctionalization through specific nanoparticles/ions (Cu, Ag, or Zn) [4] and antibiotic releasing coatings [2] are examples of chemical approaches in this category to kill the bacteria and prevent biofilm formation. However, using antibiotic releasing agents for a long time will make the bacteria resistant to those agents. On the other hand, surfaces incorporating specific nanoparticles/ions may cause cytotoxicity to the host cells [4]. The abovementioned challenges of chemical approaches highlight the importance of physical techniques to prevent implant-associated infections [2, 5].

In 1991, Clark *et al.* employed surface nanopatterns in an attempt to influence cell behavior *in vitro* and *in vivo* [6]. Thereafter, researchers have made various efforts to investigate the effects of surface nano/micro patterns as physical cues, for both bacteria and mammalian cell response. These surface-related parameters can be tuned to inhibit bacterial growth and induce tissue regeneration on the surface of bone implants [2, 5]. The challenge is fabricating patterns that eventually can selectively kill bacteria while simultaneously supporting the growth and functions of relevant host cells. Recent advances in nano/micro-fabrication techniques have enabled us to produce patterns with arbitrary shapes, roughness values, and dimensions (ranging between sub-10 nm and > 100 μm). Furthermore, these

types of patterns have shown their potential to affect the attachment, proliferation, and differentiation of cells. While mesoscale (and > 100 μm) patterns can influence the cell behavior at colony level, submicron- and microscale patterns (100 nm to 1000 nm) affect the cell response at the single cell level. At the nanoscale (at least one dimension below 100 nm), patterns can even interact with single cell receptors [5].

Among different topographies and surface features, high aspect ratio nano/submicron pillars (height/diameter > 2) have been demonstrated to function as effective cues to perturb and control not only mammalian cell response (*e.g.,* cell adhesion, proliferation, migration, and differentiation) but also bacterial response [7]. Despite a multitude of studies to discover the influence of surface topographical features on the cell and bacterial response, so many questions remain unanswered. One of the main reasons is the abundance of design parameters (*i.e.*, geometry, interspacing, height, diameter, aspect ratio, and sharpness) of such pillars together with their mechanical properties, each imposing its own effect on cells.

To answer the many open questions in this area of research, the application of highly accurate and precise nano/submicron techniques including electron beam-induced deposition (EBID), electron beam lithography (EBL), and focused ion beam (FIB) is required to reach feature sizes in the range of sub-10 nm [8] for further cell studies. Using these techniques, one can have control over every single dimension of the pillars, as a key parameter to systematically study the effects of each parameter on the cell response.

However, the abovementioned techniques suffer from an extremely low production speed and low throughput, which limits extending the platform for studying the interaction between cells and patterns [3, 9]. Therefore, developing fast and high throughput techniques is a vital step that should be taken so as to avoid spending too much time, energy, and money on producing specimens. Inductively coupled plasma reactive ion etching (ICP RIE), soft lithography, hydrothermal treatment, and nanoimprint lithography (NIL) are some examples of the fabrication methods that could help us in this regard.

As already mentioned, the mechanical properties of the nano/submicron pillars are important cues affecting bacterial and cell response. It is, therefore, highly important to understand the nanomechanical response of nanopatterns on the intended surface. For instance, the killing efficiency of nano/submicron pillars depends on the stiffness of the pillar, which determines its ability to penetrate the bacterial cell wall and damage it [10]. Moreover,

3

it has been already shown that the substrate stiffness affects stem cell differentiation [5]. Furthermore, the determination of the mechanical properties of individual nano/submicron pillars allows us to estimate the interaction force between pillars and mammalian cell/bacteria, resulting in a better understanding of the mechanisms through which nanopatterns affect bacteria/cell behavior [10]. To this end, developing a facile technique to characterize the mechanical properties of individual nanopillars *per se*, and under interaction with cells is of high importance.

1.2. Central theme and objective of the thesis

The background information presented above underscores the importance of developing nanofabrication techniques to enable us to analyse the interaction of bacteria and preosteoblast cells with patterns. The central theme of the current thesis, therefore, is the development of submicron/nano-fabrication techniques, including EBID, ICP RIE, and a combination of EBL, soft lithography, and thermal NIL, that are selected such that they can cover the whole range from nanoscale (sub-100 nm) to submicron scale (< 1000 nm). These techniques are then used to study the effects of each type of pattern and length scales on the cell response.

Another important aspect of the thesis is the study of the mechanical properties of the nano/submicron pillars. Given that such properties influence the cell-pattern interactions, a new atomic force microscopy (AFM)-based technique is presented to measure the required mechanical properties of individual nanopatterns *per se* or under interaction with bacteria or preosteoblast cells.

Finally, this thesis addresses a major limitation of the current patterning techniques, namely their inability to cover nonplanar surfaces. Recent research has demonstrated that the geometry of the scaffolds (*e.g.,* porosity, pore size, and trabecular thickness) plays a major role in determining the cell behavior [11, 12]. However, most of the available nano/submicron fabrication techniques are only applicable to flat substrates. In order to facilitate future cell studies, this thesis presents a facile and novel metal crumpling technique that can be applied to nanopatterned porous flat sheets, thereby crumpling them with our designed setup to fabricate nanopatterned scaffolds with dimensions and mechanical properties.

1.3. Thesis outline

Chapters 2, 3. In these chapters, a nanoscale additive manufacturing technique (= 3D printing) (EBID) is used to accurately design and fabricate sub-100 nm nanopillars with desired dimensions (*i.e.*, diameter, height, and interspacing), and spatial arrangement with an aim to contribute towards the understanding of the effects of the geometrical properties of nanopillars on the killing mechanism and bactericidal properties of Gram-positive (*Staphylococcus aureus*) and Gram-negative (*Escherichia coli*) bacteria. The results of this chapter serve as a guideline to optimize the abovementioned parameters in such a way that the killing efficiency against both types of bacteria is maximized.

Chapter 4. The aim of this chapter is to develop a new technique, using an AFM, to quantify the mechanical properties (*i.e.,* elastic modulus, fracture stress, and the interaction forces between bacteria and nanopillars) of individual nano/submicron pillars as fabricated in a single step. The abovementioned mechanical properties are highly relevant factors determining the bactericidal efficiency and mechanobiological response of cells on patterned surfaces.

Chapter 5. In this chapter, ICP RIE is used to fabricate high aspect ratio titanium nanopillars, called black Ti, on the surface of a Ti sheet. The use of ICP RIE significantly increases the speed and throughput of the patterning process as compared to EBID and enables us to pattern the entire surface of the Ti substrates in a single and fast step. The effects of different etching parameters on the morphology and dimension of the final black Ti patterns are studied.

Finally, the etching parameters are optimized to fabricate three distinct black Ti surfaces and the interactions of MC3T3-E1 preosteoblast cells and *S. aureus* bacteria with these surfaces are investigated with the aim to provide a new perspective on the dual-functionality of black Ti surfaces and to illustrate how various ICP RIE parameters can be designed to fabricate a nanopatterned surface with bactericidal and osteogenic properties.

Chapter 6. In this chapter, a simple crumpling technique is proposed to fabricate 3D nanopatterned porous scaffolds out of porous 2D Ti thin sheets covered with black Ti that are presented in Chapter 5. Three different porosities are created on the 2D Ti sheets. Two deformation rates are then used to crumple the specimens using our dedicated crumpling

setup. The 3D topographical properties of the crumpled structures are determined using micro-computed tomography (µCT). Then, finite element analysis (FEA) is performed to validate the results of the compression tests. Porosity, trabecular thickness, and pore size of the studied scaffolds and FEA simulations are analyzed and compared. Finally, MC3T3-E1 preosteoblasts are cultured on both polished and nanopatterned crumpled Ti scaffolds to assess the cytocompatibility of crease lines on the metabolic activity and viability of the cells.

Chapter 7. The aim of this chapter is to develop a nanofabrication technique, taking advantage of the precise control over every single dimension of the nanopatterns provided by EBID, on the one hand, and the fast and high throughput performance of ICP RIE on the other hand. The developed approach allows for enhancing the efficiency of the studies on cell-nano/submicron pillars interactions. To this end, we use EBL to fabricate two sets of submicron pillars, with the interspacing as the variable, on fused silica substrate. The interactions of MC3T3-E1 cells with these pillars are investigated.

In the second part of this chapter, to speed up the fabrication process, soft lithography is used to replicate the patterns originally created with EBL. Hybrid PDMS mold is then used to faithfully replicate the submicron pits into the substrate of interest using NIL. The parameters of the imprinting process, including molding and de-molding temperatures, chamber pressure, molding time, the type and thickness of the thermoplastic resist are selected and optimized to fully replicate the patterns without damaging the mold. NIL simplifies the process of producing patterns with a wide range of dimensions (from nanoscale to microscale) on a variety of substrates regardless of the material and geometry (*i.e.,* flat or curved).

Chapter 8. In this chapter, I briefly discuss the results of this thesis and make a number of general conclusions. Moreover, I present a number of suggestions for future research directions.

References

[1] L. Zhang, G. Yang, B.N. Johnson, X. Jia, Three-dimensional (3D) printed scaffold and material selection for bone repair, Acta Biomater 84 (2019) 16-33.

[2] K. Modaresifar, S. Azizian, M. Ganjian, L.E. Fratila-Apachitei, A.A. Zadpoor, Bactericidal effects of nanopatterns: A systematic review, Acta Biomater (2018).

[3] K. Modaresifar, L.B. Kunkels, M. Ganjian, N. Tumer, C.W. Hagen, L.G. Otten, P.-L. Hagedoorn, L. Angeloni, M.K. Ghatkesar, L.E. Fratila-Apachitei, A.A. Zadpoor, Deciphering the Roles of Interspace and Controlled Disorder in the Bactericidal Properties of Nanopatterns against Staphylococcus aureus, Nanomaterials (Basel) 10(2) (2020).

[4] I.A.J. van Hengel, M. Tierolf, L.E. Fratila-Apachitei, I. Apachitei, A.A. Zadpoor, Antibacterial Titanium Implants Biofunctionalized by Plasma Electrolytic Oxidation with Silver, Zinc, and Copper: A Systematic Review, Int J Mol Sci 22(7) (2021).

[5] S. Dobbenga, L.E. Fratila-Apachitei, A.A. Zadpoor, Nanopattern-induced osteogenic differentiation of stem cells - A systematic review, Acta Biomater 46 (2016) 3-14.

[6] Clark, P., et al., *Cell guidance by ultrafine topography in vitro.* 1991. **99**(1): p. 73-77.

[7] S.G. Higgins, M. Becce, A. Belessiotis-Richards, H. Seong, J.E. Sero, M.M. Stevens, High-Aspect-Ratio Nanostructured Surfaces as Biological Metamaterials, Adv Mater 32(9) (2020) e1903862.

[8] D.K. Oh, H. Jeong, J. Kim, Y. Kim, I. Kim, J.G. Ok, J. Rho, Top-down nanofabrication approaches toward single-digit-nanometer scale structures, Journal of Mechanical Science and Technology 35(3) (2021) 837-859.

[9] M. Ganjian, K. Modaresifar, M.R.O. Ligeon, L.B. Kunkels, N. Tümer, L. Angeloni, C.W. Hagen, L.G. Otten, P.-L. Hagedoorn, I. Apachitei, L.E. Fratila-Apachitei, A.A. Zadpoor, Nature Helps: Toward Bioinspired Bactericidal Nanopatterns, Advanced Materials Interfaces 6(16) (2019).

[10] L. Angeloni, M. Ganjian, M. Nouri-Goushki, M.J. Mirzaali, C.W. Hagen, A.A. Zadpoor, L.E. Fratila-Apachitei, M.K. Ghatkesar, Mechanical characterization of nanopillars by atomic force microscopy, Additive Manufacturing 39 (2021).

[11] S.J. Callens, R.J. Uyttendaele, L.E. Fratila-Apachitei, A.A. Zadpoor, Substrate curvature as a cue to guide spatiotemporal cell and tissue organization, 232 (2020) 119739.

[12] S. Callens, D. Fan, I. van Hengel, M. Minneboo, L.E. Fratila-Apachitei, A.A. Zadpoor, Emergent collective organization of bone cells in complex curvature fields, (2020).

2

Towards bioinspired bactericidal nanopillars

Abstract

Development of synthetic bactericidal surfaces is a drug-free route to the prevention of biomaterial- and implant-associated infections. Surface nanotopographies with specific dimensions and order (also known as surface nanopatterns) have been shown to kill various types of bacterial strains through a mechanical mechanism, while regulating stem cell differentiation and, thus, tissue regeneration. The effective ranges of dimensions required to simultaneously achieve both aims are in the < 200 nm range, which is outside the operational range of the vast majority of surface bio-functionalization techniques. Here, a nanoscale additive manufacturing (= 3D printing) technique called electron beam induced deposition (EBID) is used to fabricate nanopillars with reproducible and precisely controlled dimensions and arrangements that were within those effective ranges (i.e. a height of 190 nm, a diameter of 80 nm, and an interspacing of 170 nm). The bactericidal behaviors of the nanopatterns against both Gram-positive (Staphylococcus aureus) and Gram-negative (Escherichia coli) bacteria have been evaluated. When compared to the flat surface, the nanopatterned surfaces show a significant bactericidal activity against both E. coli and S. aureus (with respective killing efficiencies of 97 ± 1% and 36 ± 5%). Direct penetration of nanopatterns into the bacterial cell wall leads to the disruption of the cell wall and cell death. The more rigid cell wall of the Gram-positive bacterium S. aureus is consistent with the decreased killing efficiency. These findings support the development of nanopatterns with precisely controlled dimensions that are capable of killing both Gram-negative and Gram-positive bacteria. However, the potential of such nanopatterns in inducing osteogenic differentiation in mammalian cells is yet to be studied and requires overcoming the challenges associated with upscaling the area patterned with EBID.

2.1. Introduction

While the increased life expectancy is leading to increased numbers of surgical replacement of orthopedic implants, further increasing the risk of implant-associated infection (IAI) is among the main causes of the failure of those implants [1]. Opportunistic pathogens including different types of bacteria are able to attach to and grow on the implant surface, eventually forming a biofilm, which is less susceptible to antibiotics and cannot be easily cleared by the host immune system [2]. This phenomenon hinders the function of the implant and results in significant morbidity and/or mortality [3].

Different techniques have been proposed for the prevention of bacterial attachment to the implant surface and/or for killing the bacteria upon contact with the surface [4]. While the majority of non-adherent surfaces are unfavorable for the attachment of both bacterial and host cells, they are not of much utility in this case. That is because attachment and growth of host cells on the implant surface is a crucial step in the osseointegration process. One, therefore, needs surfaces that can selectively kill bacteria while supporting the growth and proliferation of host cells [5]. Consequently, there has been a surge in the efforts aimed at developing contact-killing surfaces with such properties. Non-cytotoxic bactericidal surfaces primarily work on the basis of a chemical or physical killing mechanism. As chemical methods usually deliver antibiotics [6, 7], bactericidal metallic nanoparticles such as silver [8-10], or other antibacterial agents [11], their long-term widespread use may lead to the development of bacterial resistance against the delivered agents [12-14].

On the other hand, surface topographies at the nano- and submicron-scales have been shown to be capable of killing bacteria through mechanical pathways [15, 16]. Indeed, several nanotopographical features found in nature, exhibit bactericidal behavior and have inspired the development of an alternative approach to common chemical methods [17, 18]. A great number of these surface nanotopographies are distinguished by their highly controlled spatial arrangements of their nanoscale features [19]. Recent advances in micro- and nano-fabrication techniques have enabled researchers to replicate some of these naturally occurring nanopatterns (*e.g.*, spinules of gecko skin) on synthetic materials or to develop new nanopatterns with desired design parameters such as height (depth), diameter, and interspacing [20, 21].

Reactive ion etching (RIE), hydrothermal treatment, anodizing, electron beam lithography (EBL), and nanoimprint lithography (NIL) can be considered as the most commonly used methods to create nanopatterns. However, the size range that these methods are able to produce and the controllability of the process highly differs from one technique to another [19]. In order to systematically investigate the effects of nanopattern design parameters on the bactericidal properties, it is crucial to use a technique which allows the user to control each single design parameter independently from all others while being able to precisely and reproducibly fabricate feature sizes below 100 nm [22]. Electron beam induced deposition (EBID) is a nanoscale additive manufacturing (= 3D printing) method,

which enables the user to approach feature sizes in the range of a few nanometers [23] by dissociating precursor molecules using a focused electron beam (Figure 1a). Precursor molecules dissociate into two parts, a volatile and a nonvolatile part [22]. The nonvolatile part remains on the substrate and creates a deposited layer, while the volatile part desorbs and is evacuated [24]. Some studies have shown the EBID potential to create arrays of nanopillars with dimensions of a single nanometer [22] as well as complex 2D and 3D shapes [25-32].

The effective range for the design parameters of surface nanopatterns (in the shape of pillars) in which the bacteria could be mechanically killed in the absence of any antibacterial agents (*i.e.* the range between 100 nm and 900 nm for the height; 20 nm and 207 nm for the diameter; 9 nm and 380 nm for the interspacing; and the aspect ratio higher than 2) has been recently reported [19]. In the specific cases of *E. coli* and *S. aureus* as model organisms representing Gram-negative and Gram-positive bacteria, the reported ranges of dimensions of nanopillars to induce bactericidal behavior are as follows: diameters of 70-100 nm for *S. aureus* and 70-80 nm for *E.coli*, heights of 100-900 nm for *S. aureus* and 180-300 nm for *E. coli*, and interspaces of 60-200 nm for *S. aureus* and 60-380 nm for *E. coli* [19]. To simultaneously target both Gram-positive and Gram-negative bacteria, we chose the following approximate dimensions: height = 190 nm, diameter = 80 nm, and interspace = 170 nm. It is, nevertheless, worth noting that the bactericidal behavior of nanopatterns is not only dependent on the nanopatterns dimensions but also on the type of the bacterial strains and their initial attachment to the surface [19, 33, 34]. A bacterial cell is likely to deform or sink into the nanopatterns due to the penetration of the nanopillars into the bacterial cell wall (Figure 1c). To the best of our knowledge, the present study is the first to use EBID as a powerful tool to fabricate nanopatterns with precisely controlled dimensions chosen from the above-mentioned range in order to have a nanopatterned surface with high killing efficiency against both Gram-negative and Gram-positive bacteria.
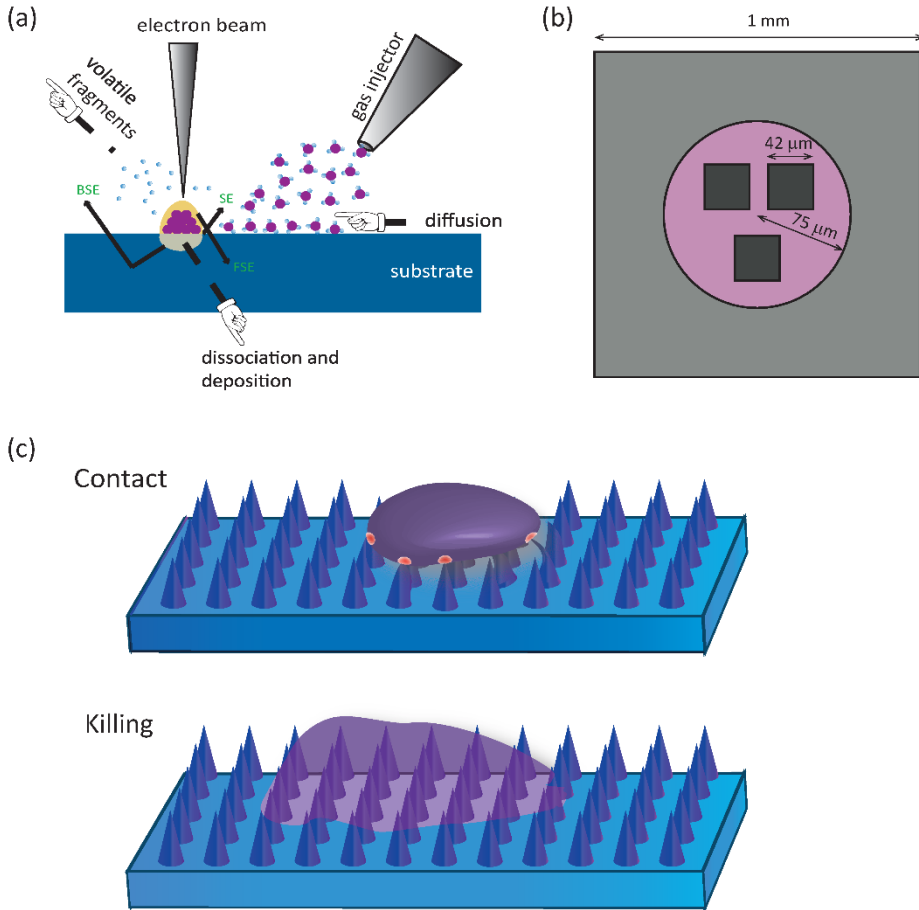
Figure 1. (a) Schematic representation of the EBID method; (b) sample design: dark gray indicates the patterned area, the pink area is close to the patterns, and the light gray area is far from the patterns; (c) a schematic drawing demonstrating the fate of bacteria residing on nanopatterns including deformation on the nanopatterns upon contact and being sunk on the nanopatterns due to the penetration of nanopillars into the bacterial cell wall.

2.2. Materials and methods

2.2.1. Nanopatterns design, fabrication, and characterization

Double-sided polished 4-inch (diameter = 10.16 cm) silicon wafers (thickness = 525 ± 25 µm, p-type) were diced into 1×1 cm² samples and cleaned with nitric acid. A stream file was designed to create nanopillars with a square arrangement possessing the approximate

dimensions of 190 nm, 80 nm, and 170 nm for their height, base diameter, and center-to-center spacing, respectively. A Nova Nano Lab 650 Dual Beam system (FEI Company, Oregon, USA) equipped with EBID and scanning electron microscopy (SEM) was used to create three nanopatterned areas of 42×42 μm² on each sample (Figure 1b). Trimethyl(methylcyclopentadienyl)-platinum(IV) or $(CH_3C_5H_4)Pt(CH_3)_3$ was used as the precursor gas and EBID was performed in the electron limited regime and at a working distance of 5 mm with 17.8 kV as the electron beam voltage and 0.60 nA as the beam current. The background vacuum of the system was 8.82 e^{-7} mbar and the EBID process started at 2.33 e^{-6} mbar (as the minimum reachable chamber pressure after opening the gas injection system and leaving the sample for two hours inside the chamber). The writing strategy was single dot exposure, using stream files generated by a MATLAB (MathWorks, US) code. The resulting nanopatterns were characterized by SEM. The height, base diameter, and tip diameter were measured for sixty different pillars per sample by using 35° tilted SEM images. The center-to-center spacing was also measured from the top view images. The mean and standard deviation of the measurements were calculated. The chemical composition of the specimens was characterized using an energy-dispersive X-ray spectroscopy (EDX) analysis performed inside an SEM (Helios NanoLab 600i dualbeam, FEI, Hillsboro, USA) on a Pt/C deposited structure with 1000 nm as the diameter and 192 nm as the height, using an image with ×16000 magnification acquired with an accelerating voltage of 5 kV. Nanopatterns were also imaged using atomic force microscopy (AFM) with a Dimension FastScan AFM (Bruker, Billerica, USA) in the ScanAsyst mode with a scan rate of 0.96 Hz and a FastScan-A probe having a nominal spring constant of 18 N/m and nominal tip radius of 5 nm. To measure the water contact angle of the nanopatterns, a thin layer of Pt-C was initially deposited on a set of silicon wafers to identify the static contact angle of Pt-C material (θ_0) by a drop shape analyzer (DSA 100, Kruss, Hamburg, Germany) using deionized water. A volume of 2 μl liquid with a falling rate of 1667 μl/min was placed on the surface using a syringe. The contact angle figure was recorded 5 s after the droplet had rested on the surface. The reported value for the measurement is the average contact angle within 30 s after the whole volume of the droplet touched the substrate. Since the nanopatterned area is too small compared to the water droplet, its contact angle was measured indirectly using the Cassie-Baxter wettability

model, assuming that air was trapped between the nanopillars [35, 36]. The following equation gives the Cassie-Baxter contact angle (θ_c):

$$cos(\theta_c) = \varphi\ (cos(\theta_0) + 1) - 1$$

Here, φ and θ_0 are the solid fraction (the ratio between the tip area of the nanopillar and the projected surface area) and the contact angle of the flat Pt-C surface, respectively. The solid fraction was calculated as follows:

$$\varphi = \frac{\pi d^2}{4i^2}$$

Where d represents the tip diameter of the nanopillar and i is the interspacing of the nanopillars.

2.2.2. Bacterial growth conditions

Gram-negative bacteria *Escherichia coli* (K12 strain) (BEI Resources, Virginia, USA) and Gram-positive bacteria *Staphylococcus aureus* (RN0450 strain) (BEI Resources, Virginia, USA) were used to investigate the bactericidal activity of nanopatterned surfaces. *E. coli* and *S. aureus* were grown on Lysogeny broth (LB) (BD Life Sciences, California, USA) and Brain Heart Infusion (BHI) (Sigma-Aldrich, Missouri, USA) agar plates at 37 °C overnight. Pre-cultures of both bacteria cells were prepared by inoculating a single colony in 100 ml autoclaved LB/BHI liquid medium, shaken at 140 rpm at 37 °C. The bacterial cells were collected at their logarithmic stage of growth and their optical density at 600 nm wavelength (OD_{600}) in the medium solution was adjusted at a value of 0.05 (55.1×10^6 CFU/ml) and 0.1 (61.6×10^6 CFU/ml) for *E. coli* and *S. aureus*, respectively.

2.2.3. Evaluation of bactericidal properties

The nanopatterned areas of the surface and the surrounding non-patterned areas (75 μm) (Figure 1b) were considered as the study (triplicate) and control groups in the bacterial studies, respectively. A thin layer of Pt-C was also deposited on a set of silicon wafers to distinguish the bactericidal effect of nanopatterns from those of the deposition material itself. Samples were immersed in 70% ethanol and subsequently dried exposed to UV light for 20 min in a sterile flow cabinet prior to addition of the bacterial culture. For each type of bacteria, a sample containing three nanopatterned areas was inoculated with 1 ml of bacterial

suspension in a 24-well plate (Cell Star, Germany). The samples were then incubated at 37 °C for 18 h. Subsequently, the adhered bacteria were fixed for SEM imaging using a fixation solution containing 4% formaldehyde (Sigma-Aldrich, Missouri, USA) and 1% glutaraldehyde (Sigma-Aldrich, Missouri, USA) in 10 mM Phosphate buffer. The samples were then washed with MilliQ water and 50%, 70%, and 96% ethanol, respectively, and eventually, soaked in hexamethyldisilazane (HMDS) (Sigma-Aldrich, Missouri, USA) for 30 min and air-dried.

A thin layer of gold was sputtered on the samples and SEM images were acquired at various magnifications and tilt angles for each sample. The total number of bacteria adhered to the surface was counted manually from the SEM images. Due to the small patterned area on the surface, it was not feasible to use other assessment methods like live/dead staining and colony forming unit (CFU) counting. The damaged/dead bacteria were distinguished by a drastic change in their morphology compared to a normal live cell or by observing disruption of their cell wall. The bactericidal efficiency of nanopatterned and non-patterned areas was determined by dividing the number of damaged/dead bacteria by the total number of bacteria in those regions.

2.2.4. Statistical analysis

To assess if there is a significant difference between the killing efficiency of different surfaces (*i.e.* silicon surface, Pt-C surface, and nanopatterned surface), an analysis of variance was conducted using the one-way ANOVA test followed by a post-hoc analysis. Depending on the results of Levene's test for the equality of variance, we made a decision about applying Bonferroni test (in case that the resultant *p*-value of Levene's test is higher than 0.05), or Games-Howell test (in case that the resultant *p*-value of Levene's test is less than 0.05). Mean ± standard deviation for the bactericidal measurements were provided. The statistical analysis was conducted using IBM SPSS Statistics 23 Software and a *p*-value less than 0.05 was considered to be statistically significant.

2.3. Results

2.3.1. Characterization of nanopatterns

Three patterned areas (42×42 μm²) were fabricated on each sample (Figure 1b) under the previously mentioned conditions. Nanopatterns were produced in the shape of pillars

(similar to a droplet-shaped structure) (Figure 2e, f). The nanopillars had a mean height of 186 nm (SD 8 nm), a base diameter of 75 nm (SD 5 nm), a tip diameter of 21 nm (SD 3 nm), and an interpillar spacing of 170 nm (Figure 2). The nanopillar density was 36 pillars per μm^2 (Figure 2c, h). The chemical composition of the EBID deposited material included ≈ 15.5% Pt, ≈ 73.4% C, and ≈ 8.7% O (Figure 2g). The result of the water contact angle measurement on the surface of Pt-C showed the hydrophilicity of the surface with a contact angle of 59 ± 2° (inset of Figure. 2g). Applying the Cassie-Baxter wettability model showed a hydrophobic contact angle of 169 ± 0.1° for the nanopatterned surface.

2.3.2. Bactericidal activity of nanopatterns

E. coli cells exhibited their normal rod-shaped morphology on flat silicon samples (Figure 3a, b) and the mean percentage of damaged/dead cells was 8.0% (SD 6.4%) on the control surfaces (Figure 5). Similar to previous studies [37], the live cells had an average length of 2.6 μm (SD 0.7 μm) and a width of 808 nm (SD 107 nm) (Figure 3a, b). On the other hand, *E.coli* cells were found extremely deformed on the nanopatterned surfaces (Figure 3e, f) with substantial amounts of disrupted bacterial cell wall and remnant cellular fragments on the nanopatterned areas (Figure 3c-e). The killing efficiency was 97.0 ± 1.2% for *E. coli* cells on the nanopatterned surfaces. The length and width of the cells on the nanopatterned surfaces could not be determined due to the drastic deformations and disruptions of the bacterial cells (Figure 3f).
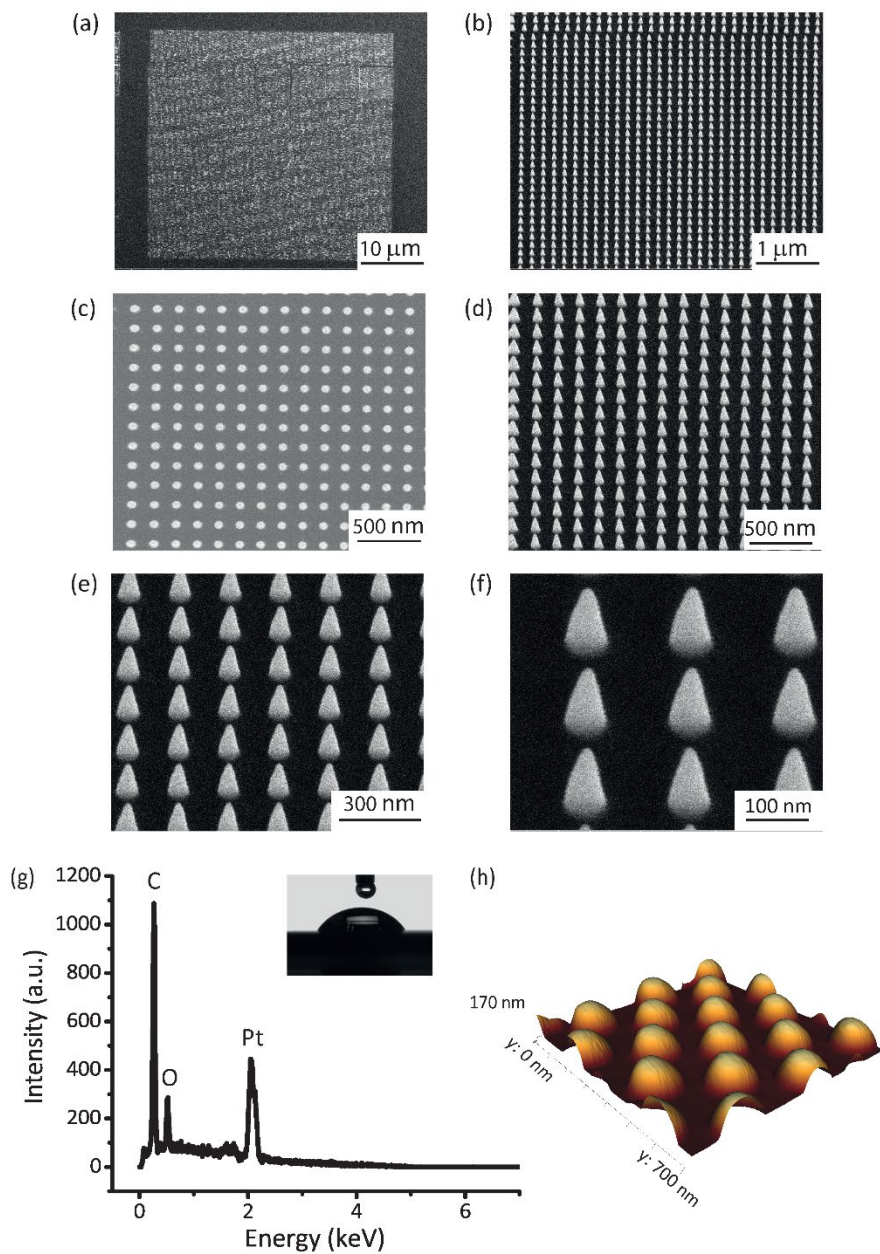
Figure 2. (a-f) SEM images of nanopillars produced by EBID at different magnifications: (a, c) top view and (b, d, e, and f) 35° tilted view. (g) EDX characterization of Pt/C deposited structure, the inset shows the water contact angle on the flat Pt-C surface (h) AFM imaging showing a 3D overview of the nanopillars.
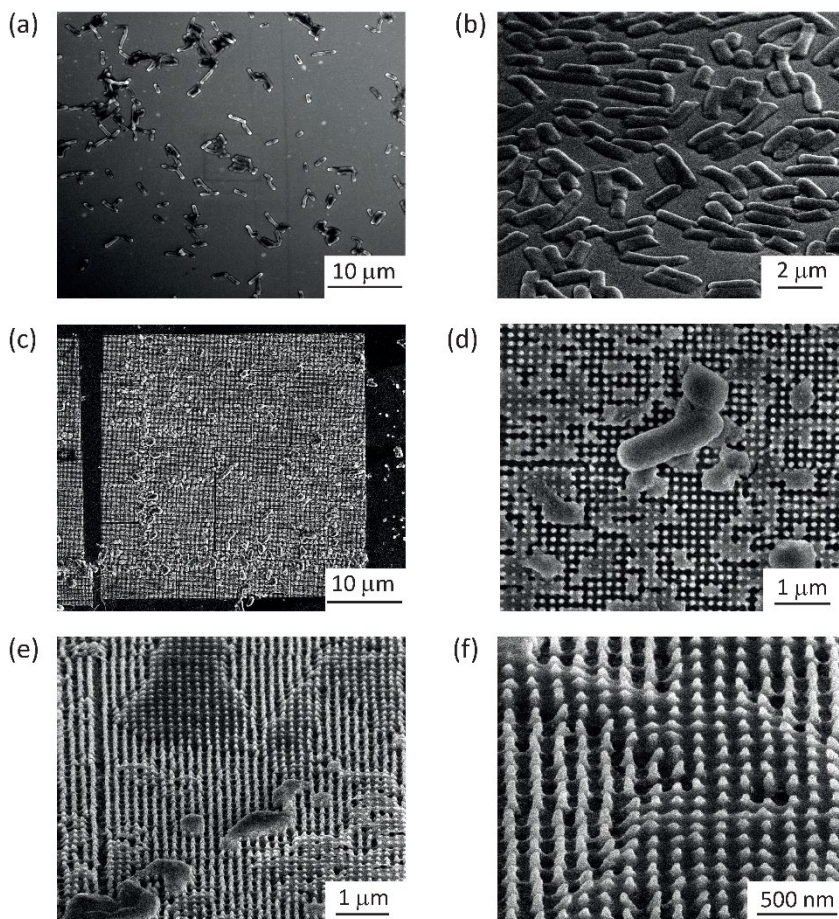
Figure 3. SEM images of *E. coli* bacteria on the control Si surface: (a) top view and (b) 50° tilted view. SEM images of *E. coli* bacteria on the nanopatterned surface after 18 h incubation: (c) top overview, (d) damaged bacteria from top view, (e) damaged bacteria from 50° tilted view, and (f) bacteria totally sunk into the nanopatterns (50° tilted view).

Similarly, *S. aureus* cells had a normal coccoid-shaped morphology and size [38] on the Si control surfaces with an average diameter of. 790 nm (SD 66 nm), and no bacterial cell was found damaged or dead (Figure 4a, b). The damaged cells, mostly sunk on the nanopillars, showed a squashed morphology and the penetration of the nanopillars into the bacterial cell wall could be clearly seen (Figure 4d, f). Additionally, bending of the nanopillars underneath the bacterial cells was observed and leftovers of bacterial components were also found on

some of the nanopillars (Figure 4e, f). The killing efficiency of the nanopatterns for *S. aureus* cells was 36.5 ± 4.7% (Figure 5). Furthermore, the bactericidal efficiency of Pt-C surface against *E. coli* and *S. aureus* was significantly lower than the nanopatterned surface ($p <$ 0.0001 and $p <$ 0.01, respectively) (Figure 5).
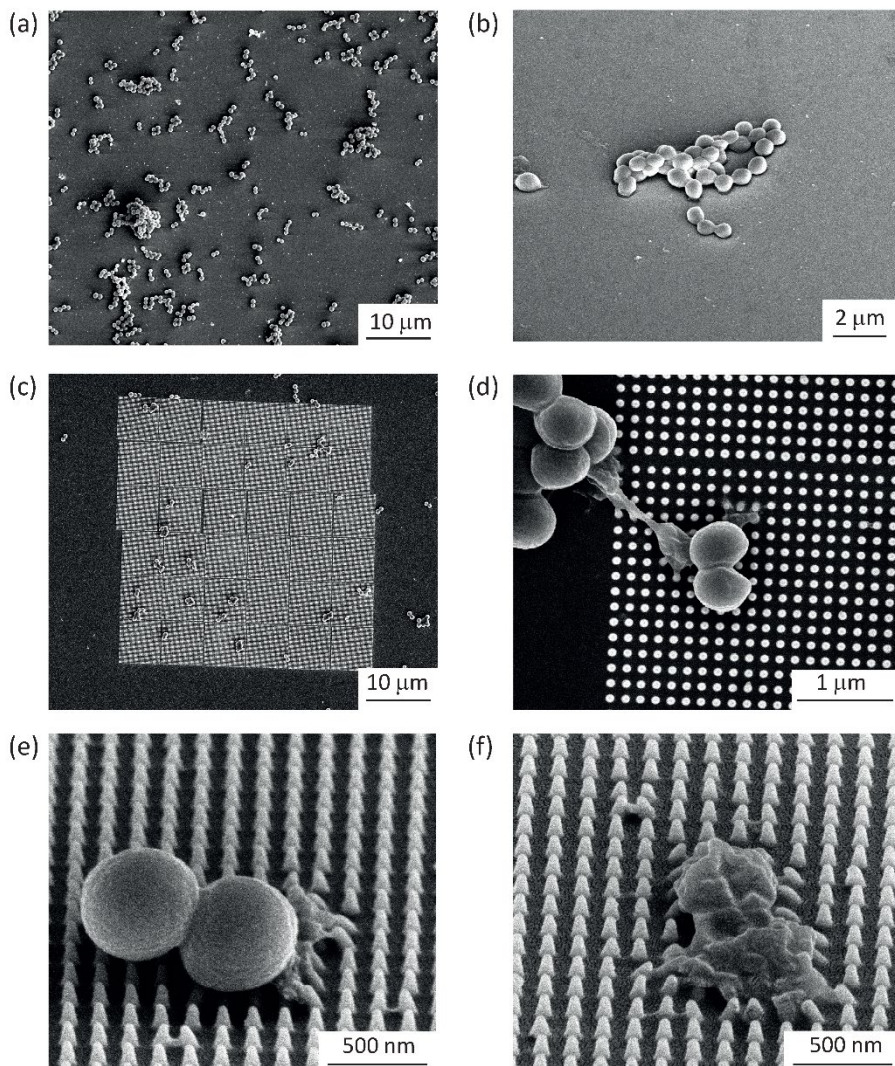
Figure 4. SEM images of *S. aureus* bacteria on the control Si surface: (a) top overview and (b) 50° tilted view. SEM images of *S. aureus* bacteria on the nanopatterned surface: (c) top overview, (d) two healthy and one dead bacteria on the pattern from top view, (e) the remnant fragments of the bacteria on the nanopillars, and (f) two dead bacteria on the nanopatterns from 50° tilted view.
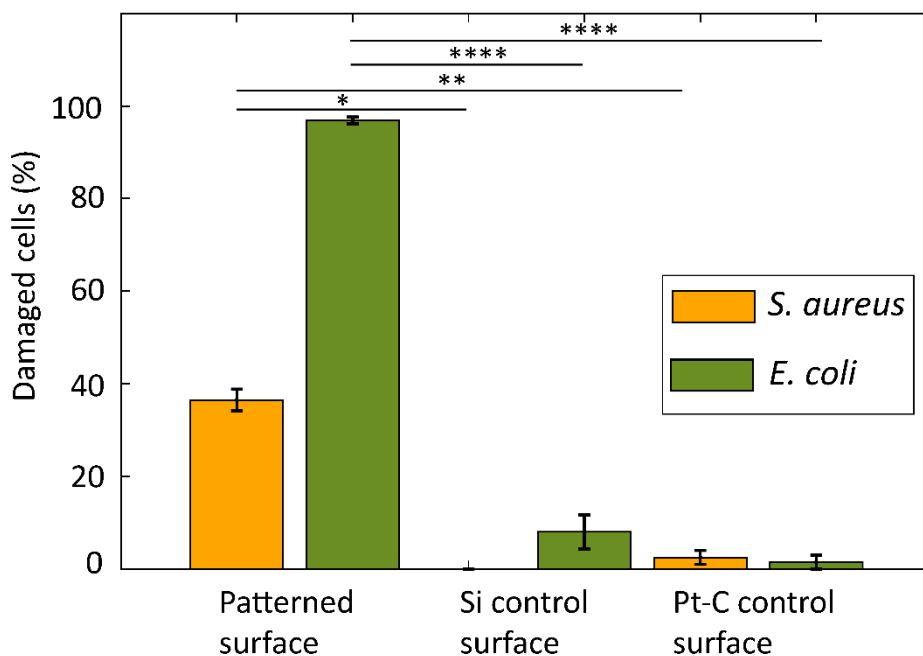
Figure 5. Quantitative characterization of the percentage of damaged *E. coli* and *S. aureus* bacterial cells on nanopatterned, Si control, and Pt-C control surfaces (* $p < 0.05$, ** $p < 0.01$, *** $p < 0.001$, and **** $p < 0.0001$). The killing efficiency was not affected by the chemical composition of the surface and the number of damaged/dead cells was significantly higher on the nanopatterned surface.

2.4. Discussion

Designing multi-biofunctional surfaces to selectively influence the behavior of mammalian cells and bacteria is of high current interest and importance for the development of implant materials as well as being a formidable challenge given the substantial differences between mammalian cells and bacteria in sensing and responding to surfaces [39]. Some of the naturally occurring nanopatterned surfaces (*e.g.*, gecko skin, cicada wings, and dragonfly wings) have shown bactericidal properties while they are not cytotoxic (Figure 6) [17, 33, 40-44].
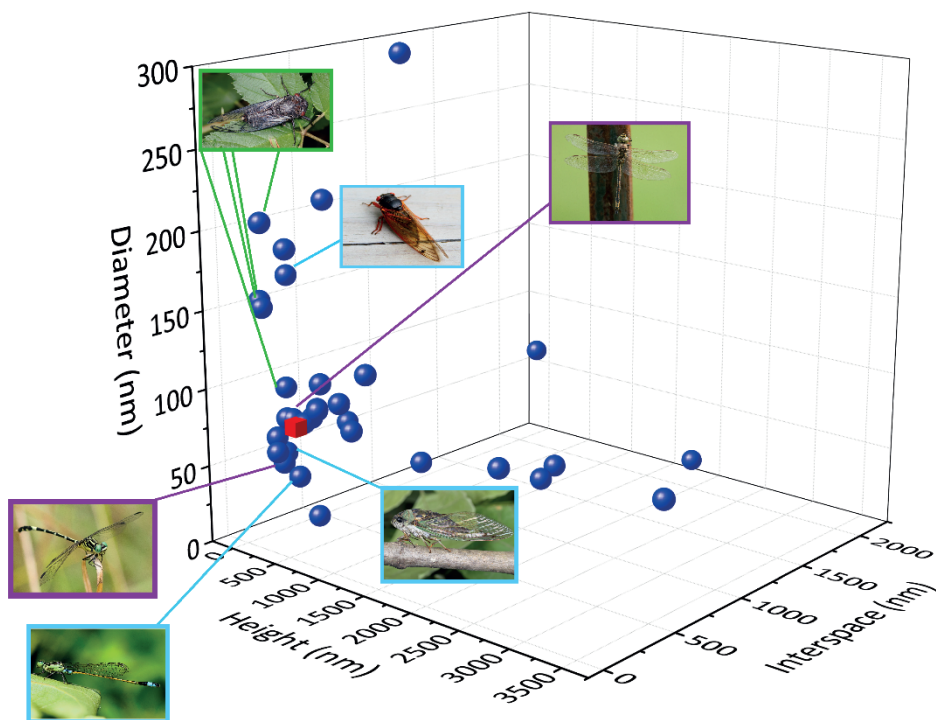
Figure 6. The dimensions of the bactericidal nanopatterns found in the literature. The nanopatterns produced for this study (represented as the red square) had dimensions close to the dimension range of naturally occurring nanopatterns. The images of insects with green and blue frames are reprinted from wikipedia.org and stock.adobe.com, respectively, with permission. The images with purple frame are taken by Roos Coy (www.therebedragonflies.com.au) and reprinted with permission.

When it comes to designing orthopedic implants, the holy grail would be having surfaces that simultaneously kill bacteria and promote osteogenesis (or osteogenic differentiation of stem cells). The main contribution of this study was application of an ultra-fine nanoscale 3D printing process with a resolution of a few nanometers to create nanopatterns with reproducible and precisely controlled dimensions that exhibit bactericidal behavior against both Gram-negative and Gram-positive bacteria. The dimensions of the nanopatterns produced in this study are within the bactericidal range found in literature and close to some of the naturally occurring bactericidal surfaces (Figure 6) [19]. The vast majority of commonly used nanofabrication techniques do not allow control over individual

dimensions of such nanostructures independently from the other dimensions. EBID makes it feasible to produce specific controllable dimensions at the nanoscale, with a resolution comparable or better than EBL [22]. Additionally, there is no need for a mask or other chemical wet processes. These characteristics make EBID an ideal method for producing nanopatterns that are required for performing systematic studies to determine which exact dimensions of the nanopatterns result in maximum bactericidal activity while promoting osteogenic differentiation of the host cells. EBID uses a precursor gas (Trimethyl(methylcyclopentadienyl)-platinum(IV) in this study) to write directly on the substrate. In the EBID process, the precursor gas molecules dissociate on the substrate under the electron beam [45]. The main components of the deposited material in this study were platinum and carbon. The platinum percentage can vary from 8.9 % to 16.8 % depending on the beam current, deposition time, and electron dosage [46].

The nanopatterned surface showed a high bactericidal efficiency against *E. coli* where almost all the bacterial cells were sunk on the nanopillars with the cell components leaked out and a distorted morphology. However, the nanopatterns could not kill *S. aureus* as efficiently as *E. coli*. Considering that the bactericidal activity of the nanopatterns is physical in nature, (corroborated by the results of Pt-C flat surface), the difference between the bactericidal efficiency against *E. coli* and *S. aureus* could be explained by the more rigid and thicker cell wall of *S. aureus* which requires higher forces to be ruptured [17, 40, 47]. Bending of the nanopillars beneath the bacteria is consistent with this hypothesis (Figure 4e, f). Other differences between Gram-negative and Gram-positive bacteria such as the size and morphology could also affect the bactericidal efficiency [48]. Moreover, as remnant fragments of *S. aureus* were observed on the nanopatterns (Figure 4e), one could speculate that the bacteria had found the surface unfavorable for adhesion and moved away from the surface. This hypothesis has been previously introduced in the literature [43]. If a number of bacteria have moved away from the surface, the antibacterial activity that includes the bactericidal effects and prevention of bacterial adhesion to the surface might have been stronger than what could be concluded from the SEM images alone. Due to the small size of the patterned areas (compared to the whole samples' surface) which could be fabricated by EBID, other methods of antibacterial activity assessment such as live/dead staining and CFU enumeration [49] were not applicable. Nevertheless, previous studies have shown that

bacteria with similar irregular/damaged morphologies are equivalent to the dead bacteria in those mentioned methods [50, 51].
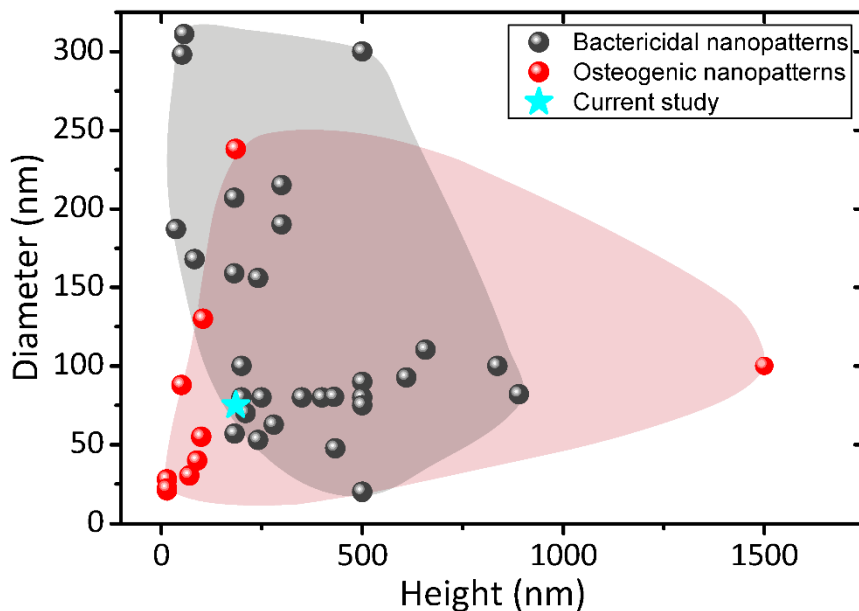
Figure 7. Comparison of the dimensions (diameter and height) of nanopillars found in the literature displaying bactericidal and osteogenic activities. This graph illustrates that the nanopattern studied here is within the area where nanopatterns possess both bactericidal and osteogenic properties.

While the direct penetration of high aspect-ratio nanopatterns into the bacterial cell wall and their consequent disruption is considered the main bactericidal mechanism of nanopatterned surfaces, many other factors have been proposed to play important roles in the bactericidal potential of nanopatterned surfaces [19]. For instance, the uniformity of the nanopatterns [52], their compaction, [53] and density [54] on the surface, and surface wettability [19] have been shown to affect the bactericidal activity. In this regard, theoretical studies with a mechanistic point of view have previously shown that the interspace and the diameter of the nanopillars could be the determining factors for applying the highest force and imposing the highest degree of stretching and deformation, and ultimately, death in bacteria [55]. Therefore, more systematic studies are needed to improve the bactericidal efficiency of nanopatterns against more resistant bacteria such as methicillin resistant *S. aureus*. Moreover, studying the behavior of mammalian cells on such nanopatterns is

required to better visualize and tag the exact overlapping range of bactericidal and osteogenic nanopatterns. So far, an overlap between the bactericidal and osteogenic ranges can already be pictured based on the data available in the literature (Figure 7) [19, 56-61]. The nanopatterns produced in this study are positioned inside the overlap area of these two important types of behavior, implying that they are likely to exhibit osteogenic properties as well. It is therefore important to further assess their osteogenic properties in future studies. Indeed, more studies on the osteogenic behavior of nanopatterned surfaces are required to more accurately define the boundaries of the osteogenic range.

Although EBID enables fabrication of nanopatterns with arbitrary shapes and accurate controllable dimensions, which is ideal for systematic studies, upscaling the patterned area is still challenging. It took 6.5 h to produce each of the $42{\times}42$ μm^2 patterned areas, check the dimensions, and refocus again to have exactly the same nanostructures. To create surfaces that are suitable for further experiments with mammalian cells such as mesenchymal stem cells (MSCs) culture, it is necessary to enlarge the patterned area, for example to $3{\times}3$ mm^2 which could be achieved by further developments of the process. One approach would be to use parallel electron beam induced deposition using a multi-beam scanning electron microscope, which enables patterning the desired area using several parallel beams (*e.g.,* $14{\times}14$ beams to expose a larger area and reduce the required deposition time to a few hours [62]). Another method, which has a comparably higher throughput and lower cost is using EBID patterns as a mask stamp for nanoimprint lithography (NIL). There are two major NIL methods: UV NIL and thermal NIL. For UV NIL, one needs to deposit the desired nanopatterns on a substrate that is highly transmissive to deep UV (*e.g.,* fused silica [63], glass [64], etc.). The thermal NIL is another technique to enlarge the nanopatterned area. Si is the preferred stamp material for thermal NIL due to its high elastic modulus, mechanical strength, and thermal expansion coefficient [65]. Transferring EBID nanopatterns composed of the precursor molecules into Si substrate as the NIL stamp, is the first step for this technique, which needs to be done by RIE [66, 67]. In both NIL methods, the following step after preparing a nanopatterned stamp is bringing the stamp in contact with the desired substrate that should have been covered by imprint polymer inside a nanoimprint machine and applying a constant pressure. After the required time, the pressure is released and the user can separate the stamp from the polymer. The final step is etching the residual layer of

the imprint polymer and the substrate using RIE. Regardless of the chosen upscaling technique, the underlying EBID technology is the key to achieving reproducible and precisely controlled nanopatterns and is therefore recommended for future studies.

Conclusion

In order to develop a bactericidal surface suitable for the fabrication of orthopedic implants, we used EBID to create nanopatterns with dimensions within the bactericidal range and comparable to nanopatterns found in nature in terms of height and diameter. The nanopatterns were produced in the shape of pillars with an approximate height of 190 nm, a diameter of 80 nm, and an interspacing of 170 nm. The nanopillars were found to mechanically rupture the cell wall of *E. coli* and *S. aureus* and showed a significantly higher bactericidal activity as compared to the non-patterned surfaces and flat surfaces coated with the same material as the pillars. However, the bactericidal efficiency for *S. aureus* was significantly lower than *E. coli*, which could be explained by the differences in the characteristics of Gram-negative and Gram-positive bacteria such as the cell wall thickness and stiffness. Further investigations are required to determine the exact killing mechanism, the role of different factors involved in that process, and the possible osteogenic activity, since the dimensions of the current nanopatterns are within the osteogenic range. Although EBID is a very powerful technique to have control over all of the dimensions of the nanopatterns in the fabrication process, the challenge of upscaling the patterned area while reducing the writing time is yet to be overcome. This is crucial for further experiments on mammalian cells, which are bigger in size than bacterial cells. Such an approach would open the way for the development of nanopatterns with simultaneous bactericidal and osteogenic potential that could be translated to clinical use in the future.

References

[1] W. Zimmerli, A. Trampuz, P.E. Ochsner, Prosthetic-joint infections, N. Engl. J. Med. 351(16) (2004) 1645-1654.

[2] C.R. Arciola, D. Campoccia, L. Montanaro, Implant infections: adhesion, biofilm formation and immune evasion, Nat. Rev. Microbiol. (2018) 1.

[3] J.M. Steckelberg, D.R. Osmon, Prosthetic joint infections, Infections Associated with Indwelling Medical Devices, Third Edition, American Society of Microbiology2000, pp. 173-209.

[4] J. Hasan, R.J. Crawford, E.P. Ivanova, Antibacterial surfaces: the quest for a new generation of biomaterials, Trends Biotechnol. 31(5) (2013) 295-304.

[5] Y. Wang, G. Subbiahdoss, J. Swartjes, H.C. van der Mei, H.J. Busscher, M. Libera, Length-Scale Mediated Differential Adhesion of Mammalian Cells and Microbes, Adv. Funct. Mater. 21(20) (2011) 3916-3923.

[6] S. Bakhshandeh, Z. Gorgin Karaji, K. Lietaert, A.C. Fluit, C.E. Boel, H.C. Vogely, T. Vermonden, W.E. Hennink, H. Weinans, A.A. Zadpoor, Simultaneous Delivery of Multiple Antibacterial Agents from Additively Manufactured Porous Biomaterials to Fully Eradicate Planktonic and Adherent Staphylococcus aureus, ACS Appl. Mater. Interfaces 9(31) (2017) 25691-25699.

[7] J. Hirschfeld, E.M. Akinoglu, D.C. Wirtz, A. Hoerauf, I. Bekeredjian-Ding, S. Jepsen, E.-M. Haddouti, A. Limmer, M. Giersig, Long-term release of antibiotics by carbon nanotube-coated titanium alloy surfaces diminish biofilm formation by Staphylococcus epidermidis, Nanomedicine 13(4) (2017) 1587-1593.

[8] M. Croes, S. Bakhshandeh, I. van Hengel, K. Lietaert, K. van Kessel, B. Pouran, B. van der Wal, H. Vogely, W. Van Hecke, A. Fluit, Antibacterial and immunogenic behavior of silver coatings on additively manufactured porous titanium, Acta Biomater. 81 (2018) 315-327.

[9] I.A. van Hengel, M. Riool, L.E. Fratila-Apachitei, J. Witte-Bouma, E. Farrell, A.A. Zadpoor, S.A. Zaat, I. Apachitei, Selective laser melting porous metallic implants with immobilized silver nanoparticles kill and prevent biofilm formation by methicillin-resistant Staphylococcus aureus, Biomaterials 140 (2017) 1-15.

[10] S. Amin Yavari, L. Loozen, F.L. Paganelli, S. Bakhshandeh, K. Lietaert, J.A. Groot, A.C. Fluit, C. Boel, J. Alblas, H.C. Vogely, Antibacterial behavior of additively manufactured

porous titanium with nanotubular surfaces releasing silver ions, ACS Appl. Mater. Interfaces 8(27) (2016) 17080-17089.

[11] X.J. Loh, Latest advances in antibacterial materials, J. Mol. Eng. Mater. 5(01) (2017) 1740001.

[12] A. Elbourne, R.J. Crawford, E.P. Ivanova, Nano-structured antimicrobial surfaces: From nature to synthetic analogues, J. Colloid Interface Sci. 508 (2017) 603-616.

[13] A. Panáček, L. Kvítek, M. Smékalová, R. Večeřová, M. Kolář, M. Röderová, F. Dyčka, M. Šebela, R. Prucek, O. Tomanec, Bacterial resistance to silver nanoparticles and how to overcome it, Nat. Nanotechnol. 13(1) (2018) 65.

[14] M.C. Enright, D.A. Robinson, G. Randle, E.J. Feil, H. Grundmann, B.G. Spratt, The evolutionary history of methicillin-resistant Staphylococcus aureus (MRSA), Proc. Natl. Acad. Sci. U. S. A. 99(11) (2002) 7687-7692.

[15] S. Ghosh, S. Niu, M. Yankova, M. Mecklenburg, S.M. King, J. Ravichandran, R.K. Kalia, A. Nakano, P. Vashishta, P. Setlow, Analysis of killing of growing cells and dormant and germinated spores of Bacillus species by black silicon nanopillars, Sci. Rep. 7(1) (2017) 17768.

[16] D.P. Linklater, S. Juodkazis, S. Rubanov, E.P. Ivanova, Comment on "Bactericidal Effects of Natural Nanotopography of Dragonfly Wing on Escherichia coli", ACS Appl. Mater. Interfaces 9(35) (2017) 29387-29393.

[17] J. Hasan, H.K. Webb, V.K. Truong, S. Pogodin, V.A. Baulin, G.S. Watson, J.A. Watson, R.J. Crawford, E.P. Ivanova, Selective bactericidal activity of nanopatterned superhydrophobic cicada Psaltoda claripennis wing surfaces, Appl. Microbiol. Biotechnol. 97(20) (2013) 9257-9262.

[18] I. Izquierdo-Barba, J.M. García-Martín, R. Álvarez, A. Palmero, J. Esteban, C. Pérez-Jorge, D. Arcos, M. Vallet-Regí, Nanocolumnar coatings with selective behavior towards osteoblast and Staphylococcus aureus proliferation, Acta Biomater. 15 (2015) 20-28.

[19] K. Modaresifar, S. Azizian, M. Ganjian, L.E. Fratila-Apachitei, A.A. Zadpoor, Bactericidal effects of nanopatterns: a systematic review, Acta Biomater. (2018).

[20] D.W. Green, K.K.-H. Lee, J.A. Watson, H.-Y. Kim, K.-S. Yoon, E.-J. Kim, J.-M. Lee, G.S. Watson, H.-S. Jung, High Quality Bioreplication of Intricate Nanostructures from a Fragile Gecko Skin Surface with Bactericidal Properties, Sci. Rep. 7 (2017).

[21] M.N. Dickson, E.I. Liang, L.A. Rodriguez, N. Vollereaux, A.F. Yee, Nanopatterned polymer surfaces with bactericidal properties, Biointerphases 10(2) (2015) 021010.

[22] W.F. Van Dorp, B. Van Someren, C.W. Hagen, P. Kruit, P.A. Crozier, Approaching the resolution limit of nanometer-scale electron beam-induced deposition, Nano Lett. 5(7) (2005) 1303-1307.

[23] M.-K. Seo, H.-G. Park, J.-K. Yang, J.-Y. Kim, S.-H. Kim, Y.-H. Lee, Controlled sub-nanometer tuning of photonic crystal resonator by carbonaceous nano-dots, Opt. Express 16(13) (2008) 9829-9837.

[24] G. Gazzadi, S. Frabboni, C. Menozzi, L. Incerti, Electrical characterization of suspended Pt nanowires grown by EBID with water vapour assistance, Microelectron. Eng. 85(5-6) (2008) 1166-1169.

[25] W. Van Dorp, C.W. Hagen, A critical literature review of focused electron beam induced deposition, J. Appl. Phys. 104(8) (2008) 10.

[26] S. Janbaz, N. Noordzij, D.S. Widyaratih, C.W. Hagen, L.E. Fratila-Apachitei, A.A. Zadpoor, Origami lattices with free-form surface ornaments, Sci. Adv. 3(11) (2017) eaao1595.

[27] T. Bret, I. Utke, P. Hoffmann, Influence of the beam scan direction during focused electron beam induced deposition of 3D nanostructures, Microelectron. Eng. 78 (2005) 307-313.

[28] T. Bret, I. Utke, P. Hoffmann, M. Abourida, P. Doppelt, Electron range effects in focused electron beam induced deposition of 3D nanostructures, Microelectron. Eng. 83(4-9) (2006) 1482-1486.

[29] R. Winkler, F.-P. Schmidt, U. Haselmann, J.D. Fowlkes, B.B. Lewis, G. Kothleitner, P.D. Rack, H. Plank, Direct-write 3d nanoprinting of plasmonic structures, ACS Appl. Mater. Interfaces 9(9) (2016) 8233-8240.

[30] J.D. Fowlkes, R. Winkler, B.B. Lewis, A. Fernandez-Pacheco, L. Skoric, D. Sanz-Hernandez, M.G. Stanford, E. Mutunga, P.D. Rack, H. Plank, High-Fidelity 3D-Nanoprinting via Focused Electron Beams: Computer-Aided Design (3BID), ACS Appl. Nano Mater. 1(3) (2018) 1028-1041.

[31] J.D. Fowlkes, R. Winkler, B.B. Lewis, M.G. Stanford, H. Plank, P.D. Rack, Simulation-guided 3D nanomanufacturing via focused electron beam induced deposition, ACS Nano 10(6) (2016) 6163-6172.

[32] L. Keller, M. Huth, Pattern generation for direct-write three-dimensional nanoscale structures via focused electron beam induced deposition, Beilstein J. Nanotechnol. 9(1) (2018) 2581-2598.

[33] K. Nowlin, A. Boseman, A. Covell, D. LaJeunesse, Adhesion-dependent rupturing of Saccharomyces cerevisiae on biological antimicrobial nanostructured surfaces, J. R. Soc., Interface 12(102) (2015) 20140999.

[34] T. Diu, N. Faruqui, T. Sjöström, B. Lamarre, H.F. Jenkinson, B. Su, M.G. Ryadnov, Cicada-inspired cell-instructive nanopatterned arrays, Sci. Rep. 4 (2014).

[35] B. Bhushan, M. Nosonovsky, The rose petal effect and the modes of superhydrophobicity, Philos. Trans. R. Soc., A 368(1929) (2010) 4713-4728.

[36] M. Sun, G.S. Watson, Y. Zheng, J.A. Watson, A. Liang, Wetting properties on nanostructured surfaces of cicada wings, J. Exp. Biol. 212(19) (2009) 3148-3155.

[37] O. Pierucci, Dimensions of Escherichia coli at various growth rates: model for envelope growth, J. Bacteriol. 135(2) (1978) 559-574.

[38] L. Harris, S. Foster, R. Richards, An introduction to Staphylococcus aureus, and techniques for identifying and quantifying S. aureus adhesins in relation to adhesion to biomaterials: review, Eur. Cells Mater. 4(3) (2002).

[39] K. Anselme, P. Davidson, A. Popa, M. Giazzon, M. Liley, L. Ploux, The interaction of cells and bacteria with surfaces structured at the nanometre scale, Acta Biomater. 6(10) (2010) 3824-3846.

[40] E.P. Ivanova, J. Hasan, H.K. Webb, V.K. Truong, G.S. Watson, J.A. Watson, V.A. Baulin, S. Pogodin, J.Y. Wang, M.J. Tobin, Natural bactericidal surfaces: mechanical rupture of Pseudomonas aeruginosa cells by cicada wings, Small 8(16) (2012) 2489-2494.

[41] V.K. Truong, N.M. Geeganagamage, V.A. Baulin, J. Vongsvivut, M.J. Tobin, P. Luque, R.J. Crawford, E.P. Ivanova, The susceptibility of Staphylococcus aureus CIP 65.8 and Pseudomonas aeruginosa ATCC 9721 cells to the bactericidal action of nanostructured Calopteryx haemorrhoidalis damselfly wing surfaces, Appl. Microbiol. Biotechnol. 101(11) (2017) 4683-4690.

[42] S.M. Kelleher, O. Habimana, J. Lawler, B. O'reilly, S. Daniels, E. Casey, A. Cowley, Cicada wing surface topography: an investigation into the bactericidal properties of nanostructural features, ACS applied materials & interfaces 8(24) (2015) 14966-14974.

[43] C.D. Bandara, S. Singh, I.O. Afara, A. Wolff, T. Tesfamichael, K. Ostrikov, A. Oloyede, Bactericidal effects of natural nanotopography of dragonfly wing on Escherichia coli, ACS Appl. Mater. Interfaces 9(8) (2017) 6746-6760.

[44] G.S. Watson, D.W. Green, L. Schwarzkopf, X. Li, B.W. Cribb, S. Myhra, J.A. Watson, A gecko skin micro/nano structure–A low adhesion, superhydrophobic, anti-wetting, self-cleaning, biocompatible, antibacterial surface, Acta Biomater. 21 (2015) 109-122.

[45] J. Wnuk, S. Rosenberg, J. Gorham, W. Van Dorp, C. Hagen, D. Fairbrother, Electron beam deposition for nanofabrication: Insights from surface science, Surf. Sci. 605(3-4) (2011) 257-266.

[46] A. Botman, M. Hesselberth, J. Mulders, Improving the conductivity of platinum-containing nano-structures created by electron-beam-induced deposition, Microelectron. Eng. 85(5-6) (2008) 1139-1142.

[47] S. Pogodin, J. Hasan, V.A. Baulin, H.K. Webb, V.K. Truong, V. Boshkovikj, C.J. Fluke, G.S. Watson, J.A. Watson, R.J. Crawford, Biophysical model of bacterial cell interactions with nanopatterned cicada wing surfaces, Biophys. J. 104(4) (2013) 835-840.

[48] E. Fadeeva, V.K. Truong, M. Stiesch, B.N. Chichkov, R.J. Crawford, J. Wang, E.P. Ivanova, Bacterial retention on superhydrophobic titanium surfaces fabricated by femtosecond laser ablation, Langmuir 27(6) (2011) 3012-3019.

[49] J. Sjollema, S.A. Zaat, V. Fontaine, M. Ramstedt, R. Luginbuehl, K. Thevissen, J. Li, H.C. van der Mei, H.J. Busscher, In vitro methods for the evaluation of antimicrobial surface designs, Acta Biomater. (2018).

[50] E.P. Ivanova, J. Hasan, H.K. Webb, G. Gervinskas, S. Juodkazis, V.K. Truong, A.H. Wu, R.N. Lamb, V.A. Baulin, G.S. Watson, Bactericidal activity of black silicon, Nat. Commun. 4 (2013).

[51] D. Widyaratih, P.-L. Hagedoorn, L. Otten, M. Ganjian, N. Tumer, I. Apachitei, C.W.K. Hagen, L. Fratila-Apachitei, A.A. Zadpoor, Towards osteogenic and bactericidal nanopatterns?, Nanotechnology (2019).

[52] L.E. Fisher, Y. Yang, M.-F. Yuen, W. Zhang, A.H. Nobbs, B. Su, Bactericidal activity of biomimetic diamond nanocone surfaces, Biointerphases 11(1) (2016) 011014.

[53] D.P. Linklater, H.K.D. Nguyen, C.M. Bhadra, S. Juodkazis, E.P. Ivanova, Influence of nanoscale topology on bactericidal efficiency of black silicon surfaces, Nanotechnology 28(24) (2017) 245301.

[54] S. Wu, F. Zuber, K. Maniura-Weber, J. Brugger, Q. Ren, Nanostructured surface topographies have an effect on bactericidal activity, J. Nanobiotechnol. 16(1) (2018) 20.

[55] M. Mirzaali, I. Van Dongen, N. Tümer, H. Weinans, S.A. Yavari, A. Zadpoor, In-silico quest for bactericidal but non-cytotoxic nanopatterns, Nanotechnology 29(43) (2018) 43LT02.

[56] J.-H. Hwang, D.-H. Lee, M.R. Byun, A.R. Kim, K.M. Kim, J.I. Park, H.T. Oh, E.S. Hwang, K.B. Lee, J.-H. Hong, Nanotopological plate stimulates osteogenic differentiation through TAZ activation, Scientific reports 7(1) (2017) 3632.

[57] T. Sjöström, L.E. McNamara, R.D. Meek, M.J. Dalby, B. Su, 2D and 3D nanopatterning of titanium for enhancing osteoinduction of stem cells at implant surfaces, Advanced healthcare materials 2(9) (2013) 1285-1293.

[58] Z. Li, J. Qiu, L.Q. Du, L. Jia, H. Liu, S. Ge, TiO2 nanorod arrays modified Ti substrates promote the adhesion, proliferation and osteogenic differentiation of human periodontal ligament stem cells, Materials Science and Engineering: C 76 (2017) 684-691.

[59] L.E. McNamara, T. Sjöström, K.E. Burgess, J.J. Kim, E. Liu, S. Gordonov, P.V. Moghe, R.D. Meek, R.O. Oreffo, B. Su, Skeletal stem cell physiology on functionally distinct titania nanotopographies, Biomaterials 32(30) (2011) 7403-7410.

[60] T. Sjöström, M.J. Dalby, A. Hart, R. Tare, R.O. Oreffo, B. Su, Fabrication of pillar-like titania nanostructures on titanium and their interactions with human skeletal stem cells, Acta Biomaterialia 5(5) (2009) 1433-1441.

[61] G.M. de Peppo, H. Agheli, C. Karlsson, K. Ekström, H. Brisby, M. Lennerås, S. Gustafsson, P. Sjövall, A. Johansson, E. Olsson, Osteogenic response of human mesenchymal stem cells to well-defined nanoscale topography in vitro, International journal of nanomedicine 9 (2014) 2499.

[62] P. Post, A. Mohammadi-Gheidari, C. Hagen, P. Kruit, Parallel electron-beam-induced deposition using a multi-beam scanning electron microscope, J. Vac. Sci. Technol., B: Nanotechnol. Microelectron: Mater., Process., Meas., Phenom. 29(6) (2011) 06F310.

[63] Y. Zhao, E. Berenschot, M. De Boer, H. Jansen, N. Tas, J. Huskens, M. Elwenspoek, Fabrication of a silicon oxide stamp by edge lithography reinforced with silicon nitride for nanoimprint lithography, J. Micromech. Microeng. 18(6) (2008) 064013.

[64] D.J. Resnick, S. Sreenivasan, C.G. Willson, Step & flash imprint lithography, Mater. Today 8(2) (2005) 34-42.

[65] L.J. Guo, Nanoimprint lithography: methods and material requirements, Adv. Mater. 19(4) (2007) 495-513.

[66] H. Cao, Z. Yu, J. Wang, J.O. Tegenfeldt, R.H. Austin, E. Chen, W. Wu, S.Y. Chou, Fabrication of 10 nm enclosed nanofluidic channels, Appl. Phys. Lett. 81(1) (2002) 174-176.

[67] A. Notargiacomo, E. Giovine, L. Di Gaspare, Ion and electron beam deposited masks for pattern transfer by reactive ion etching, Microelectron. Eng. 88(8) (2011) 2710-2713.

The role of interspace in the bactericidal properties of nanopillars

Abstract

Recent progress in nano-/micro-fabrication techniques has paved the way for the emergence of synthetic bactericidal patterned surfaces that are capable of killing the bacteria via mechanical mechanisms. Different design parameters are known to affect the bactericidal activity of nanopatterns. Evaluating the effects of each parameter, isolated from the others, requires systematic studies. Here, we systematically assessed the effects of the interspacing and disordered arrangement of nanopillars on the bactericidal properties of nanopatterned surfaces. Electron beam induced deposition (EBID) was used to additively manufacture nanopatterns with precisely controlled dimensions (i.e., a height of 190 nm, a diameter of 80 nm, and interspaces of 100, 170, 300, and 500 nm) as well as disordered versions of them. The killing efficiency of the nanopatterns against Gram-positive Staphylococcus aureus bacteria increased by decreasing the interspace, achieving the highest efficiency of 62 ± 23% on the nanopatterns with 100 nm interspacing. By comparison, the disordered nanopatterns did not influence the killing efficiency significantly, as compared to their ordered correspondents. Direct penetration of nanopatterns into the bacterial cell wall was identified as the killing mechanism according to cross-sectional views, which is consistent with previous studies. The findings indicate that future studies aimed at optimizing the design of nanopatterns should focus on the interspacing as an important parameter affecting the bactericidal properties. In combination with the controlled disorder, nanopatterns with contrary effects on bacterial and mammalian cells may be developed.

3.1. Introduction

An increasing number of orthopedic implants are being implanted every year [1], resulting in a growing number of implant-associated infections (IAIs). Despite all efforts involved in preventing infections in clinical settings, IAIs still occur and are recognized as one of the most prevalent causes of the failure of orthopedic implants [2, 3]. Such infections usually necessitate either revision surgeries or the prolonged administration of antibiotics, which diminishes the patients' quality of life, causes major side effects, significantly increases the healthcare costs, and could lead to patient morbidity or even mortality [3, 4]. Staphylococci bacteria are the most widespread infectious pathogens involved in IAIs [5]. While Staphylococcus aureus accounts for 20%–30% of IAIs following fracture fixation and

prosthetic joint infections [5-7], antibiotic treatment could act as a double-edged sword, particularly given the growing crisis of antibacterial resistance leading to the evolution of antibiotic-resistant species like Methicillin-resistant staphylococcus aureus (MRSA) [8]. Moreover, recent reports have shown that in addition to antibiotics, bacteria can develop resistance against other types of killing agents, such as silver nanoparticles [9]. Therefore, alternative approaches to the prevention of IAIs including those based on physical forces should be more seriously considered. In such approaches, specifically designed surface features kill the bacteria that reach the implant surface [10].

The recent progress in nano-/micro-fabrication techniques has made it feasible to develop surfaces ornamented with geometrical features (*e.g.,* pillars) whose arbitrary shapes, sizes, and arrangements are precisely controlled [11]. Eukaryotic and prokaryotic cells are known to interact with these patterns in different ways ending up with distinct, and even contrary, cellular responses [12, 13]. There are pieces of evidence suggesting that mechanobiological pathways trigger and control these responses [12, 14, 15]. At the same time, nature offers great examples of surfaces with nanoscale features (nanopatterns) that leave bacterial cells with no choice of response but death [10, 16, 17]. Therefore, studying the interactions between different types of cells and surface nanopatterns is of high interest, because, unlike larger length scales, nanopatterns can affect individual cell receptors, which stand first in the line for the transduction of mechanical signals [14, 18].

Inspired by nature, many synthetic replicas of naturally occurring bactericidal nanopatterns have been designed, fabricated, and tested against a wide variety of bacterial strains [17, 19]. Several design parameters such as the shape, dimensions (height, diameter, and the interspace between them), and arrangement highly influence the response of bacterial cells to surface nanopatterns [12, 20]. For example, a specific range of dimensions is known to induce bactericidal properties (*i.e.,* 100 nm < height < 900 nm; 20 nm < diameter < 207 nm; 9 nm < interspacing < 380 nm) [20].

The limited number of systematic studies has made it difficult to draw concrete conclusions regarding the isolated effects of each design parameter (*i.e.,* height, diameter, or interspacing) on the bactericidal properties of surfaces. Similarly, while extensive data is available regarding the effects of disordered nanopatterns on the response of mammalian

cells [21-23], a limited number of reports can be found on how disordered arrangement can affect the bactericidal properties of nanopatterns [24].

In the present study, we aimed to study the isolated effects of one specific design parameter (*i.e.*, interspacing) as well as controlled disorder on the functionality of a bactericidal nanopattern. Pillar-shaped nanopatterns with an approximate height of 190 nm, a diameter of 80 nm, and an interspacing of 170 nm were chosen as the reference bactericidal nanopattern, which has been shown to be effective against both Gram-positive and Gram-negative bacteria [25]. Keeping the height and diameter constant, the interspacing of the nanopillars was changed to 100, 300, and 500 nm to create new nanopatterns. These values cover the full range of possible interspacing including one that was larger than all previously reported ones (*i.e.*, 500 nm), one close to the maximum value reported before (*i.e.*, 300 nm), and one smaller than the majority of the previous studies (*i.e.*, 100 nm) [20]. The controlled disorder was the other studied parameter, creating a variant to each of the four abovementioned nanopatterns. Furthermore, *S. aureus* was used as the study organism because of its prevalence in IAIs. We used electron beam induced deposition (EBID) as a nanoscale additive manufacturing (=3D printing) technique to fabricate the nanopatterns due to its high precision and controllability that make it an unrivaled single-step method for the direct printing of 3D surface physical features at the sub-10 nm nanoscale [25-27].

3.2. Materials and methods

3.2.1. Nanopatterns Design, Fabrication, and Characterization

To introduce controlled disorder to the nanopatterns, the maximum distance at which nanopillars did not intersect when displaced towards each other was set as the maximum disorder distance. Having set the diameter of nanopatterns to 80 nm, the maximum disorder distance was defined for each nanopattern to be half of the difference between the interspacing and the diameter. Since such a small level of disorder does not substantially change the arrangement of the nanopatterns with an interspacing of 100 nm, the effects of disorder were not studied for that particular level of interspacing. The following nanopatterns were, therefore, included in the study: ordered nanopatterns with interspacing of 100, 170, 300, and 500 nm as well as disordered nanopatterns with interspacing of 170, 300, and 500 nm. We will call those patterns 100 *O*, 170 *O*, 170 *D*, 300 *O*, 300 *D*, 500 *O*, and 500 *D* where

the first number corresponds to the interspacing of the nanopillars followed by a latter indicating whether the arrangement of nanopillars has been fully ordered (*O*) or included controlled disorder (*D*).

EBID was used to fabricate the desired nanopatterns on silicon substrates as described before [25]. Briefly, 1×1 cm^2 samples were prepared by cutting double-sided polished 4-inch (diameter = 10.16 cm) silicon wafers (thickness = 525 ± 25 μm, p-type), cleaning with nitric acid, and rinsing with deionized water subsequently.

A Helios Nano Lab 650 scanning electron microscope (SEM) (FEI Company, Hillsboro, OR, USA) equipped with the apparatus required for EBID was used to create three nanopatterned areas of 20×20 μm^2 per specimen (Figure 1d). The precursor gas was Trimethyl(methylcyclopentadienyl)-platinum(IV), ($C_9H_{18}Pt$). The EBID process was performed using a working distance of 5 mm, an electron voltage of 17.8 kV, and a beam current of 0.40 nA. The background vacuum of the system was $8.82 \times e^{-7}$ mbar and the precursor gas flux was adjusted such that the total pressure was $2.33 \times e^{-6}$ mbar, after which the EBID process was started. Single-dot exposure was used as the writing strategy, using stream files generated through MATLAB (MathWorks, Natick, MA, USA) scripts.

The resulting nanopatterns were characterized by scanning electron microscopy (SEM) performing using the same equipment. The height and base diameter were measured for thirty different pillars per sample using 52° tilted SEM images. The center-to-center spacing was also measured from the top view images. The dimensions of the produced nanopatterns are reported as mean ± standard deviation (Table 1).
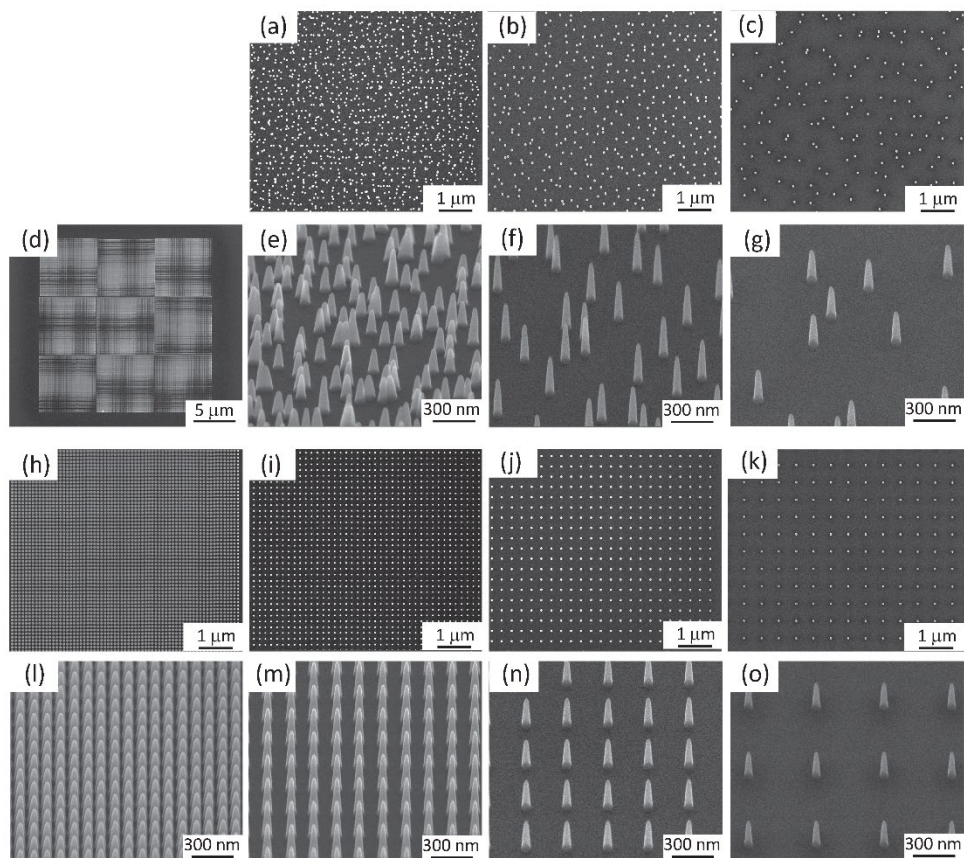
Figure 1. The scanning electron microscope (SEM) images of (a) the top view of the nanopillars with a height of 190 nm, a diameter of 80 nm, and an interspacing of 170 nm with 45 nm disorder distance (170 *D)*; (b) the top view of the nanopillars with an interspacing of 300 nm and 110 nm disorder distance (300 *D*); (c) the top view of the nanopillars with an interspacing of 500 nm and 210 nm disorder distance (500 *D*); (d) 20 × 20 μm² nanopatterned areas on a Si substrate; (e) the tilted view of 170 *D*; (f) the tilted view of 300 *D*; (g) the tilted view of 500 *D*; (h) the top view of the ordered nanopillars with an interspacing of 100 nm (100 *O*); (i) the top view of the ordered nanopillars with an interspacing of 170 nm (170 *O*); (j) the top view of the ordered nanopillars with an interspacing of 300 nm (300 *O*); (k) the top view of the ordered nanopillars with an interspacing of 500 nm (500 *O*); (l) the tilted view of 100 *O*; (m) the tilted view of 170 *O*; (n) the tilted view of 300 *O*; (o) the tilted view of 500 *O*.

Table 1. The characteristics of the nanopatterns produced by EBID.

Pattern Type	Interspace (nm)	Disorder Distance (nm)	Height (nm)	Base Diameter (nm)	Aspect Ratio	Pillar Density (no/μm²)
100 O	100	0	198 ± 7	89 ± 4	2.2 ± 0.0	100.6
170 D	170	45	200 ± 13	73 ± 9	2.7 ± 0.2	35.5
170 O	170	0	188 ± 22	67 ± 13	2.8 ± 0.2	35.5
300 D	300	110	177 ± 13	73 ± 3	2.4 ± 0.1	11.9
300 O	300	0	190 ± 28	71 ± 2	2.7 ± 0.3	11.9
500 D	500	210	201 ± 15	76 ± 4	2.6 ± 0.1	4.5
500 O	500	0	184 ± 16	72 ± 3	2.6 ± 0.1	4.5

Given that the static water contact angles could not be measured directly (due to the small size of the patterned areas), we used the Cassie-Baxter wettability model to estimate the values corresponding to different designs [28, 29]. To this aim, the contact angle of an EBID-fabricated Pt-C layer was measured by a DSA 100 drop shape analyzer (Krüss, Hamburg, Germany) using deionized water. A volume of 2 μL liquid with a falling rate of 1667 μl/min was placed on the surface and the average contact angle was recorded within 30 s after the droplet touched the surface. The measured contact angle was further used to calculate the Cassie-Baxter contact angle (Table 1) [25].

Furthermore, topography images of the nanopatterns were acquired in Quantitative Imaging (QI) mode using an AFM JPK Nanowizard 4 (Berlin, Germany) and a high aspect ratio probe (TESPA-HAR, Bruker, Germany). A set point of 20 nN, a Z length of 300 nm, and a pixel time of 10 ms were used as scanning parameters. The images were analysed by using the JPK SPM data processing software (JPK instruments, v6.1, Berlin, Germany) to obtain 3D images of the surface and the average roughness.

3.2.2. Preparation of Bacterial Cultures

Gram-positive bacteria Staphylococcus aureus (RN0450 strain) (BEI Resources, Virginia, USA) was grown on brain heart infusion (BHI) (Sigma-Aldrich, Missouri, USA) agar plates at 37 °C overnight. A pre-culture of bacteria was prepared by inoculating a single colony in 10 mL autoclaved BHI, shaken at 140 rpm at 37 °C. The bacterial cells were collected at their logarithmic stage of growth and their optical density at 600 nm wavelength (OD_{600}) in the medium solution was adjusted to a value of 0.1 to be finally cultured on the specimens. Such OD is equivalent to 148×106 colony forming units (CFUs) per milliliter.

3.2.3. Investigation of Bactericidal Properties

Two independent sets of experiments were performed to evaluate the bactericidal properties of the nanopatterns. In each set of experiments, the nanopatterned areas of each specimen and the surrounding flat areas (Figure 1d) were considered as the study and control groups (all in triplicates) in the bacterial studies, respectively. The specimens were initially sterilized by immersion in 70% ethanol and were exposed to UV light for 20 min prior to inoculation with 1 mL of the bacterial suspension in a 24-well plate (Cell Star, Germany). The specimens were then incubated at 37 °C for 18 h.

As previously explained [25], fabricating large areas of nanopatterned surfaces using EBID is not time-efficient yet, but patterning a small area would suffice for systematically studying the bactericidal effects of highly controlled nanopatterns. However, it hinders the use of certain assessment methods such as live/dead staining and CFU counting. We, therefore, exploited a method applied previously in several other studies [25, 30-33] in which morphological evaluation of bacterial cells through SEM imaging is used to distinguish between disrupted and healthy bacterial cells. The validity of this technique has been demonstrated before in studies that have used and compared different evaluation techniques in determining the bactericidal properties of nanopatterned surfaces [30, 33]. Therefore, to determine the killing efficiency of the nanopatterns, we first washed our specimens with phosphate-buffered saline (PBS) to remove any non-adherent bacteria. The adhered bacterial cells were then fixed by immersion in a PBS solution containing 4% formaldehyde (Sigma-Aldrich, St. Louis, MI, USA) and 1% glutaraldehyde (Sigma-Aldrich, USA) at 4 °C for 1 h. Subsequently, the samples were dehydrated by a series of ethanol washing (50%, 70%, and

96% ethanol, respectively) and finally with hexamethyldisilazane (HMDS) (Sigma-Aldrich, USA) for 30 min. After being air-dried, a thin layer of gold was sputtered on the specimens prior to being imaged by SEM at different magnifications and tilt angles of 0° and 52°. The killing efficiency was defined as the ratio of damaged cells to the total number of cells on the intended areas. Moreover, counting the total number of the bacterial cells attached to the nanopatterned and flat areas of each specimen enabled a comparison between the cell adhesion within the flat and nanopatterned surfaces.

3.2.4. Investigation of Nanopattern-Bacteria Interface

In order to further investigate the interactions between the bacterial cells and the nanopillars, and to analyse the possible killing mechanism of the nanopattern with the highest killing efficiency, focused ion beam scanning electron microscopy (FIB-SEM, FEI, Helios Nano Lab 650, OR, USA) was performed to acquire a cross-sectional view of the interface between cells and patterns. The specimen was tilted to 52°, at which angle the surface was milled using Gallium ions with a 7.7 pA ion beam (operating voltage = 30 kV).

3.2.5. Statistical Analysis

To determine the statistical significance of the differences between the means of different experimental groups in terms of their bacterial cells attachment, a two-way ANOVA test was performed, followed by a Sidak's multiple comparisons test, which was performed using Prism version 8.0.1 (GraphPad, San Diego, CA, USA). Similarly, the killing efficiency of different nanopatterns was statistically analyzed using the Mann-Whitney test. A p-value below 0.05 was considered to indicate statistical significance.

3.3. Results

3.3.1. Characteristics of the Fabricated Nanopatterns

Nanopillar arrays with different types of arrangements and interspacing values were successfully fabricated in 20×20 μm^2 areas on each sample (Figure 1). Notwithstanding some slight variations, the intended dimensions were achieved for all the experimental groups (Table 1). The differences in the dimensions and arrangements of the nanopillars were clearly observed in SEM images (Figure 1) and AFM images (Figure 2). The average roughness decreased by increasing the interspacing of both ordered nanopillars (from 46.8 ± 4.9 nm for

100 O to 39.1 ± 1.8 nm for 500 O) and disordered nanopillars (from 68.3 ± 4.9 nm for 170 D to 24.8 ± 2.3 nm for 500 D). The density of the nanopillars decreased by increasing the interspacing, from 100.6 pillars per μm^2 for 100 O to 4.5 pillars per μm^2 for 500 O and 500 D. The nanopatterned surfaces were hydrophobic, as estimated by using the Cassie-Baxter model, with water contact angles ranging from 154° to 176°.

3.3.2. Effect of Interspacing on Bactericidal Properties

Before analyzing the effects of the selected parameters on the bactericidal activity of the nanopatterns, the bacterial adhesion to the specimens was studied to see whether any of the fabricated nanopatterns impairs the attachment of bacterial cells. Although care was taken to ensure seeding was as homogeneous as possible, there might be local differences in the number of the bacteria attached to the specimens. However, the ratio of the number of cells attached to the nanopatterned surfaces to those attached to a similar-sized flat area did not significantly vary between the specimens, meaning that bacterial cell adhesion was similar between all experimental groups (Figure 3a).

S. aureus cells showed their typical coccoid-shaped morphology on the flat areas with no significant sign of irregularity, disruption, or death (Figure 3b). On the contrary, ruptured bacterial cells with squashed morphologies were identified on the nanopatterned areas and were marked as damaged/dead cells (Figure 3f–i). The ordered nanopatterns with larger interspacing values (*i.e.,* 300 O and 500 O) displayed significantly lower bactericidal efficiencies against *S. aureus* (8.6 ± 4.2% and 3.7 ± 2.3%, respectively) as compared to 100 O and 170 O ($p < 0.01$) (Figure 4a). While there was a significant difference in the killing efficiency between 300 O and 500 O ($p < 0.05$), no significant differences were observed between 100 O and 170 O.
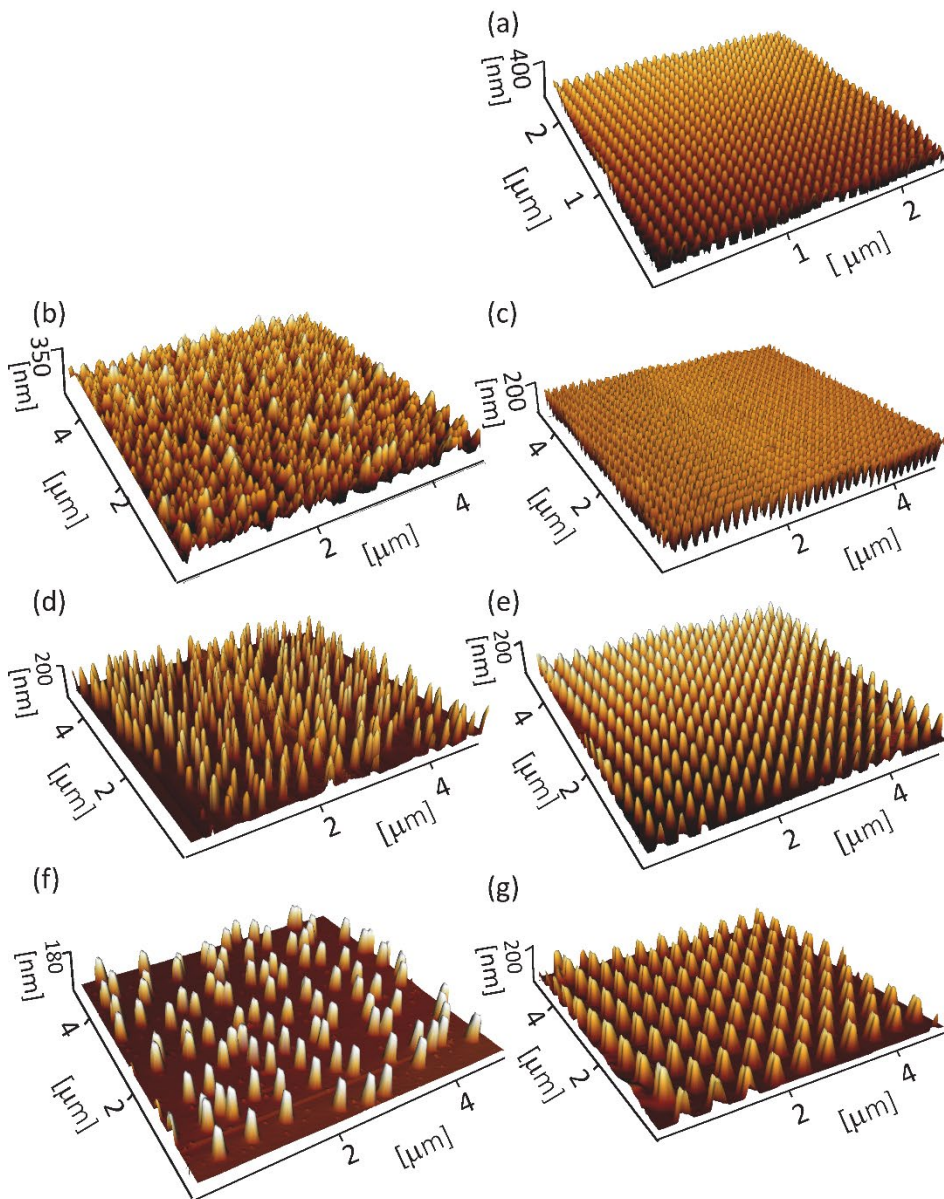
Figure 2. 3D AFM images of (a) 100 *O*; (b) 170 *D*; (c) 170 *O*; (d) 300 *D*; (e) 300 *O*; (f) 500 *D*; (g) 500 *O* nanopillars.

3.3.3. The Effects of Controlled Disorder on Bactericidal Properties

The effects of controlled disorder on the bactericidal activity of the nanopatterned surfaces were evaluated by comparing the killing efficiency of the ordered and disordered nanopatterns with the same interspacing (Figure 3c–e). Although somewhat higher values of killing efficiencies were observed for the disordered nanopatterns with larger interspacing values (*i.e.*, 300 *D* and 500 *D*) as compared to their ordered counterparts, the differences were not statistically significant (Figure 3a). The disordered nanopattern with the lower interspacing (*i.e.*, 170 *D*) showed the same bactericidal efficiency as the ordered counterpart (Figure 4b).

3.3.4. Nanopattern-Bacteria Interface

Cross-sectional views showed that nanopatterns could penetrate the bacterial cell wall and cause their death by disrupting it (Figure 5). Moreover, the bending of the nanopillars underneath the bacterial cells (Figures 3 and 5) suggested significant amounts of reciprocal forces that cells and pillars exert on each other.

3.4. Discussion

The main contribution of this study was shedding light on how interspacing and controlled disorder could affect the bactericidal properties of nanopatterns. The height and diameter of the nanopatterns produced were, therefore, kept constant while the interspacing and the arrangement of nanopillars were systematically altered in seven different study groups.

In order to elucidate the effects of these two parameters on the bactericidal properties of nanopatterns, it is crucial to first consider their killing mechanisms. The main killing mechanism of nanopatterns is widely believed to be the direct penetration of high aspect-ratio nanopatterns into the bacterial cell wall and disrupting it by exerting a high enough force [20, 31]. Since the thickness and composition of cell walls are different in Gram-negative and Gram-positive bacteria [34], the same force will not rupture different cell walls equally [16, 35]. Moreover, other factors such as hydrostatic and gravitational forces should be also considered when studying the interactions between bacteria and nanopatterns [36]
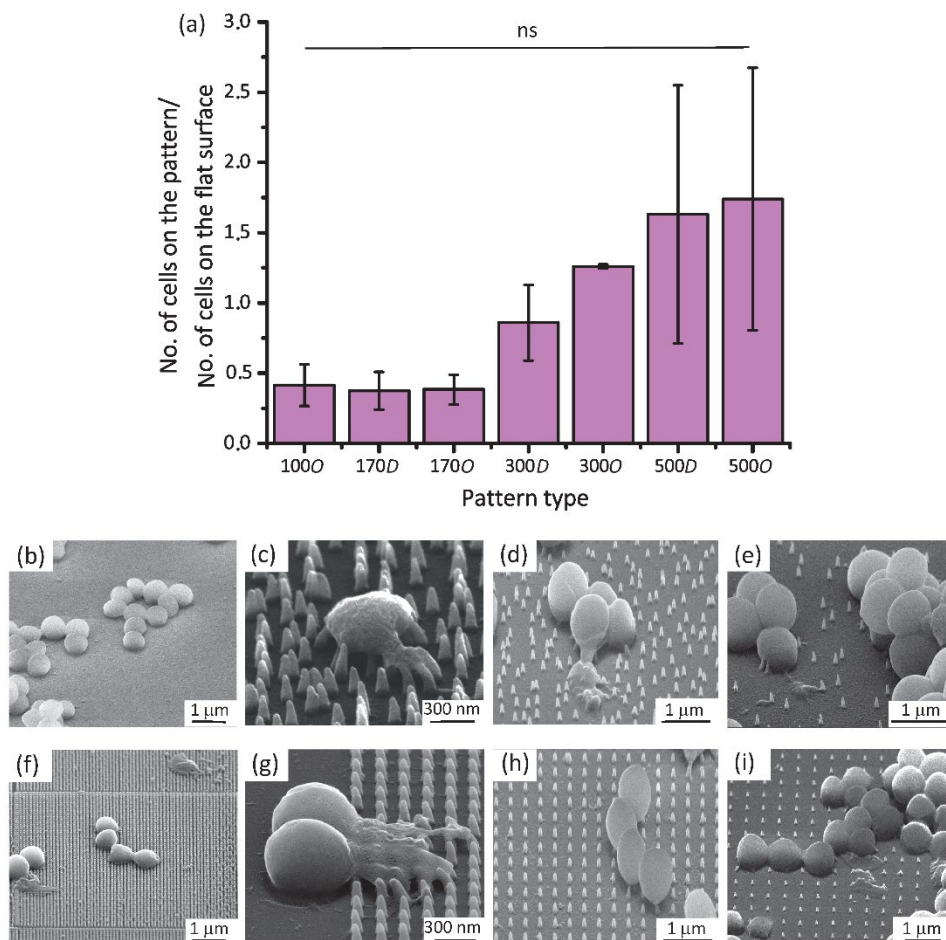
Figure 3. (a) The ratio of the bacterial cells attached to the nanopatterns to those attached to similar flat areas. No significant difference in that ratio for different types of nanopattern indicates that bacterial adhesion is similar between different groups; The SEM images of *S. aureus* bacteria on (b) the control Si surface; (c) 170 *D*; (d) 300 *D*; (e) 500 *D*; (f) 100 *O*; (g) 170 *O*; (h) 300 *O*; (i) 500 *O* at 52° tilted view. The damaged bacterial cells can be identified with irregular and unrecognizable morphologies as compared to normal cells on flat surfaces.
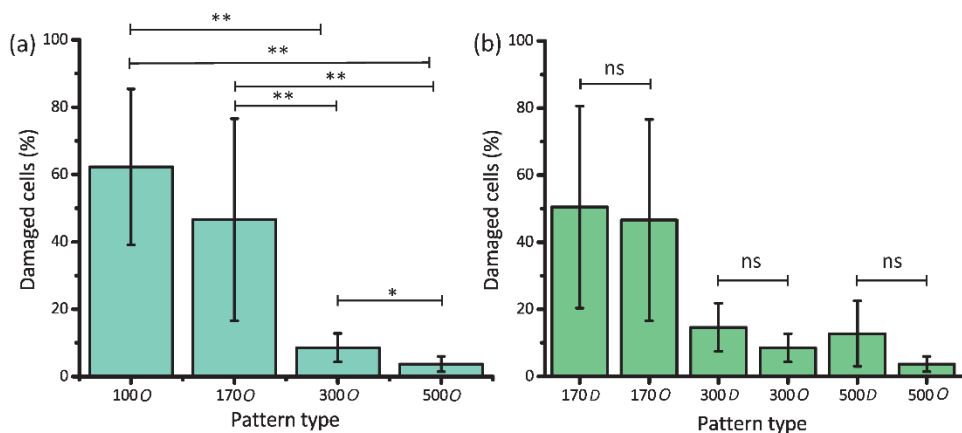
Figure 4. (a) The effects of interspacing on the bactericidal efficiency of nanopatterns (* $p < 0.05$ and ** $p < 0.01$); (b) The effects of controlled disorder on the bactericidal efficiency of nanopatterns. No significant differences were observed between the ordered and disordered nanopatterns but the value of interspacing.
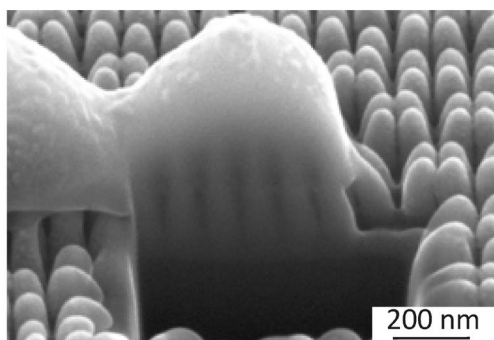
Figure 5. The SEM image of the interface between bacteria and the 100 O nanopattern. The depth of direct penetration of the nanopillars into the bacterial cell wall (about 100 nm) far exceeds the average cell wall thickness of *S. aureus* (i.e., 10–20 nm).

The results of this study showed that the cell wall of *S. aureus* could be mechanically penetrated by nanopatterns (Figure 5) and be severely damaged with an unrecognizable morphology (Figure 3), as reported previously [25, 30, 37]. However, changing the interspacing of nanopatterns could drastically affect the percentage of the damaged cells. Although aspect-ratio is a crucial design parameter of bactericidal nanopatterns, this effect

seems to overshadow the effects of the nanopatterns aspect-ratio, which is corroborated by other studies in the literature. Linklater *et al.* showed that nanopillars with a diameter of 80 nm, an interspacing of 99 nm (similar to 100 *O* in the present study), and a height of around 430 nm (much higher than 100 *O*), exhibit a comparable level of bactericidal activity against *S. aureus* [38]. Similarly, another study [39] showed that naturally occurring nanopillars with the approximate height of 430 nm, the approximate tip diameter of 48 nm, and an interspacing of around 116 nm (*i.e.*, larger height than 100 *O* but comparable interspacing), exhibit a killing efficiency of 39.4 ± 20.3% against *S. aureus* after 18 h. Computational simulations have also demonstrated that, as compared to the height, the interspacing has a substantially greater effect on the bactericidal properties of nanopillars [40]. It is plausible that a smaller interspacing and a higher density of nanopatterns result in more contact points between the bacteria and nanopatterns. This, in turn, leads to more physicomechanical interactions and higher chances of bacteria being ruptured [41], however, further studies are required to determine the minimum number of contact points that exert enough force to rupture the cell wall of different types of bacteria. According to the literature, the majority of bactericidal nanopatterns have an interspacing below 300 nm [20]. The reported values make more sense when it comes to bactericidal activity against *S. aureus*, which has a coccoid shape with a diameter larger than 500 nm [42]. For an interspacing exceeding the diameter of *S. aureus*, it is likely that bacterial cells land in between the nanopillars, thereby escaping the deadly spikes (Figure 3h, i).

An increased number of contact points for the lower values of interspacing could also contribute to some other proposed killing mechanisms. Bandara *et al.* [43] have argued that nanopillars do not directly interact with the bacterial cell membrane and showed that bacterial cells attach to surface nanopatterns via the expression of extracellular polymeric substances (EPS). Further movement of the bacteria on the surface on the one hand and strong EPS-mediated adhesion forces on the other lead to the stretching of the cell membrane beyond its rupture point. Considering this theory, an increased number of adhesion sites between surface features and expressed EPS could potentially amplify such a stretching mechanism. Although the bending of the nanopillars underneath the bacterial cells could be due to that movement rather than the bacteria weight only, further evaluations such as live imaging for real-time tracking of the bacteria on the surface, are required to confirm such a

mechanism. Additionally, AFM measurements in another study have shown that the adhesion force of an EPS-producing *S. aureus* strain attached to nanopatterns does not significantly change due to differences in interspacing [44]. Altogether, the results of the present study are more consistent with the direct penetration theory, as it can be seen that nanopatterns have actually intruded about 101 nm (SD 9 nm) (Figure 5) into the bacterial cells, which is much larger than the cell wall thickness *of S. aureus* (*i.e.,* 10–20 nm) [45].

Deviation from an ordered arrangement in nanopatterns has been shown to effectively influence the differentiation of the human mesenchymal stem cells [22] and the response of osteoblast cells [21]. Biochemical mechanotransduction pathways have been shown to be involved in translating mechanical cues (*e.g.*, disordered nanopatterns) into biochemical responses (proteomic changes) [46]. An intricate network of cellular components is associated with receiving, transducing, and interpreting the mechanical cues [14]. In contrast, the bacterial mechanotransduction mechanisms seem to be simpler since the structure and components of bacterial cells are not as complex as those of mammalian cells [15]. Moreover, the information over the influence of nanopatterns disorder on the bacterial mechanotransduction is scarcely available in the literature. Further studies are, therefore, needed to elucidate the possible mechanobiological pathways pertaining to the interactions of bacteria and nanopatterns. Similar to another study that used *E. coli* [24], our results showed no significant difference between the bactericidal efficiencies of ordered and disordered nanopatterns against *S. aureus* as long as the interspacing is kept constant. Given the killing mechanism observed in this study, it can be concluded that introducing controlled disorder either does not change the mechanical force that bacteria experience or does not increase it beyond the threshold required for cell wall rupture. The findings of this study indicate that interspacing is a highly promising design parameter that should be further optimized to achieve nanopatterned surfaces with the highest potential of bactericidal activity. In combination with controlled disorder, nanopatterns with contrary effects on bacterial and mammalian cells may be developed in order to achieve the selective biocidal activity.

Conclusions

The effects of the interspacing and controlled disorder, as two design parameters, on the bactericidal properties of nanopatterns were systematically studied. Nanopatterns with constant heights and diameters of 190 nm and 80 nm, respectively, and different values of interspacing (*i.e.*, 100, 170, 300, and 500 nm) were fabricated using EBID. A controlled disordered version of the nanopatterns with interspacings of 170, 300, and 500 nm was also fabricated. Quantifying the number of damaged *S. aureus* cells cultured on the nanopatterns for 18 h, showed that decreasing the interspacing significantly increased the bactericidal efficiency and the nanopatterns with 100 nm interspacing exhibited the highest efficiency (62.3 ± 23.1%). The nanopatterns with controlled disorder did not enhance the bactericidal efficiency compared with the ordered counterparts. Moreover, the direct penetration of nanopatterns into the bacterial cell wall and its eventual rupture due to the forces applied to it was shown to be the dominant killing mechanism of these nanopatterns which is consistent with the majority of the previous studies. Further research is required to elucidate whether interspacing and controlled disorder could affect the biochemical mechanotransduction pathways in bacteria.

References

[1] S. Kurtz, K. Ong, E. Lau, F. Mowat, M. Halpern, Projections of primary and revision hip and knee arthroplasty in the United States from 2005 to 2030, JBJS 89(4) (2007) 780-785.

[2] W. Zimmerli, A. Trampuz, P.E. Ochsner, Prosthetic-joint infections, N. Engl. J. Med. 351(16) (2004) 1645-1654.

[3] T.F. Moriarty, R. Kuehl, T. Coenye, W.-J. Metsemakers, M. Morgenstern, E.M. Schwarz, M. Riool, S.A. Zaat, N. Khana, S.L. Kates, Orthopaedic device-related infection: current and future interventions for improved prevention and treatment, EFORT open reviews 1(4) (2016) 89-99.

[4] J.M. Steckelberg, D.R. Osmon, Prosthetic joint infections, Infections Associated with Indwelling Medical Devices, Third Edition, American Society of Microbiology2000, pp. 173-209.

[5] L. Montanaro, P. Speziale, D. Campoccia, S. Ravaioli, I. Cangini, G. Pietrocola, S. Giannini, C.R. Arciola, Scenery of Staphylococcus implant infections in orthopedics, Future microbiology 6(11) (2011) 1329-1349.

[6] A. Trampuz, W. Zimmerli, Diagnosis and treatment of infections associated with fracture-fixation devices, Injury 37(2) (2006) S59-S66.

[7] S. Corvec, M.E. Portillo, B.M. Pasticci, O. Borens, A. Trampuz, Epidemiology and new developments in the diagnosis of prosthetic joint infection, The International journal of artificial organs 35(10) (2012) 923-934.

[8] N.A. Turner, B.K. Sharma-Kuinkel, S.A. Maskarinec, E.M. Eichenberger, P.P. Shah, M. Carugati, T.L. Holland, V.G. Fowler, Methicillin-resistant Staphylococcus aureus: an overview of basic and clinical research, Nat. Rev. Microbiol. 17(4) (2019) 203-218.

[9] A. Panáček, L. Kvítek, M. Smékalová, R. Večeřová, M. Kolář, M. Röderová, F. Dyčka, M. Šebela, R. Prucek, O. Tomanec, Bacterial resistance to silver nanoparticles and how to overcome it, Nat. Nanotechnol. 13(1) (2018) 65.

[10] J. Hasan, R.J. Crawford, E.P. Ivanova, Antibacterial surfaces: the quest for a new generation of biomaterials, Trends Biotechnol. 31(5) (2013) 295-304.

[11] B.D. Gates, Q. Xu, M. Stewart, D. Ryan, C.G. Willson, G.M. Whitesides, New approaches to nanofabrication: molding, printing, and other techniques, Chemical reviews 105(4) (2005) 1171-1196.

[12] K. Anselme, P. Davidson, A. Popa, M. Giazzon, M. Liley, L. Ploux, The interaction of cells and bacteria with surfaces structured at the nanometre scale, Acta Biomater. 6(10) (2010) 3824-3846.

[13] L. Ploux, K. Anselme, A. Dirani, A. Ponche, O. Soppera, V. Roucoules, Opposite responses of cells and bacteria to micro/nanopatterned surfaces prepared by pulsed plasma polymerization and UV-irradiation, Langmuir 25(14) (2009) 8161-8169.

[14] Y. Sun, C.S. Chen, J. Fu, Forcing stem cells to behave: a biophysical perspective of the cellular microenvironment, Annual review of biophysics 41 (2012) 519-542.

[15] A. Persat, Bacterial mechanotransduction, Current opinion in microbiology 36 (2017) 1-6.

[16] J. Hasan, H.K. Webb, V.K. Truong, S. Pogodin, V.A. Baulin, G.S. Watson, J.A. Watson, R.J. Crawford, E.P. Ivanova, Selective bactericidal activity of nanopatterned superhydrophobic cicada Psaltoda claripennis wing surfaces, Appl. Microbiol. Biotechnol. 97(20) (2013) 9257-9262.

[17] A. Elbourne, R.J. Crawford, E.P. Ivanova, Nano-structured antimicrobial surfaces: From nature to synthetic analogues, J. Colloid Interface Sci. 508 (2017) 603-616.

[18] M.J. Dalby, N. Gadegaard, R.O. Oreffo, Harnessing nanotopography and integrin–matrix interactions to influence stem cell fate, Nature materials 13(6) (2014) 558-569.

[19] J. Hasan, A. Roy, K. Chatterjee, P.K. Yarlagadda, Mimicking Insect Wings: The Roadmap to Bioinspiration, ACS Biomaterials Science & Engineering 5(7) (2019) 3139-3160.

[20] K. Modaresifar, S. Azizian, M. Ganjian, L.E. Fratila-Apachitei, A.A. Zadpoor, Bactericidal effects of nanopatterns: a systematic review, Acta Biomater. (2018).

[21] C. Allan, A. Ker, C.-A. Smith, P.M. Tsimbouri, J. Borsoi, S. O'Neill, N. Gadegaard, M.J. Dalby, R. Dominic Meek, Osteoblast response to disordered nanotopography, Journal of tissue engineering 9 (2018) 2041731418784098.

[22] M.J. Dalby, N. Gadegaard, R. Tare, A. Andar, M.O. Riehle, P. Herzyk, C.D. Wilkinson, R.O. Oreffo, The control of human mesenchymal cell differentiation using nanoscale symmetry and disorder, Nature materials 6(12) (2007) 997-1003.

[23] S. Dobbenga, L.E. Fratila-Apachitei, A.A. Zadpoor, Nanopattern-induced osteogenic differentiation of stem cells–A systematic review, Acta biomaterialia 46 (2016) 3-14.

[24] D. Widyaratih, P.-L. Hagedoorn, L. Otten, M. Ganjian, N. Tumer, I. Apachitei, C.W. Hagen, L.E. Fratila-Apachitei, A.A. Zadpoor, Towards osteogenic and bactericidal nanopatterns?, Nanotechnology (2019).

[25] M. Ganjian, K. Modaresifar, M.R. Ligeon, L.B. Kunkels, N. Tümer, L. Angeloni, C.W. Hagen, L.G. Otten, P.-L. Hagedoorn, I. Apachitei, L.E. Fratila-Apachitei, A.A. Zadpoor, Nature Helps: Toward Bioinspired Bactericidal Nanopatterns, Advanced Materials Interfaces (2019) 1900640.

[26] W.F. Van Dorp, B. Van Someren, C.W. Hagen, P. Kruit, P.A. Crozier, Approaching the resolution limit of nanometer-scale electron beam-induced deposition, Nano Lett. 5(7) (2005) 1303-1307.

[27] L. van Kouwen, A. Botman, C.W. Hagen, Focused electron-beam-induced deposition of 3 nm dots in a scanning electron microscope, Nano Lett. 9(5) (2009) 2149-2152.

[28] B. Bhushan, M. Nosonovsky, The rose petal effect and the modes of superhydrophobicity, Philos. Trans. R. Soc., A 368(1929) (2010) 4713-4728.

[29] M. Sun, G.S. Watson, Y. Zheng, J.A. Watson, A. Liang, Wetting properties on nanostructured surfaces of cicada wings, J. Exp. Biol. 212(19) (2009) 3148-3155.

[30] E.P. Ivanova, J. Hasan, H.K. Webb, G. Gervinskas, S. Juodkazis, V.K. Truong, A.H. Wu, R.N. Lamb, V.A. Baulin, G.S. Watson, Bactericidal activity of black silicon, Nat. Commun. 4 (2013).

[31] D.P. Linklater, S. Juodkazis, S. Rubanov, E.P. Ivanova, Comment on "Bactericidal Effects of Natural Nanotopography of Dragonfly Wing on Escherichia coli", ACS Appl. Mater. Interfaces 9(35) (2017) 29387-29393.

[32] D.P. Linklater, M. De Volder, V.A. Baulin, M. Werner, S. Jessl, M. Golozar, L. Maggini, S. Rubanov, E. Hanssen, S. Juodkazis, High aspect ratio nanostructures kill bacteria via storage and release of mechanical energy, ACS Nano 12(7) (2018) 6657-6667.

[33] D.P. Linklater, S. Juodkazis, R. Crawford, E. Ivanova, Mechanical inactivation of Staphylococcus aureus and Pseudomonas aeruginosa by titanium substrata with hierarchical surface structures, Materialia 5 (2019) 100197.

[34] L. Brown, J.M. Wolf, R. Prados-Rosales, A. Casadevall, Through the wall: extracellular vesicles in Gram-positive bacteria, mycobacteria and fungi, Nat. Rev. Microbiol. 13(10) (2015) 620-630.

[35] S. Pogodin, J. Hasan, V.A. Baulin, H.K. Webb, V.K. Truong, V. Boshkovikj, C.J. Fluke, G.S. Watson, J.A. Watson, R.J. Crawford, Biophysical model of bacterial cell interactions with nanopatterned cicada wing surfaces, Biophys. J. 104(4) (2013) 835-840.

[36] F. Xue, J. Liu, L. Guo, L. Zhang, Q. Li, Theoretical study on the bactericidal nature of nanopatterned surfaces, Journal of theoretical biology 385 (2015) 1-7.

[37] A. Jaggessar, P.K. Yarlagadda, Modelling the growth of hydrothermally synthesised bactericidal nanostructures, as a function of process conditions, Mater. Sci. Eng. (2019) 110434.

[38] D.P. Linklater, H.K.D. Nguyen, C.M. Bhadra, S. Juodkazis, E.P. Ivanova, Influence of nanoscale topology on bactericidal efficiency of black silicon surfaces, Nanotechnology 28(24) (2017) 245301.

[39] V.K. Truong, N.M. Geeganagamage, V.A. Baulin, J. Vongsvivut, M.J. Tobin, P. Luque, R.J. Crawford, E.P. Ivanova, The susceptibility of Staphylococcus aureus CIP 65.8 and Pseudomonas aeruginosa ATCC 9721 cells to the bactericidal action of nanostructured Calopteryx haemorrhoidalis damselfly wing surfaces, Appl. Microbiol. Biotechnol. 101(11) (2017) 4683-4690.

[40] M.J. Mirzaali, I. Van Dongen, N. Tümer, H. Weinans, S.A. Yavari, A.A. Zadpoor, In-silico quest for bactericidal but non-cytotoxic nanopatterns, Nanotechnology 29(43) (2018) 43LT02.

[41] G. Hazell, L.E. Fisher, W.A. Murray, A.H. Nobbs, B. Su, Bioinspired bactericidal surfaces with polymer nanocone arrays, J. Colloid Interface Sci. 528 (2018) 389-399.

[42] L. Harris, S. Foster, R. Richards, An introduction to Staphylococcus aureus, and techniques for identifying and quantifying S. aureus adhesins in relation to adhesion to biomaterials: review, Eur. Cells Mater. 4(3) (2002).

[43] C.D. Bandara, S. Singh, I.O. Afara, A. Wolff, T. Tesfamichael, K. Ostrikov, A. Oloyede, Bactericidal effects of natural nanotopography of dragonfly wing on Escherichia coli, ACS Appl. Mater. Interfaces 9(8) (2017) 6746-6760.

[44] F. Hizal, C.-H. Choi, H.J. Busscher, H.C. Van Der Mei, Staphylococcal adhesion, detachment and transmission on nanopillared Si surfaces, ACS Appl. Mater. Interfaces 8(44) (2016) 30430-30439.

[45] P.J. Wyatt, Cell wall thickness, size distribution, refractive index ratio and dry weight content of living bacteria (stapylococcus aureus), Nature 226(5242) (1970) 277.

[46] F. Kantawong, K.E. Burgess, K. Jayawardena, A. Hart, R.J. Burchmore, N. Gadegaard, R.O. Oreffo, M.J. Dalby, Whole proteome analysis of osteoprogenitor differentiation induced by disordered nanotopography and mediated by ERK signalling, Biomaterials 30(27) (2009) 4723-4731.

4

Quantitative mechanics of EBID nanopillars interacting with bacterial cells

Abstract

Surface nanopillars could play an important role in the design and fabrication of implantable medical devices by preventing the infections that are caused by the bacterial colonization of the implant surface. The mechanical properties of such nanoscale structures can influence their bactericidal efficiency. In addition, these properties are key factors in determining the fate of stem cells. In this study, we quantified the relevant mechanical properties of EBID nanopillars interacting with Staphylococcus aureus (S. aureus) using atomic force microscopy (AFM). We first determined the elastic modulus (17.7 GPa) and the fracture stress (3.0 ± 0.3 GPa) of the nanopillars using the quantitative imaging (QI) mode and contact mode (CM) of AFM. The displacement of the nanopillars interacting with the bacteria cells were measured by scanning electron microscopy (50.3 ± 9.0 nm). Finite element method based simulations were then applied to obtain the force-displacement curve of the nanopillars (considering the specified dimensions and the measured value of the elastic modulus) based on which an interaction force of 89 ± 36 nN was determined. The maximum von Mises stress of the nanopillars subjected to these forces was also determined (3.2 ± 0.3 GPa). These values were close to the maximum (i.e., fracture) stress of the pillars as measured by AFM, indicating that the nanopillars were close to their breaking point while interacting with S. aureus. These findings reveal unique quantitative data regarding the mechanical properties of nanopillars interacting with bacteria cells and highlight the possibilities to enhance the bactericidal activity of the investigated EBID nanopillars by adjusting both their geometry and mechanical properties.

4.1. Introduction

An increasing number of advanced nanotechnological applications require highly repeatable fabrication of 'three-dimensional' devices with complex and precisely-controlled geometries. Depending on the targeted feature size and the complexity of the desired geometry, nanofabrication techniques, such as two-photon polymerization (TPP) [1], imprint lithography [2-5], interference lithography [6], 3D molding [7], electron beam lithography (EBL) [8-10], electron beam-induced deposition (EBID) [10-13], ion beam lithography (IBL) [14], or focused ion beam (FIB) [10, 15, 16] could be used to fabricate such 3D structures.

At the cutting-edge of nanotechnology, however, there is often a need for the fabrication of arbitrarily complex 3D geometries with few-nanometers resolution [17]. EBID is currently the only nanofabrication technique that allows for combining 3D structures with few-nanometer (~1 nm [18]) accuracy and repeatability. Given its (theoretical) sub-nanometer resolution and mask-free nature, EBID is a highly powerful yet straightforward technique for the fabrication of cutting-edge nanodevices.

EBID is performed inside a scanning electron microscope (SEM) [19-22]. The gradual layer-by-layer addition of the deposited material creates the desired geometry that, as we have previously shown [13], can be very complex [23]. In that sense, EBID is an 'additive' manufacturing technique and, thus, distinct from subtractive (*e.g.*, RIE, FIB) and formative (*e.g.*, 3D molding) techniques. Nanofeatures can be formed on any type of substrate. The wide choice of precursor gases makes EBID a powerful technique for different types of applications, including sensors [24-26], plasmonics [12, 27], atomic force microscopy probes [17], superconductive nanowires [28], and the repair of UV lithography masks [29].

Both the structural performance and functionality of the nanostructures are dependent on the mechanical properties of the deposited material. Mechanobiological [30] and antibacterial [31-33] applications of nanopatterns highlight the 'functional' importance of understanding the mechanical behavior of EBID-made nanofeatures. For example, the mechanobiological consequences of the substrate stiffness for determining stem cell fate are currently being widely investigated [30, 34, 35]. Dual-effect nanopatterns that simultaneously stimulate stem cell differentiation and kill bacteria are envisaged as well [36]. As for antibacterial applications, the mechanical properties of the nanopillars have been shown to play a crucial role. Nanofeatures with very specific dimensions and aspect ratios are known to kill bacteria through pre-dominantly mechanical mechanisms (*i.e.*, overstretching the bacterial cell wall and rupturing cells components due to cell wall penetration) [33, 36, 37]. In general, the capability of the nanofeatures to penetrate the cell wall can be ascribed to two factors: i) the geometry of the tip, which must be as sharp as possible, and ii) the mechanical properties of the nanostructures, which determine whether the nanofeatures can sustain the interaction force with bacteria without excessive deformation and, ultimately, failure. For such applications, it is important to understand the nanomechanical behavior of EBID-made structures. Moreover, the accurate determination of the mechanical properties of single

nanopillars could allow one to estimate the interaction forces between the bacteria and nanopillars, enabling a better understanding of the killing mechanism of bacterial cells residing on nanopatterned surfaces.

In our previous studies, we have developed EBID-made nanopatterns with specific dimensions for antibacterial applications [32, 33]. We have found a killing efficiency of 97% against *E. coli*, but a lower killing efficiency (36.5%) against *S. aureus* [33]. Given that the mechanical properties of single nanopillars influence their killing efficiency against bacterial cells [31, 38], the mechanical characterization of the nanopillars is necessary to optimize our surfaces and to further understand the mechanisms involved in the bacteria-nanopatterns interaction.

Currently, however, the mechanical characterization of single EBID nanostructures is challenging and requires complex instrumentation consisting of advanced mechanical testing machines (*e.g.,* AFM or nanoindenters) mounted inside SEM chambers. Some studies [39-42] have investigated the mechanical behavior of EBID-made nanostructures by using this combination of instruments. For instance, Friedli *et al.* [39] have applied bending tests using an AFM tip installed inside an SEM machine to determine the force constant and the resonance frequency of high aspect ratio vertical nanopillars grown by EBID from the organometallic precursor $Cu(C_5HF_6O_2)_2 \cdot xH_2O$. They have demonstrated that the elastic modulus of the EBID deposited pillars is proportional to the acceleration voltage and the electron dosage used during the deposition. In another study, Lewis *et al.* [41] measured the elastic modulus of EBID-deposited 3D nanostructures (precursor: $(CH_3C_5H_4)Pt(CH_3)_3$) by compression and bending tests using a nanoindentation system installed in an SEM chamber. The compression tests resulted in values in the range of 8.6-10.5 GPa for the elastic modulus of nanopillars. Their bending tests with the same setup resulted in a value of 15.2 GPa for the elastic modulus. Although these methods enable the user to measure the mechanical properties of EBID-deposited nanostructure with arbitrary shapes, they do not apply to conventional SEM machines, as a specific setup needs to be installed. Arnold *et al.* [43] have measured the deflection of EBID deposited Pt-C nanopillars using a four-axis micromanipulator installed inside an SEM machine. The elastic modulus of the EBID nanopillars was then calculated by using nanopillars' deflection as an input for finite element simulation. Their study was followed by an analysis of the effects of beam current and

acceleration voltage on the elastic modulus of nanopillars. They concluded that at 30 kV and 5 kV as the voltage and the lowest beam current, nanopillars had the highest elastic modulus (*i.e.,* 13 GPa).

The fracture stress of nanopillars deposited by EBID has, however, not been previously measured. Utke *et al.*[42] measured the fracture stress on large volume structures deposited using $Co_2(CO)_8$ and $Au(tfac)Me_2$ as precursors. Reiser *et al.*[44] measured the stress at 7% strain of micro and nanopillars using nanoindentation and micro-compression, but not the fracture stress.

Here, we propose an approach for measuring the elastic modulus and fracture stress of EBID nanopillars without any need for any instrumentation beyond typical AFM. The elastic modulus was measured by quantitative imaging (QI) mode on individual pillars of different dimensions (height and diameter). The pillars were deposited using the same precursor, acceleration voltage, and beam current. The effects of the structure size and EBID deposition time on the elastic modulus of the material were investigated. We found a limited influence of the structure size and we concluded that the elastic modulus of EBID nanostructures can be measured by conventional AFM methods applied on larger structures deposited with the same deposition parameters. In addition, we estimated the maximum (fracture) stress of the nanopillars using contact mode (CM) AFM [45]. The force-displacement curves of the nanopillars were obtained with a finite element (FEM) model in which the measured value of the elastic modulus was assigned to the nanopillars material. With these characteristics and the displacement of the nanopillars available from the SEM image of nanopillars interacting with cultured bacteria, the interaction force between bacteria and individual nanopillars was calculated. We then compared the maximum stress of the nanopillars subjected to these forces with the maximum (fracture) stress of the nanopillars measured by AFM to evaluate their breaking strength and to elaborate on the possible approaches that could be used to optimize the design of nanopatterns and to improve their bactericidal behavior.

4.2. Materials and methods

4.2.1. Sample preparation

- *For bacterial culture:* Double-sided polished 4-inch (diameter: 10.16 cm) Si wafers (thickness 525 ± 25 μm, p-type) were diced into 1×1 cm² specimens (Disco Hi-Tec Europe GMbH, Munich, Germany) and were cleaned with nitric acid.

- *For mechanical experiments:* An array of 13×13 circular holes with a diameter of 10 μm were lithographically defined on the surface of a Si specimen (with the same properties as mentioned in the previous paragraph), so as to obtain a visible structure that could be easily detected by SEM and the optical camera of the AFM microscope. Towards that end, the Si substrate was spin-coated with a photoresist (AZ5214, MicroChem Corp, Westborough, USA) at 4000 rpm, followed by a baking step for 1 min at 110 °C. Then, the pattern was exposed through optical lithography (EVG620 mask aligner, NY, USA) and developed using MF321 (Rohm Haas Electronic Materials, UK). The previous steps were followed by inductive coupled plasma reactive ion etching (ICP RIE) (Adixen, AMS100 Bosch, l-speeder; parameters: SF_6 = 200 sccm, O_2 = 175 sccm, ICP power = 2000 W, LP power 50 W, temperature = 0 °C) for 10 s to create the intended nanofeatures of black Si, outside of the circular areas (Figure 1a). The black Si nanofeatures were also used to set the focus and stigmation during the EBID process. The EBID nanostructures were then deposited inside the circles.
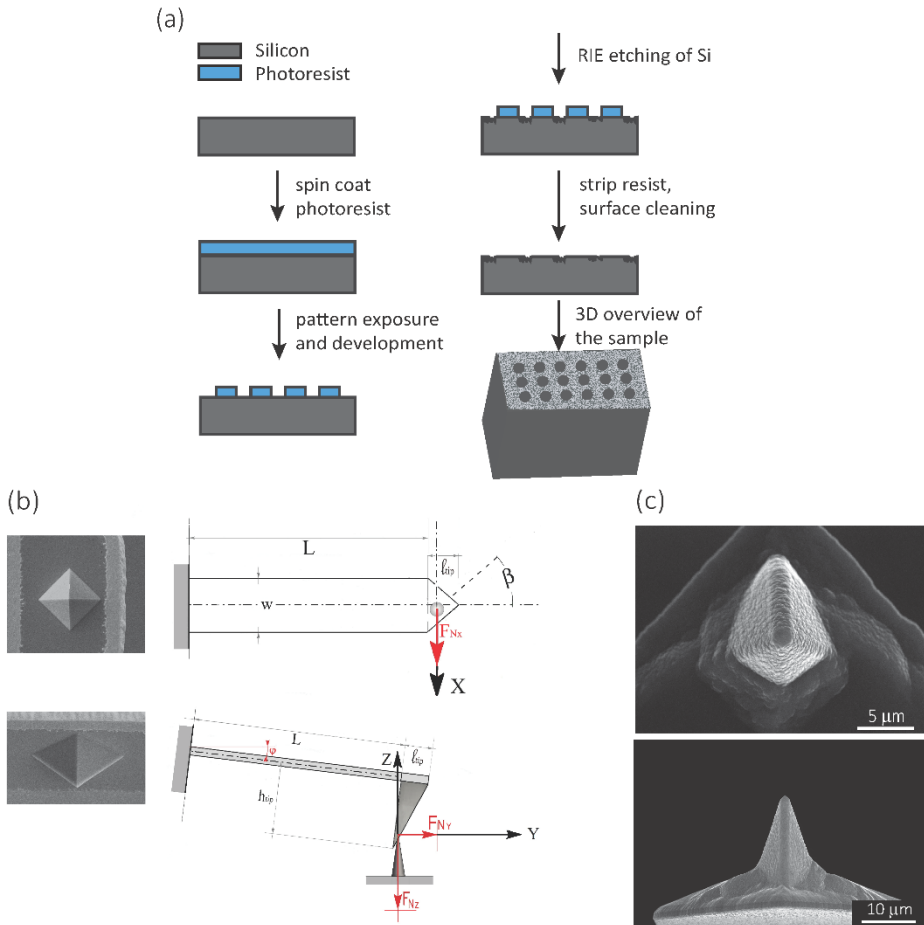
Figure 1. (a) A schematic representation of the process to create black Si on the surface of Si substrate, (b) Left: SEM images showing the top (top) and cross-sectional front (bottom) views of the AFM tip used for the measurement of the fracture force and the maximum displacement of nanopillars. Right: a schematic drawing of the top (top) and cross-sectional side (bottom) views of the AFM probe during the contact with the nanopillars. (c) SEM images showing the top (top) and cross-sectional front (bottom) views of the AFM tip used to measure the elastic modulus.

4.2.2. (Nano)pillar fabrication using EBID

A dual-beam system (Nova Nano Lab 650 Dual Beam, FEI, Oregon, USA) combining SEM with EBID was used to fabricate the (nano)pillars. Trimethyl(methylcyclopentadienyl)-platinum (IV) was used as the precursor gas. The equipment was operated using an acceleration voltage of 17.8 kV and a beam current of 0.60 nA at a working distance of 5 mm.

- For bacterial culture: Under the abovementioned conditions, three areas of 20×20 μm² were covered by the nanopillars. The writing strategy was single dot exposure (*i.e.*, writing the nanopillars one by one), using the stream files generated by a MATLAB (MathWorks, US) code. A stream file was designed to create the nanopillars with a square arrangement with the approximate dimensions of 180 nm (height), 70 nm (base diameter), and 170 nm (center-to-center spacing).

- For fracture force measurements: 11 rows of nanopillars with 20 nanopillars in each row were deposited by using the same conditions as the nanopillars deposited for the bacterial culture. The expected height and diameter were 180 nm and 70 nm, respectively. The interspacing was increased to 340 nm to prevent the neighboring nanopillars from affecting each other during the measurements.

- For elastic modulus measurements: Using the graphical user interface (GUI) accompanying the dual-beam system, a point pitch of 5.43 nm, a pixel dwell time of 10 μs, and different number of passes, we fabricated five pillars with different diameters (*i.e.,* 300, 500, 700, 1000, and 1300 nm), while Z (the parameter of height in the GUI) was set to 20 μm, as well as four pillars with different heights (corresponding to Z = 5, 10, 15, and 20 μm) with a diameter of 1000 nm. The electron dosages applied to create the pillars with different heights were 100, 200, 300, 400, and 500 nC/μm², respectively. In the case of the pillars with different diameters, the electron dosage was kept constant at 400 nC/μm².

4.2.3. Bacterial growth conditions

A Gram-positive bacterial strain (*i.e.*, *S. aureus* strain RN0450, BEI Resources, Virginia, USA) was used to investigate the bactericidal activity of the nanopatterned surfaces. *S. aureus* was grown on brain heart infusion (BHI) (Sigma-Aldrich, Missouri, USA) agar plate at 37 °C. The pre-cultures of the bacteria were prepared by inoculating 10 ml autoclaved BHI broth (Sigma-Aldrich, Missouri, USA) with a single colony and cultivation at 140 rpm (kept at 37 °C). The bacterial cells were collected at their logarithmic stage of growth and their optical density at a wavelength of 600 nm (OD_{600}) in the medium solution was adjusted to 0.1.

The nanopatterned specimens were immersed in 70% ethanol and exposed to UV light for 20 min prior to the addition of the bacterial culture. A sample containing three nanopatterned areas was inoculated with 1 ml of bacterial suspension in a 24-well plate (Cell

Star, Germany). The sample was then incubated at 37 °C for 18 h. Subsequently, the adhered bacteria were fixated for SEM imaging using a fixation solution containing 4% formaldehyde (Sigma-Aldrich, Missouri, USA) and 1% glutaraldehyde (Sigma-Aldrich, Missouri, USA) in 10 mM phosphate buffer. The samples were then washed with MilliQ water and 50%, 70%, and 96% ethanol, respectively, and eventually, soaked in hexamethyldisilazane (HMDS) (Sigma-Aldrich, Missouri, USA) for 30 min and air-dried.

4.2.4. Morphological characterization of the nanopillars

The resulting nanopatterns were characterized by SEM at different magnifications using a Nova Nano Lab 650 Dual Beam system (FEI, Oregon, USA). The heights and base diameters were measured using 52°-tilt SEM images. The center-to-center spacing of the nanopillars was measured using top-view images.

4.2.5. Quantification of the elastic modulus using AFM

The elastic modulus of the pillars was determined through the AFM experiments performed in the quantitative imaging (QI) mode and using an NM-TC probe (Bruker, Billerica, USA) with a cantilever length of 125 μm, a cantilever width of 30 μm, a spring constant of 350 N/m, a resonant frequency of 750 kHz, a tip half angle of 45°, and a tip radius of 25 nm (all nominal values) (Figure 1c). The QI images of the pillars (128×128 pixels) were acquired. In the QI mode, a force-distance curve was measured and recorded for each point of the scanned area. The Hertz's contact theory [46, 47] was used to calculate, from those curves, the elastic modulus corresponding to each scanned point and to obtain a quantitative map of the elastic modulus.

The deflection sensitivity of the cantilever was calibrated with the contact method, *i.e.,* by acquiring a deflection *vs.* displacement curve on a sapphire surface, resulting in a value of 21.33 nm/V. Since the accurate estimation of the spring constant of stiff probes cannot be obtained using the direct calibration technique [48], we assumed the spring constant of the probe to equal the nominal value and applied the relative method of calibration to estimate the corresponding tip radius [49, 50]. A fused-silica reference specimen with a nominal elastic modulus of 72 GPa (test samples kit, Bruker, Billerica, USA), which is relatively close to the elastic modulus of the material of interest, was chosen as the reference material. The tip radius was then adjusted to make the measured elastic modulus of the reference sample equal to the

nominal value at an indentation depth of 5 nm. The Poisson's ratio was set to 0.15 (as its nominal value). Under the mentioned condition, a tip radius of 90 nm was found to result in an elastic modulus of 71.13 GPa for the fused silica specimen. The experiment was then conducted on the Si substrate containing the EBID deposited pillars. A constant maximum force of 10 μN was applied to each sample to achieve an indentation of at least 5 nm. A data processing program (JPK SPM, JPK instruments, v6.1, Berlin, Germany) was then used to calculate the elastic modulus of the EBID-deposited material at each point of the scanned area and the same indentation depth of 5 nm as [51, 52]:

$$F_{app} = \frac{4}{3} E^* \sqrt{R} \, \delta^{3/2} \tag{1}$$

where F_{app} is the applied force, E^* is the reduced elastic modulus, R is the tip radius (calibrated on the reference specimen), and δ is the indentation depth (= 5 nm). The elastic modulus of the pillars can be calculated by:

$$\frac{1}{E^*} = \frac{1 - v_s^2}{E_s} + \frac{1 - v_{tip}^2}{E_{tip}} \tag{2}$$

where v_s and E_s are the Poisson's ratio and the elastic modulus of the pillar, respectively. v_{tip} is the Poisson's ratio of the tip and E_{tip} is the elastic modulus of the tip. The second term of the equation is considered negligible (*i.e.*, $E_{tip} \gg E_s$). v_s is considered to be 0.3, which is the average of the Poisson's ratios reported for its main components (*i.e.,* amorphous carbon and platinum) ($v_{platinum} = 0.39$ [53] ~ 0.396 [54], $v_{carbon} = 0.12$ ~ 0.25 [55]).

To prevent the substrate from affecting the final results, the indentation depth should be less than 10% of the pillar height [56, 57]. In all of our experiments, the indentation depth was 5 nm, which is < 7% of the minimum height of the pillars.

The average and standard deviation of the results for each pillar were calculated by extracting and fitting a Gaussian curve to the histogram of the elastic modulus values in the selected areas corresponding to the top of the pillars. The homogeneity of the elastic properties of the pillars with different diameters and heights were evaluated by comparing the mean elastic modulus calculated for areas with different sizes (with increasing distances from the center).

4.2.6. Quantification of fracture stress using contact mode AFM

The fracture force of the nanopillars was measured using an AFM (JPK Nanowizard 4, Berlin, Germany) operated in the contact mode and using an SSRM-DIA probe (Bruker, USA) (Figure 1b left) with a cantilever length of 225 μm, a cantilever width of 50 μm, a cantilever thickness of 5 μm, and a spring constant of 27 N/m, as the nominal values. The line scan rate used was 2 Hz. The tilt angle of the cantilever holder (φ in Figure 1b, bottom right) was 10°. The calibration of the probe was performed by using the thermal noise method [58], resulting in a spring constant ($k_{c,z}$) of 26.01 N/m and a sensitivity (S_z) of 58.3 nm/V.

The experiments were performed on 10 different nanopillars. The analyzed nanopillars were scanned several times in contact mode, with increasing values of the applied force, obtained by increasing the setpoint force (from 10 nN to 50 nN), until the visible rupture of the nanopillar was observed. After each contact mode scan, the topography of the same area was acquired in the QI mode, with a low setpoint force (10 nN), so as to evaluate any possible changes in the morphology of the nanopillars due to the previously applied force.

The lateral force applied to the nanopillars was calculated as reported elsewhere [45]. The applied methodology is briefly described below.

Calculation of the fracture force

The fast and slow scan directions were chosen along the x and y axes, respectively. As a result, the contact between the probe and the nanopillar occurs on one of the lateral faces on the front of the pyramidal AFM tip (Figure 1b, right). In this configuration, the force F_N applied to the nanopillar is directed along the normal to the plane of that face.

When interacting with the nanopillar, the AFM cantilever can be described as a beam subjected to the combined action of a point load and a bending moment at its free end. Using the beam theory and applying the relevant geometry considerations, F_N can be calculated [45]:

$$F_N = \frac{k_{c,z}d_z}{\sin\gamma - \frac{3}{2}\frac{(h_{tip}+\frac{t}{2})}{L}\sin\beta\cos\gamma} = \frac{F_{Setpoint}+F_{defl_{err}}}{\sin\gamma - \frac{3}{2}\frac{(h_{tip}+\frac{t}{2})}{L}\sin\beta\cos\gamma} \tag{3}$$

where $k_{c,z}d_z = F_{Setpoint} + F_{defl_{err}}$ is the measured vertical signal, $F_{setpoint}$ is the user-defined set point force, and F_{defl_err} is the additional force due to the deflection of the cantilever, which can be retrieved from the deflection error image. β is the half front angle of the base of the

pyramidal probe (Figure 1b, top right), which, considering the cantilever tilted of an angle φ, was calculated as:

$$\beta = \arctan \frac{w/2}{l_{tip} \cos \varphi}$$

(4)

γ, which is the inclination angle of the sidewall of the pyramidal tip, was calculated as:

$$\gamma = \arctan \left(\frac{l_{tip} \sin \beta}{h_{tip}} \right)$$

(5)

where the height of the AFM tip (h_{tip}), the length (l_{tip}), and the width ($w/2$) of the face of the AFM tip were measured through SEM imaging of the probe and were found to be 5.47 µm, 5 µm, and 5 µm, respectively (Figure 1b).

The magnitude of the lateral component of the force applied to the pillar can, therefore, be calculated as:

$$F_{lat} = F_N$$

(6)

4.2.7. FEM model

A nonlinear finite element solver (Abaqus, 6.14) was used to numerically simulate a 3D nanopillar with the same dimensions as those used in our bacterial cell culture experiments (*i.e.,* a base diameter of 70 nm, a height of 180 nm, and a tip diameter of 8 nm) (Figure 2a). A linear elastic material model and quadratic solid elements (C3D20) were used for all of the simulations. The elastic modulus of the material varied between 1 and 40 GPa. The Poisson's ratio was assumed to equal 0.3. To apply the displacement-controlled boundary conditions, a reference point was defined at the tip of the nanopillar, which was kinematically coupled with the corresponding nodes of the top surface of the nanopillar. The top surface of the nanopillar was free to rotate or move in all other directions (Figure 2a). The bottom surface of the nanopillar was clamped. The reaction force was calculated at the reference point. A mesh convergence study was performed by changing the minimum size of the elements from 30 nm to 2 nm. The calculated values of the maximum force varied < 5% for the finest mesh. We, therefore, selected the finest element size (*i.e.,* 2 nm) for all of our subsequent simulations.

The deflections of the nanopillars when in contact with bacteria were measured using SEM images and were used to back-calculate the interaction forces between the nanopillars

and the bacteria. In addition, the numerical simulations were used to calculate the failure lateral force of the nanopillars as the force needed to be applied to the apex of the pillar to obtain the value of the failure stress measured by the contact mode AFM method.
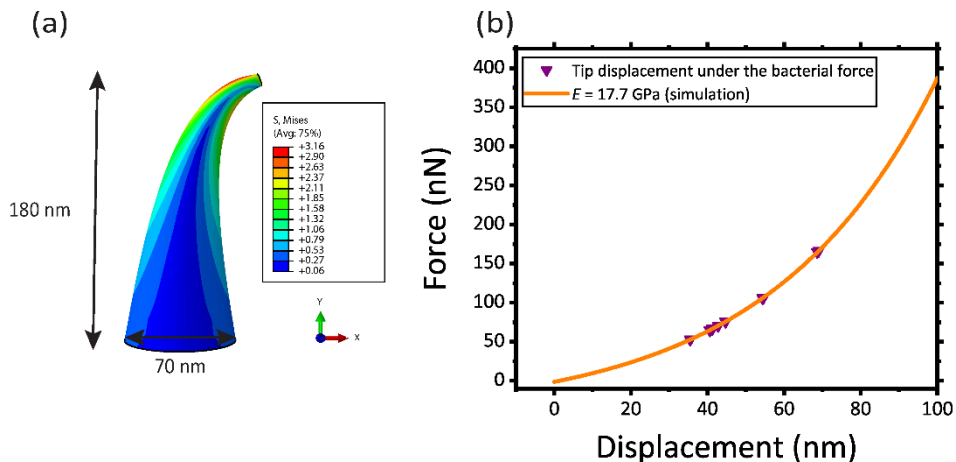
Figure 2. (a) A nanopillar was modeled in Abaqus to simulate the stresses experienced by the nanopillars due to the bacterial force. (b) The orange graph represents the force-displacement curve obtained through FEM (for the nanopillar with E = 17.7 GPa). The displacement of the tip of the nanopillars under bacterial force was fitted in the graph (purple triangles).

4.3. Results

4.3.1. Bacterial cell culture

In the case of the specimens prepared for bacterial cell culture, the EBID nanopillars covered a surface of 20×20 μm^2 (Figure 3a). The actual dimensions of the nanopillars were as follows: height =180 ± 9 nm (mean ± SD), interspacing = 170 ± 3 nm, base diameter = 70 ± 5 nm (Figure 3b). Upon contact with the cultured bacteria, a number of nanopillars underneath the bacterial cells were bent with an average lateral displacement of 50.3 ± 9.0 nm (Figure 3c-f).
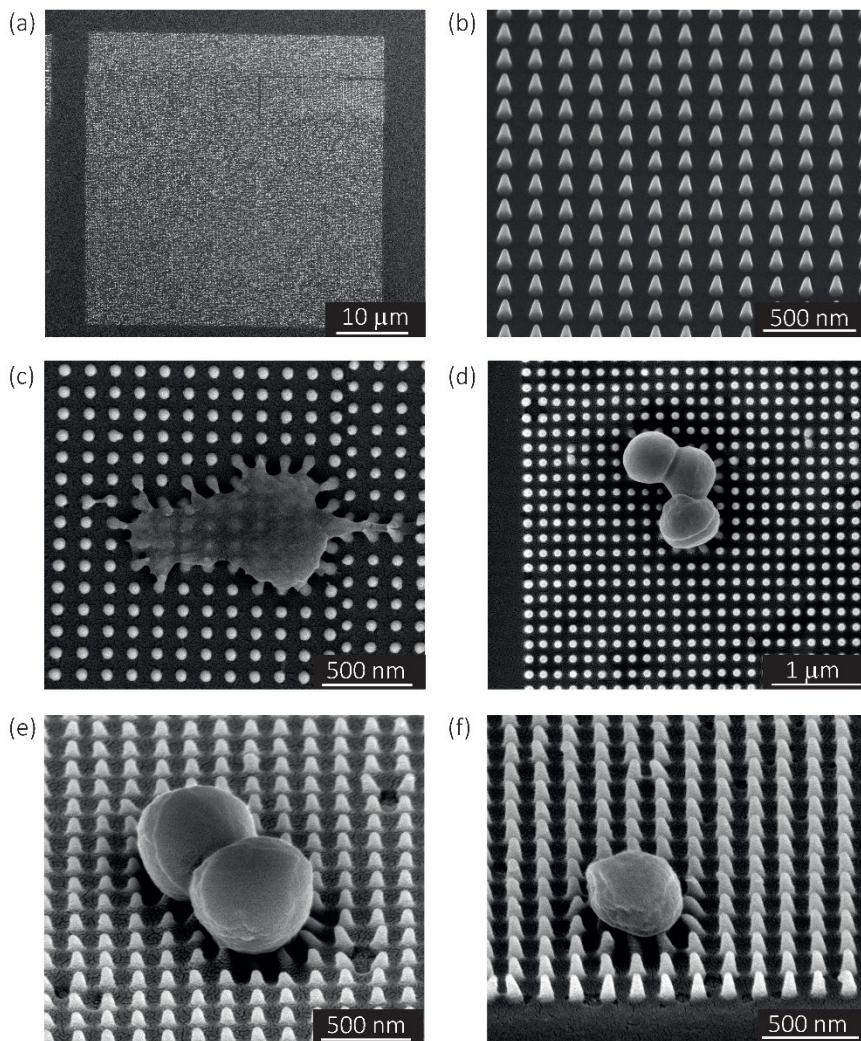
Figure 3. The SEM images of the nanopillars (with an average height of 180 nm, an average diameter of 70 nm, and average interspacing of 170 nm) produced by EBID at different magnifications: (a) top view and (b) 52°-tilted view. The SEM images of *S. aureus* bacteria on the nanopatterned surface: (c, d) the top and (e, f) 52°-tilted views.

4.3.2. Elastic modulus of the pillars

Five pillars with different base diameters (d = 1500 nm, 1180 nm, 867 nm, 646 nm, and 433 nm) and heights of 383 ± 53 nm (Figure 4a) and four pillars with diameters of 1112 ± 78 nm and different heights (Figure 4b(1): h = 464 nm, Figure 4b(2): h = 309 nm, Figure 4c(3):

h = 192 nm, Figure 4c(4) h = 82 nm) (the left subfigures show the top view while the right subfigures were taken at a 52°-tilted view) were fabricated to obtain an almost flat region large enough to perform force spectroscopy mapping measurements (in th QI mode).
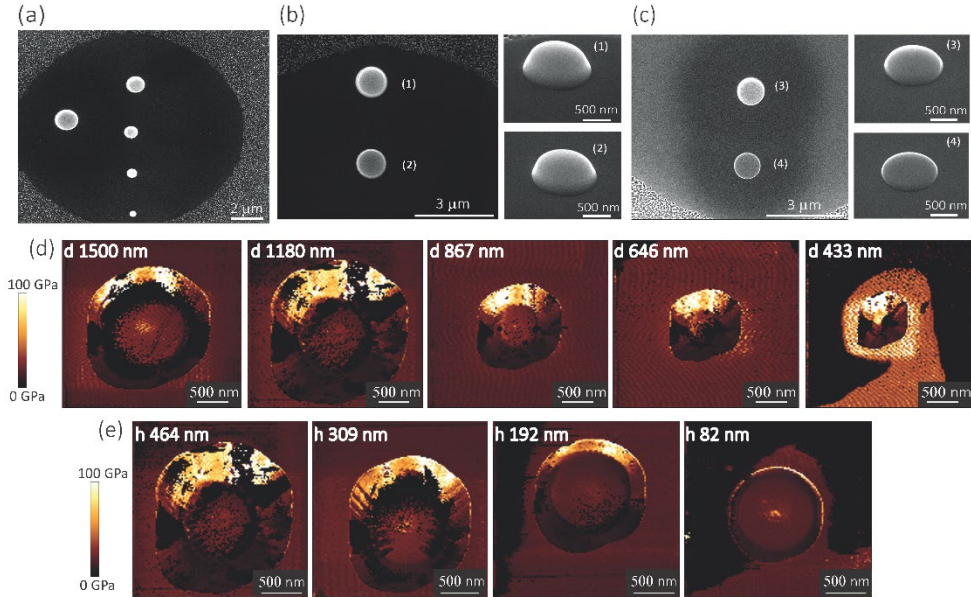
Figure 4. The SEM image of pillars with (a) different diameters: 433, 646, 867, 1180, and 1500 nm, (b, c) different heights: 1- 464 nm, 2- 309 nm, 3- 192 nm, 4- 82 nm. (The left figures were taken from the top view while the right figures were taken from 52°-tilted view). (d) The map of the elastic modulus of the pillars with different diameters obtained by AFM. (e) The map of the elastic modulus of the pillars with different heights obtained by AFM.

Above a certain distance from the pillar center, we observed a significant decrease (see the dark region at the bottom, left, and right sidewalls of the pillars) (Figure 4d, e) or increase (bright part corresponding to the upper sidewall of the pillars) (Figure 4d, e) in the measured values of the elastic modulus. This effect (underestimation/overestimation of the elastic modulus) can be explained by the fact that, when the tip-pillar contact occurred on the sidewalls of the pillar, it was asymmetric, causing the overestimation or underestimation of the contact area depending on the tilt angle of the cantilever and the position of the tip with respect to the pillar. Due to the pointy tip of one of the pillars (diameter = 433 nm), establishing symmetric contact between the AFM tip and the surface of the pillar was not feasible. Therefore, for this specific height (*i.e.,* 383 nm), 646 nm was the minimum diameter

for which the elastic modulus could be measured. The elastic modulus measured for the pillars with different heights and diameters varied between 15.9 GPa and 27.7 GPa (Figure 5a, b).
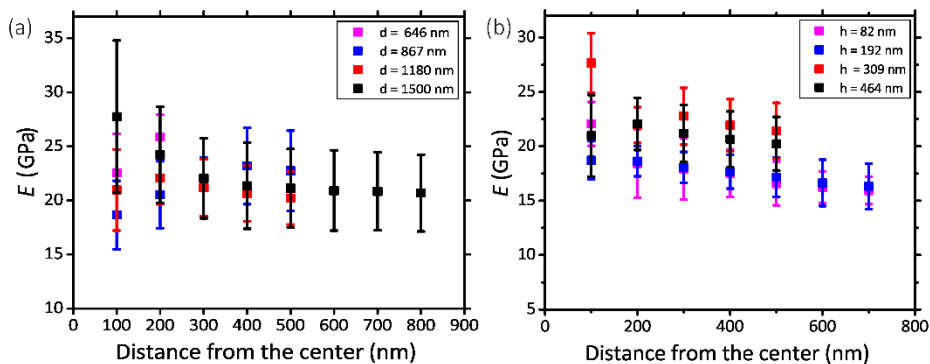
Figure 5. (a) The distribution of the elastic modulus for the pillars with different diameters in different distances from the center. (b) The distribution of the elastic modulus for the pillars with different heights (with the same diameter of 1000 nm) at different distances from the center. The pillars were deposited with an acceleration voltage of 17.8 kV and a current of 0.6 nA.

Within the distance from the center for which the tip had symmetric contact with the surface of pillars, we did not observe a significant difference between the values of elastic modulus measured for different experimental groups (*i.e.*, with different sizes) (Figure 5a, b). The different parts of the surface exhibited similar values of the elastic modulus. A 200 nm distance from the center was the minimum distance that yielded a Gaussian distribution. We, therefore, did not consider smaller areas. The elastic modulus of the pillars with different diameters overlapped (Figure 5a). The pillars with larger heights (*i.e.*, 464 nm and 309 nm) exhibited slightly (but not significantly) higher values of the elastic modulus as compared to those with the lower heights (*i.e.*, 192 nm and 82 nm) (Figure 5b). In summary, no statistically significant changes in the value of the elastic modulus were observed for different values of the diameter of the deposited structures and different distances from the center. Only a slight difference (0.16%) with the height of the structure was observed. Therefore, the elastic modulus of our nanopillars can be assumed to be the same as the elastic modulus of the structure with a similar height (*i.e.*, 192 nm). The elastic modulus measured for this structure was 17.7 ± 1.5 GPa.

4.3.3. Fracture stress

In the case of the specimens prepared for the measurement of the lateral detachment force, the nanopillars had the following dimensions: height = 196.5 ± 5.16 nm (measured by AFM), interspacing = 340 ± 1 nm in the x-direction and 1000 ± 100 nm in the y-direction, and base diameter = 68 ± 3 nm (Figure 6a, b). A few representative images of the experiments performed to measure the fracture stress are presented in Figures 6c-k. When low forces (*e.g.*, $F_{setpoint}$ = 10 nN in the example reported in Figure 6c-e) were applied, the fracture of the nanopillars was not visible in the CM images (Figure 6c, d). A little (a few nm) change in the height of the nanopillars was observed in the QI mode images aquired with very low setpoint force before and after the application (Figure 6e). This indicates that the failure of the nanopillars occurred at a height, which was very close to their apex. This is consistent with the mechanical behavior of a high aspect ratio conical structure. Indeed, when a lateral force is applied to the apex of a "sharp" conical pillar, the height of the point experiencing the maximum stress is closer to the apex of the pillar when the tip is smaller [45]. Since the decrease of the height was low and difficult to measure with enough accuracy, larger forces were applied to the nanopillars by increasing the values of the applied setpoint forces. This procedure was repeated until the pillars were clearly observed to break and the characteristics of their residues could be easily measured. In the presented example, a setpoint force (F_{lat}) of 30 nN resulted in obvious fracture of two of the three nanopillars (Figure 6f-h), for which a residue of about 26 nm was observed. Increasing the setpoint force not only increased the magnitude of the lateral force but also decreased the height at which the force was applied [45]. For some of the nanopillars (*e.g.*, the nanopillar in the center of the images in the reported example), no visible fracture was observed in the contact mode topographies with a setpoint of 30 nN (Figure 6g), but only a further decrease of the height was visible in the QI mode topography images acquired after the application of the force in the CM (Figure 6h). For those nanopillars, the setpoint force was further increased (50 nN in the reported example) (Figure 6i-k).

The values of the setpoint forces at which the fracture of the nanopillars was visible in the CM topographies were used for the calculation of the lateral force. The height of the residues obtained by applying those values of forces was used to calculate the height at which the lateral force was applied and to estimate the maximum stress.
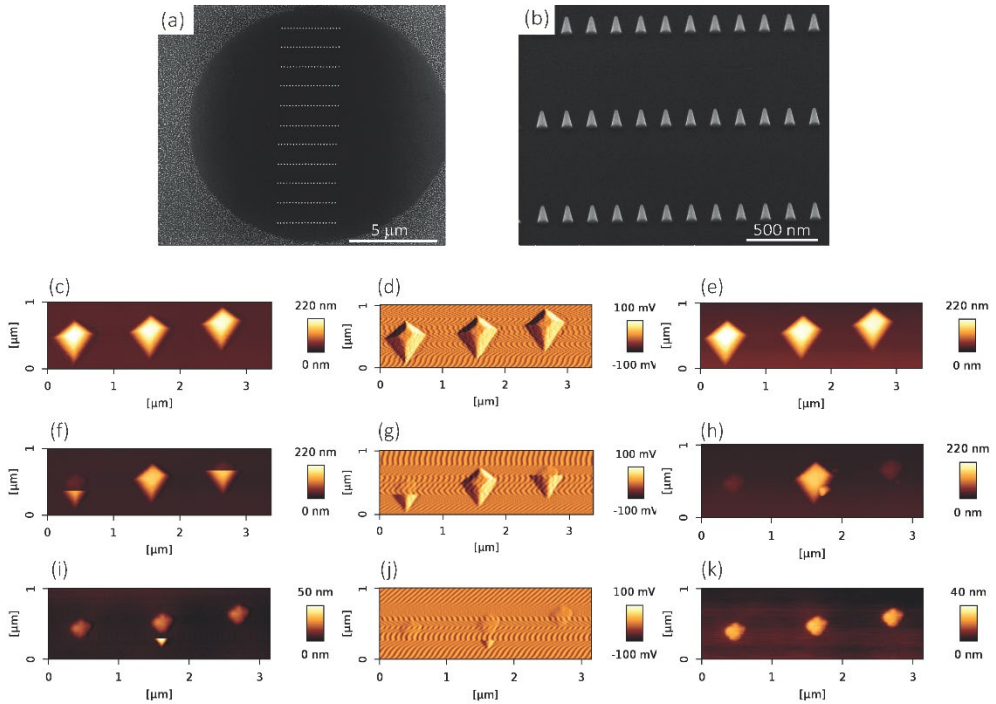
Figure 6. The SEM images of the rows of the nanopillars deposited by EBID to perform the mechanical experiments: (a) the top and (b) 52°-tilted views. (c, f, i) Contact mode topography images acquired with increasing values of setpoint forces (10 nN, 30 nN, and 50 nN, respectively); (d, g, j) vertical deflection error images acquired with increasing values of setpoint forces (10 nN, 30 nN, and 50 nN, respectively) ; (e, h, k) QI mode topography images acquired with a low, non-destructive, setpoint force (10 nN) after each contact mode scan with increasing values of the setpoint force (10 nN, 30 nN, and 50 nN, respectively).

The value of the lateral force applied to the nanopillars corresponding to the applied setpoint force was calculated using Equation (3) This lateral force is not applied to the apex of the nanopillars but at a certain lower height, due to the possible previous failure of the tip of the pillars and the eventual resting of the AFM tip against the sidewall of the pillars [45]. The height of the application of the force (h_{F_lat}) was determined as the height at which the lateral force has to be applied on a conical pillar (with the geometry characteristics of the studied pillars) to yield the maximum stress at a height corresponding to the height of the pillar residues [45]. Indeed, as previously pointed out [45], the maximum bending stress in the most loaded section can be written as:

$$\sigma_{max}(z) = \frac{MR_{res}}{I} = 4\frac{F_{lat}z}{\pi R_{res}^3} \tag{7}$$

where $M = F_{lat} z$ is the bending moment, z is the distance between the point of the application of the force and the height of the most stressed section (*i.e.*, the height of the residue h_{res}), and $I = \frac{\pi R_{res}^4}{4}$ is the area moment of inertia for a circular section. R_{res} is the radius of the section of the cone corresponding to the height of the residue, which is given as:

$$R_{res} = R_{apex} + (h_{pillar} - h_{F_{lat}} + z)\tan\alpha \tag{8}$$

where R_{apex} is the radius of the apex of the pillar, which was assumed to be 4 nm, and α is the half cone angle of the pillar.

By calculating the derivative of the $\sigma_{max}(z)$ and solving the following equation:

$$\frac{d\sigma_{max}(z)}{dz} = 0 \tag{9}$$

we obtain the equation for the distance z between the point of application of the force and the most stressed section $z_{\sigma max} = h_{F_{lat}} - h_{res}$

$$z_{\sigma max} = h_{F_{lat}} - h_{res} = \frac{R_{apex} + (h_{pillar} - h_{F_{lat}})\tan\alpha}{2\tan\alpha} \tag{10}$$

Therefore, the height of the application of the force can be determined as:

$$h_{F_{lat}} = \frac{R_{apex} + (h_{pillar} + 2h_{res})\tan\alpha}{3\tan\alpha} \tag{11}$$

We found, for eight studied nanopillars, an average value of the lateral force of 654.4 ± 69.3 nN and an average height of the residues of 26.2 ± 2.5 nm, which resulted in an average height of the application of the force of 92.8 ± 1.7 nN (from the base of the pillar). The fracture stress was then calculated by using Equation 7, which resulted in an average value of 3.0 ± 0.3 GPa.

4.3.4. FEM simulations

The mean elastic modulus determined using the AFM measurements (*i.e.*, E = 17.7 ± 1.5 GPa) was considered as the elastic modulus of the nanopillars in our FEM simulation (Figure 2a) and the force *vs.* displacement curve reported in Figure 2b was obtained. The interaction force between bacteria and the individual nanopillars was calculated from this force *vs.* displacement curve (purple triangles in Figure 2b), as the value of the force corresponding to the displacement measured by SEM imaging for the pillars interacting with

the bacteria. The mean and standard deviation of the interaction force between the bacteria and individual nanopillars was found to be 88.7 ± 36.1 nN for E = 17.7 GPa (Table 1).

Table 1. The calculated interaction force between *S. aureus* and the nanopillars.

Tip displacement (nm)	Calculated interaction force (nN) (E = 17.7 GPa)
42.8	70.4
54.6	106.6
54.4	106.1
68.7	164.8
41.1	66.2
44.7	75.7
40.6	64.9
36.5	55.1

In Figure 2a, the von Mises stress distribution of a pillar undergoing a displacement of 50.3 nm (*i.e.,* the average displacement value due to the interaction with bacteria) is shown. As expected, the maximum stress is located at the border, in a section close to the apex of the pillar, where the force is applied. This indicates that possible fractures of the conical pillars, subjected to the interaction force with the bacteria could occur at the tip of the pillars.

The von Mises stresses and the maximum principal stress were equal to 3.16 ± 0.27 GPa and 3.19 ± 0.42 Gpa, respectively, which is almost equivalent to the maximum (failure) stress found by AFM measurements (3.0 ± 0.3 GPa). This indicates that, although no visible fracture was observed by SEM imaging, the nanopillars, under the action of the bacteria, are highly deformed and are very close to their failure point.

4.4. Discussion

The main goal of this study was to quantify the relevant mechanical properties of EBID nanopillars (elastic modulus, fracture force, maximum displacement, and failure stress) and

the interaction forces between the nanostructures and the bacterial cells by the combined use of AFM and FEM simulations. The findings of this study could help us optimize the geometry and the mechanical properties of the nanopillars to improve their killing efficiency. Indeed, the results of our previous bacterial culture experiments clearly showed that metal-based EBID-deposited nanostructures have the potential to decorate the surface of biomaterials to damage/kill bacterial cells [32, 33]. However, while a killing efficiency of the nanopatterns of about 97% was observed against *E. coli* cells, the killing efficiency was significantly less for *S. aureus*. In this work, we performed an SEM analysis of the pillars underneath the *S. aureus* cells that revealed a very high deformation of the tip of the pillars due to the interaction with the bacterial cells. The average lateral displacement was 50.3 ± 9.0 nm.

As the killing efficiency is mainly attributed to the capability of the nanopillars to penetrate and damage the cell wall [33, 36, 37], the non-optimal mechanical properties of the pillars, which result in their excessive deformation could be a possible reason for the low killing efficiency of the pattern against *S. aureus*. A more in-depth investigation of the mechanical properties of our EBID nanopillars is necessary, to elucidate the possible ways through which our surfaces could be optimized and their killing efficiency can be improved.

We studied, for the first time, the effects of the size on the elastic modulus of EBID structures fabricated using the same deposition parameters (precursor, acceleration voltage, and beam current) and determined the elastic modulus of the nanopillars. The applicability of AFM mechanical characterization techniques (such as the QI mode) to the measurement of the elastic modulus of EBID nanostructures was demonstrated. AFM mechanical experiments showed that the elastic modulus of the EBID pillars is size-independent, as pillars with different sizes (diameter and height) deposited using the same parameters showed no significant differences in their elastic modulus. We could, therefore, conclude that the elastic modulus of our nanopillars could be estimated by AFM mechanical mapping measurements (*e.g.,* QI mode) on larger structures fabricated with the same deposition parameters. The very slight (non-significant) difference found in the elastic modulus of structures with different heights may have been caused by the different electron doses required to deposit pillars with different heights. Therefore, the value of the elastic modulus found for the structure with the closest height to the height of the nanopillars used in the cell experiments (structure with a height of 192 nm) was used in the FEM simulations to

determine the bacteria-pillars interaction force. The average elastic modulus for this pillar was 17.7 ± 1.5 GPa (Figure 5b).

Moreover, the fracture experiments performed on the nanopillars in the AFM contact mode were reported and were shown to represent an effective technique for the evaluation of the fracture strength of nanoscale objects. In our contact mode AFM experiments, we did not observe any failure at the interface between the nanopillars and the substrate, indicating a strong adhesion force of the nanopillars to the substrate. The nanopillars were subjected to a bending load, which was applied laterally by the AFM probe at a certain height. By modulating the setpoint force, we applied lateral forces high enough and at a position low enough to cause the failure of the pillars at a visible and easily measurable height (*i.e.*, 26.2 ± 2.5 nm). From the height of the residue, we could calculate the height of the application of the lateral force and, consequently, estimate the failure stress, which was 3.0 ± 0.3 GPa, in very good agreement with our previous results obtained on similar EBID nanopillars with different dimensions [45].

We used AFM results, in combination with computational models, to calculate the interaction force between the bacterial cells and the nanopillars and to evaluate the stress state of the nanopillars under the action of bacteria. The elastic modulus measured in the AFM experiments was considered in our computational models and the force *vs.* displacement curve of the nanopillars was plotted. The interaction force between the bacterial cell and the bent nanopillars was calculated as the value of the force corresponding to the displacement measured by the SEM imaging of the nanopillars interacting with the bacteria. The schematic drawing in Figure 7 illustrates the steps followed to measure the abovementioned parameters. The estimated value of the interaction force was 89 ± 36 nN. The maximum value of the von Mises stress (3.16 ± 0.27 GPa) occurred, as expected, in a location close to the apex of the nanopillars, and was almost equivalent to the fracture stress measured through the AFM contact mode experiments (3.0 ± 0.3 GPa). This result indicates that, although no visible fractures of the nanopillars were observed, the pillars were close to their breaking point. This means that the killing efficiency could be affected not only by the excessive elastic deformation of the tip of the conical pillars but also by some relevant plastic deformation phenomena. Furthermore, since the maximum stress is located in a section very close to the apex of the pillars (as indicated by Equation 8 and by the stress distribution in FEM in Figure

2a), the fracture events could occur in this region under the action of the bacteria and could be not observed by SEM. Indeed, due to the presence of the bacteria attached to the nanopillars, it was not possible to estimate the height of the nanopillars under the bacteria with nanometric accuracy. The possible fracture of the tip of the pillars, increasing the area of the apex of the pillars could further decrease the killing efficiency of the nanopatterned surfaces.
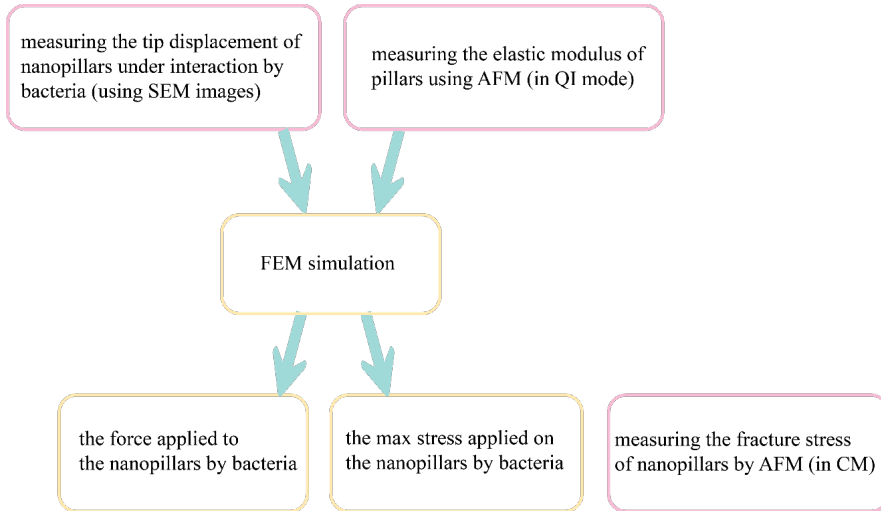
Figure 7. A schematic drawing illustrating the procedure used to evaluate the stress state of our EBID nanopillars and their interaction force with bacteria. Pink blocks indicate the experimentally measured parameters while the yellow blocks indicate the parameters determined by simulation.

From our analysis, we concluded that the killing efficiency of nanopatterned surfaces could be improved by optimizing the mechanical properties of our single pillars. More specifically, by (i) increasing the elastic modulus of the material to reduce the elastic deformation and improve the membrane penetration capability, (ii) increasing the fracture strength (σ_{max}) of the material to reduce eventual plastic deformation and tip fracture phenomena, and (iii) optimizing the geometry of the nanopillars, for example, by increasing the diameter of the cone.

The elastic modulus of the EBID-deposited structures could be increased through several methods including changing the percentage of the main components of the precursor gases: changing the beam current and acceleration voltage [43, 59], applying metal purification techniques (*e.g.,* introducing oxygen flux into the chamber during the deposition

[60, 61]), substrate annealing [62], electron beam curing [43], electron beam irradiation [63], and laser-assisted purification [64]. The abovementioned techniques may lead to higher values of the elastic modulus for the deposited structure. Coating the EBID-deposited structures with other stiff metals using atomic layer deposition (ALD) or evaporation may be another approach to obtain stiffer nanostructures [41] with possibly higher values of the killing efficiency.

The maximum stress could be increased by changing the Pt/C ratio in the EBID-deposited structures. The abovementioned purification techniques could help in increasing the Pt content in the final deposited structures, thereby adjusting the maximum (failure) stress. Changing the beam current and voltage is another way to change the composition of the material and modulate the fracture stress.

The geometry of the cone could be easily changed by varying the deposition factors, such as the overall dose, beam energy, current, and defocus [65]. Increasing the width of the cones could increase the stiffness and reduce the risk of the fracture of the tip of the cones. This could reduce the bending of the nanopillars and improve their killing efficiency, similar to what was observed by Linklater *et al.* [66]. They compared the killing efficiency of carbon nanotubes (CNTs) with the same shape, diameter, and interspace, but with different heights (*i.e.,* 1 μm and 30 μm) against *S. aureus*. They concluded that shorter CNTs have higher bactericidal efficiencies. This observation could be explained by the fact that for the same applied force, shorter CNTs (higher stiffness) experience lower tip deflections, which result in higher forces being exerted to the bacterial cells. Therefore, changing the geometry of the nanostructures, while remaining in the bactericidal and non-cytotoxic range, can be used to increase the interaction forces and, thus, enhance the bactericidal efficiency of nanopatterned surfaces.

Although the elastic modulus of the EBID-deposited nanostructures considered in the current study is suitable for osteoblast cells, enlarging the patterned area to hundreds of micrometers is a crucial step needed before studies with mammalian cells can be performed. One such method to scale up the deposited area is using a multi-beam scanning electron microscopy. This technique could increase the speed of the process by up to several hundred times (*e.g.,* by focusing 196 beams on the substrate) [67].

Conclusions

In summary, a quantitative study on the mechanical behavior of EBID nanopillars interacting with bacterial cells was performed. To achieve our objective, the challenging issue of the mechanical characterization of single pillars at the nanoscale had to be addressed. A new AFM-based approach was used to measure the elastic modulus and the fracture stress of EBID nanopillars. The elastic modulus of the nanopillars was determined by applying AFM force spectroscopy mechanical mapping (QI mode) to larger structures deposited under similar EBID conditions. Limited influence of the size was observed on the elastic modulus measured on the different studied structures and an elastic modulus of 17.7 ±1.5 GPa was found for the nanopillars. AFM experiments performed in the contact mode were conducted to push the EBID nanopillars beyond their fracture point. By measuring the applied lateral fracture force and the height of the residue after failure, we were able to determine the fracture stress of the analyzed nanopillars, namely 3.0 ± 0.3 GPa.

An FEM model was developed to calculate the interaction force between the nanopillars and the cultured *S. aureus* bacteria and to determine the stress state of the nanopillars. The interaction force between the nanopillars and bacteria was calculated as 89 ± 36 nN while the maximum von Mises stress of the nanopillars was 3.16 GPa.

In addition to generating unique quantitative data on the mechanical properties of single EBID nanopillars interacting with *S. aureus*, the current study resulted in new potential strategies for enhancing the bactericidal efficiency of nanopatterned surfaces, which have to do with the geometry and mechanical properties of the nanopillars.

References

[1] K.-S. Lee, R.H. Kim, D.-Y. Yang, S.H. Park, Advances in 3D nano/microfabrication using two-photon initiated polymerization, Progress in Polymer Science 33(6) (2008) 631-681.

[2] V.N. Truskett, M.P. Watts, Trends in imprint lithography for biological applications, Trends Biotechnol 24(7) (2006) 312-7.

[3] K.S. Han, S.H. Hong, K.I. Kim, J.Y. Cho, K.W. Choi, H. Lee, Fabrication of 3D nano-structures using reverse imprint lithography, Nanotechnology 24(4) (2013) 045304.

[4] D.J. Resnick, C. Bencher, M.J. Chopra, R.T. Bonnecaze, Shape change of cured 2D and 3D nanostructures from imprint lithography, Alternative Lithographic Technologies VII, 2015.

[5] C. Steinberg, M. Rumler, M. Runkel, M. Papenheim, S. Wang, A. Mayer, M. Becker, M. Rommel, H.-C. Scheer, Complex 3D structures via double imprint of hybrid structures and sacrificial mould techniques, Microelectronic Engineering 176 (2017) 22-27.

[6] J.H. Jang, C.K. Ullal, M. Maldovan, T. Gorishnyy, S. Kooi, C. Koh, E.L. Thomas, 3D Micro- and Nanostructures via Interference Lithography, Advanced Functional Materials 17(16) (2007) 3027-3041.

[7] B. Farshchian, S.M. Hurst, J. Lee, S. Park, 3D molding of hierarchical micro- and nanostructures, Journal of Micromechanics and Microengineering 21(3) (2011).

[8] A. Schleunitz, H. Schift, Fabrication of 3D nanoimprint stamps with continuous reliefs using dose-modulated electron beam lithography and thermal reflow, Journal of Micromechanics and Microengineering 20(9) (2010).

[9] P. Schnauber, R. Schmidt, A. Kaganskiy, T. Heuser, M. Gschrey, S. Rodt, S. Reitzenstein, Using low-contrast negative-tone PMMA at cryogenic temperatures for 3D electron beam lithography, Nanotechnology 27(19) (2016) 195301.

[10] G. Seniutinas, A. Balčytis, I. Reklaitis, F. Chen, J. Davis, C. David, S. Juodkazis, Tipping solutions: emerging 3D nano-fabrication/ -imaging technologies, Nanophotonics 6(5) (2017) 923-941.

[11] S. Jesse, A.Y. Borisevich, J.D. Fowlkes, A.R. Lupini, P.D. Rack, R.R. Unocic, B.G. Sumpter, S.V. Kalinin, A. Belianinov, O.S. Ovchinnikova, Directing Matter: Toward Atomic-Scale 3D Nanofabrication, ACS Nano 10(6) (2016) 5600-18.

[12] R. Winkler, F.P. Schmidt, U. Haselmann, J.D. Fowlkes, B.B. Lewis, G. Kothleitner, P.D. Rack, H. Plank, Direct-Write 3D Nanoprinting of Plasmonic Structures, ACS Appl Mater Interfaces 9(9) (2017) 8233-8240.

[13] S. Janbaz, N. Noordzij, D.S. Widyaratih, C.W. Hagen, L.E. Fratila-Apachitei, A.A. Zadpoor, Origami lattices with free-form surface ornaments, Science advances 3(11) (2017) eaao1595.

[14] J. Cai, Z. Zhu, P.F.A. Alkemade, E. van Veldhoven, Q. Wang, H. Ge, S.P. Rodrigues, W. Cai, W.-D. Li, 3D Volumetric Energy Deposition of Focused Helium Ion Beam Lithography: Visualization, Modeling, and Applications in Nanofabrication, Advanced Materials Interfaces 5(12) (2018).

[15] S.-H. Ahn, H.-S. Yoon, K.-H. Jang, E.-S. Kim, H.-T. Lee, G.-Y. Lee, C.-S. Kim, S.-W. Cha, Nanoscale 3D printing process using aerodynamically focused nanoparticle (AFN) printing, micro-machining, and focused ion beam (FIB), CIRP Annals 64(1) (2015) 523-526.

[16] B. Salhi, D. Troadec, R. Boukherroub, 3D silicon shapes through bulk nano structuration by focused ion beam implantation and wet etching, Nanotechnology 28(20) (2017) 205301.

[17] H. Plank, R. Winkler, C.H. Schwalb, J. Hutner, J.D. Fowlkes, P.D. Rack, I. Utke, M. Huth, Focused Electron Beam-Based 3D Nanoprinting for Scanning Probe Microscopy: A Review, Micromachines (Basel) 11(1) (2019).

[18] W.F. Van Dorp, B. Van Someren, C.W. Hagen, P. Kruit, P.A. Crozier, Approaching the resolution limit of nanometer-scale electron beam-induced deposition, Nano letters 5(7) (2005) 1303-1307.

[19] N. Silvis-Cividjian, C.W. Hagen, Electron-Beam–Induced Nanometer-Scale Deposition, Advances in Imaging and Electron Physics 143 (2006) 1-235.

[20] S. Randolph, J. Fowlkes, P. Rack, Focused, nanoscale electron-beam-induced deposition and etching, Critical reviews in solid state and materials sciences 31(3) (2006) 55-89.

[21] I. Utke, P. Hoffmann, J. Melngailis, Gas-assisted focused electron beam and ion beam processing and fabrication, Journal of Vacuum Science & Technology B: Microelectronics and Nanometer Structures Processing, Measurement, and Phenomena 26(4) (2008) 1197-1276.

[22] W. Van Dorp, C.W. Hagen, A critical literature review of focused electron beam induced deposition, Journal of Applied Physics 104(8) (2008) 10.

[23] R. Winkler, J.D. Fowlkes, P.D. Rack, H. Plank, 3D nanoprinting via focused electron beams, Journal of Applied Physics 125(21) (2019) 210901.

[24] M. Gabureac, L. Bernau, I. Utke, G. Boero, Granular Co-C nano-Hall sensors by focused-beam-induced deposition, Nanotechnology 21(11) (2010) 115503.

[25] C.H. Schwalb, C. Grimm, M. Baranowski, R. Sachser, F. Porrati, H. Reith, P. Das, J. Muller, F. Volklein, A. Kaya, M. Huth, A tunable strain sensor using nanogranular metals, Sensors (Basel) 10(11) (2010) 9847-56.

[26] W. Klauser, M. Bartenwerfer, P. Elfert, E. Krauskopf, S. Fatikow, Nano-granular Layers for Sensor Applications fabricated by Means of Electron Beam induced Deposition, Micro-Nano-Integration; 6. GMM-Workshop, VDE, 2016, pp. 1-4.

[27] C. Haverkamp, K. Hoflich, S. Jackle, A. Manzoni, S. Christiansen, Plasmonic gold helices for the visible range fabricated by oxygen plasma purification of electron beam induced deposits, Nanotechnology 28(5) (2017) 055303.

[28] S. Sengupta, C. Li, C. Baumier, A. Kasumov, S. Guéron, H. Bouchiat, F. Fortuna, Superconducting nanowires by electron-beam-induced deposition, Applied Physics Letters 106(4) (2015).

[29] J.H. Noh, M.G. Stanford, B.B. Lewis, J.D. Fowlkes, H. Plank, P.D. Rack, Nanoscale electron beam-induced deposition and purification of ruthenium for extreme ultraviolet lithography mask repair, Applied Physics A 117(4) (2014) 1705-1713.

[30] Y. Yang, K. Wang, X. Gu, K.W. Leong, Biophysical Regulation of Cell Behavior-Cross Talk between Substrate Stiffness and Nanotopography, Engineering (Beijing) 3(1) (2017) 36-54.

[31] K. Modaresifar, S. Azizian, M. Ganjian, L.E. Fratila-Apachitei, A.A. Zadpoor, Bactericidal effects of nanopatterns: A systematic review, Acta Biomater (2018).

[32] D.S. Widyaratih, P.L. Hagedoorn, L.G. Otten, M. Ganjian, N. Tumer, I. Apachitei, C.W. Hagen, L.E. Fratila-Apachitei, A.A. Zadpoor, Towards osteogenic and bactericidal nanopatterns?, Nanotechnology 30(20) (2019) 20LT01.

[33] M. Ganjian, K. Modaresifar, M.R. Ligeon, L.B. Kunkels, N. Tümer, L. Angeloni, C.W. Hagen, L.G. Otten, P.-L. Hagedoorn, I. Apachitei, L.E. Fratila-Apachitei, A.A. Zadpoor, Nature Helps: Toward Bioinspired Bactericidal Nanopatterns, Advanced Materials Interfaces (2019) 1900640.

[34] F. Han, C. Zhu, Q. Guo, H. Yang, B. Li, Cellular modulation by the elasticity of biomaterials, Journal of Materials Chemistry B 4(1) (2016) 9-26.

[35] Y. Sun, C.S. Chen, J. Fu, Forcing stem cells to behave: a biophysical perspective of the cellular microenvironment, Annual review of biophysics 41 (2012) 519-542.

[36] P.M. Tsimbouri, L. Fisher, N. Holloway, T. Sjostrom, A.H. Nobbs, R.M. Meek, B. Su, M.J. Dalby, Osteogenic and bactericidal surfaces from hydrothermal titania nanowires on titanium substrates, Sci Rep 6 (2016) 36857.

[37] S. Ghosh, S. Niu, M. Yankova, M. Mecklenburg, S.M. King, J. Ravichandran, R.K. Kalia, A. Nakano, P. Vashishta, P. Setlow, Analysis of killing of growing cells and dormant and germinated spores of Bacillus species by black silicon nanopillars, Sci Rep 7(1) (2017) 17768.

[38] F. Song, M.E. Brasch, H. Wang, J.H. Henderson, K. Sauer, D. Ren, How bacteria respond to material stiffness during attachment: a role of Escherichia coli flagellar motility, ACS applied materials & interfaces 9(27) (2017) 22176-22184.

[39] V. Friedli, I. Utke, K. Molhave, J. Michler, Dose and energy dependence of mechanical properties of focused electron-beam-induced pillar deposits from Cu(C5HF6O2)2, Nanotechnology 20(38) (2009) 385304.

[40] S. Okada, T. Mukawa, R. Kobayashi, M. Ishida, Y. Ochiai, T. Kaito, S. Matsui, J.-i. Fujita, Comparison of Young's Modulus Dependency on Beam Accelerating Voltage between Electron-Beam- and Focused Ion-Beam-Induced Chemical Vapor Deposition Pillars, Japanese Journal of Applied Physics 45(6B) (2006) 5556-5559.

[41] B.B. Lewis, B.A. Mound, B. Srijanto, J.D. Fowlkes, G.M. Pharr, P.D. Rack, Growth and nanomechanical characterization of nanoscale 3D architectures grown via focused electron beam induced deposition, Nanoscale 9(42) (2017) 16349-16356.

[42] I. Utke, J. Michler, R. Winkler, H.J.M. Plank, Mechanical Properties of 3D Nanostructures Obtained by Focused Electron/Ion Beam-Induced Deposition: A Review, 11(4) (2020) 397.

[43] G. Arnold, R. Winkler, M. Stermitz, A. Orthacker, J.H. Noh, J.D. Fowlkes, G. Kothleitner, M. Huth, P.D. Rack, H. Plank, Tunable 3D Nanoresonators for Gas-Sensing Applications, Advanced Functional Materials 28(19) (2018) 1707387.

[44] A. Reiser, L. Koch, K.A. Dunn, T. Matsuura, F. Iwata, O. Fogel, Z. Kotler, N.J. Zhou, K. Charipar, A. Pique, P. Rohner, D. Poulikakos, S. Lee, S.K. Seol, I. Utke, C. van Nisselroy, T.

Zambelli, J.M. Wheeler, R. Spolenak, Metals by Micro-Scale Additive Manufacturing: Comparison of Microstructure and Mechanical Properties, Adv Funct Mater (2020).

[45] L. Angeloni, M. Ganjian, M. Nouri-Goushki, M.J. Mirzaali, C.W. Hagen, A.A. Zadpoor, L.E. Fratila-Apachitei, M.K. Ghatkesar, Mechanical characterization of micro- and nanopillars by atomic force microscopy Nanoscale, Additive Manufacturing 39 (2021) 101858.

[46] A. Sobiepanek, M. Milner-Krawczyk, M. Lekka, T. Kobiela, AFM and QCM-D as tools for the distinction of melanoma cells with a different metastatic potential, Biosensors and Bioelectronics 93 (2017) 274-281.

[47] N. Benne, R.J. Leboux, M. Glandrup, J. van Duijn, F.L. Vigario, M.A. Neustrup, S. Romeijn, F. Galli, J. Kuiper, W. Jiskoot, Atomic force microscopy measurements of anionic liposomes reveal the effect of liposomal rigidity on antigen-specific regulatory T cell responses, Journal of Controlled Release (2019).

[48] Y. Tian, C. Zhou, F. Wang, J. Zhang, Z. Guo, D. Zhang, A novel method and system for calibrating the spring constant of atomic force microscope cantilever based on electromagnetic actuation, Rev Sci Instrum 89(12) (2018) 125119.

[49] P. Xavier, S. Bose, Nanomechanical Mapping, Hierarchical Polymer Dynamics, and Miscibility in the Presence of Chain-End Grafted Nanoparticles, Macromolecules 49(3) (2016) 1036-1048.

[50] A. Pakzad, J. Simonsen, R.S. Yassar, Gradient of nanomechanical properties in the interphase of cellulose nanocrystal composites, Composites Science and Technology 72(2) (2012) 314-319.

[51] M. Ren, T. Shi, D.J. Corr, S.P. Shah, Mechanical Properties of Micro-regions in Cement-based Material based on the PeakForce QNM Mode of AFM, Journal of Wuhan University of Technology-Mater. Sci. Ed. 34(4) (2019) 893-899.

[52] C. Li, M. Ostadhassan, T. Gentzis, L. Kong, H. Carvajal-Ortiz, B. Bubach, Nanomechanical characterization of organic matter in the Bakken formation by microscopy-based method, Marine and Petroleum Geology 96 (2018) 128-138.

[53] H. Gercek, Poisson's ratio values for rocks, International Journal of Rock Mechanics and Mining Sciences 44(1) (2007) 1-13.

[54] J. Merker, D. Lupton, M. Töpfer, H. Knake, High temperature mechanical properties of the platinum group metals, Platinum Metals Review 45(2) (2001) 74-82.

[55] R. Jana, D. Savio, V.L. Deringer, L. Pastewka, Structural and elastic properties of amorphous carbon from simulated quenching at low rates, Modelling and Simulation in Materials Science and Engineering 27(8) (2019) 085009.

[56] Y.N. Xu, M.N. Liu, M.C. Wang, A. Oloyede, J.M. Bell, C. Yan, Nanoindentation study of the mechanical behavior of TiO2 nanotube arrays, Journal of Applied Physics 118(14) (2015) 145301.

[57] J.I. Kilpatrick, I. Revenko, B.J. Rodriguez, Nanomechanics of Cells and Biomaterials Studied by Atomic Force Microscopy, Adv Healthc Mater 4(16) (2015) 2456-74.

[58] L.-O. Heim, T.S. Rodrigues, E. Bonaccurso, Direct thermal noise calibration of colloidal probe cantilevers, Colloids and Surfaces A: Physicochemical and Engineering Aspects 443 (2014) 377-383.

[59] A. Botman, M. Hesselberth, J. Mulders, Improving the conductivity of platinum-containing nano-structures created by electron-beam-induced deposition, Microelectronic Engineering 85(5-6) (2008) 1139-1142.

[60] M. Perez-Roldan, J. Mulders, P. Trompenaars, Oxygen-assisted purification of platinum structures deposited by ion and electron beam induced processes, Journal of Physics D: Applied Physics 50(20) (2017) 205307.

[61] H. Plank, J.H. Noh, J.D. Fowlkes, K. Lester, B.B. Lewis, P.D. Rack, Electron-beam-assisted oxygen purification at low temperatures for electron-beam-induced pt deposits: towards pure and high-fidelity nanostructures, ACS applied materials & interfaces 6(2) (2014) 1018-1024.

[62] M.H. Ervin, D. Chang, B. Nichols, A. Wickenden, J. Barry, J. Melngailis, Annealing of electron beam induced deposits of platinum from Pt (PF 3) 4, Journal of Vacuum Science & Technology B: Microelectronics and Nanometer Structures Processing, Measurement, and Phenomena 25(6) (2007) 2250-2254.

[63] S. Mehendale, J. Mulders, P. Trompenaars, Purification of Au EBID structures by electron beam post-irradiation under oxygen flux at room temperature, Microelectronic Engineering 141 (2015) 207-210.

[64] M.G. Stanford, B.B. Lewis, J.H. Noh, J.D. Fowlkes, P.D. Rack, Inert Gas Enhanced Laser-Assisted Purification of Platinum Electron-Beam-Induced Deposits, ACS Appl Mater Interfaces 7(35) (2015) 19579-88.

[65] B.B. Lewis, B.A. Mound, B. Srijanto, J.D. Fowlkes, G.M. Pharr, P.D.J.N. Rack, Growth and nanomechanical characterization of nanoscale 3D architectures grown via focused electron beam induced deposition, 9(42) (2017) 16349-16356.

[66] D.P. Linklater, M. De Volder, V.A. Baulin, M. Werner, S. Jessl, M. Golozar, L. Maggini, S. Rubanov, E. Hanssen, S. Juodkazis, E.P. Ivanova, High Aspect Ratio Nanostructures Kill Bacteria via Storage and Release of Mechanical Energy, ACS Nano 12(7) (2018) 6657-6667.

[67] P. Post, A. Mohammadi-Gheidari, C. Hagen, P. Kruit, Parallel electron-beam-induced deposition using a multi-beam scanning electron microscope, Journal of Vacuum Science & Technology B, Nanotechnology and Microelectronics: Materials, Processing, Measurement, and Phenomena 29(6) (2011) 06F310.

5

On the use of black Ti: behind the scenes of dual-functionality

Abstract

Despite the potential of small-scale pillars of black titanium (bTi) for killing the bacteria and directing the fate of stem cells, not much is known about the effects of the design parameters of pillars on their biological properties. Here, three distinct bTi surfaces were designed and fabricated through dry etching of the titanium surface, each featuring different pillar design. The interactions of the surfaces with MC3T3-E1 preosteoblast cells and Staphylococcus aureus bacteria were then investigated. Pillars with different heights and spatial organizations differently influenced the morphological characteristics of the cells, including their spreading area, aspect ratio, nucleus area, and cytoskeletal organization. The preferential formation of focal adhesions (FAs) and their size variations also depended on the type of topography. When the pillars were neither fully separated nor extremely tall, the colocalization of actin fibers and FAs were observed. However, the killing efficiency of these pillars against the bacteria were not as high as that of fully separated and tall pillars. This study provides a new perspective on the dual-functionality of bTi surfaces and elucidates how the surface design and fabrication parameters can be used to achieve a surface topography with balanced bactericidal and osteogenic properties.

5.1. Introduction

The increased life expectancy of humankind has encouraged the medical device industry to develop functional devices that outlive the patients. In this regard, bone implants require a long list of properties and functionalities to serve their purpose most properly. In addition to primary stability [1, 2] and bone-matching mechanical properties [3], bone implants need to be designed in such a way to promote host tissue regeneration and integration with the implant (*i.e.,* osteoinduction and osseointegration) [4-6], as well as to combat implant-associated infections (IAIs) [7-9], as one of the main causes of implant failure.

Developing designer biomaterials with better control over their biological properties and interactions with their host is proven crucial for enhancing the performance of implantable medical devices [10]. Yet achieving the optimal biological properties and controlling the interactions of bio-organisms with the biomaterial are highly dependent on the surface properties [11-14]. For instance, enhancing cell adhesion, cell growth [15, 16],

and the desired differentiation of stem cells [17, 18] are among the steps required to optimize the osseointegration of implants. Similarly, preventing IAIs through the eradication of the adherent bacteria and the aversion of biofilm formation play important roles in this regard [19]. To this aim, exploiting the advances in surface modification techniques is a necessity to achieve those rare or unprecedented properties as the surface is the frontline where the success of a biomaterial is determined. Due to the complications associated with the use of antibacterial agents [20, 21] and growth factors [22], including the high cost and resistance development by bacterial strains, the focus has largely shifted to the physical alterations of the surface.

On the other hand, inspired by the unique naturally occurring structures [23-25], synthetic bactericidal surface patterns have emerged with different geometries and dimensions [26]. Patterns that lie within a specific range of dimensions have been shown to mechanically kill different types of bacteria through a combination of different mechanisms [27-29].

Among numerous nano-/microfabrication techniques, reactive ion etching (RIE) is a simple and fast technique for creating an engineered surface topography [30]. RIE works based on dry chemical etching and physical ion bombardment of the surface. Ivanova *et al.* used RIE to create high aspect ratio nanopillars on a silicon substrate and studied their bactericidal properties for the first time [31]. The killing efficiency of the so-called black silicon (bSi, due to its black appearance) against both Gram-negative and Gram-positive bacteria was comparable to naturally occurring bactericidal surfaces. Ever since, many studies have investigated the effects of the height and density of nanopillars on the bactericidal properties of bSi, as well as the involved killing mechanisms [32, 33]. Later on, Hasan *et al.* successfully fabricated similar nanopillars on a titanium substrate (a more relevant choice of material for orthopedic applications) using inductively coupled plasma reactive ion etching (ICP RIE) [34]. They showed that bTi is as effective as bSi in killing the bacteria. Moreover, not only did bTi support the attachment and proliferation of human mesenchymal stem cells (hMSCs) but also displayed a synergistic effect in stimulating the osteogenic differentiation of cells together with the osteogenic culture medium. So far, all the mentioned studies have produced bSi and bTi under identical conditions and have only changed the etching time as a variable to achieve different pillar lengths, whereas the geometry and organization of the

pillars have been quite comparable in those studies. Recently, the effects of all the processing parameters of ICP RIE on the physicomechanical characteristics of the resulting bTi nanostructures have been systematically studied [30]. Changing other processing parameters, such as the chamber pressure and temperature can also be used to fabricate distinct nanostructured surfaces.

Due to the remarkable structural and biological differences between mammalian and bacterial cells, designing a patterned surface that fulfills dual functionality is quite challenging. In this regard, bTi seems to be a very promising biomaterial for future clinical applications, given that it holds the potential for narrowing down the gap between osteogenic and bactericidal patterns as the essential step in developing cell-instructive biomaterials. However, there are still many unknowns about the behavior of cells interacting with bTi nanopillars and how their long-term osteogenic response is related to their short-term responses (*e.g.,* morphology, spreading area, the formation of FAs, etc.).

In the present study, we provide a new perspective on the dual-functionality of different bTi surfaces with the ultimate aim of devising a guideline for the application of bTi. We hypothesized that the viability and fate of bacteria and mammalian cells are significantly affected by the processing parameters of bTi surfaces and the geometrical characteristics of the pillars covering them. By adjusting the various ICP RIE processing parameters, we produced different types of bTi surfaces in our preliminary studies and selected three out of those that represent a gradual deviation from the flat Ti surface. These three types of bTi are distinct in terms of the height and spatial organization of their pillars. To answer the research question, cytocompatibility, morphological characteristics, and the formation of FAs of MC3T3-E1 preosteoblast cells cultured on these three different bTi surfaces, were quantitatively analyzed and the relationships between them were discussed. Furthermore, the bactericidal properties of the same bTi surfaces against *Staphylococcus aureus* bacteria (as the main relevant infectious pathogen involved in IAIs) were evaluated to enable the possible identification of a bTi surface with the desired dual-functionality and to shed light on the possible killing mechanism of the studied surfaces.

5.2. Materials and methods

5.2.1. Fabrication and characterization of bTi samples

5.2.1.1. Fabrication

Annealed titanium foils with a thickness of 125 μm (99.96% purity, Goodfellow, UK) were cut to the size of a 4-inch (diameter = 10.16 cm) silicon wafer and were polished by chemical-mechanical polishing (CMP Mecapol E460, Saint-Martin-le-Vinoux, France). The surface was then coated with a photoresist to protect it against damages. The titanium wafer was further cut into 8×8 mm^2 pieces using a Disco dicer (Disco Hi-Tec Europe GMbH, Germany). The photoresist layer was subsequently removed by acetone and the samples were cleaned in ethanol and isopropyl alcohol (IPA). The samples were spin-dried prior to surface modification by ICP RIE. An ICP RIE machine (PlasmaLab System 100, Oxford Instruments, UK) was used to create three types of structures on the titanium surface, which were distinct in terms of their morphological parameters and organization. Therefore, the polished samples were glued with diffusion oil on a 4-inch quartz wafer as the carrier wafer. The etching process was performed with Cl_2 and Ar gases. The following processing parameters were the same for all three types of modified surfaces: ICP source power = 600 W, RF power = 100 W, etching time = 10 min, Cl_2 flow rate = 30 sccm, and Ar flow rate = 2.5 sccm. However, the temperature and pressure of the chamber were changed for each type of surface as follows: 0 °C and 4.0 Pa for the first group, 40 °C and 2.0 Pa for the second condition, and 40 °C and 0.5 Pa for the third condition. Following the etching process, the samples were cleaned in acetone, ethanol, and IPA, respectively (each step lasted 30 min), and were then spin-dried for further characterization and experiments.

5.2.1.2. Morphological characterization

The etched surfaces were imaged by scanning electron microscopy (SEM) (Helios NanoLab 650, FEI, US). Top and tilted view (35°) images were acquired at different magnifications to assess the morphology and spatial organization of the resultant pillars. The mean roughness (Ra) and root mean squared roughness (Rq) were also estimated for each sample as the mean ± SD of the values measured for three images of 100 μm^2 each by atomic force microscopy (AFM) (JPK Nanowizard 4, Bruker, Germany) using a high aspect ratio probe (TESPA-HAR, Bruker, Germany) in the tapping mode.

5.2.1.3. Surface chemical composition

The elemental chemical composition of the surfaces was determined using energy-dispersive X-ray spectroscopy (EDS) performed inside the SEM (Helios Nanolab 650, FEI, US). The major chemical elements were identified from the EDS spectra.

5.2.1.4. Surface wettability

The wettability of the flat Ti surface (*i.e.*, polished, non-treated Ti surfaces) and bTi surfaces were evaluated by measuring the static water contact angle in duplicate using a drop shape analyzer (DSA 100, Kruss, Germany). A volume of 1.5 μl deionized water with a falling rate of 60 μl/min was placed on the surface using a syringe. The images were recorded after 5 s.

5.2.2. Preosteoblast cell response to bTi surfaces

5.2.2.1. Pre-culture of cells and cell seeding

Preosteoblast MC3T3-E1 cells (Sigma-Aldrich, Germany) were cultured in alpha minimum essential medium (α-MEM) supplemented with 10% (v/v) fetal bovine serum (FBS) and 1% (v/v) penicillin-streptomycin (all from Thermo Fisher Scientific, US). The medium was refreshed every 2 days. The samples were sterilized by immersion in 70% ethanol and exposed to UV light for 20 min. Upon reaching confluence, cells were detached from the cell culture flask using 1X trypsin-EDTA solution (Thermo Fisher Scientific, US) and were cultured on both flat Ti and bTi surfaces (2×10^4 cells per sample) in a 48 well-plate (Greiner, Bio-One, The Netherlands), and were incubated at 37 °C and 5% CO_2 (Life Technologies, US). This cell culture procedure was followed for all the cell experiments described in the following sections. In the case of experiments taking longer than 1 day, the medium was supplemented with 50 μg/ml ascorbic acid (1:1000) and 4mM β-glycerophosphate (1:500) (both from Sigma-Aldrich, Germany) from day 2 onward. All experiments, described in the following sections, were independently performed two times, each time in quadruplicates.

5.2.2.2. PrestoBlue assay

The metabolic activity of the cells seeded on flat Ti and bTi surfaces was measured by a PrestoBlue assay after 1, 4, 7, 11, and 14 days of culture. Therefore, all surfaces (n = 4/group)

were incubated in 250 µl α-MEM supplemented with 25 µl PrestoBlue reagent (Thermo Fisher Scientific, US) for 1 h at 37 °C and 5% CO_2. Thereafter, 100 µl of the supernatant from each well was transferred to a 96 well-plate (Greiner, Bio-One, The Netherlands) in duplicate. The fluorescence was measured at an excitation wavelength of 530 nm and an emission wavelength of 595 nm with a Victor X3 microplate reader (PerkinElmer, Groningen, The Netherlands).

5.2.2.3. Immunocytochemical analysis of preosteoblast cells

In order to evaluate the short-term response of these cells to bTi surfaces and their morphological changes, the actin filaments, nucleus, and focal adhesions of the cells were stained after 1 day of culture. The specimens were first washed twice with 10X PBS (Sigma-Aldrich, Germany) and the cells were fixated using a 4% (v/v) formaldehyde solution (Sigma-Aldrich, Germany). The cell membrane was permeabilized by adding 0.5% Triton X-100/PBS (Sigma-Aldrich, Germany) at 4 °C for 5 min and then the samples were incubated in 1% BSA/PBS (Sigma-Aldrich, Germany) at 37 °C for 5 min. Subsequently, the samples were incubated in anti-vinculin mouse monoclonal primary antibody (1:100 in 1% BSA/PBS, Sigma-Aldrich, Germany) and rhodamine-conjugated phalloidin (1:1000 in 1% BSA/PBS, Thermo Fisher Scientific, US) for 1 h at 37 °C. The cells were then washed three times (5 min each time) with 0.5% Tween-20/PBS (Sigma-Aldrich, Germany) before being incubated in Alexa Fluor 488, donkey anti-mouse polyclonal secondary antibody (1:200 in 1% BSA/PBS, Thermo Fisher Scientific, US) for 1 h at room temperature. The specimens were washed again three times with 0.5% Tween-20/PBS (5 min each time), followed by 5 min washing with 1X PBS. To simultaneously visualize the cell nuclei and properly mount the samples on microscopic glass slides, 10 µl Prolong gold antifade reagent containing DAPI (4',6-diamidino-2-phenylindole) (Thermo Fisher Scientific, US) was laid on the surfaces and then five different locations of each sample were imaged using a fluorescence microscope (ZOE™ fluorescent cell imager, Bio-Rad, The Netherlands). For the SEM observations, the stained samples were washed twice with distilled water for 5 min and then dehydrated in 50%, 70%, and 96% ethanol solutions for 15 min, 20 min, and 20 min, respectively. Eventually, the samples were dried overnight at room temperature and were gold-sputtered before SEM imaging.

5.2.2.4. Fluorescent image analysis

ImageJ 1.53c (NIH, US) and focal adhesion analysis server (FAAS) [35] were used to extract and quantify data from the fluorescent images. Each image overlay was split into separate channels for further evaluation of the nucleus, F-actin, and other proteins (*i.e.,* vinculin). By thresholding the grayscale images of F-actin and vinculin, the cell spreading area, cell nucleus area, and the number and area of FAs were quantified through the Analyze Particles command. By fitting ellipses to the cell area, the minor and major diameters were measured and used to determine the aspect-ratio of the cells. A previously described method [36] was used to quantify the number and area of FA (for fully separated ones). Briefly, for 15 cells per study group, the background was subtracted from the greyscale images under the Sliding Paraboloid option with a rolling ball radius of 50 pixels. The local contrast of the image was then enhanced by running the CLAHE plugin with a block size of 19, histogram bins of 256, and a maximum slope of 6. To further minimize the background, the mathematical exponential function (EXP) was applied through the process menu. Thereafter, the brightness, contrast, and threshold were automatically adjusted before measurements using the Analyze Particles command.

5.2.3. Bacterial studies

5.2.3.1. Preparation of bacterial cultures

Gram-positive *Staphylococcus aureus* bacteria (RN0450 strain) (BEI Resources, US) were grown on brain heart infusion (BHI) (Sigma-Aldrich, US) agar plates at 37 °C overnight. A pre-culture of bacteria was prepared by inoculating a single colony in 10 ml autoclaved BHI, shaken at 140 rpm at 37 °C. The bacterial cells were collected at their logarithmic stage of growth and the optical density of the inoculum at 600 nm wavelength (OD_{600}) in the medium solution was first measured by a WPA Biowave II spectrophotometer (Biochrom, UK) and was then adjusted to a value of 0.1 (equivalent to 4×10^8 CFU/ml) to be cultured on the flat Ti and bTi surfaces. All surfaces were sterilized by immersion in 70% ethanol and exposure to UV light for 20 min. 250 µl of the bacterial inoculum was added to each surface in a 48 well-plate (Cell Star, Germany) (*i.e.,* 10^8 CFU per sample). All experiments, described in the following sections, were independently performed two times, each time in triplicate.

5.2.3.2. Bacterial metabolic activity (PrestoBlue assay)

To follow the metabolic activity of the adherent bacterial cells seeded on flat Ti and bTi surfaces, the PrestoBlue assay was performed at 1, 4, 8, and 18 hr of culture, using the same replicates for all the time points. At each time point, all surfaces were incubated in 250 μl of BHI broth supplemented with 25 μl PrestoBlue cell viability reagent (Thermo Fisher Scientific, US) for 1 hr at 37 °C. Thereafter, 100 μl of the medium from each well was transferred to a 96 well-plate (Cell Star, Germany) in duplicate. The fluorescence was measured at an excitation wavelength of 530 nm and an emission wavelength of 595 nm using a Synergy 2 microplate reader (BioTek, US).

Furthermore, to visualize the morphological state of bacterial cells on the surfaces and investigating the interactions between bacteria and surfaces, the specimens were imaged by SEM after 18 hr of culture. To this end, the adhered bacterial cells were fixated by immersion in a PBS solution containing 4% formaldehyde and 1% glutaraldehyde (both from Sigma-Aldrich, US) at 4 °C for 1 hr. Subsequently, the samples were dehydrated by washing with MilliQ water for 10 min, 50% ethanol for 15 min, 70% ethanol for 20 min, and 96% ethanol for 20 min, respectively. Eventually, they were soaked in hexamethyldisilazane (HMDS) (Sigma-Aldrich, US) for 30 min. After being air-dried, a thin layer of gold was sputtered on the samples before imaging by SEM at different magnifications and the tilt angles of 0° and 45°.

5.2.3.3. Live/dead staining

To investigate the bactericidal properties of the surfaces, the live/dead staining of the adhered bacteria was performed using L7012 Live/Dead *Bac*Light Bacterial Viability Kit (Invitrogen, US) after 18 hr of culture according to the manufacturer's instructions [30]. Briefly, the non-adherent bacteria were removed by removing the medium from wells. The samples were then washed twice by 0.85% (w/v) NaCl solution. Subsequently, the adherent bacteria were stained by a 1:1 mixture of SYTO 9 green-fluorescent and propidium iodide red-fluorescent stains for 15 min at room temperature to distinguish between the live and dead bacteria based on their membrane integrity. Following the staining, the samples were rinsed again with 0.85% (w/v) NaCl solution and were then imaged (magnification: 20x) by a Luca R 604 widefield fluorescence microscope (Andor Technology, UK). Five different

areas of each sample were imaged and the number of live and dead bacteria were quantified using the ImageJ Analyze Particles command. The percentage of the dead cells per surface was reported as the killing efficiency of the surface.

5.2.3.4. CFU counting

CFU counting was performed as a complementary method to compare the bactericidal properties of flat Ti and bTi surfaces. After 18 hr of culture, the supernatant BHI broth was collected to quantify the number of non-adherent bacterial cells. 100 μl aliquots of 10-fold serial dilutions were plated on BHI agar plates and CFUs were manually counted after overnight incubation at 37 °C. On the other hand, the bacterial cells adhered to each sample were collected by sterile cotton swabs and were ultrasonicated in 1 ml PBS for 15 min using an Elmasonic S 30 ultrasonic cleaning unit (Elma Schmidbauer GmbH, Germany). The detached bacterial cells were plated on Petrifilm™ aerobic count plates (3M, US) and were incubated at 37 °C overnight. The red dots appeared on the petrifilms as indicators of viable cells were manually counted.

5.2.4. Statistical analysis

For all of the above-mentioned experiments, the raw data was first tested for normal distribution using the D'Agostino-Pearson omnibus normality test in Prism version 8.4.3 (GraphPad, US). In the cases where the sample size was too small for such a test, the Shapiro-Wilk normality test was performed. The Brown-Forsythe and Welch ANOVA test was then performed, followed by the Dunnett's T3 multiple comparisons test to determine the statistical significance of the differences between the means of the different experimental groups. Since the results of the surface wettability experiments were found to be not normally distributed, the non-parametrical Kruskal-Wallis test was performed, followed by the Dunn's multiple comparisons test. In addition, the results of the PrestoBlue assay for both mammalian and bacterial cells were analyzed using the two-way ANOVA test, followed by the Tukey's multiple comparisons *post-hoc* analysis. A *p*-value below 0.05 was considered to indicate statistical significance.

5.3. Results

5.3.1. Physicochemical characterization of bTi surfaces

All Ti surfaces appeared black after the completion of the etching process as expected, due to the light absorption within the fabricated structures [31, 34]. Scanning electron microscopy (SEM) observations showed that three types of surface topography had been created on Ti (Figure 1a). These were distinguishable based on their geometry and spatial organization, by changing two processing parameters, namely chamber pressure and temperature. The Ti surface topography changed from the polished flat surface due to the formation of pillar-shaped structures on the surface. A temperature of 0 °C and a chamber pressure of 4.0 Pa resulted in closely-packed and short pillars, mainly connected to each other at the tip, hence resembling a porous-like surface when viewed from the top. This type of bTi is, therefore, referred to as Porous. Here, the grain boundaries of the original polished surface were also visible (Figure 1a). By increasing the temperature to 40 °C and decreasing the pressure to 2.0 Pa, the pillars appeared to be taller and more separated from each other, meaning that the height of the pillars became distinguishable to some extent in the SEM images. The pillars were, however, still connected to some degree, forming partitions of pillars on the surface. Keeping the temperature at 40 °C while decreasing the pressure to 0.5 Pa resulted in the third type of morphology in which the pillars were taller and relatively highly separated from each other, meaning that the height of the pillars could be measured. These pillars also showed clustering at the tip creating free interspaces between the clusters (Figure 1a). Henceforward, we call the former type of bTi Partition and the latter Sparse. Unlike controlled patterns consisting of surface pillars [27], it is not easy to attribute a precise interspacing value to these surface features. Precise, objective measurement of the diameter of the single pillars was also difficult as many pillars were closely connected to each other, especially in the Porous and Partition samples. However, the tip diameter of the pillars was always < 100 nm. From the SEM images, it could be estimated that the height of the pillars increased from the submicron scale, from about 350 nm in the Porous to a range of 700 nm to 1 μm in Partition, and then to the microscale in the Sparse samples (a range of 1.4 μm to 2.2 μm) (Figure 1a). Further atomic force microscopy (AFM) characterizations revealed that due to the formation of the pillars, the average roughness (R_a) of the surfaces increased from

< 50 nm in the Porous group to > 150 nm in the Partition and Sparse groups. Furthermore, the chemical characterization of the bTi surfaces indicated that the most abundant chemical elements of the surface are Ti and O (Figure 1b).

Additionally, while the flat Ti surface showed a static water contact angle of about 75°, the bTi surfaces exhibited significantly lower contact angles, indicating their superhydrophilic properties. The approximate water contact angle measured for the Porous surface was 15°, which significantly decreased to < 6.0° for the Partition and Sparse groups (Figure 1c).

5.3.2. Short-term response of preosteoblast cells

MC3T3-E1 preosteoblast cells showed different morphologies on the different types of bTi after 1 day in culture (Figure 2a). While the cells possessed a well-spread and polygonal shape on flat Ti, their directionality highly increased on the etched samples, from the Porous to the Partition and to the Sparse specimens (Figure 2a). This change in shape was associated with a decrease in cell area and an increase in the aspect ratio (Figure 2a and Figure 3a, b). On the Partition samples, the cells developed long filopodia around cell periphery to attach to these surfaces whereas on the Sparse surfaces, the majority of the cells were highly elongated with a significant number of the cells also showing to be isotropic (*i.e.*, nearly fully rounded). None of the bTi surfaces were found to be cytotoxic, as the results of the PrestoBlue assay showed that the metabolic activity of the cells significantly increased over the course of the 14 days of culture without any significant differences compared to the flat Ti (Figure 2b). Moreover, the cells did not show any profound preferential adhesion toward any of the surfaces (flat Ti and bTi) as the average number of the adhered cells per mm² of the specimen surface was not significantly different between any of the experimental groups, including the control and bTi groups (Figure S2a).
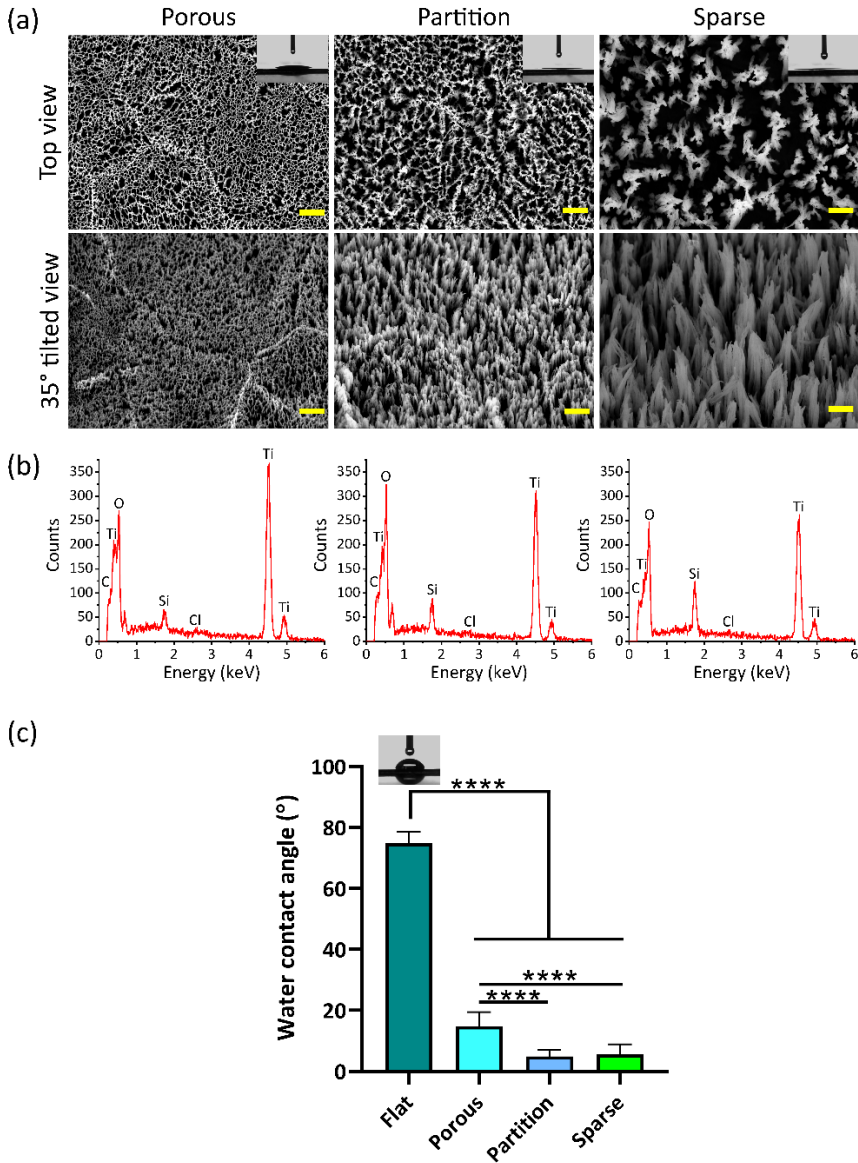
Figure 1. (a) The top- and tilted-view SEM images of the Porous, Partition, and Sparse bTi specimens made through ICP RIE, showing distinct surface morphologies and spatial organization of the pillars. The insets depict the water droplets residing on each surface after 5 s. Scale bar = 1 μm. (b) Representative EDS spectra of Porous, Partition, and Sparse bTi specimens, showing the most abundant chemical elements identified on each surface. (c) The mean water contact angle of the bTi surfaces as compared to the flat Ti surface. ****$p < 0.0001$.

101
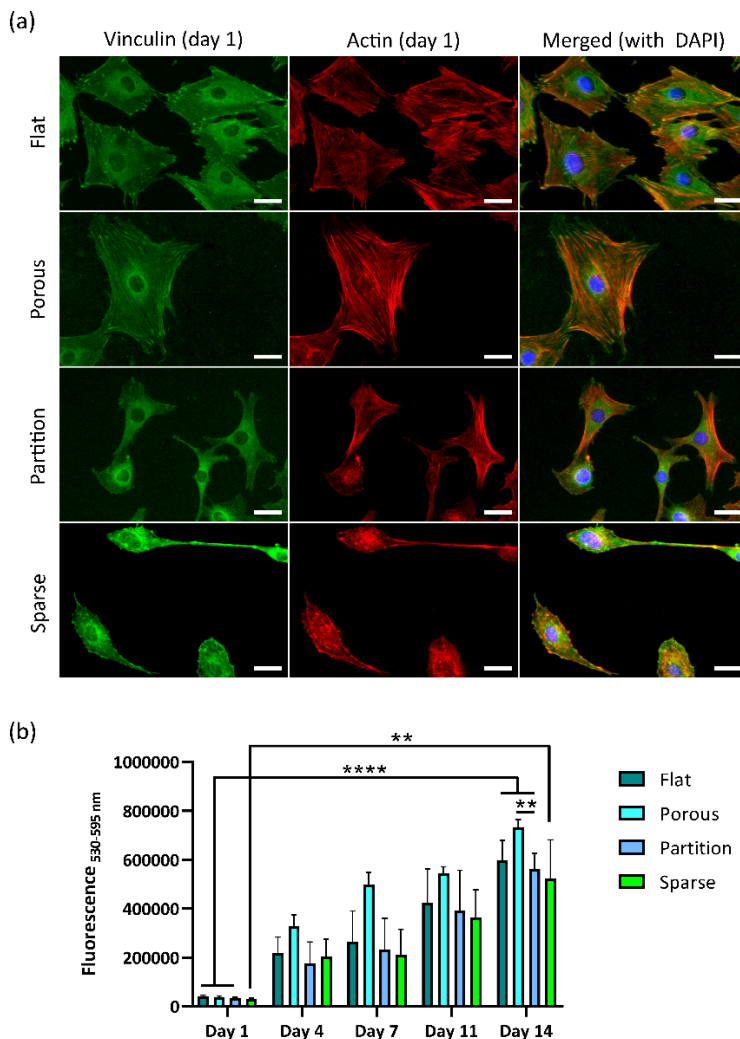
Figure 2. (a) The immunocytochemical staining of vinculin (green), actin (red), and nucleus (blue, merged with the last two channels) for the MC3T3-E1 preosteoblast cells cultured on the flat Ti, Porous, Partition, and Sparse bTi specimens after 1 day. All surfaces except Sparse support the spreading of cells. Unlike the polygonal cell morphology on those samples, the majority of the cells are highly elongated on the Sparse specimens. Moreover, the colocalization of FAs and actin fibers can be detected in the Porous and Partition groups but not on the surface of the Sparse specimens. Scale bar = 30 μm. **(b)** The metabolic activity of the preosteoblast cells cultured on the flat Ti and bTi surfaces measured by the PrestoBlue assay over 14 days. The increased metabolic activity of the cells with time indicates the cytocompatibility of all surfaces. ** $p < 0.01$, **** $p < 0.0001$.
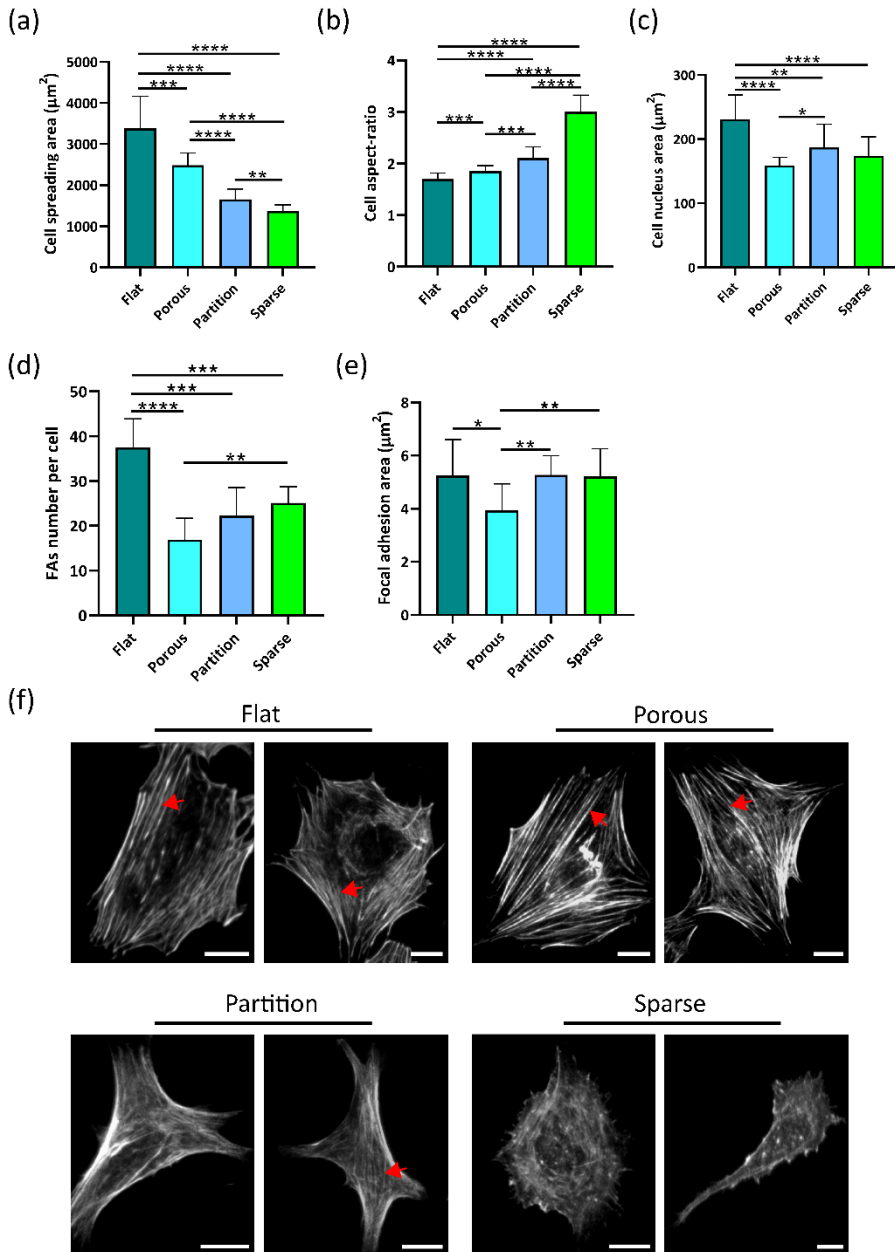
Figure 3. The morphological characteristics and early response of the preosteoblast cells cultured on the flat Ti and bTi surfaces after 1 day of culture. (a) Spreading area. (b) Cell aspect ratio. (c) Cell nucleus area. (d) Number of focal adhesions per cell. (e) Focal adhesion area. * $p < 0.05$, ** $p < 0.01$, *** $p < 0.001$, **** $p < 0.0001$. (f) The gray-scale images of the cytoskeleton. Scale bar = 20 μm.

In addition to differences in cell area and aspect ratio, the nucleus area of the cells was also significantly decreased on all types of bTi as compared to flat Ti (Figure 3c). However, the trend was not similar to the cell spreading area. For instance, although the cells had a larger area on the Porous specimens as compared to the Partition specimens, the opposite was observed for the cell nucleus area.

The focal adhesions (FAs) formed at the periphery of the cells on the flat Ti, Partition, Porous, and Sparse specimens (Figure 2a). The average number of FAs per cell was significantly lower on all bTi specimens as compared to flat Ti (Figure 3d). The area of FA corresponding to flat Ti, Partition, and Sparse groups was on average 5.2 μm^2, which significantly decreased to 3.9 μm^2 in the Porous samples (Figure 3e). Furthermore, different cytoskeleton organization was observed. For the cells residing on the flat Ti and Porous specimens, clear actin stress fibers were formed, which were primarily oriented along the cell length (Figure 2a and Figure 3f). This organization decreased on the Partition surfaces and almost disappeared on the Sparse surfaces.

5.3.3. Early bactericidal effects of bTi surfaces

The live/dead staining of the adherent *S. aureus* bacteria after 18 hr (Figure 4a and b) showed that all bTi surfaces had bactericidal activity, which increased from the Porous to the Partition and to the Sparse surfaces. On average, only 8% of the bacterial cells were found dead on flat Ti samples. The mean percentage of dead bacteria increased to 25 (SD 5%), 35 (SD 5%), and 42 (SD 7%) for the Porous, Partition, and Sparse specimens, respectively. The morphological evaluation of bacteria by SEM showed that they had a normal coccoid shape on flat Ti while they were stretched on the Porous specimens with a flattened morphology (Figure 4a). On Partition surfaces, stretching of the bacteria between adjacent pillars was even more visible. The penetration of the pillars into the cell wall was also detected, especially in the cells residing on top of the pillars (Figure 4a). The bacteria also bent the pillars underneath them (Figure 4a), which might impose additional mechanical forces on the bacterial cell wall [37]. The bacteria adhered to the Sparse specimens were observed to be both stretched between the lateral sides of adjacent pillars and punctured by the sharp tips of the pillars (Figure 4a). The cells were even present in the interspaces between the clustered pillars as some of these spaces exceed the size of the bacteria (~ 800 nm in diameter). Cells with normal

morphology were hardly present on this type of surface. These findings were confirmed by the quantitative results of the CFU counting that showed that there is a significant difference between the flat Ti and bTi (Partition and Sparse) in terms of the number of bacteria capable of forming a colony after being cultured on these samples (Figure 4c). As expected, none of the surfaces had an influence on the viability of non-adherent bacteria (Figure S2d).

Moreover, performing the PrestoBlue assay at four different time points indicated that the bacterial metabolic activity is significantly lower on all bTi surfaces as compared to flat Ti at least after the first hour after culture (Figure 4d). This difference was also observed at 4, 8, and 18 hr of culture. Comparing the different types of bTi, the metabolic activity of the bacteria increased until 4 hr and then remained at the same level until 8 hr after which it declined.

5.4. Discussion

Developing cell-instructive biomaterials could shift the paradigm in fabrication of orthopedic implants. The introduction of bactericidal bSi surfaces [31] drew attention to the use of (ICP) RIE for the fabrication of high aspect ratio pillars on the surface. Consequently, bactericidal bTi has been introduced as a promising biomaterial for preventing IAIs [34]. To date, numerous studies [32, 33, 38] have focused on the biological properties of bSi and bTi surfaces, trying to optimize the dimensions of the pillars by changing one single processing parameter (*i.e.*, etching time). It was reported that fine changes in the characteristics of such etched structures may influence their biological properties [39]. Yet a wider range of surfaces can be produced by taking advantage of other (ICP) RIE processing parameters [30]. Therefore, the optimum etched surfaces for a certain or multiple bio-functionality are yet to be established. Moreover, the literature offers limited data over the interactions of bTi surfaces with mammalian cells, especially those involved in the regeneration of bone tissue. Not much is known about the relationship between the early and long-term responses of the cells interacting with different bTi surfaces. Therefore, we tried to further explore the fabrication process (*i.e.*, the chlorine-based maskless ICP RIE of Ti) and generate a couple of distinct bTi surfaces in an attempt to find a surface that provides the best dual-functionality (from both osteogenic and bactericidal points of view).
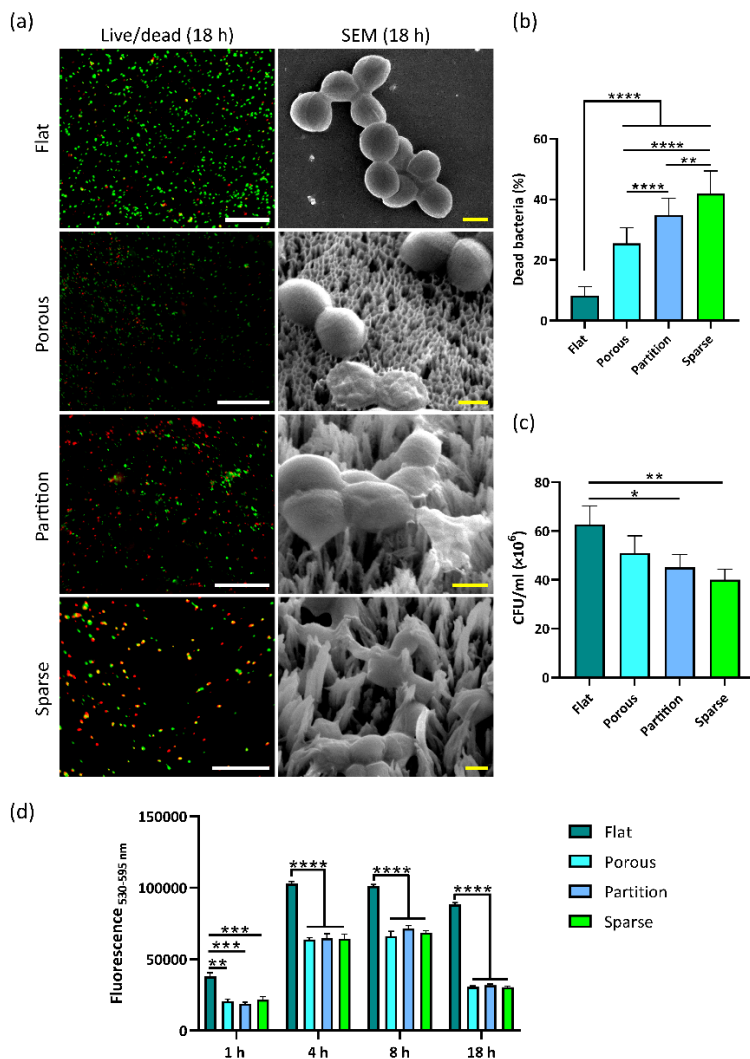
Figure 4. The bactericidal properties of flat Ti and bTi surfaces. (a) The representative live/dead and SEM images of *S. aureus* cells cultured on surfaces for 18 hr. Green and red cells indicate viable and dead bacterial cells in the live/dead images, respectively. Scale bar = 20 μm and 500 nm for the live/dead and SEM images, respectively. (b) The quantification of non-viable bacterial cells based on live/dead images. (c) The results of CFU counting showed a similar trend regarding the bactericidal properties of the bTi surfaces. (d) The metabolic activity of the bacterial cells cultured on the flat Ti and bTi surfaces, measured by the PrestoBlue assay over 18 hr. At 4 hr, higher metabolic activity was measured but it did not continue increasing. * $p < 0.05$, ** $p < 0.01$, *** $p < 0.001$, **** $p < 0.0001$.

5.4.1. Looking at the Ti pillars from a physicochemical perspective

Among the ICP RIE processing parameters, the temperature and pressure of the chamber are two variables that significantly impact the etching rate and morphology of the resulting structures [30]. At higher pressures, the energy of ions and radicals decreases as a result of increased number of collisions between them, which eventually decreases the etching rate (*i.e.,* yields shorter pillars for a constant etching time). Increasing the temperature enhances the etching rate of the pillars. By changing these two conditions, we generated surfaces with increased pillar heights and interspaces between the clustered pillars. These changes are, however, not systematic as the height and interspace changed simultaneously in each bTi design. Yet, each surface was distinct from the rest by its unique combination of the height and organization of the pillars. Therefore, the biological properties of these surfaces should be associated with a combination of both of those parameters and not with the isolated effects of either. The height of the pillars increased from less than 400 nm to more than 1400 nm whereas the diameter was always less than 100 nm leading to an enhanced aspect ratio of the resultant structures. The interspace between the clustered/connected pillars also increased with the increase in height.

The chemical characterization of the bTi surfaces showed that the pillars mainly consist of Ti and O. The presence of an oxide layer on the surface has been confirmed by X-ray photoelectron spectroscopy (XPS) analysis in other ICP RIE studies [34, 39]. Furthermore, during the etching process, chlorine as the main etchant gas, the aluminum-made chamber wall, the quartz carrier wafer, and the organic solvents used for cleaning can respectively introduce negligible amounts of Cl, Al, Si, and C to the final etched Ti surface. Nevertheless, the bio-inertness of titanium is still preserved in form of TiO_x as the main component of the etched structures [30].

All bTi surfaces used in this study were found to be superhydrophilic. The trend of the measured water contact angle of the surfaces was in line with a previous study [30] that showed that decreasing the temperature and, thus, the formation of more compact nanostructures leads to larger water contact angles as compared to the specimens fabricated at higher temperatures (*e.g.,* 40 °C). Hasan *et al.* [34] have shown that the wettability of bTi enhances with an increased surface roughness. Similarly, the rougher samples in our study (Partition and Sparse) are the most hydrophilic surfaces. Yet the opposite trend in the

relationship between wettability of bTi surfaces and the surface roughness in another study [39] suggests that the wettability model applicable to these types of surfaces is largely dependent on the dimensions of the pillars, as well as their interspacing [40].

5.4.2. Adaptation of preosteoblast cells to bTi surfaces

The results of this study together with other previous studies form a body of evidence to refute any possible cytotoxicity of bTi surfaces as long as the aspect ratio of the pillars remains below 20 [41, 42]. Based on the metabolic activity measurements and microscopic observations, preosteoblast cells could easily proliferate on all types of the bTi studied here. However, the cells varied in terms of their morphology and cytoskeleton organization, which influence the behavior of preosteoblasts as anchorage-dependent cells. Cells try to find as much suitable anchorage points as possible upon which the integrins can optimally bind to the protein ligands adsorbed on the surface [43, 44]. On the Porous specimens, there are plenty of physical features that cells can reach onto without stretching their membrane extremely. This is starting to change on the Partition samples where cells need to develop membrane extensions in the form of filopodia to attach on the taller and partitioned pillars. The Sparse samples do not provide cells with close-enough features. Consequently, the cells tend to minimize their spreading area and keep connected via very long extensions leading to the elongated shapes observed [43]. The gradual increase in the aspect ratio of the cells from flat Ti to Sparse surfaces should, therefore, be considered in this context.

The formation of FAs and the global cytoskeletal remodeling via the formation of actin bundles play a crucial role in determining the ultimate cell fate [45]. Even the smallest surface features (2-4 nm in height) made of titanium have been shown to trigger a rapid reorganization of the cytoskeleton [46]. The analysis of FAs showed that by developing more directional protrusions in the cells residing on the Partition and Sparse specimens, FAs are regularly formed in the proximity of these polarized regions. This phenomenon is corroborated by previous studies that showed that the anisotropy of FAs distribution increases as the cell aspect ratio increases [47, 48]. On the flat Ti, however, the formation of FAs could be detected at the periphery of the cells and also in the more internal regions of the cell body (closer to the cell nucleus). Moreover, on these surfaces, FAs were mainly oval-shaped and aligned with the actin fibers along their long axis (Figure 2a). The colocalization

of FAs and actin fibers indicates the maturation of FAs and the establishment of a strong adhesion by coupling to the actin fibers (*i.e.,* stable FAs with a slow turnover rate) [43, 49]. On the contrary, the FAs of the cells residing on the Partition and Sparse specimens were relatively round and not yet mature. The colocalization of FAs and actin fibers is hardly recognizable on the Sparse samples. The actin fibers are well-oriented only inside the well-spread cells on the flat Ti and Porous specimens. On the other surfaces, the cells may be either already in the polarization phase or the contractile spreading phase, according to their morphology and cytoskeletal organization (Figure 2a and 3f) [50]. In the contractile spreading phase, the actin bundles are still being formed and the cells intend to form strong adhesion to the surface. The abundant presence of filopodia in these cells and their smaller areas indicate such effort by the cells. It can, therefore, be concluded that the cells undergo a more difficult or slower adaptation to the Partition and Sparse surfaces as compared to the other surfaces.

5.4.3. FA-mediated mechanical interactions with the surface

The difference in the size of FAs (denoted by their area) on different surfaces may also indicate different levels of mechanical tensions exerted on the cells. The average size of FAs is significantly larger on the Partition, Sparse, and flat Ti groups as compared to the Porous specimens. That is likely because the cells struggle to effectively adhere to very smooth surfaces (*e.g.,* flat Ti) or to highly separated pillars of the Sparse group, which is why they form larger FAs. The dynamic and force-dependent process of recruiting proteins, such as vinculin [51] to the focal adhesion sites is yet to be fully understood [52]. Not only could this process be cell type-dependent [11] but may also vary when studying the different types of surface topography and different culturing times. For instance, similar to the results of this study, the MC3T3-E1 cells have been shown to form larger FAs on surfaces with increased pillar interspacing [53]. In comparison, hMSCs form larger FAs as their spreading area increases [54] while neuronal stem cells exhibit an increased expression of FAs (increasing the adhesion) on grooves and pillars with smaller interspacing as compared to their more separated counterparts [55]. Nevertheless, the variations in the size of FAs in this study indicate different local traction forces that the cells exert on the pillars. It has been shown that although a correlation between the size of FAs and traction forces exists during the initial stages of adhesion, the same does not apply to mature adhesions [56]. In other words, mature

FAs can withstand extremely increased tensions (up to sixfold) without any changes in their size. As described above, the FAs of cells residing on the Porous samples are mature long-lasting ones while the FAs present on the surface of the Sparse specimens are rather nascent adhesions. Moreover, super-resolution imaging has shown that some of the studies that had concluded such correlations between the size of FAs and the generated force, had, in fact, considered multiple small adhesions as a large adhesion [57]. Further evaluations of the adhesion forces using novel AFM-based methods and computational analysis are necessary to improve our understanding of FA-mediated mechanical interactions of cells with such pillars [58].

The size and distribution of FAs also affect the nuclear morphology and remodeling as the nuclear dynamics are controlled by the tensions that are exerted at the adhesion points and propagate through the actin fibers to their nuclear cap [59, 60]. It has been argued that applying higher tensions to the cell nuclei via smaller FAs, which are unevenly distributed and, therefore, stretch the nuclei to some extent, enhances the osteogenic differentiation [60]. In our study, heterogeneous distribution of FAs in Partition and Sparse samples has changed the fully rounded morphology of cell nuclei in many cells toward a more elongated morphology (Figure 3f). The changes in the size and orientation of nuclei together with the forces exerted via FAs may explain the long-term osteogenic response of the cells on the different surfaces.

5.4.4. Early interactions of bacteria with bTi

Bactericidal properties are one of the core values of RIE-modified surfaces. The commonly accepted theories regarding the early stage interactions of the bacteria with such surfaces have been explained previously [28]. In the present study, no signs of pillar penetration were observed in the *S. aureus* bacteria interacting with the Porous specimens as all the pillars were connected to each other at their tips. Still, bacteria stretched their cell envelope to be able to find anchorage points on the surface (Figure 4b). While 25 ± 5% of the adhered bacteria were dead on the Porous specimens, the percentage of the dead bacteria reached its peak (42 ± 7%) for the Sparse group where a combination of the direct penetration of the pillars into the cell wall, the bending of the pillars, the stretching of the cell wall between adjacent pillars, and the sliding down between the pillars were observed (Figure 4b). The

killing efficiency of these bTi surfaces is expected to be even higher against Gram-negative bacteria such as *E. coli* and *P. aeruginosa* due to their thinner cell wall and rod-shaped morphology that increase their susceptibility to the sharp tips of the pillars [27, 31, 32]. Although the killing efficiency of the Sparse specimens against *S. aureus* is similar to Ti etched for 10 min in the study by Linklater *et al.* [39], higher killing efficiencies have been also reported for both bSi and bTi, in which the height and arrangement of the pillars are comparable to the Sparse group [34, 41]. It is noteworthy that the killing efficiency of a surface could vary against different strains of a species due to the differences present in the strain-dependent characteristics of the cells including their motility [61].

It has been shown that the number of dead *S. aureus* cells on bTi surfaces significantly increases over time (from ~20% after 4 hr to more than 75% after 24 hr) [34]. A similar conclusion can be made for our experiments. The metabolic activity of the bacterial cells attached to bTi surfaces is significantly lower than those attached to the flat Ti at any time point. However, comparing the metabolic activity of bacterial cells within the bTi groups, it increases up to 4 hr and then decreases therefrom. It might confirm that the first 4 hr is the window of opportunity within which bactericidal topographies can inhibit bacterial colonization on the surface. We cannot, however, attribute the decreased metabolic activity solely to the death of bacterial cells. Assuming that the different types of bTi surfaces in this study exert forces of different magnitudes to the bacterial cells, it would be expected that different signaling pathways may come into play and regulate the cell adhesion, motility, and metabolic activity [62-65]. Further studies are required to scrutinize the killing mechanisms of such surfaces by using a mechanistic approach.

Overall, comparing the response of the preosteoblast cells and bacteria to that of the bTi surfaces investigated in this study showed that the Partition surfaces with a pillar height of 700 nm-1000 nm and a partially-separated organization exhibits both bactericidal and osteogenic properties. Such a surface was capable of killing a significant percentage of the adherent bacteria while promoting the osteogenic response of cells. These observations suggest that achieving a specific design with balanced bactericidal and osteogenic properties is possible within the capabilities of ICP RIE. In summary, etching the titanium surfaces for 10 min with a combination of Cl_2 and Ar gasses (flow rates: 30 and 2.5 sccm, respectively), at

a high temperature (*i.e.*, 40 °C), and under a moderate chamber pressure (*i.e.*, 2.0 Pa) produces pillars with differential effects on the bacteria and mammalian cells.

Conclusions

In summary, we investigated the dual-functionality of a series of bTi surfaces as well as the possible mechanisms behind those functionalities. Superhydrophilic etched Ti surfaces containing pillars with distinct heights and spatial organization were produced by changing the pressure and temperature of the chamber during the ICP RIE process. Although all groups of the modified Ti surfaces studied here were cytocompatible for the MC3T3-E1 preosteoblast cells, they induced significantly different cell shapes, area, aspect ratio, nucleus area, cytoskeletal organization, and patterns of FA formation. When the pillars were very tall and separated (*i.e.,* Sparse surfaces), the cells possessed the least area possible and exhibited extremely elongated shapes. Moreover, the actin fibers were no longer well-oriented and the colocalization of FAs and actin fibers was lost. On the other hand, on the Porous and Partition surfaces, the cells were well-spread with polygonal shapes. Bacteria responded differently to these surfaces too. Sparse surfaces showed the highest killing efficiency against the bacteria. A combination of direct penetration of the pillars into the cell wall and cell wall stretching between adjacent pillars was observed in this group. Overall, the results of this study show that various ICP RIE conditions can be used to create Ti surfaces that are capable of instructing mammalian cells while killing bacteria. Based on our findings, the Partition surfaces establish a balance between osteogenic and bactericidal properties, which makes it a good candidate for further studies in vivo as a prerequisite for its final use in clinical settings.

Supporting information

(a)

(b)
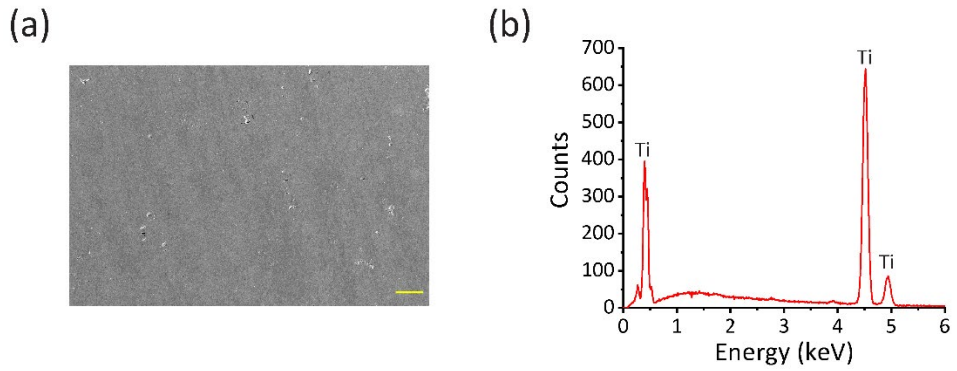
Figure S1. (a) SEM image of polished non-etched Ti surface (flat Ti). Scale bar = 20 μm. (b) Representative EDS spectrum of flat Ti.
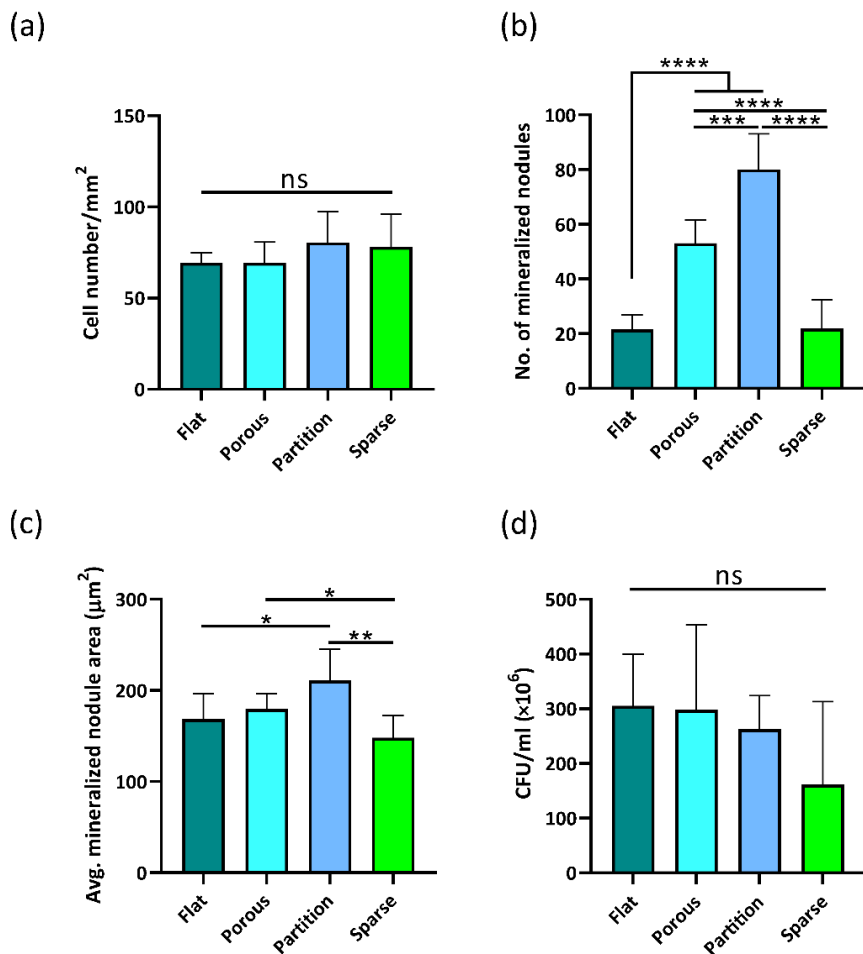
Figure S2. (a) The average number of attached preosteoblast cells per mm^2 of flat Ti and bTi surfaces. (b) The average number of mineralized nodules on different surfaces after 14 days of culture. (c) The average area of single mineralized nodules deposited in matrix on flat Ti and bTi surfaces. (d) The results of CFU counting of non-adherent bacterial cells.

References

[1] A. Falco, M. Berardini, P. Trisi, Correlation Between Implant Geometry, Implant Surface, Insertion Torque, and Primary Stability: In Vitro Biomechanical Analysis, INT J ORAL MAX IMPL 33(4) (2018) 824-830.

[2] I.C. Chou, S.Y. Lee, C.P. Jiang, Effects of implant neck design on primary stability and overload in a type IV mandibular bone, INT J NUMER METH BIO 30(11) (2014) 1223-1237.

[3] R. Hedayati, M. Sadighi, M. Mohammadi-Aghdam, A.A. Zadpoor, Mechanical behavior of additively manufactured porous biomaterials made from truncated cuboctahedron unit cells, Int. J. Mech. Sci. 106 (2016) 19-38.

[4] E. García-Gareta, M.J. Coathup, G.W. Blunn, Osteoinduction of bone grafting materials for bone repair and regeneration, Bone 81 (2015) 112-121.

[5] A. Barradas, H. Yuan, C.A. van Blitterswijk, P. Habibovic, Osteoinductive biomaterials: current knowledge of properties, experimental models and biological mechanisms, Eur. Cells Mater. 21 (2011) 407-429.

[6] A.L. Overmann, C. Aparicio, J.T. Richards, I. Mutreja, N.G. Fischer, S.M. Wade, B.K. Potter, T.A. Davis, J.E. Bechtold, J.A. Forsberg, Orthopaedic osseointegration: Implantology and future directions, J. Orthop. Res. 38(7) (2020) 1445-1454.

[7] C.R. Arciola, D. Campoccia, L. Montanaro, Implant infections: adhesion, biofilm formation and immune evasion, Nat. Rev. Microbiol. (2018) 397–409.

[8] A. Trampuz, A.F. Widmer, Infections associated with orthopedic implants, Curr. Opin. Infect. Dis. 19(4) (2006) 349-356.

[9] U. Filipović, R.G. Dahmane, S. Ghannouchi, A. Zore, K. Bohinc, Bacterial adhesion on orthopedic implants, Adv. Colloid Interface Sci. 283 (2020) 102228.

[10] L. Li, J. Eyckmans, C.S. Chen, Designer biomaterials for mechanobiology, Nat. Mater. 16(12) (2017) 1164–1168.

[11] K. Anselme, P. Davidson, A. Popa, M. Giazzon, M. Liley, L. Ploux, The interaction of cells and bacteria with surfaces structured at the nanometre scale, Acta Biomater. 6(10) (2010) 3824-3846.

[12] M.M. Stevens, J.H. George, Exploring and engineering the cell surface interface, Science 310(5751) (2005) 1135-1138.

[13] H. Amani, H. Arzaghi, M. Bayandori, A.S. Dezfuli, H. Pazoki-Toroudi, A. Shafiee, L. Moradi, Controlling cell behavior through the design of biomaterial surfaces: a focus on surface modification techniques, Adv. Mater. Interfaces 6(13) (2019) 1900572.

[14] D. Baptista, L. Teixeira, C. van Blitterswijk, S. Giselbrecht, R. Truckenmüller, Overlooked? Underestimated? Effects of substrate curvature on cell behavior, Trends Biotechnol. 37(8) (2019) 838-854.

[15] X. Zhao, L. Jin, H. Shi, W. Tong, D. Gorin, Y. Kotelevtsev, Z. Mao, Recent advances of designing dynamic surfaces to regulate cell adhesion, Colloid Interface Sci. Commun. 35 (2020) 100249.

[16] K. Metavarayuth, P. Sitasuwan, X. Zhao, Y. Lin, Q. Wang, Influence of surface topographical cues on the differentiation of mesenchymal stem cells in vitro, ACS Biomater. Sci. Eng. 2(2) (2016) 142-151.

[17] N. Logan, P. Brett, The control of mesenchymal stromal cell osteogenic differentiation through modified surfaces, Stem Cells Int. 2013 (2013).

[18] G. Abagnale, M. Steger, V.H. Nguyen, N. Hersch, A. Sechi, S. Joussen, B. Denecke, R. Merkel, B. Hoffmann, A. Dreser, Surface topography enhances differentiation of mesenchymal stem cells towards osteogenic and adipogenic lineages, Biomaterials 61 (2015) 316-326.

[19] M. Croes, S. Bakhshandeh, I. van Hengel, K. Lietaert, K. van Kessel, B. Pouran, B. van der Wal, H. Vogely, W. Van Hecke, A. Fluit, Antibacterial and immunogenic behavior of silver coatings on additively manufactured porous titanium, Acta Biomater. 81 (2018) 315-327.

[20] A. Panáček, L. Kvítek, M. Smékalová, R. Večeřová, M. Kolář, M. Röderová, F. Dyčka, M. Šebela, R. Prucek, O. Tomanec, Bacterial resistance to silver nanoparticles and how to overcome it, Nat. Nanotechnol. 13(1) (2018) 65-71.

[21] S.B. Levy, B. Marshall, Antibacterial resistance worldwide: causes, challenges and responses, Nat. Med. 10(12) (2004) S122-S129.

[22] H.S. Azevedo, I. Pashkuleva, Biomimetic supramolecular designs for the controlled release of growth factors in bone regeneration, Adv. Drug Delivery Rev. 94 (2015) 63-76.

[23] J. Hasan, H.K. Webb, V.K. Truong, S. Pogodin, V.A. Baulin, G.S. Watson, J.A. Watson, R.J. Crawford, E.P. Ivanova, Selective bactericidal activity of nanopatterned

superhydrophobic cicada Psaltoda claripennis wing surfaces, Appl. Microbiol. Biotechnol. 97(20) (2013) 9257-9262.

[24] K. Nowlin, A. Boseman, A. Covell, D. LaJeunesse, Adhesion-dependent rupturing of Saccharomyces cerevisiae on biological antimicrobial nanostructured surfaces, J. R. Soc., Interface 12(102) (2015) 20140999.

[25] G.S. Watson, D.W. Green, L. Schwarzkopf, X. Li, B.W. Cribb, S. Myhra, J.A. Watson, A gecko skin micro/nano structure–A low adhesion, superhydrophobic, anti-wetting, self-cleaning, biocompatible, antibacterial surface, Acta Biomater. 21 (2015) 109-122.

[26] J. Hasan, R.J. Crawford, E.P. Ivanova, Antibacterial surfaces: the quest for a new generation of biomaterials, Trends Biotechnol. 31(5) (2013) 295-304.

[27] K. Modaresifar, S. Azizian, M. Ganjian, L.E. Fratila-Apachitei, A.A. Zadpoor, Bactericidal effects of nanopatterns: A systematic review, Acta biomaterialia 83 (2019) 29-36.

[28] D.P. Linklater, V.A. Baulin, S. Juodkazis, R.J. Crawford, P. Stoodley, E.P. Ivanova, Mechano-bactericidal actions of nanostructured surfaces, Nat. Rev. Microbiol. 19 (2020) 8-22.

[29] M. Ganjian, L. Angeloni, M.J. Mirzaali, K. Modaresifar, C.W. Hagen, M.K. Ghatkesar, P.-L. Hagedoorn, L.E. Fratila-Apachitei, A.A. Zadpoor, Quantitative mechanics of 3D printed nanopillars interacting with bacterial cells, Nanoscale 12(43) (2020) 21988-22001.

[30] M. Ganjian, K. Modaresifar, H. Zhang, P.-L. Hagedoorn, L.E. Fratila-Apachitei, A.A. Zadpoor, Reactive ion etching for fabrication of biofunctional titanium nanostructures, Sci. Rep. 9(1) (2019) 1-20.

[31] E.P. Ivanova, J. Hasan, H.K. Webb, G. Gervinskas, S. Juodkazis, V.K. Truong, A.H. Wu, R.N. Lamb, V.A. Baulin, G.S. Watson, Bactericidal activity of black silicon, Nat. Commun. 4 (2013).

[32] M. Michalska, F. Gambacorta, R. Divan, I.S. Aranson, A. Sokolov, P. Noirot, P.D. Laible, Tuning antimicrobial properties of biomimetic nanopatterned surfaces, Nanoscale 10(14) (2018) 6639-6650.

[33] G. Hazell, P.W. May, P. Taylor, A.H. Nobbs, C. Welch, B. Su, Studies of black silicon and black diamond as materials for antibacterial surfaces, Biomater. Sci. 6(6) (2018) 1424-1432.

[34] J. Hasan, S. Jain, K. Chatterjee, Nanoscale topography on black titanium imparts multi-biofunctional properties for orthopedic applications, Scientific reports 7 (2017) 41118.

[35] M.E. Berginski, S.M. Gomez, The Focal Adhesion Analysis Server: a web tool for analyzing focal adhesion dynamics, F1000Research 2 (2013).

[36] U. Horzum, B. Ozdil, D. Pesen-Okvur, Step-by-step quantitative analysis of focal adhesions, MethodsX 1 (2014) 56-59.

[37] E.P. Ivanova, D.P. Linklater, M. Werner, V.A. Baulin, X. Xu, N. Vrancken, S. Rubanov, E. Hanssen, J. Wandiyanto, V.K. Truong, The multi-faceted mechano-bactericidal mechanism of nanostructured surfaces, Proc. Natl. Acad. Sci. U. S. A. 117(23) (2020) 12598-12605.

[38] L.D. Ghosh, J. Hasan, A. Jain, N.R. Sundaresan, K. Chatterjee, A nanopillar array on black titanium prepared by reactive ion etching augments cardiomyogenic commitment of stem cells, Nanoscale 11(43) (2019) 20766-20776.

[39] D.P. Linklater, S. Juodkazis, R. Crawford, E. Ivanova, Mechanical inactivation of Staphylococcus aureus and Pseudomonas aeruginosa by titanium substrata with hierarchical surface structures, Materialia 5 (2019) 100197.

[40] M. Sun, G.S. Watson, Y. Zheng, J.A. Watson, A. Liang, Wetting properties on nanostructured surfaces of cicada wings, J. Exp. Biol. 212(19) (2009) 3148-3155.

[41] J. Hasan, S. Raj, L. Yadav, K. Chatterjee, Engineering a nanostructured "super surface" with superhydrophobic and superkilling properties, RSC Adv. 5(56) (2015) 44953-44959.

[42] T.L. Clainche, D. Linklater, S. Wong, P. Le, S. Juodkazis, X.L. Guével, J.-L. Coll, E.P. Ivanova, V. Martel-Frachet, Mechano-Bactericidal Titanium Surfaces for Bone Tissue Engineering, ACS Appl. Mater. Interfaces 12 (2020) 48272-48283.

[43] Y. Zhukova, C. Hiepen, P. Knaus, M. Osterland, S. Prohaska, J.W. Dunlop, P. Fratzl, E.V. Skorb, The role of titanium surface nanostructuring on preosteoblast morphology, adhesion, and migration, Adv. Healthcare Mater. 6(15) (2017) 1601244.

[44] M. Ermis, E. Antmen, V. Hasirci, Micro and Nanofabrication methods to control cell-substrate interactions and cell behavior: A review from the tissue engineering perspective, Bioact. Mater. 3(3) (2018) 355-369.

[45] P.S. Mathieu, E.G. Loboa, Cytoskeletal and focal adhesion influences on mesenchymal stem cell shape, mechanical properties, and differentiation down osteogenic, adipogenic, and chondrogenic pathways, Tissue Eng., Part B 18(6) (2012) 436-444.

[46] D. Khang, J. Choi, Y.-M. Im, Y.-J. Kim, J.-H. Jang, S.S. Kang, T.-H. Nam, J. Song, J.-W. Park, Role of subnano-, nano-and submicron-surface features on osteoblast differentiation of bone marrow mesenchymal stem cells, Biomaterials 33(26) (2012) 5997-6007.

[47] A. Ray, O. Lee, Z. Win, R.M. Edwards, P.W. Alford, D.-H. Kim, P.P. Provenzano, Anisotropic forces from spatially constrained focal adhesions mediate contact guidance directed cell migration, Nat. Commun. 8(1) (2017) 1-17.

[48] M.D. Cabezas, B. Meckes, C.A. Mirkin, M. Mrksich, Subcellular Control over Focal Adhesion Anisotropy, Independent of Cell Morphology, Dictates Stem Cell Fate, ACS Nano 13(10) (2019) 11144-11152.

[49] J. Xia, Y. Yuan, H. Wu, Y. Huang, D.A. Weitz, Decoupling the effects of nanopore size and surface roughness on the attachment, spreading and differentiation of bone marrow-derived stem cells, Biomaterials 248 (2020) 120014.

[50] N.C. Gauthier, T.A. Masters, M.P. Sheetz, Mechanical feedback between membrane tension and dynamics, Trends Cell Biol. 22(10) (2012) 527-535.

[51] D.W. Dumbauld, T.T. Lee, A. Singh, J. Scrimgeour, C.A. Gersbach, E.A. Zamir, J. Fu, C.S. Chen, J.E. Curtis, S.W. Craig, How vinculin regulates force transmission, Proc. Natl. Acad. Sci. U. S. A. 110(24) (2013) 9788-9793.

[52] F. Martino, A.R. Perestrelo, V. Vinarský, S. Pagliari, G. Forte, Cellular mechanotransduction: from tension to function, Front. Physiol. 9 (2018) 824.

[53] B. Ghezzi, P. Lagonegro, N. Fukata, L. Parisi, D. Calestani, C. Galli, G. Salviati, G.M. Macaluso, F. Rossi, Sub-Micropillar Spacing Modulates the Spatial Arrangement of Mouse MC3T3-E1 Osteoblastic Cells, Nanomaterials 9(12) (2019) 1701.

[54] X. Wang, X. Hu, I. Dulińska-Molak, N. Kawazoe, Y. Yang, G. Chen, Discriminating the independent influence of cell adhesion and spreading area on stem cell fate determination using micropatterned surfaces, Sci. Rep. 6(1) (2016) 1-13.

[55] K. Yang, K. Jung, E. Ko, J. Kim, K.I. Park, J. Kim, S.-W. Cho, Nanotopographical manipulation of focal adhesion formation for enhanced differentiation of human neural stem cells, ACS Appl. Mater. Interfaces 5(21) (2013) 10529-10540.

[56] J. Stricker, Y. Aratyn-Schaus, P.W. Oakes, M.L. Gardel, Spatiotemporal constraints on the force-dependent growth of focal adhesions, Biophys. J. 100(12) (2011) 2883-2893.

[57] S. Di Cio, J.E. Gautrot, Cell sensing of physical properties at the nanoscale: Mechanisms and control of cell adhesion and phenotype, Acta Biomater. 30 (2016) 26-48.

[58] Y. Song, J. Soto, B. Chen, L. Yang, S. Li, Cell engineering: Biophysical regulation of the nucleus, Biomaterials 234 (2020) 119743.

[59] M. Versaevel, T. Grevesse, S. Gabriele, Spatial coordination between cell and nuclear shape within micropatterned endothelial cells, Nat. Commun. 3(1) (2012) 1-11.

[60] I. Casanellas, A. Lagunas, Y. Vida, E. Pérez-Inestrosa, J.A. Andrades, J. Becerra, J. Samitier, Matrix Nanopatterning Regulates Mesenchymal Differentiation through Focal Adhesion Size and Distribution According to Cell Fate, Biomimetics 4(2) (2019) 43.

[61] K. Jindai, K. Nakade, K. Masuda, T. Sagawa, H. Kojima, T. Shimizu, S. Shingubara, T. Ito, Adhesion and bactericidal properties of nanostructured surfaces dependent on bacterial motility, RSC Adv. 10(10) (2020) 5673-5680.

[62] L. Rizzello, B. Sorce, S. Sabella, G. Vecchio, A. Galeone, V. Brunetti, R. Cingolani, P.P. Pompa, Impact of nanoscale topography on genomics and proteomics of adherent bacteria, ACS Nano 5(3) (2011) 1865-1876.

[63] A. Persat, Bacterial mechanotransduction, Curr. Opin. Microbiol. 36 (2017) 1-6.

[64] C. Berne, C.K. Ellison, A. Ducret, Y.V. Brun, Bacterial adhesion at the single-cell level, Nat. Rev. Microbiol. 16(10) (2018) 616-627.

[65] Y.F. Dufrêne, A. Persat, Mechanomicrobiology: how bacteria sense and respond to forces, Nat. Rev. Microbiol. (2020) 1-14

6

Metal crumpling for the fabrication of nanopatterned meta-biomaterials

Abstract

We propose the controlled crumpling of nanopatterned, surface-porous flat metallic sheets as an efficient alternative to origami-inspired folding for the fabrication of volume-porous biomaterials. The resulting scaffolds should be capable of carrying the musculoskeletal loads and the surface nanopatterns should be preserved during the crumpling process. We designed and fabricated a simple setup for the controlled crumpling of meta-biomaterials. Before crumpling, laser cutting was used to introduce pores to the sheets. Mechanical testing of the crumpled specimens showed that they demonstrate substantial mechanical properties that are strongly dependent on the size of the pores present in the initial flat sheet but are independent from the level of compaction. The morphological features (e.g., trabecular spacing and thickness) of such meta-biomaterials can be tuned by regulating the level of compaction during the crumpling process. We then fabricated nanopatterned 3D titanium (Ti) scaffolds through inductively coupled plasma reactive ion etching of polished Ti sheets. Using the controlled crumpling setup, nanopatterned porous Ti sheets were crumpled at two deformation velocities (i.e., 2 and 100 mm/min). We measured the mechanical and geometrical properties of the scaffolds as a function of the surface-porosity and deformation velocity. Micro-computed tomography scans and computational simulations of crumpled scaffolds were performed to study the morphological characterization of the resulting meta-biomaterials. The pore size and porosity (mean ± SD %) of the scaffolds remained within the range of those reported for trabecular bone. We also fabricated two-layer scaffolds to improve the mechanical properties of the crumpled scaffolds. Finally, the in vitro cell culture (using MC3T3-E1 preosteoblasts) demonstrated the cytocompatibility of the nanopatterned scaffolds. Moreover, the aspect ratio of the cells residing on the bTi nanopatterned scaffolds was found to be significantly higher than those cultured on the control scaffolds. This suggests that the nanopatterned surface may have higher potential for inducing the osteogenic differentiation of the preosteoblasts.

6.1. Introduction

One of the main challenges in orthopedic surgery is finding a remedy for segmental bone defects, as the current clinical solutions are associated with major limitations [1, 2]. Therefore, the quest for ideal bone substitutes that mimic the various properties of the bone is ongoing. Affording synthetic bone substitutes with functionalities that allow them to

regulate cell behavior (*e.g.*, cell adhesion, proliferation, and osteogenic differentiation) could greatly increase their chance of successful osseointegration. For example, it is well known that the cell behavior is affected by the physical [3, 4], mechanical [5, 6], and geometrical [7] properties of their environment. For instance, cell proliferation, migration, and differentiation can be influenced by the physical cues of the substrate, including stiffness [8, 9], viscoelasticity [10], and submicron/nano topographies [3, 4, 11] of the substrate they reside on. Moreover, it is now established that the geometrical properties of the substrate at a larger scale can also regulate the behaviour of stem cell [7].

The introduction of nanotopographies to the surface of bone substitutes is particularly appealing, because well-designed surface ornaments may be able to (simultaneously) kill bacteria [4, 11-14], induce osteogenesis [3, 15], and modulate the immune response [16]. Nowadays, most 3D lattice structures are manufactured using additive manufacturing (AM, =3D printed) techniques. Given the fact that most of the micro/nano-patterning techniques are planar in nature, they cannot be easily applied to porous meta-biomaterials whose surface areas are primarily internal and non-planar (*i.e.*, 3D) [4]. Several techniques have been, therefore, proposed to start from an initially flat sheet, decorate the surface with nanopatterns, and transform the flat construct to a 3D object through crumpling [17, 18], origami [19], or kirigami [20]. As opposed to origami and kirigami that tend to create regular, precise geometries, crumpling introduces random geometric configurations and creases, leading to 3D structures that are less sensitive to geometric and topological imperfections [18].

The morphologies of mammalian brain cortex [21, 22], DNA packaging in viral capsids [23, 24], flower leaves in buds [25], the wing folding of insects in cocoons [26], and the confinement of chromatin in the nucleus of a cell [27, 28] are all examples of naturally occurring crumpled objects. In addition to replicating such structures, crumpling provides an opportunity to create unusual combinations of material specifications that can be hardly found in nature [17, 18, 29].

Well-designed flat thin sheets crumpled under controlled conditions may be used to create crumpling-based metamaterials [18]. To date, many different techniques have been employed to crumple thin sheets, including hand crumpling [17], distributing a net of wires around loosely crumpled thin sheet [18, 29], leaving the loosely crumpled specimen at

ambient pressure [30], and using a cylindrical die [31-34]. While hand crumpling is considered the easiest and the most commonly used method, it suffers from irreproducibility and uncontrollability. Moreover, measuring the applied force is not feasible in this method [17]. Crumpling using a die is a controlled technique that enables the measurement of the applied force and the level of compaction [17]. It is, therefore, a promising candidate to fabricate meta-biomaterials. Here, we present a novel class of meta-biomaterials that combine controlled crumpling with surface nanopatterns and laser-cut surface porosities. We used a cylindrical die to crumple laser-cut porous Ti sheets that were first nanopatterned with inductively coupled plasma reactive ion etching (ICP RIE) to create black titanium (bTi) [12]. To protect the nanopatterns during the crumpling process, the sheets were coated with a thin layer of polyvinyl alcohol (PVA). The mechanical properties of the crumpled structures were measured using mechanical testing, while their morphological properties were determined using micro-computed tomography (μCT). Moreover, the finite element method (FEM) was used to simulate the crumpling process. Furthermore, we investigated the cytocompatibility of the nanopatterned specimens using in vitro cell culture assays (*i.e.,* live/dead and metabolic activity) and scanning electron microscopy (SEM), respectively.

6.2. Materials and Methods

6.2.1. Sample preparation

Annealed Ti sheets with a thickness of 125 μm were used for this study (99.96% purity, Goodfellow, Huntingdon, UK). The sheets were cut to the size of a 4-inch (diameter = 10.16 cm) silicon wafer and were polished by chemical mechanical polishing (CMP Mecapol E460, Saint-Martin-le-Vinoux, France). Following this step, the 4-inch titanium sheets were cut into 22.5×22.5 mm^2 pieces using a laser micromachine (Optec Laser Systems, Belgium).

6.2.2. Fabrication and characterization of bTi samples

The black Ti nanopatterns were fabricated on the polished Ti specimens using an ICP RIE machine (PlasmaLab System 100, Oxford Instruments, UK). The Ti specimens were glued with a thermal joint compound (type 120, Wakefield Engineering, USA) to a 4-inch fused silica carrier wafer. Cl_2 and Ar were the etching gasses. The etching process was performed under the following condition: ICP power = 600 W, RF power = 100 W, Cl_2 flow

rate = 30 sccm, Ar flow rate = 2.5 sccm, chamber pressure = 0.02 mbar, temperature = 40 °C, and etching time = 10 min. Following the etching process, the specimens were cleaned in acetone, ethanol, and isopropyl alcohol (IPA) (consecutive steps of 30 min each), and were then spin-dried. High-resolution scanning electron microscopy (SEM) images were taken with a Helios (FEI Helios G4 CX dual-beam workstation, Hillsborough, OR, USA) microscope at 10 kV and 43 pA.

6.2.3. Design and manufacturing of the surface-porous flat sheets

The size of the 2D flat sheet (22.5×22.5 mm^2), the number of the pores per specimen (12×12), and the center-to-center interspacing (1.875 mm) of the pores were kept constant while the diameter of the pores was varied (1.46 mm, 1.53 mm, and 1.59 mm) using CAD software (Solidworks 2019, Dassault Systèmes). The designs of the flat specimens with three different surface porosities (*i.e.,* 48.0%, 52.5%, and 57.2%) were exported to the laser micromachining in the STL format. In total, 18 specimens were laser cut from non-polished Ti sheets (for mechanical testing) while three specimens were laser cut from the polished Ti sheets (for nanopatterning and cell culture). The laser parameters were as follow: frequency = 50 kHz, diode current = 4 A, laser firing rate = 30 kHz, and the number of repetitions = 40. Consequently, the samples were cleaned in acetone, ethanol, and IPA (consecutive steps of 30 min each), and were spin-dried.

6.2.4. Mechanical experiments

6.2.4.1. Design of the crumpling setup

To crumple the surface-porous Ti sheets, a cylindrical die was fabricated with a fused deposition modeling (FDM) 3D printer (Ultimaker 2+, Ultimaker, The Netherlands), polylactic acid (PLA) filaments, and a 0.25 mm nozzle. Prior to crumpling, the Ti sheets were pre-rolled into a cylindrical shape around a stainless-steel bar (d = 7.2 mm) (Figure 1a).

6.2.4.2. Compression tests

The crumpling process (Figure 1a) was carried out using a universal mechanical testing bench (Plus/Lloyd Instruments Ltd, England) equipped with a 5 kN load cell. Before compressing the pre-rolled sheets, the specimens were coated two times with PVA (Resin Technology, France), each step followed by thermal treatment at 50 °C for 1 hr. The

125

specimens were then placed inside the die and were compressed using the same stainless-steel bar, which was attached to the universal test bench. Two different compression velocities of 2 mm/min and 100 mm/min were applied to study the effects of deformation velocity.

Single-layer specimens

The single-layer specimens were compressed with a compression velocity of 2 mm/min (three unpolished specimens for each group of surface porosity) and at a compression velocity of 100 mm/min (three unpolished specimens for each group of surface porosity). The tests were continued until a cross-head displacement of 17 mm was reached (initial length = 22.5 mm). In the case of the cell culture specimens, three polished specimens and three nanopatterned specimens, with a surface porosity of 57.2% were crumpled at a velocity of 2 mm/min.

Double-layer specimens

The double-layer scaffolds were also created by placing two specimens with the same porosity (*i.e.,* 57.2%) on top of each other, rolling them, and placing them into the PLA die. The two-layer specimens were then compressed with a velocity of 2 mm/min. To prevent the scaffolds from being damaged, the test was continued until a cross-head displacement of 15 mm was reached.
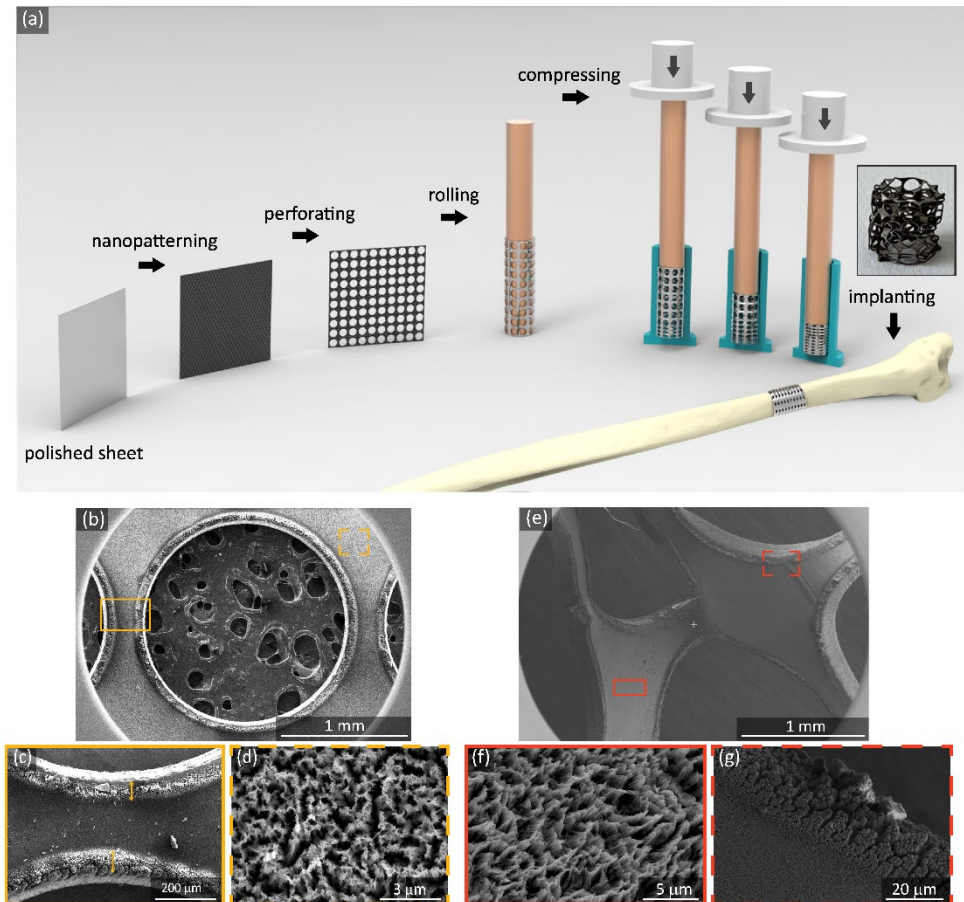
Figure 1. (a) A schematic illustration of the steps involved in the crumpling of nanopatterned porous Ti sheets. (b) A low-magnification (= ×74) SEM image of a laser-cut pore on the surface of a Ti sheet. (c) A low-magnification (= ×300) SEM image of the nanopatterned Ti sheets shows that the laser beam affects the nanopatterns within a 60-120 μm radius. (d) A high-magnification (= ×20000) SEM image of the bTi nanopatterns far away from the laser beam. Nanopatterns with a distance that was > 120 μm had a normal morphology and remained intact. (e) A low-magnification (= ×80) SEM image of the crumpled scaffold. (f) A high-magnification (mag = ×10000) SEM image of the bTi nanopatterns on the Ti sheet after crumpling process. (g) A high-magnification (= ×1000) SEM image of the undesired artifacts created during the laser cutting process after crumpling.

6.2.5. FEM model

Finite element (FE) simulations were performed using Abaqus (Abaqus 2017, Simulia, US). A dynamic explicit nonlinear solver was used to simulate the crumpling of the cylindrical specimens. The total mass of the model was artificially increased to reduce the computational time. Additionally, a uniform mass scaling factor of 10^6 was used, which limits the kinetic energy to <1% of the internal energy while reducing the computational time by three orders of magnitude. Both the punch and the die were modeled as rigid surfaces and the specimens were discretized using 4-node fully integrated shell elements (*i.e.,* S4). An elastoplastic material model (von Mises yield function, tabular input of strain hardening data) was used to model the mechanical behavior of Ti. The material model was fitted to the experimental data obtained from the literature [35]. A surface-to-surface contact definition was implemented using a penalty contact enforcement algorithm to capture the contact behavior between the die and specimen as well as the self-contact of the specimen. A friction coefficient of 0.30 was used. The samples were compressed up to 17 mm by adding a displacement boundary condition to the punch.

6.2.6. Morphological characterization

The single-layer crumpled specimens were imaged using a μ-CT scanner (Phoenix Nanotom, GE Sensing Inspection Technologies GmbH, Germany). The acquisition parameters were: tube current = 230 μA, tube voltage = 100 kV, and resolution = 4.5 μm × 4.5 μm × 4.5 μm. The acquired data were then reconstructed and saved as DICOM images. The reconstructed data were down-sampled by using a custom-made script in MATLAB (Matlab R2019a). The voxel sizes of the down-sampled scans were: 9 μm × 9 μm × 9 μm. Each down-sampled scan was divided into eight regions of interest (ROIs) through the length of the scanned scaffold and was imported into the Dragonfly software (Object Research Systems, Canada). For each ROI, the compressed sheet was segmented using a thresholding technique, and an additional segmentation mask was created based on the smallest cylinder that could cover the entire compressed sheet. The segmented sheet and the cylindrical mask were used in the Bone Analysis plugin of Dragonfly to determine the porosity (%), trabecular thickness (Tb.Th, μm), and pore size (Tb.Sp, μm) of the compressed specimens.

The morphological parameters determined based on the μCT scans were compared to those obtained using FE analyses. Prior to comparison, the deformed specimens were exported from Abaqus to 3-Matic (3-Matic 15.0; Materialise, Leuven, Belgium) in the STL format and were converted into volumes after assigning the compressed specimens a uniform thickness of 125 μm and wrapping them (smallest detail: 0.02, protect thin walls and preserve surface structure options are on). The volumes were then divided into 8 ROIs and were post-processed using Dragonfly as described above.

6.2.7. Sample preparation for cell culture

To prepare the 3D nanopatterned Ti samples for cell culture and to access the inner layer (covered with nanopatterns), we un-crumpled the specimens by hand. To remove the PVA coating, the specimens were placed in acetone and water (40 °C) (each for two hrs). The specimens were then sterilized in an autoclave at 121 °C for 20 min.

6.2.8. Cell response to the surface

6.2.8.1. Cell seeding and culture

MC3T3-E1 preosteoblast cells (Sigma-Aldrich, Germany) were seeded on the control (polished Ti, $n = 5$) and nanopatterned un-crumpled specimens ($n = 5$) in a 24 well-plate with a density of 125000 cells/well. The specimens were incubated in the alpha minimal essential medium (α-MEM) supplemented with 10% (v/v) fetal bovine serum (FBS) and 1% (v/v) penicillin-streptomycin (all from Thermo Fisher Scientific, US) for 3 or 7 days (37 °C, 5% CO_2). The culture medium was refreshed every 2-3 days, starting from day 2 of the experiment.

6.2.8.2. Metabolic activity

The metabolic activity of the MC3T3-E1 cells was determined using the PrestoBlue assay (Thermo Fisher Scientific, US) on days 3 and 7. The specimens were transferred into a new 24 well-plate and were incubated in 450 μl of fresh culture medium with 50 μl of PrestoBlue cell viability reagent for one hr at 37 °C. After incubation, 100 μl of the supernatant from each well was transferred to a 96 well plate in duplicate and the fluorescence was measured at an excitation wavelength of 530 nm and an emission wavelength of 595 nm with a Victor X3 microplate reader (PerkinElmer, The Netherlands).

6.2.8.3. Cell viability and SEM imaging

A live/dead cell staining assay (Thermo Fisher Scientific, US) was performed to investigate the viability of the cultured cells after 7 days. The samples were washed 3 times with 10X PBS and were incubated in PBS containing 2 µM Calcein AM and 3 µM Ethidium homodimer-1 for 30 min at room temperature. After staining, the cells were washed with PBS and were imaged with a fluorescent microscope (ZOE cell imager, Bio-Rad, The Netherlands). Consequently, the stained specimens were fixed with 4% paraformaldehyde (Sigma Aldrich, Germany) for 15 min and were rinsed 2 times with distilled water for 5 min. The samples were then dehydrated in a series of graded ethanol/water solutions (Sigma-Aldrich, Germany) as follows: 15 min in 50%, 20 min in 70%, and 20 min in 96%. The specimens were dried overnight and were gold-sputtered prior to SEM imaging.

6.2.8.4. Image analysis

ImageJ 1.53c (NIH, US) was used to quantify the data from the SEM images. Thereafter, the Analyze Particles command was used to measure the cell aspect ratio by fitting ellipses to the cell body area. Furthermore, the values of the cell area and perimeter were used to calculate the cell shape index as described elsewhere [36].

6.2.9. Statistical analysis

For all of the above-mentioned experiments, the raw data was first tested for normal distribution using the D'Agostino-Pearson omnibus normality test in Prism version 9.1.2 (GraphPad, US). The two-way ANOVA test was performed followed by the Sidak's multiple comparisons test to determine statistical significance of the differences between the means of different groups. A p-value below 0.05 was considered to indicate statistical significance.

6.3. Results

6.3.1. Laser cutting

The STL files describing the geometry of the flat specimens were imported into the laser machine and were used to cut through the 4-inch titanium foil (Figure 1b). The damage inflicted to the sheet by the cutting process was limited to a radius of ~120 µm away from the laser beam (Figure 1c).

6.3.2. Fabrication and characterization of the bTi nanopatterns

The desired nanopatterns that are characteristic of bTi were formed on the surface of the Ti sheets (Figure 1d). After crumpling and the removal of the PVA layer, the bTi nanopatterns were analyzed using SEM (Figure 1e-g). The nanopatterns (Figure 1f) and the micro-features formed on the surface during the laser cutting process (Figure 1g) were fully preserved and remained intact during the crumpling process.

6.3.3. Compression tests

The force-deflection curves were typical for porous biomaterials [37, 38] including such characteristic features as an initially linear increase in deflection with force, a relatively long plateau region with fluctuations, followed by a compaction region where stress rapidly increased (Figure 2a). The peaks and valleys in the force-deflection curves (Figure 2a) were caused by the formation of shear lines (Figure 2c, d) and the build-up of the stress after the load was transferred to neighboring layers.

Regardless of the deformation velocity, the specimens with the lowest surface porosity (*i.e.,* 48%) required relatively higher compression forces to reach the same deformation (Figure 2a) than the specimens with the surface porosities of 52.5% and 57.2%. Even though a higher rate of deformation (*i.e.,* 100 mm/min) did not increase the force needed to reach the same level of compaction, it decreased the standard deviation of the applied force (Figure 2a).

In the case of a lower deformation velocity and for the specimens with a surface porosity of 57.2%, two layers of Ti sheets enhanced the mechanical properties of the crumpled structure and up to 112% higher forces were required to compress them as compared to the single-layer specimens (Figure 2b).

The force-displacement curves corresponding to all the crumpled specimens suggest that the strengths of the crumpled structures remain almost constant as the level of compaction increases. At the same time, their strength is determined according to the geometrical design of the flat material (Figure 2a, b).
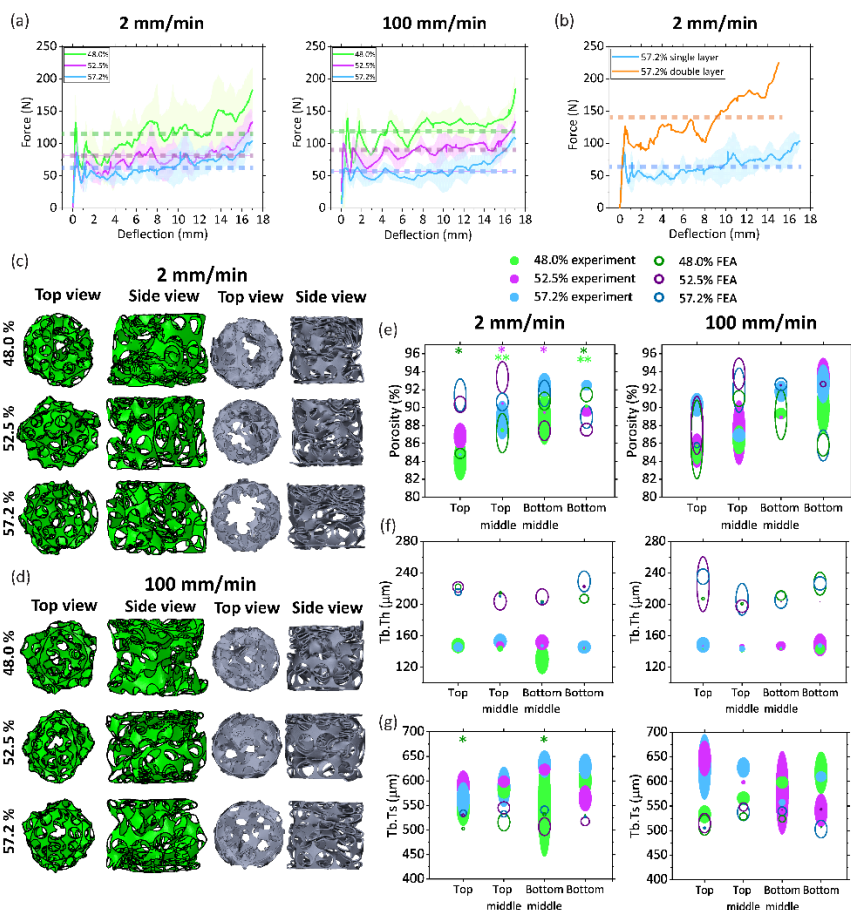
Figure2. (a) The force-deflection curves recorded during the crumpling process for the Ti sheets with three levels of surface porosity (*i.e.,* 48.0%, 52.5%, and 57.2%) and crumpled using two different deformation velocities of 2 mm/min and 100 mm/min. The straight lines represent the results of the experiments while the hatched area represents the standard deviation of three different specimens. The dashed lines represent the mean strength of the crumpled scaffolds as a function of the pore size. (b) The force-deflection curves of the single- and double-layer porous Ti sheets (surface porosity = 57.2%), crumpled using a deformation velocity of 2 mm/min. The top and side views of the crumpled specimens resulting from the FEA simulations and μCT imaging for the deformation velocities of (c) 2 mm/min and (d) 100 mm/min. The distribution of the (e) porosity, (f) trabecular thickness, and (g) pore size for the specimens with different surface porosities that were crumpled using different deformation velocities. The greater oval diameter indicates the standard deviation of the corresponding values (* *p* < 0.05 and ** *p* < 0.01).

6.3.4. FEA and μCT

The top and side views of the 3D scanned and simulated samples confirmed that changing the deformation velocity from 2 mm/min to 100 mm/min did not alter the general morphology of the final scaffolds (Figure 2c, d). Given the fact that the specimens were rolled around a cylindrical bar and were confined in a die (Figure 1a), the final morphology of the μCT-imaged specimens was more cylindrical.

Crumpling the Ti sheets with the surface porosities of 48.0%, 52.5%, and 57.2% with a deformation velocity of 2 mm/min resulted in the volume porosities of 87.6 ± 2.8%, 89.1 ± 1.6%, and 89.7 ± 3.5% for the crumpled scaffolds, respectively (Table 1). By increasing the deformation velocity to 100 mm/min, the volume porosities changed to 87.6 ± 2.8%, 88.7 ± 3.8%, and 90.4 ± 2.9%, respectively (Table 1). The results of the FEA simulations were in line with those of the experiments (Table 1), indicating that while increasing the surface porosity of the sheets slightly increased the volume porosity of the crumpled scaffolds, the changes in the volume-porosity were relatively small.

The porosity, trabecular thickness, and pore size values were uniformly distributed throughout the scaffolds (Figure 2e-g) except for the specimens with surface porosities of 48.0% and 52.5% and crumpled with a deformation velocity of 2 mm/min for which there was a significant difference between the porosity values of two different segments along the length of the scaffolds (Figure 2e).

Although the trabecular thickness values were uniformly distributed along the length of the scaffold and there was no significant difference between the different segments, the values resulting from the FEA simulations were relatively higher than those obtained experimentally (Figure 2f).

Table 1. Morphological characteristic of the different types of porous scaffolds.

Deformation velocity (mm/min)	Surface porosity (%)	Volume porosity φ (%)				Sheet thickness (Tb.Th) (μm)				Pore size (Tb.Sp) (μm)			
	Flat specimen	**3D scaffold**											
		μCT	SD	FEA model	SD	μCT	SD	FEA model	SD	μCT	SD	FEA model	SD
2	48.0	87.6	2.8	88.6	0.7	144.8	4.4	211.7	3.1	581.3	34.6	520.4	3.1
	52.5	89.1	1.6	89.7	0.5	146.3	5.7	214.5	2.8	594.1	26.7	525.0	2.8
	57.2	89.7	3.5	90.7	0.3	147.9	5.8	214.4	1.5	603.5	38.8	534.0	1.2
100	48.0	87.6	2.8	88.1	1.6	142.8	2.5	211.5	3.0	578.6	38.4	517.9	2.4
	52.5	88.7	3.8	89.7	1.5	147.1	5.7	207.6	2.7	590.7	53.4	537.3	2.5
	57.2	90.4	2.9	90.0	1.0	145.6	4.5	218.6	3.7	606.1	39.9	521.4	3.7

Tb.Th. trabecular thickness, Tb. Sp., trabecular spacing (*i.e.,* pore size)

In the FEA simulations, there was a significant difference between the pore size values calculated for two different segments of the specimens with a surface porosity of 48.0% that were crumpled at 2 mm/min. For the other specimens, there was no significant difference between the pore size values corresponding to the different segments along the length of the crumpled specimens (Figure 2g).

6.3.5. Cytocompatibility of un-crumpled scaffolds

At day 7, the vast majority of the cells were found to be viable on both polished and nanopatterned un-crumpled specimens (Figure 3a). Moreover, the cells were uniformly distributed on both types of the specimens (Figure 3a, b) and had a normal morphology (Figure 3c). Furthermore, there was no indication that the artifacts created during the cutting procedure had affected cell viability (Figure 3a, d).

6.3.6. Metabolic activity and morphological characteristics of cells

The metabolic activity of the cells seeded on the polished scaffolds was significantly higher than those cultured on the nanopatterned surfaces on both days 3 and 7. For each experimental group analyzed separately, the metabolic activity of the cells significantly increased with time (Figure 3e). The cells residing on the nanopatterned scaffolds were more rounded as compared to the cells cultured on the polished scaffolds after 3 days of culture (Figure 3f). After 7 days, however, the cell shape index on the nanopatterned scaffolds significantly decreased (Figure 3f). Similarly, while the cell aspect ratio was not significantly different between the surfaces after 3 days, the cells were more elongated after 7 days on the nanopatterned scaffolds. In addition, a significant change in the cell aspect ratio between 3 and 7 days was only observed on the nanopatterned scaffolds (Figure 3g).

6.4. Discussion

In this study, for the first time, an efficient crumpling technique was proposed to fabricate porous 3D metallic scaffolds from initially flat nanopatterned sheets. Crumpling is an interesting alternative to origami and kirigami approaches as it greatly simplifies the process of going from a flat construct to a 3D porous structure. Given the stochastic nature of the crease patterns and folding sequences, the resulting structure is highly resistant to minor imperfections, while highly regular origami/kirigami lattices are very sensitive to the slightest deviations from the perfect geometry. Moreover, controlled crumpling offers a high degree of tunability in terms of the mechanical properties and morphological features. For example, the porosity and pore size of the final 3D scaffold can be tuned by adjusting the geometrical features of surface porous sheet and the level of compaction during the crumpling process. The mechanical properties of the crumpled specimens can be increased by increasing the thickness of the sheet or by using multiple sheets stacked on top of each other.
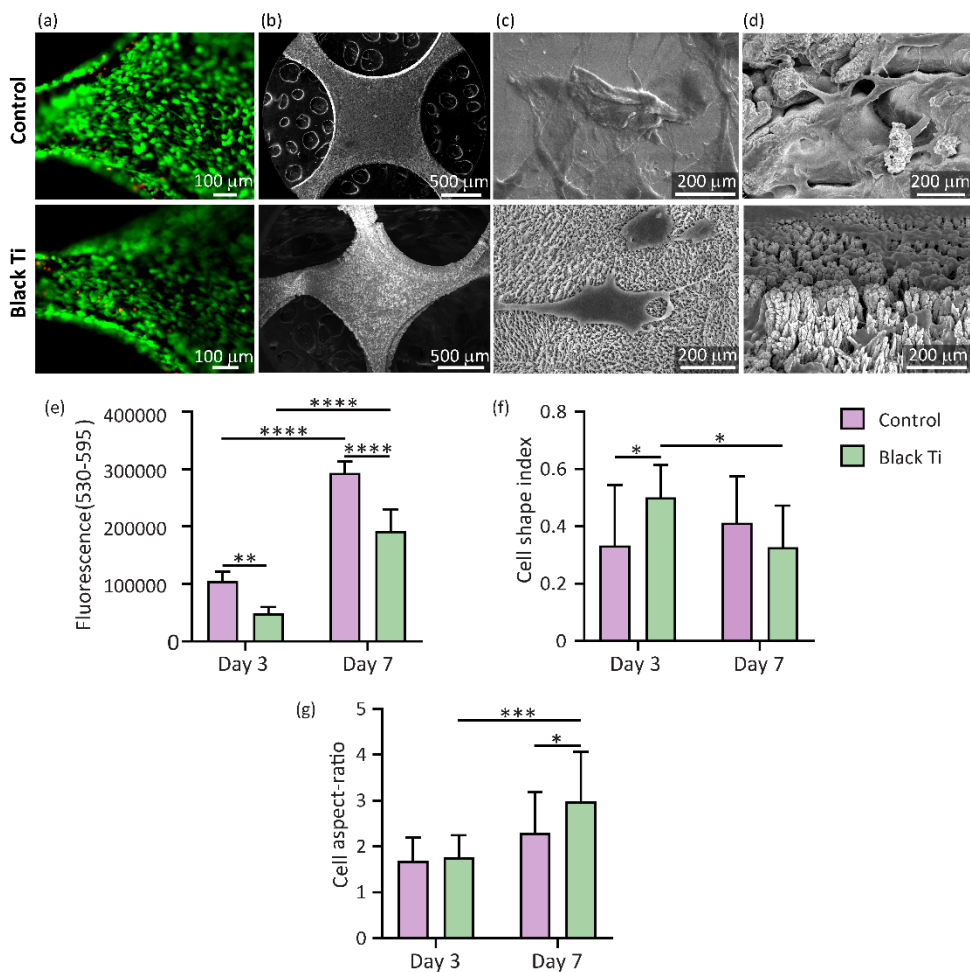
Figure 3. (a) Live/dead staining and (b) SEM imaging of the MC3T3-E1 cells after 7 days of culture on the surface of the control and nanopatterned un-crumpled specimens. High magnification SEM images (day 7) of the MC3T3-E1 cells residing on the surface of (c) the control and nanopatterned un-crumpled specimens and (d) on the laser cutting artifacts. (e) The metabolic activity (day 7) of the preosteoblast cells cultured on the control and nanopatterned un-crumpled specimens measured through the PrestoBlue assay. (f) The cell shape index and g) the cell aspect ratio of the of MC3T3-E1 preosteoblast cells on the surface of the control and nanopatterned un-crumpled specimens after 3 and 7 days of culture ($*$ $p < 0.05$ and $**$ $p < 0.01$, $***$ $p < 0.001$, $****$ $p < 0.001$).

Within the context of meta-biomaterials, nano/micro-patterned 3D structures that guide stem cells along the desired pathway of differentiation are essential [39, 40]. The 3D

geometry of the biomaterials used in bone tissue engineering, including their porosity and pore size, are crucial factors determining the biological response of these materials elicit upon implantation [41]. A proper choice of the porosity, pore size, pore shape, and pore distribution facilitates cell oxygenation, migration, spreading, settlement, and feeding (*i.e.,* transportation of metabolites and nutrients) [18, 41-44]. The same morphological parameters also affect the mechanical properties of the scaffold [44]. Even though highly porous scaffolds increase the potential for bone ingrowth, they generally offer limited mechanical performance [41]. The porosity of bone tissue engineering scaffolds should, therefore, be chosen such that the conflicting biological and mechanical requirements are simultaneously satisfied. The native bony tissue has different porosity values depending on its type (*i.e.,* cortical or trabecular). For instance, cortical bone (compact bone) has a relatively dense structure (porosity = 5-25%) with longitudinally cylindrical elements, while trabecular (spongy) bone has a highly porous structure (porosity = 40-95%) with a network of trabeculae [41, 45]. However, native bone is highly vascularized, meaning that higher porosities are likely to be needed at the beginning of the tissue regeneration process where mass transport should occur through diffusion. Porosities > 60% are suggested to be suitable for bone scaffolds [45]. All the experimental groups in this study had the volume porosities that were within this suggested range.

As for the pore size, the suggested range is 300–900 μm [45]. Similar to the porosity, all the six experimental groups considered here satisfied this requirement as well (Table 1). According to the results of μCT imaging and FEA simulations, increasing the deformation velocity did not influence the morphology, volume porosity, trabecular thickness, and pore size of the final scaffold, which means that a higher deformation velocity (*i.e.,* 100 mm/min) can be applied to speed up the process and enhance the throughput. In the simulations, the surface-porous sheets were rolled with the same diameter as that of the bar. However, they were not confined in a cylindrical die. This can explain the differences observed between the final morphology of the scaffolds resulted from the simulations and experiments (Figure 2c, d). Moreover, at the higher deformation velocity, less deviations from the average values of the morphological properties were observed (Figure 2e-g), suggesting that a higher rate of deformation leads to a more uniform crumpled structure.

The differences between the trabecular thickness of the μCT scanned samples and those obtained computationally (Figure 2f) can be explained by the process used for converting the simulation results from a geometry based on shell elements to a geometry based on solid elements. Although a uniform thickness of 125 μm was assigned to the shell-based structure, the thickness slightly (*i.e.*, by approximately +14 μm) increased after applying the wrapping operation that was used to protect thin walls from collapsing.

Using multiple stacked sheets for crumpling results in a higher degree of structural integrity and higher values of the scaffold stiffness. Moreover, the forces required for reaching the same level of crumpling increase when multiple stacked sheets are used (Figure 2b). A different choice of material and a thicker layer of the Ti sheets could also increase the mechanical properties of the scaffold. However, thicker metal sheets are less bendable [46].

It has been demonstrated that nanotopographical features on the surface of biomaterials can significantly influence the cell behavior [3]. One of the major challenges associated with controlled crumpling is to protect the nanopatterns from being damaged during the crumpling process. The PVA layer coated on the surface of nanopatterned scaffolds was successful in fully protecting the applied nanopatterns. The live/dead and cell metabolic activity assays showed that the preosteoblasts can survive and proliferate after adhesion to the un-crumpled scaffolds and that the presence of nanopatterns does not affect the cytocompatibility of the scaffolds. Similar bTi nanopatterns formed on the surface of a flat Ti sheet have been previously shown to enhance cell proliferation [4]. The laser-cutting artifacts and the ridges created during the crumpling process did not adversely affect the cell response. Previous studies have been shown that bTi nanopatterns applied to flat Ti sheet are capable of killing bacteria via mechanical interactions [4, 12] and of increasing matrix mineralization [4] by preosteoblasts. Furthermore, an elongated cell morphology is considered beneficial for osteogenic commitment [4, 47-50]. After 7 days, we observed a significant increase in the elongation of the cells residing on the nanopatterned scaffolds (Figure 3g). The measured values of the cell shape index and aspect ratio indicate that the cells attached to the nanopatterned scaffolds have a greater tendency to transform from an initial rounded shape to an elongated and polarized morphology as compared to the cells attached to the polished specimens (Figure 3f, g). It is worth mentioning that we only functionalized one side of the scaffolds, the nanopatterning process may deliver more impact when the surface

functionalization is applied to both sides of the sheet. Based on the results reported here, controlled crumpling is a novel candidate for the fabrication of 3D porous bone scaffolds decorated with surface nanopatterns. Further studies, therefore, are required to more thoroughly clarify the potential of these porous meta-biomaterials.

Conclusion

To address the limitations of the existing techniques for the production of nanopatterned meta-biomaterials, a promising crumpling method was developed that allows for the fabrication of 3D metallic scaffolds with the desired size, volume porosity, and mechanical properties from nanopatterned surface-porous sheets. Since the crumpling process starts from a 2D flat sheet, enables us to incorporate nanopatterns with desired shapes onto the substrate. The nanopatterns were protected and remained intact during the crumpling process. Three different surface porosities led to three different volume porosities, meaning that the final porosity can be controlled through the rational design of the flat construct. According to the μCT and FEA results, the deformation velocity did not significantly influence the morphological and mechanical properties of the final scaffolds. We also designed a double-layer structure to enhance the mechanical properties of the crumpled scaffold. Finally, the response of the MC3T3-E1 preosteoblast cells to the nanopatterned scaffolds was generally indicative of high degrees of cytocompatibility and potentially also an osteogenic behavior. The presented controlled crumpling approach, therefore, constitutes a promising route for the realization of nanopatterned meta-biomaterials with tunable dimensions, porosities, and mechanical properties. The combination of volume porosity and bTi nanotopographies with dual functionalities could be used to improve bone tissue engineering. Future studies should further evaluate the *in vitro* and *in vivo* performance of these meta-biomaterials, paving the way for their ultimate clinical adoption.

References

[1] Y. Li, P. Pavanram, J. Zhou, K. Lietaert, F. Bobbert, Y. Kubo, M. Leeflang, H. Jahr, A.A.. Zadpoor, Additively manufactured functionally graded biodegradable porous zinc, 8(9) (2020) 2404-2419.

[2] Y. Li, J. Zhou, P. Pavanram, M. Leeflang, L. Fockaert, B. Pouran, N. Tümer, K.-U. Schröder, J. Mol, H. Weinans, Additively manufactured biodegradable porous magnesium, 67 (2018) 378-392.

[3] S. Dobbenga, L.E. Fratila-Apachitei, A.A. Zadpoor, Nanopattern-induced osteogenic differentiation of stem cells A systematic review, Acta Biomater 46 (2016) 3-14.

[4] K. Modaresifar, M. Ganjian, L. Angeloni, M. Minneboo, M.K. Ghatkesar, P.-L. Hagedoorn, L.E. Fratila-Apachitei, A.A. Zadpoor, On the Use of Black Ti as a Bone Substituting Biomaterial: Behind the Scenes of Dual-Functionality, (2021) 2100706.

[5] Y. Yang, K. Wang, X. Gu, K.W. Leong, Biophysical regulation of cell behavior—cross talk between substrate stiffness and nanotopography, 3(1) (2017) 36-54.

[6] F. Han, C. Zhu, Q. Guo, H. Yang, B. Li, Cellular modulation by the elasticity of biomaterials, 4(1) (2016) 9-26.

[7] S.J. Callens, R.J. Uyttendaele, L.E. Fratila-Apachitei, A.A. Zadpoor, Substrate curvature as a cue to guide spatiotemporal cell and tissue organization, 232 (2020) 119739.

[8] D.E. Discher, P. Janmey, Y.-L.. Wang, Tissue cells feel and respond to the stiffness of their substrate, 310(5751) (2005) 1139-1143.

[9] A.J. Engler, S. Sen, H.L. Sweeney, D.E. Discher, Matrix elasticity directs stem cell lineage specification, 126(4) (2006) 677-689.

[10] O. Chaudhuri, L. Gu, D. Klumpers, M. Darnell, S.A. Bencherif, J.C. Weaver, N. Huebsch, H.-p. Lee, E. Lippens, G.N. Duda, D.J. Mooney, Hydrogels with tunable stress relaxation regulate stem cell fate and activity, 15(3) (2016) 326-334.

[11] K. Modaresifar, S. Azizian, M. Ganjian, L.E. Fratila-Apachitei, A.A. Zadpoor, Bactericidal effects of nanopatterns: A systematic review, Acta Biomater 83 (2019) 29-36.

[12] M. Ganjian, K. Modaresifar, H. Zhang, P.-L. Hagedoorn, L.E. Fratila-Apachitei, A.A. Zadpoor, Reactive ion etching for fabrication of biofunctional titanium nanostructures, 9(1) (2019) 1-20.

[13] M. Ganjian, K. Modaresifar, M.R. Ligeon, L.B. Kunkels, N. Tümer, L. Angeloni, C.W. Hagen, L.G. Otten, P.-L. Hagedoorn, I. Apachitei, L.E. Fratila-Apachitei, A.A. Zadpoor, Nature helps: toward bioinspired bactericidal nanopatterns, 6(16) (2019) 1900640.

[14] K. Modaresifar, L.B. Kunkels, M. Ganjian, N. Tümer, C.W. Hagen, L.G. Otten, P.-L. Hagedoorn, L. Angeloni, M.K. Ghatkesar, L.E. Fratila-Apachitei, A.A. Zadpoor, Deciphering the roles of interspace and controlled disorder in the bactericidal properties of nanopatterns against Staphylococcus aureus, 10(2) (2020) 347.

[15] M. Nouri-Goushki, L. Angeloni, K. Modaresifar, M. Minneboo, P.E. Boukany, M.J. Mirzaali, M.K. Ghatkesar, L.E. Fratila-Apachitei, A.A. Zadpoor, Interfaces, 3D-Printed Submicron Patterns Reveal the Interrelation between Cell Adhesion, Cell Mechanics, and Osteogenesis, 13(29) (2021) 33767-33781.

[16] M. Nouri-Goushki, A. Isaakidou, B. Eijkel, M. Minneboo, Q. Liu, P.E. Boukany, M.J. Mirzaali, L.E. Fratila-Apachitei, A.A. Zadpoor, 3D printed submicron patterns orchestrate the response of macrophages, 13(34) (2021) 14304-14315.

[17] M.C. Fokker, S. Janbaz, A.A. Zadpoor, Crumpling of thin sheets as a basis for creating mechanical metamaterials, RSC Advances 9(9) (2019) 5174-5188.

[18] M.J. Mirzaali, M. Habibi, S. Janbaz, L. Vergani, A.A. Zadpoor, Crumpling-based soft metamaterials: the effects of sheet pore size and porosity, Scientific Reports 7(1) (2017).

[19] S.J. Callens, A.A. Zadpoor, From flat sheets to curved geometries: Origami and kirigami approaches, 21(3) (2018) 241-264.

[20] T. van Manen, S. Janbaz, M. Ganjian, A.A. Zadpoor, Kirigami-enabled self-folding origami, Materials Today 32 (2020) 59-67.

[21] B. Mota, S. Herculano-Houzel, Cortical folding scales universally with surface area and thickness, not number of neurons, 349(6243) (2015) 74-77.

[22] T. Tallinen, J.Y. Chung, F. Rousseau, N. Girard, J. Lefèvre, L. Mahadevan, On the growth and form of cortical convolutions, 12(6) (2016) 588-593.

[23] E. Katzav, M. Adda-Bedia, A. Boudaoud, A statistical approach to close packing of elastic rods and to DNA packaging in viral capsids, 103(50) (2006) 18900-18904.

[24] P.K. Purohit, J. Kondev, R. Phillips, Mechanics of DNA packaging in viruses, 100(6) (2003) 3173-3178.

[25] S. Deboeuf, E. Katzav, A. Boudaoud, D. Bonn, M. ADDA-BEDIA, Compaction of thin sheets: crumpling and folding, 21st French Mechanics Congress, Bordeaux, FR, 2013.

[26] J.H. Brackenbury, Wing folding and free-flight kinematics in Coleoptera (Insecta): a comparative study, 232(2) (1994) 253-283.

[27] N. Kleckner, D. Zickler, G.H. Jones, J. Dekker, R. Padmore, J. Henle, J. Hutchinson, A mechanical basis for chromosome function, 101(34) (2004) 12592.

[28] H. Heng, J.W. Chamberlain, X.-M. Shi, B. Spyropoulos, L.-C. Tsui, P.B. Moens, Regulation of meiotic chromatin loop size by chromosomal position, 93(7) (1996) 2795-2800.

[29] M. Habibi, M. Adda-Bedia, D. Bonn, Effect of the material properties on the crumpling of a thin sheet, Soft Matter 13(22) (2017) 4029-4034.

[30] Y. Lin, Y. Wang, Y. Liu, T.M. Hong, Crumpling under an ambient pressure, 101(12) (2008) 125504.

[31] S. Deboeuf, E. Katzav, A. Boudaoud, D. Bonn, M. Adda-Bedia, Comparative study of crumpling and folding of thin sheets, 110(10) (2013) 104301.

[32] K. Matan, R.B. Williams, T.A. Witten, S.R. Nagel, Crumpling a thin sheet, 88(7) (2002) 076101.

[33] A.D. Cambou, N. Menon, Orientational ordering in crumpled elastic sheets, 112(1) (2015) 14003.

[34] S. Cottrino, P. Viviès, D. Fabrègue, E. Maire, Mechanical properties of crumpled aluminum foils, 81 (2014) 98-110.

[35] T. van Manen, S. Janbaz, M. Ganjian, A.A. Zadpoor, Kirigami-enabled self-folding origami, 32 (2020) 59-67.

[36] S. Park, H.-H. Park, K. Sun, Y. Gwon, M. Seong, S. Kim, T.-E. Park, H. Hyun, Y.-H. Choung, J. Kim, Hydrogel nanospike patch as a flexible anti-pathogenic scaffold for regulating stem cell behavior, 13(10) (2019) 11181-11193.

[37] F. Bobbert, K. Lietaert, A.A. Eftekhari, B. Pouran, S. Ahmadi, H. Weinans, A.A. Zadpoor, Additively manufactured metallic porous biomaterials based on minimal surfaces: A unique combination of topological, mechanical, and mass transport properties, 53 (2017) 572-584.

[38] R. Hedayati, S. Ahmadi, K. Lietaert, B. Pouran, Y. Li, H. Weinans, C. Rans, A.A. Zadpoor, Isolated and modulated effects of topology and material type on the mechanical properties of additively manufactured porous biomaterials, 79 (2018) 254-263.

[39] A. Higuchi, Q.-D. Ling, Y. Chang, S.-T. Hsu, A. Umezawa, Physical cues of biomaterials guide stem cell differentiation fate, 113(5) (2013) 3297-3328.

[40] M.F. Griffin, P.E. Butler, A.M. Seifalian, D.M. Kalaskar, Control of stem cell fate by engineering their micro and nanoenvironment, 7(1) (2015) 37.

[41] X. Chen, H. Fan, X. Deng, L. Wu, T. Yi, L. Gu, C. Zhou, Y. Fan, X. Zhang, Scaffold Structural Microenvironmental Cues to Guide Tissue Regeneration in Bone Tissue Applications, Nanomaterials (Basel) 8(11) (2018).

[42] N.E. Fedorovich, E. Kuipers, D. Gawlitta, W.J. Dhert, J. Alblas, Scaffold porosity and oxygenation of printed hydrogel constructs affect functionality of embedded osteogenic progenitors, 17(19-20) (2011) 2473-2486.

[43] M. Miron-Mendoza, J. Seemann, F.J.B. Grinnell, The differential regulation of cell motile activity through matrix stiffness and porosity in three dimensional collagen matrices, 31(25) (2010) 6425-6435.

[44] Y. Li, H. Jahr, J. Zhou, A.A. Zadpoor, Additively manufactured biodegradable porous metals, Acta Biomater (2020).

[45] B. Zhang, X. Pei, C. Zhou, Y. Fan, Q. Jiang, A. Ronca, U. D'Amora, Y. Chen, H. Li, Y. Sun, X. Zhang, The biomimetic design and 3D printing of customized mechanical properties porous Ti6Al4V scaffold for load-bearing bone reconstruction, Materials & Design 152 (2018) 30-39.

[46] F.S.L. Bobbert, S. Janbaz, T. van Manen, Y. Li, A.A. Zadpoor, Russian doll deployable meta-implants: Fusion of kirigami, origami, and multi-stability, Materials & Design 191 (2020).

[47] J. Hasan, S. Jain, K. Chatterjee, Nanoscale topography on black titanium imparts multi-biofunctional properties for orthopedic applications, Scientific reports 7 (2017) 41118.

[48] S. Oh, K.S. Brammer, Y.J. Li, D. Teng, A.J. Engler, S. Chien, S. Jin, Stem cell fate dictated solely by altered nanotube dimension, Proc. Natl. Acad. Sci. U. S. A. 106(7) (2009) 2130-2135.

[49] S. Watari, K. Hayashi, J.A. Wood, P. Russell, P.F. Nealey, C.J. Murphy, D.C. Genetos, Modulation of osteogenic differentiation in hMSCs cells by submicron topographically-patterned ridges and grooves, Biomaterials 33(1) (2012) 128-136.

[50] G. Kumar, C.K. Tison, K. Chatterjee, P.S. Pine, J.H. McDaniel, M.L. Salit, M.F. Young, C.G. Simon Jr, The determination of stem cell fate by 3D scaffold structures through the control of cell shape, Biomaterials 32(35) (2011) 9188-9196.

7

Nanoimprinting for high-throughput replication of osteogenic nanopillars

Abstract

Developing high-throughput nanopatterning techniques that also allow for precise control over the dimensions of the fabricated features is essential for the study of cell-nanopattern interactions. Here, we developed a process that fulfills both of these criteria. Firstly, we used electron-beam lithography (EBL) to fabricate precisely controlled arrays of submicron pillars with varying values of interspacing on a large area of fused silica. Two types of etching procedures with two different systems were developed to etch the fused silica and create the final desired height. We then studied the interactions of preosteoblasts (MC3T3-E1) with these pillars. Varying interspacing was observed to significantly affect the morphological characteristics of the cell, the organization of actin fibers, and the formation of focal adhesions. The expression of osteopontin (OPN) significantly increased on the patterns, indicating the potential of the pillars for inducing osteogenic differentiation. The EBL pillars were thereafter used as master molds in two subsequent processing steps, namely soft lithography and thermal nanoimprint lithography for high-fidelity replication of the pillars on the substrates of interest. The molding parameters were optimized to maximize the fidelity of the generated patterns and minimize the wear and tear of the master mold. Comparing the replicated feature with those present on the original mold confirmed that the geometry and dimensions of the replicated pillars closely resemble those of the original ones. The method proposed in this study, therefore, enables the precise fabrication of submicron- and nanopatterns on a wide variety of materials that are relevant for systematic cell studies.

7.1. Introduction

The rapid expansion of cell-based therapies in a variety of pathological circumstances [1-3] along with the emergence of recent generations of cell-instructive biomaterials [4] have underscored the importance of directing the (stem) cell fate. While stem cells demonstrate an extensive capacity for commitment to certain lineages in response to many biochemical and/or biophysical exogenous stimuli [5, 6], the complications associated with the use of biochemical agents, such as the high cost of growth factors and their potential adverse effects [7-9], have motivated researchers to investigate the physical interactions of cells and biomaterials to a deeper extent.

Among such physical stimuli, submicron and nanoscale topographies have been demonstrated to be particularly effective in controlling such cell behaviors as proliferation, migration, and differentiation [10-12]. While many studies have been performed to elucidate the biological effects of surface patterns at the nanoscale (below 100 nm) [13-16], less is known about the optimum dimensions at the submicron scale (100-1000 nm) [6, 17-19] for inducing specific cell responses.

Despite much effort dedicated to understanding the effects of surface topography on the various types of cell behavior, many aspects of such interactions remain poorly understood. One of the main reasons is the large number of design parameters that define the geometry and arrangement of such topographies. Each of those design parameters may influence the cell response in a unique way both in isolation and in combination with other design parameters. Moreover, the intracellular pathways by which the cells sense and respond to their microenvironment are highly complex [7, 13, 20]. There is, therefore, a need for extensive systematic studies to understand the effects of different design parameters on the interactions between submicron and nanoscale surface patterns and cell behavior. Such systematic studies are, however, hampered by practical considerations regarding the nanofabrication techniques. The currently available techniques for the fabrication of precisely controlled submicron and nanoscale patterns include electron beam induced deposition (EBID) [21-23], electron beam lithography (EBL) [24, 25], two-photon polymerization [26], etc. All of these techniques suffer from a major limitation, namely low throughout. A low throughput means that it is infeasible to pattern large surface areas. Some other techniques are available for high throughput patterning of surfaces at the nanoscale and submicron scales, including reactive ion etching [27, 28], anodizing [29], and hydrothermal treatment [30-32]. These high throughput techniques, however, offer limited geometrical precision and usually lack the capability to change each design parameter independent from the others. There is, therefore, an urgent need for high throughput yet precise nanofabrication technique for the patterning of bio-instructive surfaces at the submicron and nanoscales. Nanoimprint lithography (NIL) is a facile fabrication technique that offers a number of unique advantages, including high throughput and scalability [33, 34], being able to pattern a large variety of geometrical features and materials with ultrahigh resolutions [35], simplicity, and low cost [36]. Given these favorable properties, NIL is widely used for the

fabrication of biosensors [37, 38], photovoltaics [39, 40], bactericidal [7, 41] and osteogenic nanopatterns [13, 42-44], and flexible electronics [45-47].

Here, we use a combination of EBL and NIL for high throughput patterning of bio-instructive surfaces with geometrically precise submicron pillars. Variations in the interspacing of high aspect ratio submicron pillars fabricated by two-photon polymerization have been recently shown to induce osteogenic differentiation in preosteoblasts [6]. The settling state of the cells on the pillars and traction forces applied to the pillars resulting in their tips to be displaced were hypothesized to determine the long-term osteogenic response of the cells. Nevertheless, the relatively low stiffness of the pillars could be a reason why they bent underneath the cells, thus, it is still an unanswered question whether the same pillar geometry and dimensions would induce the same biological response if there is no tip displacement and bending. Moreover, these pillars were fabricated on a very small area (1 mm^2) which limits practicing certain biological assays. In this study, to show the potential of the fabrication process developed in this study, we used EBL to pattern a large area (3 × 5 mm^2) of fused silica substrates (significantly stiffer than the polymeric resin used in two-photon polymerization) with submicron pillars whose dimensions were similar to those of the abovementioned study. The EBL parameters, including resist type, resist thickness, exposure parameters (*e.g.,* beam current, spot size, and electron dosage), and mask thickness were optimized to generate submicron pillars with the highly precise dimensions in as short of a processing time as possible. We then, for the first time, cultured preosteoblasts on a fused silica substrate containing submicron pillars that were made of the same material to study the interaction of the preosteoblasts with the submicron features of fused silica and verify that the effects of the submicron pillars on those cells are independent from the chemical properties and stiffness of the material. Moreover, we created hybrid PDMS molds (replica of the master mold) that enabled us to replicate the patterns multiple times, thereby substantially decreasing the costs and time associated with the proposed nanofabrication process and making it possible to economically produce large enough number of specimens. Fused silica was chosen as the final substrate and by finding the appropriate hard mask, thermoplastic resist, etching gasses, and nanoimprint parameters, the desired submicron patterns were successfully replicated from the hybrid PDMS replica mold into the fused silica substrate. The high transparency and mechanical properties of fused silica make it a proper

candidate for both UV and thermal NIL. Although there are some studies on transferring the nano/submicron features into the different types of polymers using NIL technique, to the best of our knowledge, there is no study on transferring them onto fused silica which has more relevant properties for the intended research and clinical applications.

7.2. Materials and methods

7.2.1. Master mold fabrication by EBL

The process steps involved in the fabrication of the master mold are illustrated in Figure 1a. Double side polished 4-inch (diameter = 10.16 cm) fused silica wafers (thickness = 525 ± 25 µm) (University Wafers Inc, MA, USA) were cleaned in the Piranha solution (a mixture of 3:1 (v/v) H_2SO_4 (Honeywell, Bucharest, Romania) and H_2O_2 (VWR international, Amsterdam, The Netherlands)) at room temperature for 12 min, were rinsed with deionized (DI) water, and were dried with a nitrogen gun. The wafer was then covered with a thin layer of photoresist to protect its surface from damage. Subsequently, the wafer was diced into 1×1 cm^2 specimens using a disco dicer (Disco Hi-Tec Europe GMbH, Munich, Germany). After dicing, the photoresist layer was removed by placing the pieces into acetone (Sigma-Aldrich, The Netherlands) combined with ultrasonication for 20 min. The cleaning process was followed by immersing the specimens in isopropyl alcohol (IPA, Sigma-Aldrich, The Netherlands) and DI water, respectively, and drying them with a nitrogen gun.

Polymethyl methacrylate (PMMA) resist (495, A8) (495 K molecular weight, 8 wt% in anisole, Microchem Corp, USA) was spun coat on the fused silica substrate at 3000 rpm and was baked at 185 °C on a hotplate for 20 min. Once it cooled down, PMMA ARP 679.02 (950 K, ALLRESIST GmbH, Germany) was spun coat on the specimen at 6000 rpm. The specimen was then baked at 185 °C for 10 min. A multilayer resist was used to make the lift-off process easier. The resist thickness was measured using a Dektak profilometer (Bruker, Karlsruhe, Germany). Then, 15 nm of chromium (Cr) with a rate of 0.5 °A/sec was evaporated on the specimens using an e-beam evaporator (Temescal FC-2000, Ferrotec, Germany) to make them conductive before e-beam exposure. The PMMA resist was directly patterned using EBL (Raith EBPG 5200) operated at an acceleration voltage of 100 kV and a beam current of 364 pA. The designed file included circular features with a diameter of 250 nm and two different values of interspacing, namely 700 nm and 1000 nm. As the optimized electron

dosage had to be determined for each dimension, a broad range dose test was performed from 500 μC/cm² to 2000 μC/cm². After exposure, the Cr layer was removed by immersing the specimens in a Cr etchant (Chromium Etchant N1, MicroChemicals, Ulm, Germany) for 20 sec. The specimens were then rinsed in DI water for 5 min and were dried with a nitrogen gun. The PMMA resist was developed using a methyl isobutyl ketone (MIBK, Sigma-Aldrich, The Netherlands)/IPA 1:3 solution for 75 sec, rinsing in IPA for 30 sec, and drying with a nitrogen gun. To remove the resist residues from the holes, the specimens were exposed to an oxygen plasma (PVA Tepla M4L Gas Plasma System, Corona, USA) with an oxygen gas flow rate of 200 sccm and a power of 100 W for 20 sec. After the plasma treatment, 60 nm Cr was deposited on the specimen as a mask using an e-beam evaporator (evaporation rate = 0.5 °A/sec, chamber pressure = 1.5×10^{-6} mbar). A lift-off process was performed to remove the resist from the area around the features. To do so, N-Methyl-2-pyrrolidone (NMP, Sigma-Aldrich, The Netherlands) was heated up to 80 °C and was used for soaking the specimens for 2 hours. To transfer the patterns into the substrate and create the submicron pillars, two different etching methods of the fused silica were investigated: ICP RIE (Adixen AMS 100 I-speeder, Alcatel, France) or RIE (Sentech Etchlab 200, Sentech Instruments, Germany). In the case of ICP RIE, a gas mixture of $C_4F_8/CH_4/He$ (15/15/150 sccm) was used for different durations to reach the desired height. The other etching parameters were as follows: a source power of 2500 W, a bias voltage of 23 V, and a temperature of 0 °C. In the case of RIE, a gas mixture of CHF_3/O_2 (68/5 sccm) with an RF power of 102 W, a bias voltage of 340 V, and a chamber pressure of 15 μbar were used. As the submicron pillars were formed on the fused silica substrate, the Cr mask was removed by immersing the specimens into the Cr etchant for 20 sec. This process was followed by rinsing the specimen with DI water for 5 min. The final step before SEM inspection was cleaning the specimens with the piranha solution for 12 min to remove the organic and polymeric contaminants which had formed on the substrate during the etching process, followed by rinsing with DI water for 5 min and drying with a nitrogen gun.
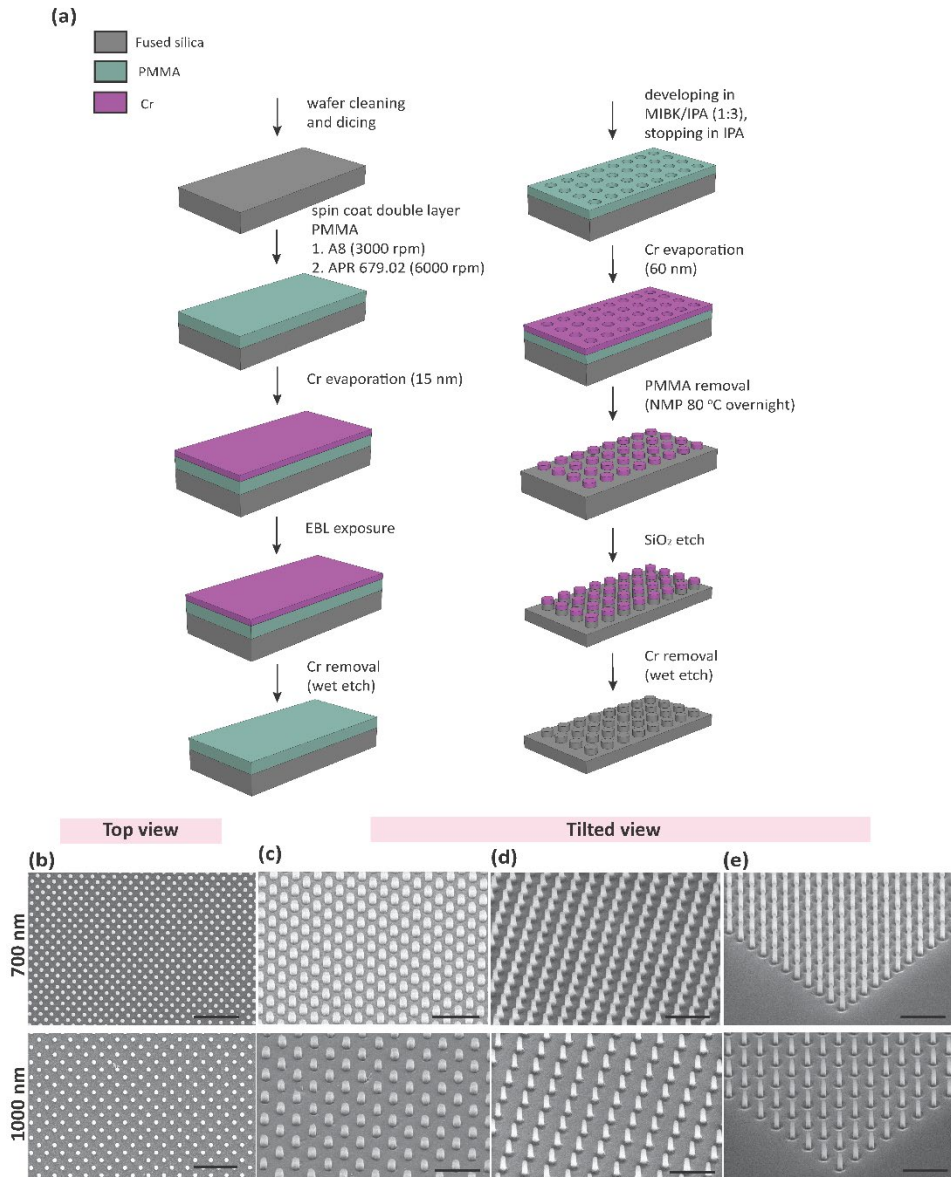
Figure 1. (a) A schematic drawing of the procedure of fabricating submicron pillars on the fused silica master mold using electron beam lithography. Top (b) and tilted (c-e) SEM images of the resulting submicron pillars with the interspacing values of 700 and 1000 nm formed on the fused silica substrate. Scale bar = 2 μm. (c) submicron pillars after 255 s of etching using ICP RIE, (d) submicron pillars after 8 min of etching using ICP RIE, and (e) submicron pillars after 90 min of etching using RIE.

Top and tilted SEM images of the resultant master mold were taken using a Helios Nano Lab 650 (FEI company, US) SEM, with an acceleration voltage of 10 kV and a beam current of 50 pA. The diameter and height of the submicron pillars were measured from the tilted SEM images, while the interspacing values were measured from the top view SEM images.

7.2.2. Interactions of MC3T3-E1 preosteoblast cells with the patterned surfaces

All the fused silica specimens were sterilized prior to cell seeding by immersing them in 70% ethanol and exposing them to UV light for 20 min. The specimens were rinsed twice with 10X phosphate buffered saline (PBS, Sigma-Aldrich, Germany), were submerged in a solution of 50 µg/ml bovine fibronectin (Sigma-Aldrich, US), and were incubated at 37 °C and 5% CO_2 for 30 min to improve the cell adhesion [48]. MC3T3-E1 preosteoblast cells (Sigma-Aldrich, Germany) cultured in the alpha minimum essential medium (α-MEM) supplemented with 10% (v/v) fetal bovine serum (FBS) and 1% (v/v) penicillin-streptomycin (all from Thermo Fisher Scientific, US) were seeded on the specimens (1×10^4 cells per sample) in a 24 well-plate (Greiner, Bio-One, The Netherlands) and were incubated at 37 °C and 5% CO_2.

After 1 day of culture, the specimens (n = 3) were washed twice with 10X PBS and the cells were fixated using a 4% (v/v) formaldehyde solution (Sigma-Aldrich, Germany). Following the cell membrane permeabilization using 0.5% Triton X-100/PBS (Sigma-Aldrich, Germany) at 4 °C for 5 min, the samples were incubated in 1% BSA/PBS (Sigma-Aldrich, Germany) at 37 °C for 5 min. The specimens were then incubated in anti-vinculin mouse monoclonal primary antibody (1:100 in 1% BSA/PBS, Sigma-Aldrich, Germany) and rhodamine-conjugated phalloidin (1:1000 in 1% BSA/PBS, Thermo Fisher Scientific, US) for 1 h at 37 °C. The cells were then washed three times with 0.5% Tween-20/PBS (Sigma-Aldrich, Germany) and were incubated in Alexa Fluor 488 (*i.e.*, donkey anti-mouse polyclonal secondary antibody, 1:200 in 1% BSA/PBS, Thermo Fisher Scientific, US) for 1 h at room temperature. After washing with 0.5% Tween-20/PBS and 1X PBS, the samples were mounted on microscopic glass slides using 10 µl of the Prolong gold antifade reagent containing DAPI (4',6-diamidino-2-phenylindole) (Thermo Fisher Scientific, US). Finally, the specimens were imaged using a fluorescence microscope (ZOE™ fluorescent cell imager,

Bio-Rad, The Netherlands). For the SEM observations, the stained samples (n=3) were washed twice with distilled water for 5 min and were then dehydrated in 50%, 70%, and 96% ethanol solutions for 15 min, 20 min, and 20 min, respectively. After air-drying overnight at room temperature, the samples were gold-sputtered before SEM imaging.

To evaluate the osteogenic properties of the patterned surfaces, the cells were stained for osteopontin (OPN) after 21 days of culture in osteogenic medium. Following the fixation and permeabilization of cells, they were incubated with OPN antibody conjugated to Alexa fluor 488 (1:100 in BSA/PBS, Santa Cruz Biotechnology, US) for 1 hr at 37 °C (n = 3).

ImageJ 1.53c (NIH, US) was used to quantify the morphological characteristics of the cells as well as the area of focal adhesions and OPN according to methods described before[49, 58].

7.2.3. Contact angle measurements

A drop shape analyzer (KRUSS DSA100, Germany) was used to evaluate the wettability of the surfaces used for cell culture (*i.e.,* the flat and patterned surfaces, n=3). A droplet of deionized water with a volume of 3.0 μL was placed on the surface. The images were recorded after 5 sec.

7.2.4. Fabrication of the hybrid PDMS replica molds

A schematic drawing illustrating the process steps of soft lithography is presented in Figure 2a. Prior to performing hybrid PDMS molding, the fused silica master mold was first placed, for 30 min, in a vacuum desiccator close enough to a glass petri dish containing a droplet of octyltrichlorosilane (OTS) (Gelest Inc., Germany) to coat the surface of the master mold with a hydrophobic layer, thereby preventing the cured hybrid PDMS layer from sticking to the master mold. The hybrid PDMS mold consisted of two layers: a thin layer of hard-PDMS (hPDMS) (a 30-40 μm stiff layer), that was in direct contact with the patterns during the molding process, and a PDMS (a 3-5 mm flexible layer) that formed the bulk of the replica mold. The hPDMS was made by mixing 0.85 g of 7-8% (vinylmethylsiloxane)-dimethylsiloxane copolymer, trimethylsiloxy terminated (Gelest Inc., Germany), 2.0 μl of 2,4,6,8-Tetramethyl-2,4,6,8-tetravinylcyclotetrasiloxane (Sigma Aldrich, Germany), and 3.0 μl of platinum-divinyltetramethyldisiloxane complex in xylene (Gelest Inc., Germany) for 5

min. This combination was left in a vacuum desiccator for 30 min to remove the air bubbles present in the mixture. After this step, 0.25 g of (25-35% methylhydrosiloxane)-dimethylsiloxane (PDMS copolymer, 25-35 cSt, Gelest Inc, Germany) was added to the previous mixture, was mixed for 3 min, was poured, and was spun coat on the fused silica master mold for 40 sec using a spinning rate of 1000 rpm, followed by curing in an oven at 60 °C for 20 min. PDMS (Sylgard 184, Dow Inc., Midland, MI, U.S.A.) combined with the curing agent at a weight ratio of 10:1 was mixed thoroughly, cast on the master mold, and desiccated in vacuum for 30 minutes to remove the air bubbles. The fused silica master mold (with the hybrid PDMS on top) was then cured in an oven at 40 °C for 16 h. After curing, the hybrid PDMS was carefully peeled off from the substrate. The master and the replica molds were finally sterilized by IPA. We verified that the same master mold could be used at least 5 times to apply the patterns into PDMS without a significant loss of fidelity.

The quality of the patterns replicated into the hybrid PDMS was evaluated using SEM. Prior to SEM imaging, the PDMS substrates were gold-sputtered.

7.2.5. Cross-sectional characterization using FIB milling

In order to measure the depth of the replicated patterns (submicron pits) on the hybrid PDMS mold, focused ion beam scanning electron microscopy (FIB-SEM) was performed in a FIB microscope (FEI, Helios G4 CX dual beam workstation, Hillsborough, USA). The specimen was tilted to 52° and the surface was milled using Gallium ions with a 7 pA ion beam (acceleration voltage = 30 kV).

7.2.6. Pattern transfer from the hybrid PDMS replica mold to the substrate of interest by thermal nanoimprint

The details of the process steps involved in NIL are presented in Figure 2b.

Firstly, Cr (30 nm) was evaporated on the 1×1 cm^2 fused silica specimens. PMMA (950 A3) (950 K molecular weight, 3 wt% in anisole, Microchem Corp, USA) was then spun coated on the specimens at 4250 rpm, and baked on a hotplate at 185 °C for 20 min. The nanoimprinting was carried out using a commercial thermal nanoimprinting EVG bonder (EVG 520, EVgroup, Austria). The hybrid PDMS replica mold containing submicron pits and the fused silica specimens were brought into contact with each other (hybrid PDMS on top and fused silica at the bottom). The temperature was then increased to above the glass

transition temperature (T_g) of PMMA (140 °C) (T_g of PMMA = 105 °C). The hybrid PDMS mold was then pressed into the PMMA layer with a set force of 1250 N for 3 min at the embossing temperature. After imprinting, the chamber was cooled down below T_g (80 °C in this study) with a rate of 2 °C/min. The slow cooling rate was chosen to reduce the thermal stress caused by cooling in the material. To prevent the polymeric microstructures from flattening and rounding of the edges, the embossing force was maintained during the cooling down process. The force was released one min after reaching 80 °C (de-embossing temperature). The cooling down process was continued to reach 40 °C, and then the hybrid PDMS mold and the fused silica specimen were separated gently and taken out from the chamber afterward.

To transfer the submicron pillars formed on the PMMA into the fused silica substrate underneath, we first used oxygen plasma to remove the residues of the PMMA that rest in between the pillars (Figure 2b) in a process called *descum*. The descum process was performed using 20 sccm O_2 plasma, with a power of 20 W, and at a chamber pressure of 40 µbar in a plasma etcher- RIE Etchlab 200 (Sentech Instruments, Germany) for 2 min.

To have access to the surface of the fused silica specimens, the Cr layer was etched using a Chlorine-based ICP RIE machine (PlasmaLab System 100, Oxford Instruments, UK) while employing PMMA as the mask. The etching process was conducted under the following conditions: RF power = 50 W, Cl_2 = 50 sccm, O_2 = 5 sccm, temperature = 40 °C, chamber pressure = 12.5 µbar, and etching time = 90 sec. Once the patterns were transferred into the Cr layer, the PMMA mask could be removed. To do so, the specimens were soaked in NMP at 80 °C overnight. This step was followed by transferring the submicron pillars into the fused silica substrate, by using the Cr layer as the mask during the etching step. The fused silica was etched using ICP RIE (Adixen AMS100 I-speeder, Alcatel, France), by $C_4F_8/CH_4/He$: 15/15/150 sccm as the etching gasses for 4 min and 15 sec, and with a source power of 2500 W, an RF power of 250 W, a bias voltage of 23 V, and at 0 °C. The Cr mask was then etched away using the Cr etchant and the specimens were dried using a nitrogen-gun and were gold-sputtered before SEM imaging.
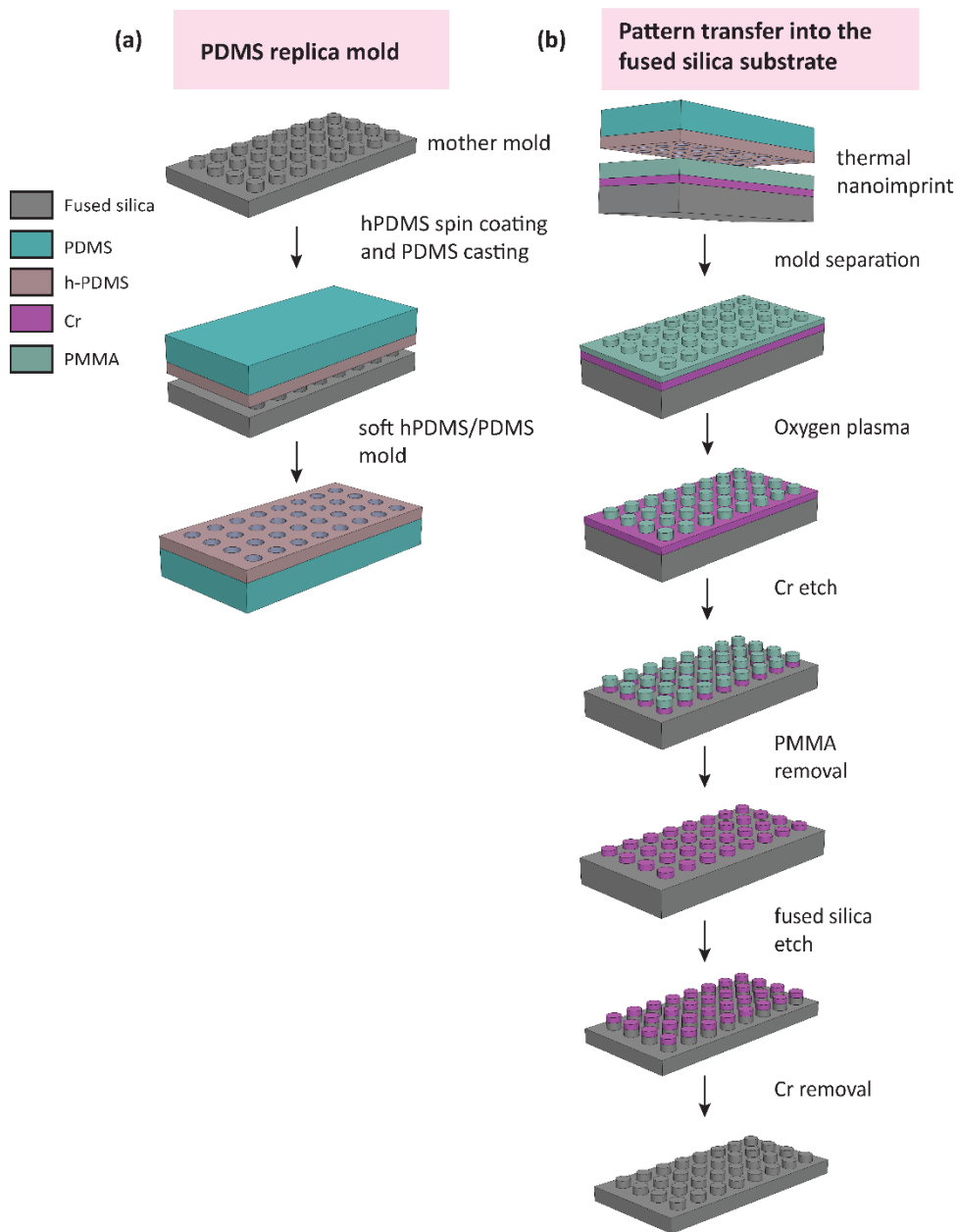
Figure 2. A schematic drawing of (a) the process steps involved in the preparation of the hPDMS/PDMS daughter molds and (b) the thermal nanoimprint process used to transfer the submicron pits from the hPDMS/PDMS mold to the fused silica substrate.

7.2.7. Statistical analysis

To statistically analyze the results of cell culture experiments, the raw data was first tested for normal distribution using the D'Agostino-Pearson omnibus normality test in Prism version 9.1.2 (GraphPad, US). For normally distributed datasets, the Brown–Forsythe and Welch ANOVA test was performed, followed by the Dunnett's T3 multiple comparisons test to determine the statistical significance of the differences between the means of the different experimental groups. For the datasets which did not pass the normality test, the non-parametrical Kruskal–Wallis test was performed, followed by the Dunn's multiple comparisons test. All data are presented as mean ± standard deviation and a p-value below 0.05 was considered to indicate statistical significance.

7.3. Results

7.3.1. Fabrication and characterization of the master mold

In the case of ICP RIE and after 255 s of etching, the submicron pillars with an interspacing of 700 nm had a height of 508 ± 24 nm and a diameter of 269 ± 19 nm while the submicron pillars with an interspacing of 1000 nm had a height of 523 ± 25 nm and a diameter of 275 ± 22 nm (Figure 1c). After 8 min of ICP RIE etching, the submicron pillars with an interspacing of 700 nm had a height of 990 ± 37 nm and a diameter of 245 ± 22 nm while the submicron pillars with an interspacing of 1000 nm had a height of 1046 ± 31 nm and a diameter of 255 ± 31 nm (Figure 1d). In the case of RIE, after 90 min of etching, a height of 973 ± 43 nm and a diameter of 206 ± 14 nm was reached for the submicron pillars with an interspacing of 700 nm while the submicron pillars with an interspacing of 1000 nm had a height of 1068 ± 41 nm and a diameter of 222 ± 13 nm (Figure 1e).

7.3.2. Adaptation of preosteoblasts to the patterned surfaces

MC3T3-E1 preosteoblast cells presented different morphologies on the flat and patterned surfaces (the ones etched using ICP RIE for 8 min) after 1 day of culture (Figure 3a-c and Figure S1). While the majority of the cells had a polygonal shape on the flat surfaces, more cells with a stellate or polarized shape [6] could be recognized on the patterned surfaces (Figure 3a). The actin fibers in most of the cells residing on the flat areas were oriented towards the vertices of the polygonal shape of the cell body (Figure 3b). Interestingly, actin

fibers were collectively organized more homogenously along the whole cell body in the polarized cells residing on the submicron pillars with an interspacing of 700 nm. Nevertheless, the cytoskeleton was less organized in the cells cultured on the submicron pillars with an interspacing of 1000 nm as compared to the last two surfaces. Further SEM observations revealed different settling states for the cells residing on submicron pillars with different values of interspacing. A "top state" was identified for the cells residing on the submicron pillars with an interspacing of 700 nm, meaning that the cell body was laid on top of the submicron pillars (Figure 3c, d and Figure S2). The cells on the submicron pillars with an interspacing of 1000 nm, however, presented a "mixed state" in which the areas of the cell closer to the cell nucleus seemed to be in a "top state" while farther from these regions (*i.e.,* at the cell periphery), showed a "bottom state". At these regions, the cell was not only in contact with both the tip and lateral sides of the pillars but also with the substrate.

The cell projected area decreased as the interspacing of the submicron pillars increased (Figure 4a). An opposite trend was observed for the cell aspect ratio (*i.e.,* more polarization for the larger interspacing value). However, the cell shape index (*i.e.,* the roundness of the cells) was not significantly different between the flat and patterned surfaces. Despite the differences in the cell nucleus projected area and shape index between the flat controls and the patterned surfaces with an interspacing of 700 nm, a discernible trend was not observed regarding the effects of interspacing on the morphological characteristics of the nucleus (Figure 4b).

The average FA area was found to be significantly affected by the surface topography. The cells residing on the submicron pillars with an interspacing of 700 nm formed significantly smaller FAs as compared to the flat controls and patterned surfaces with an interspacing of 1000 nm (Figure 4c). Finally, the expression of OPN in the matrix was significantly upregulated on the patterned surfaces (Figure 3c and 4d). The pillars with an interspacing of 1000 nm were found to have a significantly higher potential for promoting OPN expression as compared to the pillars with an interspacing of 700 nm.
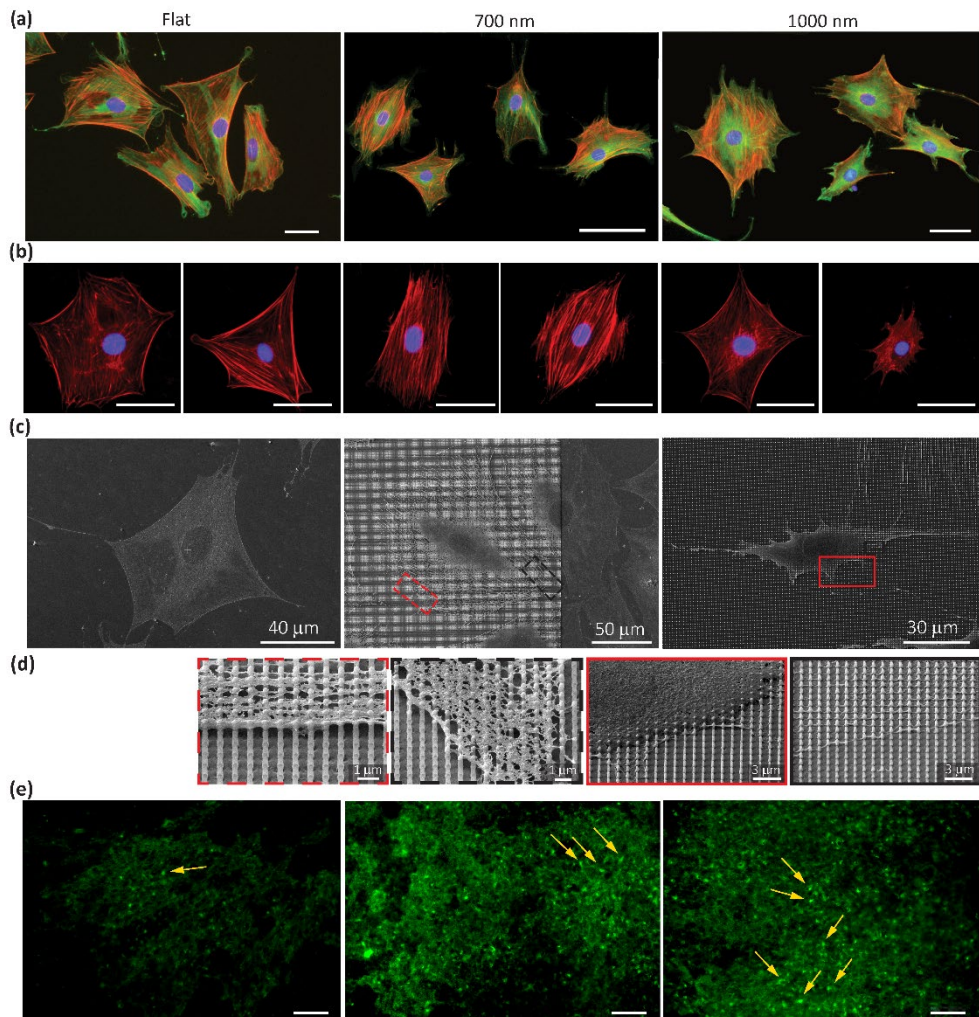
Figure 3. (a) Immunofluorescent staining of vinculin (green), actin (red), and nucleus (blue) of the MC3T3-E1 preosteoblast cells cultured on the flat and patterned specimens for 1 day. Scale bar = 100 μm. (b) Representative images of the cytoskeletal organization of the cells residing on the flat and patterned specimens (red: actin and blue: nucleus). Scale bar = 20 μm. (c) Top view SEM images of the representative cell morphology on the flat and patterned specimens. (d) Highly magnified tilted SEM views of the settlement state of the cells on the patterned specimens and their interactions with the single pillars at cell periphery. (e) The expression of OPN visualized using immunostaining after 21 days.

7.3.3. Water contact angle

While the contact angle for the flat fused silica was $34.0 \pm 3.3°$ ($n = 3$), it was significantly decreased to $7.0 \pm 4.3°$ ($n = 3$) on the patterned fused silica specimens with an interspacing of 700 nm and to $9.0 \pm 6.3°$ ($n = 3$) on the patterned fused silica specimens with an interspacing of 1000 nm, indicating the super-hydrophilicity of the patterned surfaces (Figure 4e).

7.3.4. Fabrication and characterization of the replica mold

The hybrid PDMS mold, containing two sets of submicron pit arrays were successfully replicated from the fused silica master mold with the shorter submicron pillars (the one illustrated in Figure 1c and Table 1). The patterns replicated into the PDMS were geometrically similar to the original patterns (Figure 5a). SEM images indicated no irregularity, clogging, or any other artifacts or signs of incomplete replication of the submicron pits or any damaging of the imprinted substrate (Figure 5a, b). The average diameter and interspacing of the replicated submicron pits, measured on SEM images, confirm the precision of the imprinted patterns (Table 1). To quantify the submicron pits, FIB milling of the submicron pits was performed. The depths measured were 428 ± 55 nm and 402 ± 25 nm for the submicron pits with the interspacing values of 700 nm and 1000 nm, respectively (Figure 5c).

The SEM images of the fused silica master mold, after gently peeling off the hybrid PDMS from it, revealed that the morphology of the submicron pillars had not changed and that there were no significant differences between the dimension of the submicron pillars before PDMS molding and after it (Figure 5d and Table 1). Furthermore, only negligible amounts of PDMS residues remained in-between the submicron pillars, confirming that the fused silica master mold can be used for several rounds of molding without being damaged.
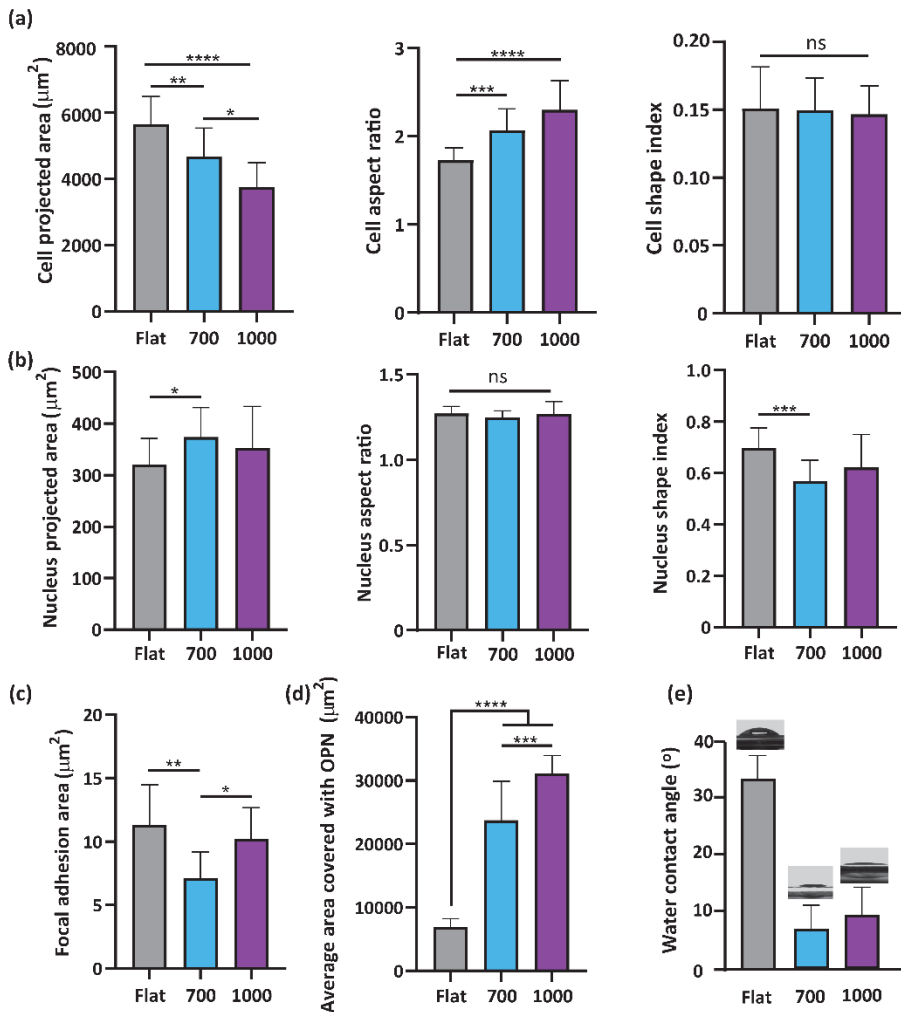
Figure 4. (a) The morphological characteristics of the preosteoblasts *(i.e.,* projected area, aspect ratio, and shape index) cultured on the flat (n = 3) and patterned (n = 3) specimens after 1 day. (b) The morphological characteristics of the cell nucleus *(i.e.,* projected area, aspect ratio, and shape index) cultured on the flat (n = 3) and patterned (n = 3) specimens after 1 day. At least 250 cells were analyzed for each geometrical parameter. (c) The average focal adhesion area of the cells residing on the flat (n = 3) and patterned (n = 3) specimens. At least 10 cells were analyzed per study group. (d) The average area covered with OPN after 21 days (n = 3). At least 8 images were taken from each sample of each study group for quantification of OPN area. (e) Water contact angle on the flat (n = 3) and patterned (n = 3) specimens. (* $p < 0.05$, ** $p < 0.01$, *** $p < 0.001$, and **** $p < 0.0001$).

7.3.5. Characterization of the patterns transferred into the fused silica substrate through thermal nanoimprinting

The heights of the transferred submicron pillars with the interspacing values of 700 nm and 1000 nm, after 255 sec etching of fused silica using Cr mask, were respectively 473 ± 25 nm and 430 ± 91 nm (Table 1, Figure 5e).

Table 1. The means and standard deviations of the dimensions of the submicron patterns produced/replicated after the application of every fabrication technique.

| Mold	Pattern type	Design interspacing = 700 nm		Design interspacing = 1000 nm	
		diameter (nm)	interspacing (nm)	diameter (nm)	interspacing (nm)
master mold (fused silica) before molding	submicron pillars	269 ± 19	712 ± 13	275 ± 22	1013 ± 21
replica mold (hybrid PDMS)	submicron pits	293 ± 20	685 ± 24	245 ± 28	980 ± 33
master mold (fused silica) after molding	submicron pillars	275 ± 19	702 ± 14	291 ± 16	1003 ± 15
Final patterns (fused silica)	submicron pillars	235 ± 19	720 ± 12	221 ± 13	1022 ± 18
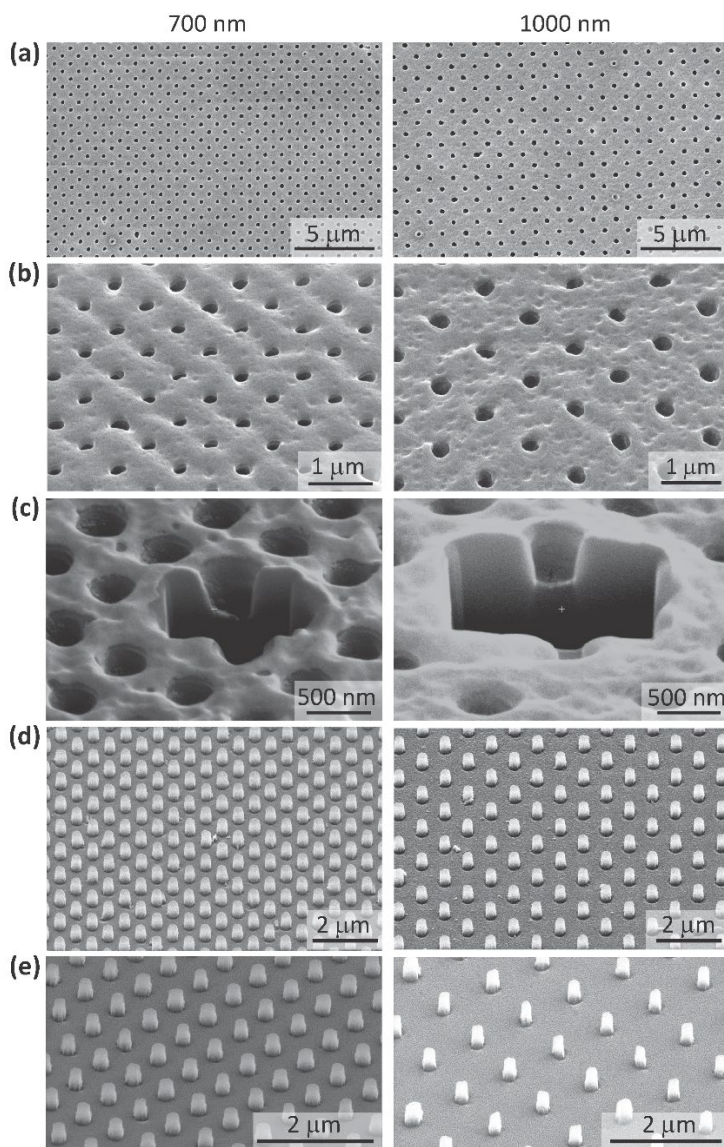
Figure 5. (a) Top and (b) tilted SEM images of the replica patterns (*i.e.,* submicron pits) that were successfully transferred into the hybrid PDMS mold. (c) SEM image of the hybrid PDMS replica mold after FIB milling showing the depth of the submicron pits. (d) SEM images of submicron pillars present on the master mold after peeling off the PDMS that confirm the patterns were nicely transferred into the PDMS without damaging or destroying the master mold. (e) SEM images of the successfully transferred submicron pillars into the fused silica substrate.

163

7.4. Discussion

The design and fabrication of bioinspired and/or rationally designed nanoscale and submicron patterns on the surface of biomaterials could enhance their functionality by eliciting certain cell responses and guiding cells towards the desired lineages. The development of high-throughput and highly precise fabrication processes that make it feasible to fabricate large areas of patterned surfaces on a variety of substrates regardless of their composition and geometry (*i.e.,* flat or curved) is of great importance. The main challenge here lies in simultaneously achieving high geometrical precision and high throughput. There has hardly been any nanofabrication technique that can satisfy both requirements. For instance, such techniques as ICP RIE and hydrothermal treatment enable the rapid production of nano/submicron patterns over a large area but are limited in their geometrical precision when compared with low-throughput techniques, such as EBID, EBL, or FIB, while also not being able to adjust every single design parameter independent from the others [21, 22]. The main aim of this study, therefore, is the development of a rapid and accurate fabrication process to overcome the abovementioned challenges. Nanoimprint lithography offers geometrical precision and high resolutions on the one hand and high-throughput on the other. Moreover, it provides the opportunity to transfer the patterns into the flat and curved substrates as well [50-52]. The availability of such techniques is expected to enable more extensive studies of the interactions between cells and nanopatterns, thereby broadening our knowledge of how cells interact with surface topography and how topographical cues can be exploited to promote tissue regeneration. While other materials, such as titanium alloys, may be more suitable as bone substitutes, we used fused silica in the current study to benefit from its high transparency that makes it an ideal material for both thermal and UV nanoimprint lithography, as well as for imaging purposes during cell studies.

7.4.1. Interactions of MC3T3-E1 cells with patterns

The early-stage adaptation of the cells to the surface and their interactions with the topographical cues of the surface largely determine the long-term response of cells, including their osteogenic differentiation [6]. It has been shown that cell shape and area affect the cytoskeletal organization, as well as the formation and distribution of FAs, which together modulate the stem cells fate [53-55]. Cell shape can also regulate the phenotype

independently from tension-based mechanisms [56]. Moreover, in the case of high aspect ratio pillars, direct nuclear mechanotransduction pathways could determine the cell fate [57]. In our study, the submicron pillars significantly affected the morphological characteristics of the cells in terms of area and aspect ratio. In agreement with a number of reports available in the literature, the presence of the pillars on the biomaterial surface decreased the cell spreading area [58-60]. The spreading area decreased further as the pillar interspacing increased [58-60]. It seems that as the pillars become more separated, the cells tend to confine their area to secure their initial adhesion points as well as an optimized membrane trafficking [61, 62]. The differences in the cytoskeletal organization and FA area between the 700 nm and 1000 nm submicron pillars could be interpreted within this context. The cells residing on the 1000 nm submicron pillars likely undergo a slower adaptation as their actin fibers are not yet well-oriented (as compared to the cells residing on the 700 nm submicron pillars). On the other hand, a larger FAs area on the 1000 nm submicron pillars may be indicative of the fact that the cells are still attempting to form stronger adhesions to the surface.

The increased cell aspect ratio (*i.e.,* elongation) is believed to be beneficial for osteogenic differentiation [18, 63]. The increase in the cell aspect ratio has been shown to increase the anisotropy of FAs [53, 64]. Similarly, we observed that the FAs are preferentially formed at the periphery of smaller and more elongated cells, especially on the 1000 nm submicron pillars. The increased expression of OPN on the 1000 nm pillars suggests that the elongation of the cells and the differential distribution of FAs at the early stages of adaptation to the surface may favorably promote osteogenic differentiation.

Different settling states in the cells residing on the submicron pillars with different interspacing values could be another factor and/or indicator of the varied cytoskeletal organization. The "top state" observed on the submicron pillars with an interspacing of 700 nm ensures that the cells maintain a global convex geometry (from the cell periphery towards the nucleus), which is shown to be associated with higher forces exerted on the nucleus and eventually lead to higher levels of osteogenic differentiation [65]. The "mixed state" observed on the submicron pillars with an interspacing of 1000 nm, on the other hand, imposes a different geometry on the cells at some regions as there is a significant difference in the height between the nuclear area (the thickest part of the cell body) and the cell periphery (deeply sunk into the submicron pillars). This might hinder or delay the global cytoskeletal

organization. In a previous study involving pillars with the same dimensions made of a commercial polymer, the pillars with an interspacing of 700 nm, which induced a "top state" to the cells, showed the highest expression of OPN [6]. Since the pillars in that study were bent underneath the cells, the traction forces were, therefore, assumed to have been transferred all the way to the nucleus via a direct mechanotransduction pathway, affecting the long-term osteogenic response of the cells. In the present study, however, the pillars were stiff enough to not be bent. There may, therefore, be some differences in the cell traction forces observed in these two studies.

In the current study, the pillars inducing the "mixed state" maximized the expression of OPN. It could, therefore, be postulated that engulfing the high aspect ratio pillars by cells in a "mixed state" of the settlement could also trigger direct or indirect mechanotransduction pathways that eventually increase the expression of osteogenic markers, such as OPN [62]. Given that a higher substrate stiffness and a reduced cell area lead to the exertion of larger traction forces [59], further studies using traction force microscopy might shed some light on the roots of the differences in the OPN expression between the pillars with different interspacing values. Nevertheless, the results of this study show that submicron pillars with specific geometry and dimensions have a significant influence on the osteogenic differentiation of cells regardless of their material. Therefore, having the possibility to produce such submicron pillars using high-throughput methods that enable generation of a large number of samples with acceptable reproducibility on various substrates is essential for further research.

7.4.2. Water contact angle

The super-hydrophilicity of the patterned surfaces is consistent with Wenzel model[66, 67]. In this model, it is assumed that the liquid penetrates in between the pillars. The contact angle of a rough surface (θ_w) can then be estimated using the following equation:

$$\cos(\theta_w) = r\cos(\theta) \tag{1}$$

where θ_w and θ are respectively the contact angles of the droplet on the patterned and flat substrates and r is the ratio of the real surface area to the projected surface area, called the roughness factor. Assuming the pillars to be cylindrical in shape with a diameter of d, a height of h, and a pitch of p, r can be calculated as[26]:

$$r = \frac{A_{real}}{A_{projected}} = \frac{p^2 + 4(\frac{\pi dh}{4})}{p^2} = 1 + \frac{\pi dh}{p^2} \qquad (2)$$

Based on the Wenzel relation (Equation (1)), a hydrophilic surface ($\theta < 90°$) becomes more hydrophilic after patterning ($\theta_w < \theta$)[63]. Substituting the dimensions of the submicron pillars ($d = 245$ nm, $h = 990$ nm for $p = 700$ nm and $d = 255$ nm, $h = 1046$ nm for $p = 1000$ nm) and $\theta = 34°$ into Equations (1) and (2) yields $r = 2.14$ and $cos(\theta_w) > 1$ for $p = 700$ nm, and $r = 1.54$ and $cos(\theta_w) > 1$ for $p = 1000$ nm. $cos(\theta_w) > 1$ in both cases indicates that the surface becomes completely wet (*i.e.*, the surface is super-hydrophilic), which is consistent with the results of our experiments, where the measured contact angle was $7 \pm 4°$ and $9 \pm 6°$ for $p = 700$ nm and $p = 1000$ nm, respectively (Figure 4e).

7.4.3. Hybrid PDMS molding

The PDMS molds suffer from some limitations. First, due to the low elastic modulus of PDMS, patterns with very high or very low aspect ratio deform, collapse, or buckle and create some defects on the patterned areas during the molding process, meaning that the patterns cannot be fully transferred during the PDMS molding [68]. On the other hand, the low elastic modulus of PDMS (≈ 1.5 MPa) also limits the minimum feature size of the transferable patterns (*i.e.*, ~500 nm) [71, 72]. In order to improve the accuracy and resolution, Schmid *et al.*,[71] have developed hPDMS that offers enhanced mechanical properties [72]. Having hybrid PDMS molds allows for reaching a resolution of 10 nm [35], which is the resolution that can be reached by rigid molds. We, therefore, applied hPDMS to the substrate prior to PDMS casting to precisely imprint the submicron pillars from the master mold into the hybrid PDMS replica mold. This hybrid mold was then used in the thermal nanoimprint process thanks to its low deformation and high flexibility. Comparing the dimension of the patterns present on the hybrid PDMS substrate with the original submicron pillars (*i.e.*, those of the master mold) indicated that the deviations in the diameter of the pillars are only 9-10% while deviations of 3-4% were observed for the interspacing values.

7.4.4. Thermal nanoimprint lithography

As PDMS is inert and hydrophobic, there is no need to perform any post-processing on it prior to bringing it into contact with PMMA, and the poor adhesion between PDMS and PMMA is an advantage during the nanoimprint process. After nanoimprinting, optimizing

the etching parameters to properly transfer the patterns from PMMA to the final substrate is the key step that affects the feature sizes. Although Pandey *et al.*[35] have previously shown the potential of PDMS as the master mold in thermal nanoimprint processes, they did not continue the process to transfer the patterns into the final substrate. In other words, while they transferred the patterns of the PDMS mold to the PMMA layer, which was coated on the final substrate, they did not use the PMMA or any hard mask to etch the final substrate and transfer the patterns into it. Here, the nanoimprinting process was followed by the proper etching steps to have the desired patterns transferred into the substrate of interest.

The nanoimprinting process parameters, including the applied force, thermoplastic material, embossing temperature, time, and chamber pressure determine the resolution and quality of the transferred patterns. The values reported in the literature for the embossing temperature, while using PMMA as the resist, vary between 120 and 180 °C [73]. At very low temperatures, PMMA is not formable enough to follow the height pattern of the master mold, resulting in incomplete pattern transfer or in features that possess a lower aspect ratio than desired. On the contrary, embossing at a very high temperature may crush or destroy the master mold [74]. In our study, the embossing temperature was set to 140 °C. However, PMMA was used as the mask to transfer the submicron pillars first to Cr. Then, the Cr mask was employed to transfer the submicron pillars into the fused silica substrate. Therefore, as long as the height of the submicron pillars formed on PMMA is high enough to etch the unwanted Cr layer, the embossing temperature is not the critical parameter. The applied force and its uniformity are the other crucial parameters to achieve homogeneous and high-resolution patterns throughout the substrate surface and to prevent the mold and its underlying substrate from being damaged. Applying very high forces will damage the hybrid PDMS mold with the degree of mold deformation increasing with the applied force [35]. On the other hand, very low forces result in the nanopatterns not being thoroughly transferred. Achieving full imprinting with high fidelity of the transferred patterns is, therefore, challenging and requires proper optimization of the involved parameters. In our study, 250 N was high enough to fully transfer the submicron pillars into the PMMA without damaging the hybrid PDMS master mold.

Following the above-mentioned process steps led to the realization of high-quality replicas from a single master mold. Inspecting the dimensions and quality of the final patterns

transferred into the fused silica substrates (Figure 5e) and comparing it with the master mold (Figure 1c) indicates that there are only minor deviations in the diameter and interspacing of the submicron pillars (Table 1). In the case of the submicron pillars with an interspacing of 700 nm, the deviations were around 12% for the diameter and 1% for the interspacing. As for the submicron pillars with an interspacing of 1000 nm, the deviations were around 19% for the diameter and 1% for the interspacing. Considering the fact that the patterned area was relatively large, the effects of such deviations on the patterned area, in its entirety, are not significant. In other words, optimized processing parameters lead to high-fidelity replica molds despite the large number of the steps involved. These results confirm that pattern replication by thermal nanoimprinting produces precisely formed submicron patterns with minimal surface defects. Nanoimprint lithography appears to be the best candidate for decorating the surface of biomaterials with cell-instructive nano/submicron pillars [75].

Conclusions

In summary, we developed a precise and facile method for high throughput patterning of various types of surfaces with nanoscale and submicron patterns whose geometries are precisely controlled. First, we used electron beam lithography to fabricate two arrays of submicron pillars with precise dimensions and controlled shape over a large area (3×5 mm^2) of a fused silica substrate. Assessing the adaptation of MC3T3-E1 preosteoblast cells to the fabricated patterns showed that varying the interspacing of the submicron pillars significantly influences the cytoskeletal organization, cell area, cell elongation, and formation of focal adhesions. The interactions of the cells with the submicron pillars were found to be subordinate to the settling state of the cells. The "top state" observed on submicron pillars with an interspacing of 700 nm shifted to a "mixed state" on submicron pillars with an interspacing of 1000 nm, meaning that in the latter, the cells not only interacted with the top of the pillars but also engulfed the whole pillar and came into contact with its lateral sides as well as the substrate. Both types of pillars significantly increased the expression of OPN as compared to a flat control surface. Afterwards, to overcome the restrictions of many fabrication techniques, namely being expensive and time-consuming, we used soft lithography to replicate the submicron pillars present on the original mold into the hybrid PDMS mold. The shape, morphology, and depth of the replicated patterns were analyzed with SEM and FIB, and the results confirmed the geometric fidelity of the hybrid replica. As

PDMS is not the material of choice for cell studies, we used hybrid PDMS molds as the master mold in thermal nanoimprint lithography to transfer the patterns to the thermoplastic resist coated on the desired final substrate (fused silica in our study). The results of this study clearly show the advantages of nanoimprint lithography as a unique high-throughput yet precise method for the patterning of large areas of bio-instructive surfaces, while guarantying the quality and resolution of the nanopatterns required for further biological assessments. The height/depth of the final patterns can be adjusted by optimizing the applied force and embossing temperature as well as through the application of specific etching steps.
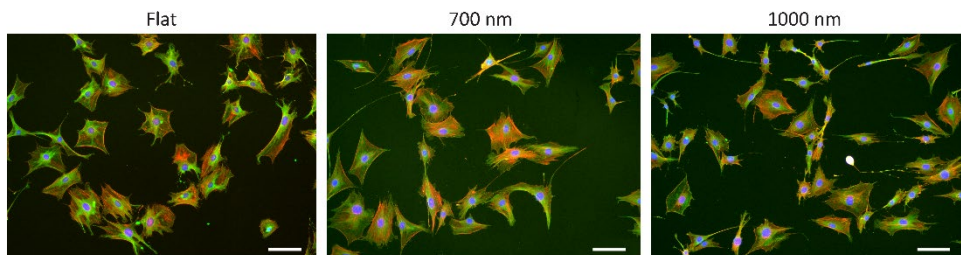
Supporting Information

Figure S1. Immunofluorescent staining of vinculin (green), actin (red), and nucleus (blue) of the MC3T3-E1 preosteoblast cells cultured on the flat and patterned specimens for 1 day.
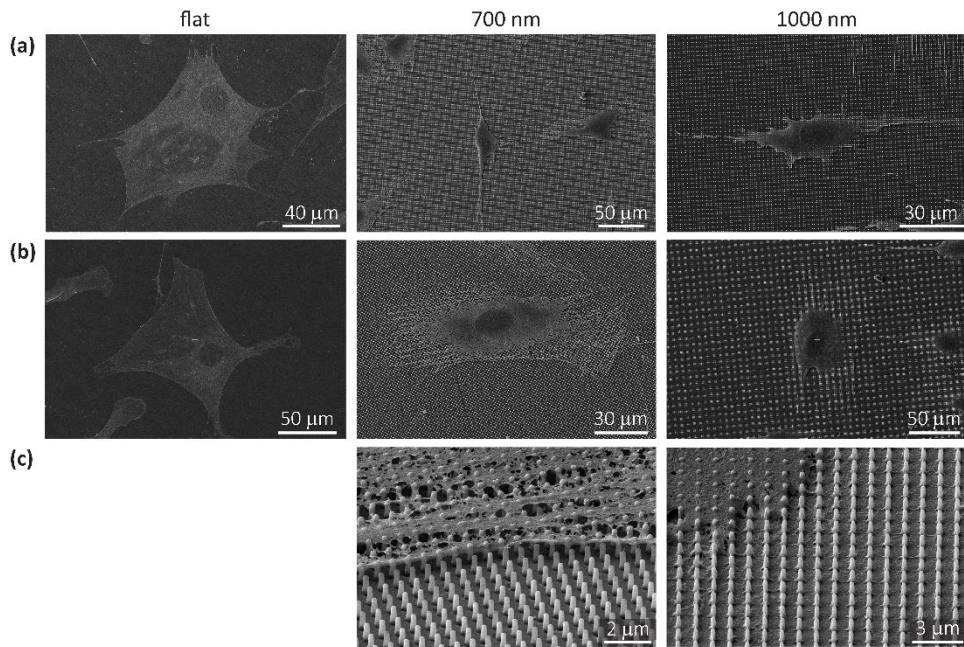
Figure S2. (a, b) Top view SEM images of the representative cell morphology on the flat and patterned specimens. (c) Highly magnified tilted SEM views of the settlement state of the cells on the patterned specimens and their interactions with the single pillars at cell periphery.

References

[1] A. Ekblad-Nordberg, L. Walther-Jallow, M. Westgren, C. Götherström, Prenatal stem cell therapy for inherited diseases: past, present, and future treatment strategies: concise review, Stem Cells Transl. Med. (2019).

[2] J. Ng, C.B. Little, S. Woods, S. Whittle, F.Y. Lee, S. Gronthos, S. Mukherjee, D.J. Hunter, D.L. Worthley, Stem cell directed therapies for osteoarthritis: the promise and the practice: concise review, Stem Cells (2019) .

[3] L. Zhao, A.D. Kaye, A.J. Kaye, A. Abd-Elsayed, Stem cell therapy for osteonecrosis of the femoral head: current trends and comprehensive review, Curr. Pain Headache Rep. 22 (6) (2018) 41.

[4] M. Ventre, P.A. Netti, Engineering cell instructive materials to control cell fate and functions through material cues and surface patterning, ACS Appl. Mater. Interfaces 8 (24) (2016) 14896–14908.

[5] A. Augello, C. De Bari, The regulation of differentiation in mesenchymal stem cells, Hum. Gene Ther. 21 (10) (2010) 1226–1238.

[6] M. Nouri-Goushki, L. Angeloni, K. Modaresifar, M. Minneboo, P.E. Boukany, M.J. Mirzaali, M.K. Ghatkesar, L.E. Fratila-Apachitei, A.A. Zadpoor, 3D-printed submicron patterns reveal the interrelation between cell adhesion, cell mechanics, and osteogenesis, ACS Appl. Mater. Interfaces 13 (29) (2021) 33767–33781.

[7] K. Modaresifar, S. Azizian, M. Ganjian, L.E. Fratila-Apachitei, A.A. Zadpoor, Bactericidal effects of nanopatterns, a systematic review, Acta Biomaterialia 83 (2019) 29–36.

[8] M. Salandova, I.A.J. van Hengel, I. Apachitei, A.A. Zadpoor, B.C.J. van der Eerden, L.E. Fratila-Apachitei, Inorganic agents for enhanced angiogenesis of orthopedic biomaterials, Adv. Healthc. Mater. 10 (12) (2021) e2002254.

[9] M. Fazel, H.R. Salimijazi, M. Shamanian, M. Minneboo, K. Modaresifar, I.A.J. van Hengel, L.E. Fratila-Apachitei, I. Apachitei, A.A. Zadpoor, Osteogenic and an-tibacterial surfaces on additively manufactured porous Ti-6Al-4V implants: combining silver nanoparticles with hydrothermally synthesized HA nanocrystals, Mater. Sci. Eng. C Mater. Biol. Appl. 120 (2021) 111745.

[10] H.N. Kim, A. Jiao, N.S. Hwang, M.S. Kim, D.-H. Kim, K.-Y. Suh, Nanotopography-guided tissue engineering and regenerative medicine, Adv. Drug Deliv. Rev. 65 (4) (2013) 536–558.

[11] C.R. Pedrosa, D. Arl, P. Grysan, I. Khan, S.p. Durrieu, S. Krishnamoorthy, M.-C. Durrieu, Controlled nanoscale topographies for osteogenic differentiation of mesenchymal stem cells, ACS Appl. Mater. Interfaces 11 (9) (2019) 8858–8866

[12] M.J. Dalby, N. Gadegaard, R.O. Oreffo, Harnessing nanotopography and integrin–matrix interactions to influence stem cell fate, Nat. Mater. 13 (6) (2014) 558–569.

[13] S. Dobbenga, L.E. Fratila-Apachitei, A.A. Zadpoor, Nanopattern-induced osteogenic differentiation of stem cells–a systematic review, Acta Biomater. 46 (2016) 3–14.

[14] K. von der Mark, J. Park, S. Bauer, P. Schmuki, Nanoscale engineering of biomimetic surfaces: cues from the extracellular matrix, Cell Tissue Res. 339 (1) (2010) 131.

[15] T. Sjostrom, M.J. Dalby, A. Hart, R. Tare, R.O. Oreffo, B. Su, Fabrication of pillar-like titania nanostructures on titanium and their interactions with human skeletal stem cells, Acta Biomater. 5 (5) (2009) 1433–1441.

[16] L.E. McNamara, T. Sjostrom, K.E. Burgess, J.J. Kim, E. Liu, S. Gordonov, P.V. Moghe, R.M. Meek, R.O. Oreffo, B. Su, M.J. Dalby, Skeletal stem cell phys- iology on functionally distinct titania nanotopographies, Biomaterials 32 (30) (2011) 7403–7410.

[17] C.-H. Chen, C.-C. Tsai, P.-T. Wu, I.-K. Wang, J. Yu, W.-B. Tsai, Modulation of neural differentiation through submicron-grooved topography surface with modified polydopamine, ACS Appl. Bio. Mater. 2 (1) (2018) 205–216.

[18] S. Watari, K. Hayashi, J.A. Wood, P. Russell, P.F. Nealey, C.J. Murphy, D.C. Genetos, Modulation of osteogenic differentiation in hMSCs cells by submicron topographically-patterned ridges and grooves, Biomaterials 33 (1) (2012) 128–136.

[19] M.J. Dalby, N. Gadegaard, R. Tare, A. Andar, M.O. Riehle, P. Herzyk, C.D. Wilkinson, R.O. Oreffo, The control of human mesenchymal cell differentiation using nanoscale symmetry and disorder, Nat. Mater. 6 (12) (2007) 997–1003.

[20] Y. Sun, C.S. Chen, J. Fu, Forcing stem cells to behave: a biophysical perspective of the cellular microenvironment, Annu. Rev. Biophys. 41 (2012) 519–542.

[21] M. Ganjian, K. Modaresifar, M.R. Ligeon, L.B. Kunkels, N. Tümer, L. Angeloni, C.W. Hagen, L.G. Otten, P.-L. Hagedoorn, I. Apachitei, L.E. Fratila-Apachitei, A.A. Zadpoor,

Nature helps: toward bioinspired bactericidal nanopatterns, Advanced Materials Interfaces 6 (16) (2019) 1900640.

[22] K. Modaresifar, L.B. Kunkels, M. Ganjian, N. Tümer, C.W. Hagen, L.G. Otten, P.-L. Hagedoorn, L. Angeloni, M.K. Ghatkesar, L.E. Fratila-Apachitei, A.A . Zadpoor, Deciphering the roles of interspace and controlled disorder in the bacterici- dal properties of nanopatterns against Staphylococcus aureus, Nanomaterilas 10 (2) (2020) 347.

[23] D.S. Widyaratih, P.-L. Hagedoorn, L.G. Otten, M. Ganjian, N. Tümer, I. Apachitei, C.W. Hagen, L.E. Fratila-Apachitei, A.A. Zadpoor, Towards osteogenic and bactericidal nanopatterns? Nanotechnology 30 (20) (2019) 20LT01.

[24] D.K. Oh , H. Jeong , J. Kim , Y. Kim , I. Kim , J.G. Ok , J. Rho , Top-down nanofabrication approaches toward single-digit-nanometer scale structures, J. Mech. Sci. Technol. 35 (3) (2021) 837–859 .

[25] M.N. M.N.U. Hashim, M. Md Arshad, A.R. Ruslinda, S. Rahman, M. Fathil, M.H. Ismail, Top-down nanofabrication and characterization of 20 nm silicon nanowires for biosensing applications, Plos One 11 (3) (2016) e0152318.

[26] M. Nouri-Goushki, M.J. Mirzaali, L. Angeloni, D. Fan, M. Minneboo, M.K. Ghatkesar, U. Staufer, L.E. Fratila-Apachitei, A.A . Zadpoor, 3d printing of large areas of highly ordered submicron patterns for modulating cell behavior, ACS Applied Materials and Interfaces 12 (1) (2019) 200–208.

[27] M. Ganjian, K. Modaresifar, H. Zhang, P.-L. Hagedoorn, L.E. Fratila-Apachitei, A.A. Zadpoor, Reactive ion etching for fabrication of biofunctional titanium nanostructures, Scientific Reports 9 (1) (2019) 1–20.

[28] E.P. Ivanova, J. Hasan, H.K. Webb, G. Gervinskas, S. Juodkazis, V.K. Truong, A.H.F. Wu, R.N. Lamb, V.A. Baulin, G.S. Watson, J.A. Watson, D.E. Mainwaring, R.J. Crawford, Bactericidal activity of black silicon, Nature Communications 4 (1) (2013) 1–7.

[29] F. Hizal, I. Zhuk, S. Sukhishvili, H.J. Busscher, H.C. van der Mei, C.-H. Choi, interfaces, Impact of 3D hierarchical nanostructures on the antibacterial efficacy of a bacteria-triggered self-defensive antibiotic coating, ACS Applied Materials and Interfaces 7 (36) (2015) 20304–20313.

[30] G. Yi, Y. Yuan, X. Li, Y. Zhang, ZnO nanopillar coated surfaces with substrate-dependent superbactericidal property, Small 14 (14) (2018) 1703159.

[31] P.M. Tsimbouri, L. Fisher, N. Holloway, T. Sjostrom, A. Nobbs, R.D. Meek, B. Su, M.J. Dalby, Osteogenic and bactericidal surfaces from hydrothermal ti- tania nanowires on titanium substrates, Scientific Reports 6 (1) (2016) 1–12.

[32] A. Jaggessar, A. Mathew, H. Wang, T. Tesfamichael, C. Yan, P.K. Yarlagadda, Mechanical, bactericidal and osteogenic behaviours of hydrothermally synthesised TiO_2 nanowire arrays, Journal of the Mechanical Behavior of Biomedical Materials 80 (2018) 311–319.

[33] S.H. Ahn, L.J. Guo, Large-area roll-to-roll and roll-to-plate nanoimprint lithography: a step toward high-throughput application of continuous nanoimprinting, ACS Nano 3 (8) (2009) 2304–2310.

[34] S.H. Ahn, L.J. Guo, High-speed roll-to-roll nanoimprint lithography on flexible plastic substrates, Adv. Mater. 20 (11) (2008) 2044–2049.

[35] A. Pandey, S. Tzadka, D. Yehuda, M. Schvartzman, Soft thermal nanoimprint with a 10 nm feature size, Soft Matter 15 (13) (2019) 2897–2904 .

[36] A. Jaggessar, H. Shahali, A. Mathew, P. Yarlagadda, Bio-mimicking nano and micro-structured surface fabrication for antibacterial properties in medical implants, J. Nanobiotechnol. 15 (1) (2017) 64.

[37] H. Su , X.R. Cheng , T. Endo , K. Kerman , Photonic crystals on copolymer film for label-free detection of DNA hybridization, Biosens. Bioelectron. 103 (2018) 158–162.

[38] J. Ahn , S. Kwon , S. Jung , W.S. Lee , J. Jeong , H. Lim , Y.B. Shin , J. Lee , Fabrication of pyrrole-based electrochemical biosensor platform using nanoimprint lithography, Adv. Mater. Interfaces 5 (8) (2018) 1701593.

[39] M. Vaisman, N. Jain, Q. Li , K.M. Lau, E. Makoutz, T. Saenz, W.E. McMahon, A.C. Tamboli, E.L. Warren, GaAs solar cells on nanopatterned Si substrates, IEEE J. Photovoltaics 8 (6) (2018) 1635–1640 .

[40] W.-C. Tsao, Q.-C. Zeng, Y.-H. Yeh, C.-H. Tsai, H.-F. Hong, C.-Y. Chen, T.-Y. Lin, Y.-Y. Huang, C.-W. Tsao, J.-W. Pan, Efficiency evaluation of a hybrid miniatur- ized concentrated photovoltaic for harvesting direct/diffused solar light, J. Opt. (2019).

[41] F. Viela, I. Navarro-Baena, J.J. Hernández, M.R. Osorio, I. Rodríguez, Moth–eye mimetic cytocompatible bactericidal nanotopography: a convergent design, Bioinspiration Biomimetics 13 (2) (2018) 026011.

[42] F. Kantawong, K.E. Burgess, K. Jayawardena, A. Hart, R.J. Burchmore, N. Gadegaard, R.O. Oreffo, M.J. Dalby, Whole proteome analysis of osteoprogenitor differentiation induced by disordered nanotopography and mediated by ERK signalling, Biomaterials 30 (27) (2009) 4723–4731.

[43] J.R. Wang, S.F. Ahmed, N. Gadegaard, R.D. Meek, M.J. Dalby, S.J. Yarwood, Nanotopology potentiates growth hormone signalling and osteogenesis of mesenchymal stem cells, Growth Horm. IGF Res. 24 (6) (2014) 245–250.

[44] M.J. Dalby, N. Gadegaard, R. Tare ,A. Andar, M.O. Riehle, P. Herzyk, C.D. Wilkinson, R.O. Oreffo, The control of human mesenchymal cell differentiation using nanoscale symmetry and disorder, Nat. Mater. 6 (12) (2007) 997–1003.

[45] S. Li, D. Chu, A review of thin-film transistors/circuits fabrication with 3D self- aligned imprint lithography, Flexible Printed Electron. 2 (1) (2017) 013002.

[46] Z. Wang, P. Yi, L. Peng, X. Lai, J. Ni, Continuous fabrication of highly conductive and transparent ag mesh electrodes for flexible electronics, IEEE Trans. Nan- otechnol. 16 (4) (2017) 687–694.

[47] X. Gao, Y. Huang, X. He, X. Fan, Y. Liu, H. Xu, D. Wu, C. Wan, Mechanically enhanced electrical conductivity of polydimethylsiloxane-based composites by a hot embossing process, Polymers 11 (1) (2019) 56 .

[48] S. Callens, D. Fan, I. van Hengel, M. Minneboo, L.E. Fratila-Apachitei, A.A. Zadpoor, Emergent collective organization of bone cells in complex curvature fields, bioRxiv (2020)

[49] U. Horzum, B. Ozdil, D.J.M. Pesen-Okvur, Step-by-step quantitative analysis of focal adhesions, MethodsX 1 (2014) 56–59 .

[50] V. Bhingardive, L. Menahem, M. Schvartzman, Soft thermal nanoimprint lithography using a nanocomposite mold, Nano Res. 11 (5) (2018) 2705–2714.

[51] K.L. Lai, M.H. Hon, I.C. Leu , Pattern formation on polymer resist by solvent-assisted nanoimprinting with PDMS mold as a solvent transport medium, J. Micromech. Microeng. 21 (7) (2011).

[52] W.-X. Su, C.-Y. Wu, Y.-C. Lee, Anti-reflection nano-structures fabricated on curved surface of glass lens based on metal contact printing lithography, Microelectron. Eng. 214 (2019) 15–20.

[53] M.D. Cabezas, B. Meckes, C.A. Mirkin, M. Mrksich, Subcellular control over focal adhesion anisotropy, independent of cell morphology, dictates stem cell fate, ACS Nano 13 (10) (2019) 11144–11152 .

[54] M. Bao, J. Xie, A. Piruska, W.T.S. Huck, 3D microniches reveal the importance of cell size and shape, Nature Communications 8 (1) (2017) 1–12.

[55] F. Jiao, Y. Zhao, Q. Sun, B. Huo, Spreading area and shape regulate the apoptosis and osteogenesis of mesenchymal stem cells on circular and branched mi- cropatterned islands, Journal of Biomedical Materials Research 108 (10) (2020) 2080–2089.

[56] A. Ron, E.U. Azeloglu, R.C. Calizo, M. Hu, S. Bhattacharya, Y. Chen, G. Jayaraman, S. Lee, S.R. Neves-Zaph, H. Li, Cell shape information is transduced through tension-independent mechanisms, Nat. Commun. 8 (1) (2017) 1–15.

[57] H. Seong, S.G. Higgins, J. Penders, J.P. Armstrong, S.W. Crowder, A.C. Moore, J.E. Sero, M. Becce, M.M. Stevens, Size-tunable nanoneedle arrays for influencing stem cell morphology, gene expression, and nuclear membrane curvature, ACS Nano 14 (5) (2020) 5371–5381.

[58] K. Modaresifar, M. Ganjian, L. Angeloni, M. Minneboo, M.K. Ghatkesar, P.-L. Hagedoorn, L.E. Fratila-Apachitei, A.A. Zadpoor, On the use of black Ti as a bone substituting biomaterial: behind the scenes of dual-functionality, Small (2021) 2100706.

[59] F. Viela, D. Granados, A. Ayuso-Sacido, I. Rodríguez, Biomechanical cell regulation by high aspect ratio nanoimprinted pillars, Adv. Funct. Mater. 26 (31) (2016) 5599–5609.

[60] C.W. Kuo, D.-Y. Chueh, P. Chen, Investigation of size–dependent cell adhesion on nanostructured interfaces, J. Nanobiotechnol. 12 (1) (2014) 1–10.

[61] F. Viela, D. Granados, A. Ayuso-Sacido, I. Rodríguez, Biomechanical cell regulation by high aspect ratio nanoimprinted pillars, Adv. Funct. Mater. 26 (31) (2016) 5599–5609.

[62] S.G. Higgins, M. Becce, A. Belessiotis-Richards, H. Seong, J.E. Sero, M.M. Stevens, High-aspect-ratio nanostructured surfaces as biological metamaterials, Adv. Mater. 32 (9) (2020) e1903862.

[63] J. Hasan, S. Jain, K. Chatterjee, Nanoscale topography on black titanium imparts multi-biofunctional properties for orthopedic applications, Sci. Rep. 7 (2017) 41118.

[64] A. Ray, O. Lee, Z. Win, R.M. Edwards, P.W. Alford, D.-H. Kim, P.P. Provenzano, Anisotropic forces from spatially constrained focal adhesions mediate contact guidance directed cell migration, Nat. Commun. 8 (1) (2017) 1–17.

[65] M. Werner, S.B. Blanquer, S.P. Haimi, G. Korus, J.W. Dunlop, G.N. Duda, D.W. Grijpma, A. Petersen, Surface curvature differentially regulates stem cell migration and differentiation via altered attachment morphology and nuclear deformation, Adv. Sci. 4 (2) (2017) 1600347.

[66] D. Quéré, Wetting and roughness, Annual Review of Materials Research 38 (2008) 71–99.

[67] N. Vrancken, S. Sergeant, G. Vereecke, G. Doumen, F. Holsteyns, H. Terryn, S. De Gendt, X. Xu, Superhydrophobic breakdown of nanostructured surfaces characterized in situ using ATR–FTIR, Langmuir 33 (15) (2017) 3601–3609.

[68] E. Baquedano, R.V. Martinez, J.M. Llorens, P.A. Postigo, Fabrication of silicon nanobelts and nanopillars by soft lithography for hydrophobic and hydrophilic photonic surfaces, Nanomaterials 7 (5) (2017) 109.

[69] T.W. Odom, J.C. Love, D.B. Wolfe, K.E. Paul, G.M. Whitesides, Improved pattern transfer in soft lithography using composite stamps, Langmuir 18 (13) (2002) 5314–5320.

[70] C. Masciullo, A. Sonato, F. Romanato, M. Cecchini, Perfluoropolyether (PFPE) intermediate molds for high-resolution thermal nanoimprint lithography, Nano- materials 8 (8) (2018) 609.

[71] H. Schmid, B. Michel, Siloxane polymers for high-resolution, high-accuracy soft lithography, Macromolecules 33 (8) (2000) 3042–3049.

[72] C. Zheng, Nanofabrication: principles, capabilities, and limits, Springer, 2016.

[73] A. Shamsi, A. Amiri, P. Heydari, H. Hajghasem, M. Mohtashamifar, M. Esfandiari, Low cost method for hot embossing of microstructures on PMMA by SU-8 masters, Microsyst. Technol. 20 (10–11) (2013) 1925–1931.

[74] M. Kim, B.-U. Moon, C.H. Hidrovo, Enhancement of the thermo-mechanical properties of PDMS molds for the hot embossing of PMMA microfluidic de- vices, J. Micromech. Microeng. 23 (9) (2013) 095024

[75] J. Chen, J. Shi, A. Cattoni, D. Decanini , Z. Liu, Y. Chen, A.-M. Haghiri-Gosnet, A versatile pattern inversion process based on thermal and soft UV nanoimprint lithography techniques, Microelectron. Eng. 87 (5–8) (2010) 899–903.

8

General discussion and conclusions

General Discussion

With the main purpose of developing fabrication techniques to produce nano/submicron patterns with dual-biofunctionality (*i.e.,* directing stem cell fate and at the same time killing the bacteria adhered to the surface of bone implants), this thesis was focused on expanding the applications of the current nanofabrication methodologies in the design of biomaterials and implants. In general, the results of this thesis show that surface nano/submicron features, with specific dimensions and mechanical properties, create the type of stimulus required to influence both bacterial and mammalian cell responses. A number of relevant topics are highlighted and discussed in the following subsections.

8.1. Comparison between available nanofabrication techniques

A wide range of nano/submicron fabrication techniques has emerged in the recent years. The minimum feature sizes that these methods can fabricate as well as the controllability, speed, and throughput of the processes widely vary from one process to another. Moreover, the type of the materials that can be processed is highly dependent on the principle and specifications of the selected nanofabrication technique

In this section, the techniques developed in the previous chapters are presented and compared with each other to provide a general overview of their advantages and disadvantages.

8.1.1. Accuracy and resolution

Among the developed fabrication techniques, electron beam-induced deposition (EBID) and electron beam lithography (EBL) use focused electron beam to create the desired 3D nanostructures on the substrate. With careful optimization of the beam parameters, these techniques can reach sub-10 nm resolutions [1]. For instance, Van Drop *et al.* could successfully fabricate arrays of dots with a diameter of 2 nm and an interspacing of 4 nm using EBID [2]. The resolution of the patterns fabricated with EBL is determined by the resist contrast, beam spot size, electron scattering, the proximity effect of the primary and secondary electrons, and resist development [3]. By fine-tuning of these parameters,

Manfrinato *et al.* could successfully fabricate 2 nm features with a pitch of 10 nm using the hydrogen silsesquioxane (HSQ) resist [3].

Using soft lithography, patterns with the feature sizes above 500 nm can be easily replicated into PDMS [4]. However, the low elastic modulus of PDMS limits the minimum feature size and maximum aspect ratio of the patterns that can be faithfully replicated. Using a combination of hard PDMS (hPDMS, a thin and stiff layer with thickness = 30-40 μm) and PDMS (as a thick and flexible support layer with thickness = 1-5 mm) can extend the range of applicability of soft lithography to replicate patterns containing sub-10 nm feature sizes [5, 6].

Nanoimprint lithography (NIL) is a promising technique to generate patterns with a resolution of sub-10 nm [7]. The resolution of NIL is mostly determined by the resolution of the master mold, which is usually fabricated by EBL or optical lithography. However, the uniformity of applied force, the thickness of the thermoplastic material, chamber pressure, and smoothness of the substrate all play important roles in the fidelity of the transferred patterns. Recently, Thirumalai *et al.,* have demonstrated the potential of NIL to replicate patterns with a feature size of 2.4 nm [8].

As opposed to the above-mentioned techniques that can guarantee the fabrication of sub-100 nm features, the accuracy and controllability of inductively coupled plasma enhanced reactive ion etching (ICP RIE) are quite low. Even though proper selection of the etching parameters allows for some levels of control over the general morphology, total height, and approximate interspacing of the created pillars, full control over the shape and diameter of the pillars is not feasible with ICP RIE. For instance, in the case of black Ti presented in this thesis (Chapter 5), we could not change the diameter of the nanopillars by changing the etching parameters despite the fact that it did not exceed 100 nm [9].

8.1.2. Speed

Although an electron beam can be focused into a very small spot, thereby creating very high-resolution features, it is fundamentally limited in its throughput due to the sequential nature of such exposures. Therefore, EBID and EBL are considered to be the slowest techniques considered in the current thesis. There is, however, a major difference between EBL and EBID with EBL being 100 to 1000 times faster than EBID [3].

Given such low throughputs, electron beam-based techniques are limited in their capability to fabricate samples that can be used for the study of cell-nanopatterns interaction, as their speed limits the surface area and number of available specimens. However, EBL can be used to fabricate the master mold that is then employed for soft lithography and NIL. Both soft lithography and NIL are promising nanopatterning techniques with low cost, high-throughput, and high degrees of reproducibility. NIL, in particular, is a facile and high-yield solution for the mass production of micro/nanopatterns over the entire wafer area. A single master mold fabricated using slow and high-resolution techniques can be used over 20 times to transfer the generated patterns with high fidelity and within a short time [4, 10].

As opposed to electron beam-based techniques, ICP RIE is a fast and high-throughput technique. Using ICP RIE, patterns can be created within a few minutes and in a single step, without any need for a mask. Moreover, the desired process recipe can be run on the entire specimen, which can be as large as a 4-inch wafer. Novel approaches have been developed in this thesis to incorporate the surface patterns into the 3D metallic surfaces

8.1.3. Choice of the material

Using EBID, a variety of metallic structures can be deposited through a proper choice of the precursor gas. The most commonly used precursor gases are based on organometallics containing Pt, Fe, W, Ni, Cu, and Au [11]. One of the limitations with EBID-made structures is the existence of a high level of carbon content in the final metallic structures. This phenomenon is caused by the organometallic precursors. Post-purification techniques need to be applied to decrease the amount of organic impurities and increase the metallic content. Moreover, while using EBID, the patterns and the substrate are of different materials; new precursors should be developed for biomaterials. Soft lithography only works with a limited number of materials. Using this technique, patterns can only be replicated on the surface of elastomeric materials (mostly PDMS). Despite all the favorable properties of PDMS and other elastomeric materials, they do not necessarily meet the mechanical and material properties required for all applications. EBL and NIL, on the other hand, can be applied to the vast majority of practically relevant substrates, from polymers [12] and dielectrics [13-17] to semi-conductors [18-21] and metals [15, 22, 23]. For each of those materials, the appropriate resist, hard mask, and etching process should be selected. Maskless dry ICP RIE process has

been already established to create nanopillars on Ti [9, 24], Si [25], GaN [26], and GaAs [27] substrates. However, by adjusting etching gasses and parameters, the ICP RIE process can be developed for some other types of metals and semiconductors.

8.2. Bactericidal properties

8.2.1. EBID nanopillars

The results of our study (Chapters 2 and 3) illustrated that nanopillars can mechanically rupture and thoroughly damage *E. coli* and *S. aureus* [28]. Decreasing the interspacing between the nanopillars could significantly improve the bactericidal effect (Chapter 3). As it is believed that the dominant killing mechanism is the penetration of nanopillars into the bacterial cell wall, the high density of nanopillars provides more contact points between the nanopillars and bacteria, resulting in much more physicomechanical interactions and increasing the chance of damaging or killing the bacteria [28]. In addition, our results (Chapter 3) show that, as long as the interspacing is constant, introducing controlled disorder in the arrangement of the nanopillars does not enhance the killing efficiency of the nanopillars against *S. aureus*. The killing efficiency of nanopillars against *E. coli* was much higher than against *S. aureus*. This could be explained by the thicker and more rigid cell wall of *S. aureus*, which necessitates higher forces being exerted for the same killing efficiency.

8.2.2. bTi surfaces

Culturing of *S. aureus* on three distinct bTi surfaces fabricated using ICP RIE revealed that all bTi surfaces are bactericidal (Chapter 5). The pressure and temperature of the chamber were considered the parameters that have the major impact on the shape and morphology of the resultant bTi surfaces. Therefore, three distinct bTi surfaces from Porous-like bTi to Partition and then to Sparse were achieved by changing these two parameters. The results of live/dead staining revealed that the bactericidal efficiency has significantly increased from the Porous morphology to Partition and Sparse, meaning that Sparse bTi has the highest killing efficiency. However, the results of our study suggest the hypothesis that the principal killing mechanism is different for each type of the bTi surface. For instance, on the Porous bTi, the bacteria were mostly damaged because of the stretching of their cell wall on the surface. On the Sparse bTi, on the other hand, the bacteria were damaged/killed through a combination of different mechanisms: the stretching of the bacterial cell wall

between neighboring pillars, penetration of the pillars into the cells wall, and bending of the pillars. The killing efficiency of such surfaces is expected to be even higher against Gram-negative bacteria where their thinner cell wall makes the penetration of the pillars into the bacteria much easier [30]. The results of our study show the capability of the ICP RIE technique to fabricate bactericidal patterns on the surface of Ti, as one of the most suitable materials for bone implants.

8.3. Investigation of MC3T3-E1 cell response

8.3.1. Adaptation of preosteoblast cells to fused silica submicron pillars

Assessing the response of the MC3T3-E1 preosteoblasts to the fused silica submicron pillars revealed that changing the interspacing significantly influences the cytoskeletal organization, cell area, cell elongation, and formation of focal adhesions (Chapter 7). As compared with flat fused silica substrates, the cells residing on the submicron pillars were more elongated with a decreased area. By increasing the interspacing of the pillars from 700 nm to 1000 nm, the spreading area decreased even further (Chapter 7). The results could be explained by the fact that by increasing the interspacing, the cells tend to minimize the area to secure their initial adhesion points or keep an optimized membrane trafficking. Moreover, the increased aspect ratio of the cells (*i.e.,* elongation) on submicron pillars is believed to be beneficial for osteogenic differentiation [24, 30]. It has been shown that the area and morphology of the cells influence the cytoskeletal organization and formation and distribution of FAs, which together regulate the stem cell fate [31, 32].

8.3.2. Adaptation of Preosteoblast Cells to bTi Surfaces

Based on the metabolic activity measurements and microscopic observations, preosteoblast cells could proliferate on all types of bTi surfaces (Chapter 5). However, the cells exhibit different morphologies and cytoskeletal organizations on each surface. Generally speaking, the cells try to find as many proper anchorage points as possible. The Sparse surfaces do not provide close-enough anchorage points for them. Therefore, the cells minimize their area and stay connected to the anchorage points through elongation of their morphology. On the Porous bTi surfaces, however, there are enough physical features that allow the cells to stay anchored without having to extremely stretch their membrane.

The results of our study are in consistent with the results of studies where the morphology of cells cultured on submicron pillars are studied [33]. According to those studies, cells tend to confine their area and present an elongated morphology on more separated pillars. However, other physical cues, such as the dimensions and aspect ratio of the features and their mechanical properties play important roles in determining the stem cell fate too [29].

8.4. Mechanical characterization of 3D printed nanopillars by AFM

Contact mode (CM) and Quantitative imaging (QI) are well-established modes in AFM. We developed (Chapter 4) a new application for these modes that, together with finite element modeling (FEA) simulations, enables us to measure the mechanical properties of EBID nanopillars (including elastic modulus, fracture force, the maximum displacement of the tip under the interaction with the bacteria, and failure stress), as well as the interaction forces between the nanopillars and the bacterial. To the best of our knowledge, it was the first time that the fracture stress of the Pt-C EBID nanopillars was measured. However, our measured values are in agreement with those reported in the literature on bigger structures deposited by EBID using other types of precursors (1–3 GPa) [35]. This confirms the potential of our AFM-based method for measuring the mechanical properties of nanopillars.

The findings of our study are instrumental in optimizing the geometry and the mechanical properties of nanopillars aimed at improving their killing efficiency.

From our analysis, we concluded that the mechanical properties of the nanopillars is one of the key parameters that can help to increase the bactericidal efficiency of nanopillars. The mechanical properties of EBID nanopillars can be tuned by (i) increasing the elastic modulus of the deposited structure with changing the beam parameters (*i.e.,* voltage, beam current, electron dose, etc.) to increase the penetration of the pillars into the bacterial membrane, (ii) increasing the fracture strength of the material to prevent the fracture of the tip, and (iii) optimizing the geometry of the nanopillars, for example, by increasing the diameter of nanopillars.

8.5. Metal crumpling for the fabrication of nanopatterned meta-biomaterials

To address the limitation of the nanofabrication techniques for creating nanopatterns on nonplanar/3D surfaces, a novel crumpling technique was proposed and developed to fabricate 3D metallic scaffolds as (regenerative) bone substitutes with desired size, porosity, and mechanical properties from flat nanopatterned porous Ti sheets (Chapter 6). To be suitable for bone substitute application, a crumpled scaffold requires to be eligible to carry the musculoskeletal loads while its regenerative capabilities (*i.e.,* surface nanopatterns) are preserved during the process of crumpling. Three different surface porosities of the 2D sheets led to three different volume porosity of the 3D scaffolds, meaning that the final porosity can be controlled by the rational design of the porosity of the initial sheet. µCT and FEA showed that applying low or high deformation velocity did not significantly change the morphological and mechanical properties of the final scaffolds. The adaptation of MC3T3-E1 preosteoblast cells to nanopatterned scaffolds was found to be similar to previous reports on identical nanopatterns created on flat Ti sheets. The various functionalities of our design including the adjustablity of the dimensions, porosity, pore size, deformation velocity, mechanical properties, and its potential to incorporate nanopatterns make the crumpling technique a potent one to fabricate bone substitutes with enhanced biofunctionalites.

8.6. Recommendations for future research

Although this thesis has contributed to the development of novel fabrication techniques with an aim to study cell-nanopatterns interactions, there is still a long list of questions that remain unanswered. Here, I highlight some general and some specific suggestions for future work to answer those questions.

Nanotopography

Recent progress in nanofabrication techniques has attracted the interest of researchers in various fields of inquiry. The ever-increasing accuracy and precision of these techniques are providing unprecedented opportunities for controlling the general shape as well as every single dimension of the fabricated nanostructures. However, there are still several challenges that need to be addressed in future studies to foster the applications of these feature sizes.

- Although EBID is a precise and accurate nanofabrication method with the potential to 3D print nanofeatures with arbitrarily shape and morphologies with sub-10 nm resolutions [35], upscaling the patterned area remains challenging. To create nanopatterned surfaces that are suitable for cell culture studies using mammalian cells, it is highly important to upscale the patterned area. One solution could be using multiple electron beams in parallel. For instance, Gheidari *et al.* [35] have already developed an EBID system that sheds an array of 14×14 focused beams onto the specimen to expose a larger area and speed up the process by 196 times. Another technique that can help to improve EBID throughput is the application of thermal nanoimprint lithography. In this regard, the substrate that contains the EBID nanopatterns is used as the master mold. The master mold can be used several times to transfer the patterns onto the substrate of interest.

- It is crucial to expand the applications of the current nano/submicron techniques with an aim to produce the cell-instructive features on the surface of widely used biomaterials for bone substitutes.

- As there are different types of cues that can affect the cell response, including surface (local) geometry, nanoscale topography, chemical, and the mechanical properties of the substrate, there is a need for a methodological platform that enables us to change all the aforementioned parameters both independently and in combination with each other. Such a platform would enable us to better understand how different parameters affect the cell response.

- Using *in-silico* approaches can help one to predict the best geometrical and mechanical properties for nanopatterns in a way that they exhibit bactericidal response and, at the same time, regulate the stem cell fate.

Regarding 3D geometry

- Currently, there is a wide range of nanofabrication techniques that could be used to create patterns on flat substrates. However, for bone implant applications, there is a need for non-flat patterned substrates with specific geometries. The geometrical features of the substrate can regulate the cell response as well [36]. Therefore, to assess the influence of nanofeatures and geometry at the same time, it is important to further develop the current nanofabrication techniques and make them applicable to non-planar substrates.

- In the case of nanopatterned scaffolds, the effects of porosity, shape, size, and distribution of the pores on the seeding, spreading, migration, and settlement of cells, on the one hand, and on the mechanical properties of the scaffolds, on the other hand, need to be further investigated.

- There is a need for a crumpling setup that can create small-scale scaffolds with dimensions comparable to those of the mice bone to conduct *in vivo* experiments on crumpled nanopatterned scaffolds.

- In addition to crumpling, folding and origami are some other techniques that can help us achieve the desired 3D geometry while also satisfying the design requirements in terms of surface nanopattern.

References

[1] P.A. Crozier, C.W. Hagen, Applications, High-Resolution Electron-Beam-Induced Deposition, Nanofabrication (2008), 399-430.

[2] W.F. Van Dorp, B. Van Someren, C.W. Hagen, P. Kruit, P.A. Crozier, Approaching the resolution limit of nanometer-scale electron beam-induced deposition, Nanoletters 5(7) (2005), 1303-1307.

[3] V.R. Manfrinato, L. Zhang, D. Su, H. Duan, R.G. Hobbs, E.A. Stach, K.K. Berggren, Resolution limits of electron-beam lithography toward the atomic scale, Nanoletters 13(4) (2013), 1555-1558.

[4] Z. Cui, Nanofabrication: Principles, Capabilities, and Limits, Springer 2016.

[5] A. Pandey, S. Tzadka, D. Yehuda, M. Schvartzman, Soft thermal nanoimprint with a 10 nm feature size, Soft Matter 15(13) (2019) 2897-2904.

[6] D. Qin, Y. Xia, G.M. Whitesides, Soft lithography for micro- and nanoscale patterning, Nat Protoc 5(3) (2010) 491-502.

[7] D.K. Oh, H. Jeong, J. Kim, Y. Kim, I. Kim, J.G. Ok, J. Rho, Top-down nanofabrication approaches toward single-digit-nanometer scale structures, Journal of Mechanical Science and Technology 35(3) (2021) 837-859.

[8] J. Thirumalai, Micro/Nanolithography: A Heuristic Aspect on the Enduring Technology, (2018).

[9] M. Ganjian, K. Modaresifar, H. Zhang, P.-L. Hagedoorn, L.E. Fratila-Apachitei, A.A. Zadpoor, Reactive ion etching for fabrication of biofunctional titanium nanostructures, Scientific Reports 9(1) (2019) 1-20.

[10] J. Chen, J. Shi, A. Cattoni, D. Decanini, Z. Liu, Y. Chen, A.-M. Haghiri-Gosnet, A versatile pattern inversion process based on thermal and soft UV nanoimprint lithography techniques, Microelectronic Engineering 87(5-8) (2010) 899-903.

[11] J.D. Wnuk, S.G. Rosenberg, J.M. Gorham, W.F. van Dorp, C.W. Hagen, D.H. Fairbrother, Electron beam deposition for nanofabrication: Insights from surface science, Surface Science 605(3-4) (2011) 257-266.

[12] K. Scholten, E.J.M. Meng, nanoengineering, Electron-beam lithography for polymer bioMEMS with submicron features, 2(1) (2016) 1-7.

[13] P. Sadeghi, K. Wu, T. Rindzevicius, A. Boisen, S. Schmid, Fabrication and characterization of Au dimer antennas on glass pillars with enhanced plasmonic response, Nanophotonics 7(2) (2017) 497-505.

[14] V. Canalejas-Tejero, A.L. Hernández, R. Casquel, S.A. Quintero, M.F. Laguna, M. Holgado, Fabrication of Si3N4/SiO2 tiered resonant nanopillars with nickel caps arrays: application for optochemical sensing, Optical Materials Express 8(4) (2018).

[15] G. Yoon, D. Lee, J. Rho, Demonstration of Equal-Intensity Beam Generation by Dielectric Metasurfaces, Engineering (148) (2019).

[16] M.N. Hossain, J. Justice, P. Lovera, B. McCarthy, A. O'Riordan, B. Corbett, High aspect ratio nano-fabrication of photonic crystal structures on glass wafers using chrome as hard mask, 25(35) (2014) 355301.

[17] Z. Li, Q. Xiang, M. Zheng, K. Bi, Y. Chen, K. Chen, H. Duan, Microengineering, Fabrication of 3D SiOx structures using patterned PMMA sacrificial layer, Journal of Micromechanics and Microengineering 28(2) (2018) 024005.

[18] Y. Zheng, X. Kai, P. Gao, J. Duan, Fabrication tolerance analysis of grating couplers between optical fibers and silicon waveguide, Optik 201 (2020) 163490.

[19] J.L. Hammond, M.C. Rosamond, S. Sivaraya, F. Marken, P. Estrela, Fabrication of a horizontal and a vertical large surface area nanogap electrochemical sensor, Sensors 16(12) (2016) 2128.

[20] L. D'Ortenzi, R. Monsù, E. Cara, M. Fretto, S. Kara, S. Rezvani, L. Boarino, Electrical contacts on silicon nanowires produced by metal-assisted etching: a comparative approach, Nanoscale Research Letters 11(1) (2016) 1-6.

[21] M.N. M. N, U. Hashim, M. Md Arshad, A.R. Ruslinda, S. Rahman, M. Fathil, M.H. Ismail, Top-down nanofabrication and characterization of 20 nm silicon nanowires for biosensing applications, Plos One 11(3) (2016) e0152318.

[22] C. Hammann, C.T.H. Heerkens, C. Hagen, A.A. Zadpoor, L.E. Fratila-Apachitei, Direct submicron patterning of titanium for bone implants, Microelectronic Engineering 195 (2018) 13-20.

[23] S.F. Gilmartin, K. Arshak, D. Bain, W.A. Lane, D. Collins, A. Arshak, B. McCarthy, S.B. Newcomb, M. Walsh, Development of a titanium plasma etch process for uncooled titanium nanobolometer fabrication, Microelectronic Engineering 86(4-6) (2009) 971-975.

[24] J. Hasan, S. Jain, K. Chatterjee, Nanoscale topography on black titanium imparts multi-biofunctional properties for orthopedic applications, Scientific Reports 7(1) (2017) 1-13.

[25] E.P. Ivanova, J. Hasan, H.K. Webb, G. Gervinskas, S. Juodkazis, V.K. Truong, A.H.F. Wu, R.N. Lamb, V.A. Baulin, G.S. Watson, J.A. Watson, D.E. Mainwaring, R.J. Crawford, Bactericidal activity of black silicon, Nature Communications 4(1) (2013) 1-7.

[26] Y. Zhao, H. Wang, W. Zhang, J. Li, Y. Shen, Z. Huang, J. Zhang, A. Dingsun, Controllable process of nanostructured GaN by maskless inductively coupled plasma (ICP) etching, Microengineering, 27(11) (2017) 115004.

[27] P. Lova, V. Robbiano, F. Cacialli, D. Comoretto, C. Soci, interfaces, Black GaAs by metal-assisted chemical etching, ACS Appl. Mater. Interfaces 10(39) (2018) 33434-33440.

[28] K. Modaresifar, L.B. Kunkels, M. Ganjian, N. Tumer, C.W. Hagen, L.G. Otten, P.-L. Hagedoorn, L. Angeloni, M.K. Ghatkesar, L.E. Fratila-Apachitei, A.A. Zadpoor, Deciphering the Roles of Interspace and Controlled Disorder in the Bactericidal Properties of Nanopatterns against Staphylococcus aureus, Nanomaterials (Basel) 10(2) (2020).

[29] K. Modaresifar, M. Ganjian, L. Angeloni, M. Minneboo, M.K. Ghatkesar, P.-L. Hagedoorn, L.E. Fratila-Apachitei, A.A. Zadpoor, On the Use of Black Ti as a Bone Substituting Biomaterial: Behind the Scenes of Dual-Functionality, Small (2021) e2100706.

[30] S. Watari, K. Hayashi, J.A. Wood, P. Russell, P.F. Nealey, C.J. Murphy, D.C. Genetos, Modulation of osteogenic differentiation in hMSCs cells by submicron topographically-patterned ridges and grooves, Biomaterials 33(1) (2012) 128-136.

[31] M. Ermis, E. Antmen, V. Hasirci, Micro and Nanofabrication methods to control cell-substrate interactions and cell behavior: A review from the tissue engineering perspective, Bioactive Materials 3(3) (2018) 355-369.

[32] S. Oh, K.S. Brammer, Y.J. Li, D. Teng, A.J. Engler, S. Chien, S. Jin, Stem cell fate dictated solely by altered nanotube dimension, 106(7) (2009) 2130-2135.

[33] M. Nouri-Goushki, L. Angeloni, K. Modaresifar, M. Minneboo, P.E. Boukany, M.J. Mirzaali, M.K. Ghatkesar, L.E. Fratila-Apachitei, A.A. Zadpoor, 3D-Printed Submicron Patterns Reveal the Interrelation between Cell Adhesion, Cell Mechanics, and Osteogenesis, ACS Appl. Mater. Interfaces 13 (29) (2021) 33767–33781.

[34] I. Utke, J. Michler, R. Winkler, H. Plank, Mechanical Properties of 3D Nanostructures Obtained by Focused Electron/Ion Beam-Induced Deposition: A Review, 11(4) (2020) 397.

[35] A. Mohammadi-Gheidari, 196 Beams in a Scanning Electron Microscope, (2013).

[36] S. Callens, D. Fan, I. van Hengel, M. Minneboo, L.E. Fratila-Apachitei, A.A. Zadpoor, Emergent collective organization of bone cells in complex curvature fields, (2020).

Acknowledgments

Around 4 years ago, I came to the Netherlands to start my Ph.D. journey. At the very beginning, I expected a straightforward way, with very few ups and downs. Nevertheless, I was wrong, and this journey was full of unexpected challenges. Without having so many friendly people around, I could not finish the final step of my official student life.

Maman joon and **baba** joon, my lovely parents, I would like to state my most profound appreciation to you. I am quite fortunate and grateful to grow up under your parenting. Maman joon, having you with your lovely heart is my most valuable treasure. Baba joon, since adolescence, whatever my decision was, I was quite sure that I would have your unconditional support. My dear brother, **Mohammad**, I was 6 years old when you were born, and I do not remember how life was for me before you came. With you, I always have the kindest friend and consultant, even when we are far away from each other.

I would like to express my gratitude to my promotor and supervisor: Prof **Amir A. Zadpoor** and Dr. **Lidy E. Fratila-Apachitei**. I was fortunate enough to perform my Ph.D. under your supervision at TU Delft. The door of your office was always open to me. Amir! I admire your project management and leadership style, giving freedom to your students, and motivating all your colleagues and collaborators. I remember one day, during the first year of my Ph.D., I came to your office while complaining about an issue that I had for one of my measurements. I was looking for a way to measure a specific parameter on my sample, and the available systems did not have that option. After hearing the whole story from me, you just calmly said:" Ok! But I am pretty sure that you will find a way for it." Interestingly, that simple response was enough for me and soon I found a solution. When working with you, there is no dead-end even in the most frustrating moments. I also enjoyed our discussions over non-scientific topics.

Dear Lidy, your comments and feedback guided me step by step through my Ph.D. We started with long meetings and sometimes they took 3 to 4 hrs in the first year. After knowing and understanding each other much better, we ended up with very short and to-the-point meetings (which sometimes took only 10 minutes) in the last year of my Ph.D.

I am so blessed and fortunate to have such kind family members in the neighboring countries, Belgium and Germany. **Amme Mahvash**, **Adi** joon, **Elham**, **Mehrvash**, **Jacques**, **Daei Vahid**, and **Atefeh** joon, words cannot express my appreciation for your kindness and emotional support during these four years. Although we could not see each other very often, thinking of your presence around, your unconditional love, and your positive energy made me feel at home. Amme Mahvash, I will never forget the first day that I came to the Netherlands. You came from Belgium to Schiphol airport to say welcome and not let me feel homesick. Daei joon, your support and advice were with me from the very beginning of this journey, when I was still in Iran and wanted to apply for this position. Whenever I needed some help, I was sure that I will have your support.

Moreover, I want to send my gratitude to my former supervisor during my previous educational life, Dr. **Mohammadreza Kolahdouz**, who introduced me to the amazing world of nanofabrication and helped me during the application process.

While you are far away from your family, the journey of life gives you sympathetic and warm-hearted friends that you can count on them in every situation: **Fayezeh**, **Nasibeh** & **Amir**, **Zahra** (Kolahdouz) & **Masoud**, **Zahra** (Shams) & **Hamidreza**, **Zahra** & **Sara** (Nodehi), **Somayeh** and **Behnam**, **Maedeh** & **Javad**, **Maryam** & **Ali** (Sobhani), **Narges** & **Mohammad**, **Sara** (Marzban), **Helda** and **Amir Hossein**, **Khashayar** & **Sara**, **Elmira**, **Kiana** and **Danial**, **Rezvan**, and **Sadaf**. Having you around as my true friends while living hundreds of kilometers away from my family makes life much easier and sweeter for me.

My dear **Zahra** (Shariati) and **Neda**, although we were physically far away during these years, I feel you so close whenever I need you. True friendship does not count miles.

Fayezeh! Words cannot describe how grateful I am to have you as my sister, close friend, and neighbor. You are a "happiness distributor" and a "source of positive energy" for all the people you know.

Zahra (Kolahdouz)! We knew each other a little from Iran. Although we were here together, in the Netherlands, only for 3 months, I find you so close to me and enjoy our discussions over different topics. No matter how far you are now, true friends are never apart, maybe in distance but never in heart.

helping me in my cleanroom processes. I would also thank **Rob Luttjeboer** and **Sander van Asperen** (with his friendly and smiley face) for their support, training, and assisting me to work in their lab.

Special words of appreciation go to our former and current kind secretaries: **Sabrina**, **Mirjam**, **Angelique**, **Nadine**, **Marjolijn,** and **Marit.**

Franciose, you were one of the first colleagues that I met on the first day of my Ph.D. I still remember that during our short meeting, you told me:" if you have any questions about living in the Netherlands, count on my help and do not hesitate to ask me." And you meant it. You were never an ordinary colleague for me; you were (and are) my friend and Dutch sister as well. I always remember how nice, honest, and gentle you were to everyone, positively affecting the lives of so many colleagues and making them feel at home in the Netherlands. I was so lucky to have had the opportunity to share my office with you for more than 3.5 years.

Khashayar, first of all, I would like to thank you for introducing me to the world of biology, which was very far away from my background at the beginning. You always answered my biology-related questions so patiently. I have to admit that you are an excellent teacher. I enjoyed all the discussions we had, all brainstorming sessions, all collaborative research and publications, and all nice chats about various topics.

Yageng (Dr. **Li** :D), we shared our office for more than 2.5 years, and I always admire your passion for research and ambition. You were a trustable source of any software-related question for our colleagues and patiently looked for the proper solution for them.

Eline, **Costanza**, **Kirsten**, and **Katerina**, thanks for bringing more colors to our Ph.D. life by organizing the exciting events at the Ph.D. council.

Nazli, aside from being an amazing colleague, you are one of the most generous and kind-hearted people I know and my role model as a successful woman in academia. And of course, still, I am waiting for the day that you can join us in coffee breaks or lunch ;)

Livia, I will not forget the evenings that we spent together in the lab till late. Although that part of the research took much more than we expected, in the end, the outcome was sweet and fruitful. Working with you made all impossibles possible.

Our dear **Sander**, imagining our labs without you seems impossible. You were always open to the lab users' requests.

Michelle, I am truly thankful for your involvement in my research. Without you, it was not possible to perform such high-quality cell experiments.

I would like to thank my other colleagues: **Shahram, Teunis**, **Mohammad**, **Sebastien**, **Mahdiyeh**, **Ingmar**, **Sara (Azizian)**, **Niko**, **Mauricio**, **Pedro**, **Jiahui**, **Pier**, **Gerwin**, **Dirk**, **Monica**, **Ebrahim**, **Maria**, **Vahid, Eric**, **Juan**, and **Shima** who helped me with my project.

During my Ph.D., I had the pleasure to work with several bright and sharp MSc students, and parts of this thesis would not be possible without them. I would like to thank **Dwisetya S Widyaratih**, **Manon R. O. Ligeon**, **Lorenzo B. Kunkels**, and **Dionysios Rompolas** for their help.

در دایره ی قسمت ما نقطه ی تسلیمیم

لطف آن چه تو اندیشی حکم آن چه تو فرمایی

"حافظ"

Mahya Ganjian

Aug 2021

Delft

List of publications

A. Journals

- **M. Ganjian**, S. Janbaz, T. van Manen, N. Tümer, K. Modaresifar, M. Minneboo, L.E. Fratila-Apachitei, A.A. Zadpoor, Controlled metal crumpling as an alternative to folding for the fabrication of nanopatterned meta-biomaterials, (2021), Submitted.

- **M. Ganjian**, K. Modaresifar, D. Rompolas, L.E. Fratila-Apachitei, A.A. Zadpoor, Nanoimprinting for high-throughput replication of geometrically precise pillars in fused silica to regulate cell behaviour, (2021), Acta Biomaterialia.

- T. van Manen, **M. Ganjian**, K. Modaresifar, L.E. Fratila-Apachitei, A.A. Zadpoor, Automated folding of origami lattices: from nanopatterned sheets to stiff meta-biomaterial, (2021), ArXiv.

- K. Modaresifar, **M. Ganjian**, P.J. Díaz-Payno, M. Klimopoulo, L.E. Fratila-Apachitei, A.A. Zadpoor, Mechanotransduction in high aspect ratio nanostructured meta-biomaterials: the role of cell adhesion, contractility, and transcriptional factors**,** (2021), Submitted.

- K. Modaresifar, **M. Ganjian**, L. Angeloni, M. Minneboo, M.K. Ghatkesar, P.-L. Hagedoorn, L.E. Fratila-Apachitei, A.A. Zadpoor, On the Use of Black Ti as a Bone Substituting Biomaterial: Behind the Scenes of Dual-Functionality, (2021), Small, 2100706

- L. Angeloni, **M. Ganjian**, M. Nouri-Goushki, M.J. Mirzaali, C.W. Hagen, A.A. Zadpoor, L.E. Fratila-Apachitei, M.K. Ghatkesar, Mechanical characterization of nanopillars by atomic force microscopy, 39 (2021), Additive Manufacturing, 101858.

- **M. Ganjian**, L. Angeloni, M.J. Mirzaali, K. Modaresifar, C.W. Hagen, M.K. Ghatkesar, P.-L. Hagedoorn, L.E. Fratila-Apachitei, A.A. Zadpoor, Quantitative mechanics of 3D printed nanopillars interacting with bacterial cells, 12(43) (2020), Nanoscale, 21988-22001.

- K. Modaresifar, L.B. Kunkels, **M. Ganjian**, N. Tümer, C.W. Hagen, L.G. Otten, P.-L. Hagedoorn, L. Angeloni, M.K. Ghatkesar, L.E. Fratila-Apachitei, A.A. Zadpoor,

Deciphering the roles of interspace and controlled disorder in the bactericidal properties of nanopatterns against Staphylococcus aureus, 10(2) (2020), Nanomaterials, 347.

- T. van Manen, S. Janbaz, **M. Ganjian**, A.A. Zadpoor, Kirigami-enabled self-folding origami, 32 (2020), Materials Today, 59-67

- **M. Ganjian**, K. Modaresifar, M.R. Ligeon, L.B. Kunkels, N. Tümer, L. Angeloni, C.W. Hagen, L.G. Otten, P.-L. Hagedoorn, I. Apachitei, L.E. Fratila-Apachitei, A.A. Zadpoor, Nature helps: Toward bioinspired bactericidal nanopatterns, (2019), Advanced Materials Interfaces, 1900640.

- **M. Ganjian,** K. Modaresifar, H. Zhang, P.-L. Hagedoorn, L.E. Fratila-Apachitei, A.A. Zadpoor, Reactive ion etching for fabrication of biofunctional titanium nanostructures, 9(1) (2019), Scientific Reports, 1-20.

- D.S. Widyaratih, P.-L. Hagedoorn, L.G. Otten, **M. Ganjian**, N. Tümer, I. Apachitei, C.W. Hagen, L.E. Fratila-Apachitei, A.A. Zadpoor, Towards osteogenic and bactericidal nanopatterns?, 30(20) (2019), Nanotechnology, 20LT01.

- K. Modaresifar, S. Azizian, **M. Ganjian**, L.E. Fratila-Apachitei, A.A. Zadpoor, Bactericidal effects of nanopatterns: a systematic review, 83 (2019), Acta Biomaterialia, 29-36.

- E. Esmaeli, **M. Ganjian**, H. Rastegar, M. Kolahdouz, Z. Kolahdouz, G. Q. Zhang, Sensors and Actuators B: Chemical, 247 (2017), 498-504.

- **M. Ganjian**, M. Kolahdouz, A. Aletayeb, M. Norouzi, P. Ebrahimi, S. Pourjafari and M. S. S. Mousavi, 146 (2017), Vacuum, 548-553.

B. Conferences

- **M. Ganjian**, L. Angeloni, L.E. Fratila-Apachitei, A.A. Zadpoor, Mechanobactericidal of EBID nanopillars, Word Biomaterial Congress (WBC), Glasgow (virtual), United Kingdam (2020, oral presentation).

- **M. Ganjian**, K. Modaresifar, L.E. Fratila-Apachitei, A.A. Zadpoor, Kicking eukaryotic and prokaryotic cells at sub-50 nm: How precise could it be?, European Society of Biomaterials (ESB), Dresden, Germany (2019, poster presentation).

- **M. Ganjian**, K. Modaresifar, L.E. Fratila-Apachitei, A.A. Zadpoor, Titanium nanostructures produced by inductively coupled plasma reactive ion ething and their effects on cells, Dutch Bio-Medical Engineering Conference (BME), Egmond aan Zee, The Netherlands (2019, oral presentation).

- K. Modaresifar, **M. Ganjian**, L.E. Fratila-Apachitei, A.A. Zadpoor, Surface physical nanocues with bactericidal activity, Dutch Bio-Medical Engineering Conference (BME), Egmond aan Zee, The Netherlands (2019, oral presentation).

- **M. Ganjian**, K. Modaresifar, L.E. Fratila-Apachitei, A.A. Zadpoor, The effects of RIE conditions on the characteristics of black Ti structures, Micro and Nanoengineering (MNE), Copenhagen, Denmark (2018, poster presentation).

Curriculum Vitae

Mahya Ganjian was born on 17 September 1990 in Tehran, Iran. She received the B.Sc. and M.Sc. degrees in Electrical Engineering from University of Tehran, Iran, in 2013 and 2016, respectively. She was a researcher in Thin Film Laboratory, in 2014-2017. During her master study, she was working on the third-generation solar cells, fabrication of quantum dots, growth control of zinc nanowires, and development and applications of ionic polymer-metal composite (IPMC)s. In 2017, she started her Ph.D. in the Biomechanical Engineering department at the faculty of Mechanical, Maritime, and Materials Engineering of Delft University of Technology, The Netherlands, where she worked on the applications of nanopatterns with specific dimensions and mechanical properties on the surface of the novel biomaterials for bone tissue engineering applications, under the supervision of Prof. Amir A. Zadpoor and Dr. Lidy E. Fratila-Apachitei.